Perovskite-Based Chemiresistive Gas Sensors for Automotive Exhaust Emissions

Fundamentals, DFT Modeling, and Experimental Validation Using Ag-Doped $BiFeO_3$

Dr. Amogh Anil Sambare

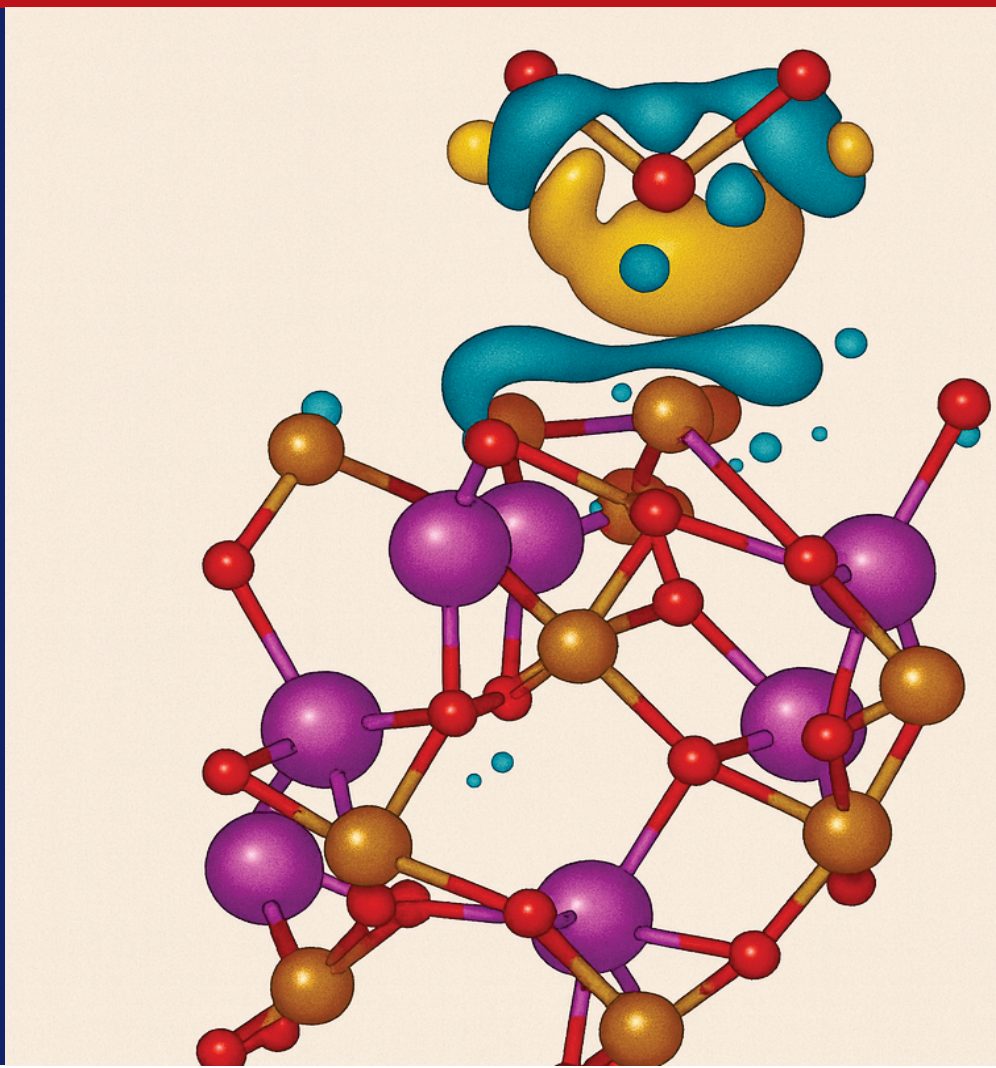

Perovskite-Based Chemiresistive Gas Sensors for Automotive Exhaust Emissions: Fundamentals, DFT Modeling, and Experimental Validation Using Ag-Doped $BiFeO_3$

By:
Dr. Amogh Anil Sambare

Perovskite-Based Chemiresistive Gas Sensors for Automotive Exhaust Emissions: Fundamentals, DFT Modeling, and Experimental Validation Using Ag-Doped $BiFeO_3$

Author: Dr. Amogh Anil Sambare

Publishing Year: 2025

ISBN: **978-93-91044-86-2**

Price Rs. 899.00
US $ 299.00

Published By :
Imperial Publications
304 De Elmas Sonawala Cross Rd 2
Goregaon E Mumbai-400063, Maharashtra India
info@imperialpublications.com, www.imperialpublications.com

Designed, Layout, Typeset Printed by: **VPS DIGITAL PRINT**
A-1/18, Ambedkar Nagar, BaprolaVihar, New Delhi-110043

Cover Page Designed by: **VPS DIGITAL PRINT**

Preface

The growing concern over environmental pollution and the urgent need for reliable detection of toxic gases have driven extensive research in recent years toward the development of advanced sensing materials. Among various materials, perovskite-based oxides have emerged as a promising class owing to their unique structural flexibility, multifunctionality, and chemical stability. This book presents a comprehensive exploration of such materials—particularly Bismuth Ferrite ($BiFeO_3$) and its silver-doped derivatives—for their potential application in high-temperature chemiresistive gas sensors.

The motivation for this work stems from the increasing global demand for compact, efficient, and cost-effective sensing systems that can operate reliably under harsh environmental conditions, such as those found in automotive exhausts and industrial emissions. Bismuth Ferrite (BFO), a multiferroic perovskite oxide, offers a rare combination of electrical, magnetic, and optical properties, making it a versatile candidate for gas detection applications. However, the practical performance of BFO-based sensors depends strongly on surface chemistry, defect states, and electronic structure—all of which can be precisely tailored through doping and nanostructuring.

This book integrates both theoretical and experimental perspectives. The first part focuses on Density Functional Theory (DFT) investigations of gas adsorption phenomena on pure and Ag-doped $BiFeO_3$ surfaces, providing atomistic insights into charge transfer, adsorption energetics, and electronic structure modifications. The second part discusses the experimental synthesis and characterization of BFO and Ag-BFO nanostructures, including their crystal, morphological, and spectroscopic features. The third part bridges these findings through gas sensing performance studies, detailing sensitivity, selectivity, and response–recovery dynamics for key environmental gases such as CO, NO, NO_2, and SO_2.

An important highlight of this book is the introduction of multivariate statistical analysis, specifically Principal Component Analysis (PCA), to interpret sensor response patterns. This approach demonstrates the potential of doped BFO materials for selective gas discrimination, marking a significant step toward intelligent sensor design and “electronic nose” development.

The book is intended for graduate students, researchers, and professionals in materials science, nanotechnology, solid-state physics, and environmental engineering. It will also serve as a valuable reference for those working on sensor materials design, computational materials modeling, and multifunctional oxide research.

I am deeply grateful to my mentors, colleagues, and the research community for their invaluable guidance, insightful discussions, and constant encouragement throughout this work. My heartfelt appreciation goes to my parents for their unwavering support and blessings, to my wife Shraddha for her patience and inspiration, and to my daughter Advika for being a source of endless joy and motivation. I also extend my sincere thanks to my institution-Deen Dayal Upadhyay KAUSHAL Kendra, Dr. Babasaheb Ambedkar Marathwada University, Chhatrapati Sambhajinagar-for providing an intellectually stimulating environment and the necessary research infrastructure that made this work possible.

It is my sincere hope that this book will inspire further research in the field of perovskite-based gas sensors and contribute to the broader scientific endeavor of developing cleaner, safer, and smarter technologies for a sustainable future.

Dr. Amogh Anil Sambare
Assistant Professor
Deen Dayal Upadhyay KAUSHAL Kendra
Dr. Babasaheb Ambedkar Marathwada University
Chhatrapati Sambhajinagar, India
(2025)

Table of Content

Overview of Automotive Exhaust Pollution and Chemiresistive Gas Sensing Principles

This chapter provides a comprehensive overview of pollutants emitted from automotive exhausts and their impact on human health and the environment. It further discusses various gas-sensing technologies and classification principles, emphasizing the importance of developing robust chemiresistive gas sensors for reliable detection under harsh operating conditions. The chapter concludes by outlining the critical performance parameters governing sensor behavior, thereby laying the foundation for subsequent discussions on nanostructured materials and advanced sensing mechanisms in later chapters.

1.1 Pollutants from Automotive Exhausts

The term *automotive exhaust* refers to the mixture of air pollutants released into the atmosphere when a vehicle's engine burns fuels such as gasoline, diesel, kerosene, oil, or other fossil fuels [1,2,3]. During engine operation, these fuels undergo combustion to generate power; however, even under optimal conditions, the process remains incomplete, leading to the emission of a variety of gaseous and particulate pollutants. Long-term exposure to automotive exhaust has been associated with an increased risk of respiratory problems, cardiovascular diseases, and cancer [4,5]. Air pollution caused by vehicular emissions poses a serious threat not only to human health but also to the natural environment. Both individuals and ecosystems are adversely affected by the particulate pollution generated from vehicle exhausts [6]. In general, the emissions from automobiles have multiple negative consequences, extending beyond human well-being to affect global ecological stability [7].

At the onset of motorized transportation, vehicle emissions were recognized as a significant contributor to air pollution. These emissions contain dust, soot, and other fine particles that can be easily carried into the atmosphere by wind currents. Numerous studies have demonstrated a strong association between air pollution and various health disorders, including respiratory ailments, cardiovascular diseases, and certain types of cancer [8].

To address this growing problem, diverse approaches have been adopted to minimize pollution caused by automobiles. These include the development of advanced low-emission vehicle technologies and the implementation of more stringent emission regulations for cars and trucks [9]. On days characterized by high levels of haze or smog, individuals can also take preventive measures—such as improving indoor ventilation and avoiding prolonged outdoor activities—to minimize exposure to pollutants [10].

During normal operation, a vehicle releases numerous pollutants into the atmosphere. These contaminants may enter the air we breathe or even infiltrate water systems, thereby affecting both terrestrial and aquatic environments. Several of these exhaust components have been directly linked to respiratory and cardiovascular disorders [11]. Human health and ecosystem integrity are both vulnerable to the toxic effects of these pollutants [12]. Vehicle exhaust emissions can disrupt natural systems, contaminate groundwater with hazardous substances, and significantly contribute to the acceleration of global warming [13]. Overall,

automobiles are major contributors to three key forms of environmental degradation—air pollution, water pollution, and noise pollution [14].

Automobile exhaust is known to contain numerous toxic compounds that irritate the respiratory system [15]. The degradation of urban air quality is primarily caused by pollutants such as carbon monoxide, nitrogen dioxide, sulfur dioxide, and hydrocarbons, including unburned fuel vapors [16]. To protect public health and environmental quality, guidelines for automobile emissions have been formulated and enforced worldwide [17].

Automotive exhausts thus remain a major source of air pollution, releasing a wide spectrum of harmful substances that exert both direct and indirect effects on living organisms and the environment [18]. The principal pollutants emitted from vehicle exhaust include the following:

I. **Carbon Monoxide (CO):**
Carbon monoxide is a colorless, odorless, and highly toxic gas produced by the incomplete combustion of fuel. It interferes with the body's oxygen transport mechanism by forming carboxyhemoglobin, thereby reducing oxygen delivery to tissues and organs. Exposure to elevated CO levels may cause headaches, nausea, dizziness, and, in severe cases, death [19].

II. **Nitrogen Oxides (NO_x):**
Nitrogen oxides are a group of reactive gases generated at high combustion temperatures in engines. They play a major role in the formation of photochemical smog and acid rain and are associated with respiratory conditions such as asthma and bronchitis [20].

III. **Particulate Matter (PM):**
Particulate matter consists of fine solid particles and liquid droplets suspended in the atmosphere, including dust, soot, and metallic residues. Due to their small aerodynamic diameter, these particles can penetrate deep into the respiratory tract, causing respiratory and cardiovascular complications [21].

IV. **Volatile Organic Compounds (VOCs):**
VOCs are organic chemicals emitted as gases from fuel components and lubricants. Compounds such as benzene and formaldehyde contribute to the formation of photochemical smog and are linked to respiratory disorders and carcinogenic effects [22].

V. **Hydrocarbons (HCs):**
Hydrocarbons arise from unburned or partially burned fuel and play a critical role in smog formation through atmospheric photochemical reactions. Chronic exposure to hydrocarbons is associated with respiratory illnesses, eye irritation, and certain cancers [23].

VI. **Sulfur Dioxide (SO_2):**
Sulfur dioxide is a toxic gas produced when fuels containing sulfur compounds undergo combustion. It aggravates respiratory diseases, especially asthma, and is a primary contributor to acid rain, which damages vegetation, soils, and aquatic ecosystems [24].

To mitigate the harmful effects of these pollutants, a range of regulatory measures and technological innovations have been implemented globally. Emission standards now limit the allowable quantity of pollutants emitted by vehicles [25]. Furthermore, advanced control technologies such as catalytic converters, which promote the oxidation of CO and hydrocarbons and the reduction of NO_x, along with diesel particulate filters (DPFs) that capture fine soot particles, have been developed to significantly reduce exhaust emissions [26]. These advancements mark important progress toward cleaner and more sustainable transportation systems.

Over the past century, the exponential growth of motorized transport has made vehicular emissions one of the largest contributors to urban air pollution. In the 1970s and 1980s, the introduction of leaded gasoline, diesel combustion, and inefficient engines caused a dramatic rise in atmospheric pollutants. With the introduction of catalytic converters and stricter emission norms such as Euro standards**,** EPA Tier regulations, and Bharat Stage norms, significant progress has been achieved in reducing exhaust emissions. Nonetheless, the growing number of vehicles worldwide continues to challenge air quality management efforts.

1.2 Impact of Automotive Exhaust Pollutants

Automotive exhaust emissions contain a complex mixture of toxic gases and particulate matter that adversely affect both human health and the natural environment. Pollutants such as carbon monoxide, nitrogen oxides, particulate matter, lead, and sulfur dioxide are among the major contributors to atmospheric degradation. It is estimated that vehicle exhaust fumes are responsible for more than a quarter of a million premature deaths each year in the United States alone [27].

1.2.1 Carbon Monoxide (CO)

Carbon monoxide is a highly toxic gas produced by the incomplete combustion of fuels such as gasoline, diesel, and oil. Inhalation of CO reduces the oxygen-carrying capacity of blood, impairing oxygen delivery to vital organs and tissues. Prolonged or high-level exposure may lead to cardiovascular complications, stroke, and respiratory disorders such as asthma. Compared to gasoline engines, diesel engines generally emit higher quantities of carbon monoxide [28].

1.2.2 Lead (Pb)

Lead is a toxic heavy metal that poses serious health risks, particularly to children. Exposure to lead can impair brain development and damage the nervous and cardiovascular systems. Children may be exposed through contact with contaminated surfaces, soil, or deteriorating lead-based paints. The severity of lead toxicity depends on the level and duration of exposure as well as individual genetic factors. Chronic exposure can result in neurological deficits, while acute poisoning may cause severe mental impairment or even death [29].

1.2.3 Nitrogen Dioxide (NO_2)

Nitrogen dioxide is a reactive gas that can damage the airways and contribute to respiratory and cardiovascular diseases. It is primarily produced during the combustion of fossil fuels such as gasoline and diesel. Diesel engines, in particular, are known to emit higher concentrations of nitrogen oxides compared to gasoline engines. Chronic exposure to NO_2 has been linked to asthma, decreased lung function, and increased susceptibility to respiratory infections [30].

1.2.4 Sulfur Dioxide (SO_2)

Sulfur dioxide emissions from motor vehicles are a major precursor to acid rain formation. When released into the atmosphere, SO_2 reacts with water vapor to form sulfuric acid, which lowers the pH of lakes and streams. Acid rain damages aquatic ecosystems, corrodes buildings and infrastructure, and harms vegetation [31].

In addition to primary pollutants such as CO, NO_x, and hydrocarbons, vehicle exhausts also emit carbon dioxide (CO_2), methane (CH_4), and nitrous oxide (N_2O), which are major greenhouse gases contributing to climate change. Secondary pollutants like tropospheric ozone and photochemical smog are formed through atmospheric reactions between NO_x and hydrocarbons under sunlight, exacerbating respiratory distress and reducing visibility in urban areas.

1.2.5 Other Physiological Effects

In addition to their acute toxicity, automotive exhaust pollutants can exert long-term physiological effects on the human body. Continuous exposure to nitrogen dioxide and particulate matter has been associated with chronic respiratory conditions such as asthma, bronchitis, and emphysema. Moreover, ultrafine particles in exhaust gases have been linked to increased risks of cardiovascular diseases and lung cancer [32].

1.2.6 Broader Impacts of Exhaust Pollutants

The pollutants emitted from automotive exhausts have wide-ranging implications for human health, environmental balance, and climate systems. Some of the most significant impacts include:

1. **Human Health:** Continuous exposure to exhaust pollutants can result in respiratory and cardiovascular diseases, including asthma, bronchitis, and heart ailments. Long-term inhalation of polluted air is also correlated with higher incidences of cancer and other chronic health problems [33].

2. **Environmental Impact:** Vehicular emissions contribute to the formation of photochemical smog and acid rain, both of which damage vegetation, soil, and aquatic life. Additionally, particulate matter reduces visibility and makes the air more difficult to breathe [34].

3. **Climate Change:** Automotive pollutants such as carbon dioxide (CO_2), methane, and nitrous oxide act as greenhouse gases, trapping heat in the Earth's atmosphere. This process contributes to global warming, leading to consequences such as rising sea levels, extreme weather events, prolonged droughts, and heatwaves [35].

4. **Air Quality Degradation:** Exhaust pollutants increase atmospheric concentrations of particulate matter, nitrogen oxides, carbon monoxide, and hydrocarbons, all of which deteriorate air quality. Poor air quality has been directly linked to respiratory distress, cardiovascular diseases, and premature mortality [36].

5. **Ozone Formation and Depletion:** Nitrogen oxides and volatile organic compounds released from vehicles participate in photochemical reactions that generate ground-level ozone. This pollutant, a major component of smog, irritates the respiratory tract and exacerbates existing pulmonary conditions [37].

1.2.7 Mitigation and Control Strategies

To reduce the adverse effects of automotive exhaust pollutants, governments and industries have introduced stringent emission regulations that limit permissible pollutant levels [38]. Advanced technologies such as catalytic converters, which facilitate the oxidation of CO and hydrocarbons and the reduction of NO_x, and diesel particulate filters (DPFs), which trap fine particulate matter, have proven highly effective in controlling emissions. Furthermore, the global shift toward cleaner transportation alternatives—including electric vehicles, hybrid engines, and improved public transportation systems—represents a vital step toward reducing the environmental footprint of the automotive sector.

1.3 Prominent Methods for Sensing Gases from Automotive Exhaust

Monitoring exhaust gases is essential for evaluating engine performance, ensuring compliance with emission standards, and developing strategies for pollution reduction. Various sensing technologies have been designed to detect specific pollutants in automotive exhaust streams with high sensitivity and selectivity. The most prominent methods include the following:

1.3.1 Metal Oxide Semiconductor (MOS) Sensors

Metal oxide semiconductor (MOS) sensors operate based on changes in the electrical resistance of a metal oxide material when exposed to target gases. Interaction between gas molecules and the sensor surface alters the carrier concentration within the semiconductor, leading to a measurable resistance change. This variation is proportional to the gas concentration. MOS sensors are widely used for detecting carbon monoxide (CO), nitrogen oxides (NO_x), and hydrocarbons (HCs) due to their robustness, low cost, and fast response characteristics [39].

1.3.2 Infrared (IR) Sensors

Infrared sensors employ the principle of infrared light absorption at specific wavelengths corresponding to the vibrational modes of gas molecules. When exhaust gases pass through the sensor chamber, the degree of IR light absorption indicates the concentration of the target gas. IR sensors are extensively used to monitor gases such as carbon monoxide and hydrocarbons, offering high selectivity and long-term stability, though they can be relatively expensive and sensitive to optical contamination.

1.3.3 Electrochemical Sensors

Electrochemical sensors utilize a combination of electrodes and an electrolyte to generate an electrical current when a target gas undergoes an electrochemical reaction at the sensing electrode. The magnitude of this current is directly proportional to the gas concentration. These sensors are particularly effective for detecting oxygen (O_2) and carbon monoxide (CO), providing high accuracy and low power consumption. However, they generally have a limited operational lifespan and are sensitive to temperature and humidity variations [40].

1.3.4 Semiconductor Sensors

Semiconductor gas sensors function by detecting variations in electrical conductivity caused by gas adsorption or desorption on the surface of a semiconductor material. The resulting change in conductivity corresponds to the concentration of the target gas. These sensors are widely applied for detecting carbon monoxide and nitrogen oxides and are known for their rapid response times and compact design. However, they may suffer from cross-sensitivity and require precise temperature control for optimal performance [41].

1.3.5 Laser-Based Sensors

Laser-based sensors employ tunable laser absorption spectroscopy to identify specific gases through their unique absorption lines at precise wavelengths. By measuring the intensity of absorbed laser light, the concentration of gases such as carbon monoxide (CO), nitrogen dioxide (NO_2), and sulfur dioxide (SO_2) can be accurately determined. These sensors provide exceptional precision, fast response, and the capability for real-time, in-situ measurements, though they are typically more complex and expensive than conventional techniques [42].

1.3.6 Optical Fiber Sensors

Optical sensors utilize fiber-optic cables coated with gas-sensitive materials. When exposed to target gases, changes in light transmission, reflection, or scattering occur within the optical fiber, which are correlated to gas concentration. Optical fiber sensors are particularly suitable for monitoring CO, NO_2, and SO_2 due to their resistance to electromagnetic interference, remote-sensing capability, and adaptability to harsh exhaust environments [43].

1.3.7 Comparative Evaluation

Each of these sensing techniques offers distinct advantages and limitations depending on the target gas, environmental conditions, and application requirements. MOS and semiconductor sensors are economical and compact but may exhibit reduced selectivity. Infrared and laser-based sensors provide superior accuracy and long-term stability, though they are costlier and require optical maintenance. Electrochemical sensors deliver precise measurements at low power, while optical fiber sensors excel in remote and high-temperature environments. Selecting an appropriate sensing technology thus depends on factors such as gas composition, sensitivity range, durability, cost constraints, and intended automotive application.

Sensing Method	**Detection Principle**	**Typical Target Gases**	**Key Advantages**	**Limitations**
Metal Oxide Semiconductor (MOS)	Change in electrical resistance of a metal-oxide layer due to surface adsorption of gas molecules	CO, NO_x, H_2, VOC compounds	Low-cost, compact, fast response, high sensitivity	Requires elevated temperature; cross-sensitivity to humidity and other gases
Infrared (IR)	Absorption of characteristic infrared wavelengths corresponding to vibrational modes of gas molecules	CO, CO_2, CH_4, HCs	High selectivity and stability; non-contact optical measurement	Expensive optics; sensitive to contamination and vibration
Electrochemical	Redox reaction at electrodes generates a current proportional to gas concentration	O_2, CO, H_2S, NO_2	High accuracy, low power consumption, good linearity	Limited operational lifetime; affected by temperature/humidity
Semiconductor (non-oxide)	Change in electrical conductivity of semiconducting material upon gas adsorption/desorption	CO, NO_2, NH_3	Rapid response, miniaturizable, low power	Stability and selectivity issues; requires calibration

Optical Fiber	Variation in light transmission, reflection, or scattering through coated optical fiber when gas interacts with sensing layer	CO, NO_2, SO_2	Immune to electromagnetic interference; enables remote and harsh-environment sensing	Fragile fibers; complex fabrication; higher cost
Laser-Based (TDLAS / Photoacoustic)	Measurement of gas-specific absorption lines using tunable lasers	CO, NO_2, SO_2, CH_4	Exceptional precision and real-time response; in-situ capability	High instrument cost; needs optical alignment and maintenance

Table 1.1 Comparative overview of common gas sensing technologies

1.4 Classifications of Gas Sensing Principles

Gas-sensing technologies are generally classified based on the fundamental detection principle employed to identify and quantify target gases. These principles determine the nature of the interaction between the sensing element and the gas molecules and, consequently, influence the sensitivity, selectivity, and response characteristics of the sensor. Broadly, gas sensors can be categorized into physical, chemical, and biological sensing types [44–46].

Physical Gas Sensing

Physical gas sensing relies on the intrinsic physical properties of gases, such as thermal conductivity, density, or refractive index. In this approach, the target gas interacts with the sensor without undergoing a chemical reaction. The sensing mechanism typically involves measuring variations in temperature, pressure, mass, or light transmission caused by the presence of the gas [44].

Common physical sensing methods include:

- **Thermal Conductivity:** Measures the rate at which a gas conducts heat; useful for detecting binary gas mixtures.
- **Infrared (IR) Absorption:** Detects characteristic IR absorption wavelengths corresponding to specific gas molecules.
- **Mass Spectroscopy:** Identifies gases based on the mass-to-charge ratio of ionized species.
- **Optical Absorption:** Monitors changes in light absorption or transmission caused by the target gas.
- **Surface Acoustic Wave (SAW):** Detects frequency shifts in acoustic waves propagating along a piezoelectric substrate upon gas adsorption.

Physical sensors typically offer fast response times, high stability, and reusability, but they may lack selectivity when multiple gases are present simultaneously.

Chemical Gas Sensing

Chemical gas sensing operates on the principle of chemical interactions between the target gas and the sensing material. These interactions—such as redox reactions, adsorption, or catalytic processes—induce

measurable changes in the material's electrical properties, including resistance, conductivity, current, or potential [45].

Common chemical sensing methods include:

- **Electrochemical Sensors:** Measure current generated from gas-induced electrochemical reactions at electrodes.
- **Catalytic Combustion Sensors:** Detect heat produced during the oxidation of combustible gases on a catalyst surface.
- **Semiconductor Sensors:** Utilize changes in electrical conductivity of semiconducting materials upon gas adsorption.
- **Metal Oxide Sensors:** Rely on surface reactions between gas molecules and metal oxide semiconductors, leading to resistance changes.
- **Quartz Crystal Microbalance (QCM):** Detects changes in resonant frequency of a quartz crystal due to gas adsorption on its surface.

Chemical sensors are widely used due to their high sensitivity, compact size, and cost-effectiveness, though they may suffer from cross-sensitivity and limited stability in varying humidity or temperature conditions.

Biological Gas Sensing

Biological gas sensing involves biochemical interactions between the target gas and a biological recognition element, such as enzymes, antibodies, microorganisms, or DNA sequences. These biosensors exploit specific binding or catalytic reactions to generate measurable signals, such as changes in enzyme activity, protein conformation, or gene expression [46].

Common biological sensing methods include:

- **Enzyme-Based Sensors:** Detect gases that serve as substrates or inhibitors for specific enzyme-catalyzed reactions.
- **Microbial Sensors:** Utilize living microorganisms that produce measurable electrical or optical responses upon gas exposure.
- **Immunological Sensors:** Employ antibodies that selectively bind to gas-related antigens or molecular markers.
- **Genetic Sensors:** Involve engineered DNA or RNA sequences that respond to target gases by altering gene expression or fluorescence.

Biological sensors provide exceptional selectivity and biocompatibility, making them suitable for environmental monitoring and medical diagnostics. However, they often require controlled conditions for stability and are less robust for high-temperature or harsh automotive environments

Each sensing category offers unique advantages and is best suited for specific applications and target gases. Physical sensors excel in durability and rapid detection, chemical sensors in sensitivity and cost-effectiveness, and biological sensors in selectivity and specificity. In practice, hybrid systems combining multiple sensing principles—such as chemo-optical or electrochemical–biological sensors—are increasingly

being developed to enhance overall performance, reliability, and selectivity under complex environmental conditions.

1.5 Need for a Robust Chemiresistive Gas Sensing System

Chemiresistive gas sensors operate on the principle that the electrical resistance of a conductive or semiconductive material changes in response to exposure to a target gas or vapor. The sensing material—commonly based on metal oxides, carbon nanostructures, or conducting polymers—undergoes surface reactions with gas molecules, altering its charge carrier concentration and consequently its resistance. This simple yet highly effective mechanism makes chemiresistive sensors one of the most widely used gas-sensing technologies for applications such as environmental monitoring, industrial process control, and medical diagnostics [47].

A robust chemiresistive gas sensing system is essential because such sensors are often deployed in harsh and variable environments where they must maintain stable performance over extended periods. Automotive exhaust monitoring, for instance, involves exposure to high temperatures, fluctuating humidity, corrosive gases, and particulate contaminants, all of which can degrade sensor stability and accuracy. Therefore, the design of a robust sensing system must ensure thermal endurance, chemical resilience, and mechanical durability under these demanding conditions [48].

Developing such robustness involves a combination of material engineering, structural optimization, and intelligent system integration. Key strategies include:

- **Selection of Appropriate Sensing Materials:** Using thermally and chemically stable materials—such as metal oxides, perovskites, or doped nanocomposites—that maintain sensitivity and selectivity under extreme operating conditions.
- **Encapsulation and Packaging:** Proper encapsulation protects the sensing element from environmental contaminants such as dust, moisture, and corrosive gases, enhancing long-term stability.
- **Calibration and Conditioning:** Implementing accurate calibration techniques and pre-conditioning cycles ensures reproducible sensor behavior across varying environmental parameters.
- **Advanced Signal Processing:** Employing algorithms for noise reduction, drift compensation, and pattern recognition improves both the precision and reliability of sensor output.

Overall, the need for a robust chemiresistive gas sensing system lies in its ability to deliver consistent, accurate, and long-term performance, even in challenging environmental conditions. Such reliability is crucial for ensuring the safety, efficiency, and environmental compliance of systems where these sensors are applied—particularly in automotive exhaust monitoring, where accurate detection of toxic gases directly supports emission control and regulatory compliance.

1.6 Performance Parameters for Chemiresistive Gas Sensors

Chemiresistive gas sensors—often referred to as metal oxide semiconductor (MOS) gas sensors—function by measuring variations in the electrical resistance of a semiconducting material when exposed to target gas molecules. Their performance is determined by several key parameters that collectively define the sensor's reliability, accuracy, and practical applicability. Understanding and optimizing these parameters is essential

for the development of high-performance gas sensing systems, particularly for demanding environments such as automotive exhaust monitoring.

The primary performance parameters include the following:

I. Sensitivity

Sensitivity refers to the ability of a sensor to detect small concentrations of a specific gas. It represents the magnitude of resistance (or conductance) change per unit concentration of the analyte, typically expressed in terms of resistance ratio (R_a/Rg) or resistance change per parts per million (ppm) of the target gas. High sensitivity allows detection of trace-level gases, making this parameter vital for early detection and low-concentration monitoring applications.

II. Selectivity

Selectivity describes the sensor's capability to distinguish the target gas from other interfering species. A highly selective sensor responds predominantly to the desired gas, minimizing cross-sensitivity to other environmental constituents. Achieving good selectivity often requires careful material design, surface modification, and doping, which promote specific surface reactions or adsorption characteristics for particular gas molecules.

III. Response Time

Response time is defined as the duration required for the sensor to reach 90% of its total resistance change upon exposure to the target gas. A shorter response time indicates faster gas–surface interaction kinetics and efficient charge transfer mechanisms. Rapid response is critical in automotive exhaust sensing, where gas concentrations fluctuate dynamically.

IV. Recovery Time

Recovery time refers to the period needed for the sensor to return to its baseline resistance once the target gas is removed. A shorter recovery time enables the sensor to monitor rapidly changing gas concentrations and ensures reliable operation under transient conditions. Recovery efficiency can be enhanced through optimal operating temperature control and the use of materials with low adsorption energy barriers.

V. Linearity

Linearity indicates how proportionally the sensor output changes with variations in gas concentration. A sensor exhibiting high linearity ensures that the measured resistance (or voltage) maintains a direct and predictable relationship with concentration, simplifying calibration and data interpretation. Nonlinear responses may require correction through signal-processing algorithms.

VI. Stability

Stability measures the ability of the sensor to maintain consistent performance over extended periods of operation. Factors influencing stability include material degradation, surface contamination, and environmental variations. A stable sensor produces repeatable readings with minimal drift, even after prolonged exposure to high temperatures or reactive gases. Long-term stability is particularly essential for continuous monitoring applications in automotive and industrial systems.

VII. Temperature and Humidity Dependence

Chemiresistive gas sensors are inherently sensitive to ambient temperature and humidity, which can affect adsorption/desorption rates and carrier mobility in the sensing material. Excessive humidity may cause water molecule adsorption, altering surface reactions, while temperature fluctuations can shift the baseline resistance. Therefore, characterizing and compensating for temperature and humidity dependence is vital for maintaining sensor accuracy under real-world conditions.

- **Performance Optimization Strategies:** Enhancing gas sensor performance involves optimizing the sensing material, structural design, and system integration.
- **Material Engineering:** Nanostructuring, surface functionalization, and selective doping improve sensitivity and selectivity.
- **Temperature Control:** Using microheaters or temperature modulation enhances gas adsorption and desorption rates.
- **Signal Conditioning:** Implementing advanced algorithms reduces noise and drift.
- **Hybrid Architectures:** Combining MOS with optical or electrochemical elements enables multisensing and improved accuracy.

1.7 Summary

Automotive exhaust refers to the complex mixture of air pollutants released into the atmosphere during the combustion of fuels such as gasoline, diesel, kerosene, and other fossil fuels. During vehicle operation, these emissions are continuously discharged into the surrounding environment, contributing significantly to air pollution. Long-term exposure to automotive pollutants has been strongly associated with various health disorders, including respiratory illnesses, cardiovascular diseases, and several forms of cancer. Extensive research has established the link between vehicular emissions and adverse effects on both human health and environmental sustainability.

Among the major pollutants emitted from vehicle exhausts are carbon monoxide (CO), nitrogen oxides (NO_x), hydrocarbons (HCs), and particulate matter (PM). These toxic substances can infiltrate the air we breathe and, in some cases, contaminate soil and water systems, leading to long-term ecological damage. Vehicular emissions not only degrade air quality but also contribute to global warming, acid rain, and ground-level ozone formation. To mitigate these impacts, regulatory frameworks and emission standards have been established worldwide to safeguard public health and ensure environmental protection.

To accurately detect and quantify these harmful gases, several sensing technologies have been developed, including metal oxide semiconductor (MOS) sensors, infrared (IR) sensors, electrochemical sensors, semiconductor sensors, optical fiber sensors, and laser-based systems. Each sensing approach offers distinct advantages in terms of sensitivity, selectivity, response time, and operating conditions. The choice of technique depends on the specific application, target gas, and environmental parameters.

Gas sensing mechanisms are broadly classified into physical, chemical, and biological categories. Physical gas sensing relies on changes in measurable physical properties such as thermal conductivity, refractive index, or mass. Chemical gas sensing involves surface or bulk chemical interactions that alter electrical resistance or conductivity. Biological gas sensing exploits biochemical reactions, such as enzyme activity or

receptor–ligand interactions, to detect target gases. Hybrid sensing systems that combine multiple principles are increasingly being developed to achieve improved performance, selectivity, and reliability.

Finally, the development of a robust chemiresistive gas sensing system is essential for effective monitoring in harsh environments, such as automotive exhausts, where conditions involve extreme temperatures, high humidity, and chemically reactive species. The robustness of a chemiresistive sensor depends on the selection of suitable sensing materials, stable encapsulation, precise calibration, and advanced signal-processing algorithms. A well-designed and durable chemiresistive sensing system ensures accurate, consistent, and long-term detection of exhaust gases, thereby supporting environmental protection, regulatory compliance, and sustainable transportation technologies.

Future Outlook

As global emission regulations become increasingly stringent, the demand for intelligent, low-cost, and durable gas sensing systems continues to grow. The integration of nanostructured materials**,** AI-assisted data analytics, and Internet-of-Things (IoT) frameworks is expected to revolutionize gas sensing technology. The next chapter explores advances in nanostructured and perovskite-based chemiresistive materials**,** focusing on their synthesis, structural characteristics, and application potential in real-time automotive exhaust monitoring.

References:

1. Beppu, K. (2018). Pd/SrFe1–xTixO3−δ as Environmental Catalyst: Purification of Automotive Exhaust Gases. ACS Applied Materials & Interfaces, 10(26), 22182–22189. https://doi.org/10.1021/ACSAMI.8B05169

2. Plachá, M. (2020). Pore-scale filtration model for coated catalytic filters in automotive exhaust gas aftertreatment. Chemical Engineering Science, 226, 0. https://doi.org/10.1016/J.CES.2020.115854

3. Peron, G. (2019). Perovskites as Alternatives to Noble Metals in Automotive Exhaust Abatement: Activation of Oxygen on LaCrO 3 and LaMnO 3. Topics in Catalysis, 62(1), 244–251. https://doi.org/10.1007/S11244-018-1120-1

4. Nishibori, M. (2008). Long-term stability of Pt/alumina catalyst combustors for micro-gas sensor application. Journal of The European Ceramic Society, 28(11), 2183–2190. https://doi.org/10.1016/J.JEURCERAMSOC.2008.02.018

5. Zhang, F.-H. (2019). High performance In2(MoO4)3@In2O3 nanocomposites gas sensor with long-term stability. Journal of Alloys and Compounds, 805, 180–188. https://doi.org/10.1016/J.JALLCOM.2019.06.369

6. Jiang, Y. (2019). Air quality, human behavior and urban park visit: a case study in Beijing. Journal of Cleaner Production, 240, 0. https://doi.org/10.1016/J.JCLEPRO.2019.118000

7. Ghosh, A. (2017). Modeling the sensing characteristics of chemi-resistive thin film semi-conducting gas sensors. Physical Chemistry Chemical Physics, 19(34), 23431–23443. https://doi.org/10.1039/C7CP04241H

8. Kim, K.-H. (2015). A review on the human health impact of airborne particulate matter. Environment International, 74(74), 136–143. https://doi.org/10.1016/J.ENVINT.2014.10.005

9. Rao, S. K. (2020). Unequivocal evidence of enhanced room temperature sensing properties of clad modified Nd doped mullite Bi2Fe4O9 in fiber optic gas sensor. Journal of Alloys and Compounds, 838, 0. https://doi.org/10.1016/J.JALLCOM.2020.155603

10. Stabile, L. (2017). The effect of natural ventilation strategy on indoor air quality in schools. Science of The Total Environment, 595, 894–902. https://doi.org/10.1016/J.SCITOTENV.2017.03.048

11. Heck, J. E. (2013). Childhood Cancer and Traffic-Related Air Pollution Exposure in Pregnancy and Early Life. Environmental Health Perspectives, 121, 1385–1391. https://doi.org/10.1289/EHP.1306761

12. Kordasht, H. K. (2020). Biosensing of microcystins in water samples; recent advances. Biosensors and Bioelectronics, 165, 0. https://doi.org/10.1016/J.BIOS.2020.112403

13. Kumar, S. (2011). Aldehyde, Ketone and Methane Emissions from Motor Vehicle Exhaust: A Critical Review. American Chemical Science Journal, 1(1), 1–27. https://doi.org/10.9734/ACSJ/2011/214

14. Tsujita, W. (2005). Gas sensor network for air-pollution monitoring. Sensors and Actuators B-Chemical, 110(2), 304–311. https://doi.org/10.1016/J.SNB.2005.02.008

15. Castoldi, L. (2020). An Overview on the Catalytic Materials Proposed for the Simultaneous Removal of NOx and Soot. Materials, 13(16), 16. https://doi.org/10.3390/MA13163551

16. Akbarzadeh, M. A. (2018). The association between exposure to air pollutants including PM10, PM2.5, ozone, carbon monoxide, sulfur dioxide, and nitrogen dioxide concentration and the relative risk of developing STEMI: A case-crossover design. Environmental Research, 161, 299–303. https://doi.org/10.1016/J.ENVRES.2017.11.020

17. Cames, M. (2013). Critical evaluation of the European diesel car boom - global comparison, environmental effects and various national strategies. Environmental Sciences Europe, 25(1), 1. https://doi.org/10.1186/2190-4715-25-15

18. Yu, J. (2017). High-sensitivity low-power tungsten doped niobium oxide nanorods sensor for nitrogen dioxide air pollution monitoring. Sensors and Actuators B-Chemical, 238(238), 204–213. https://doi.org/10.1016/J.SNB.2016.07.001

19. Mehta, S. (2007). Carbon Monoxide Poisoning. Medical Journal, Armed Forces India, 63(4), 362–365. https://doi.org/10.1016/S0377-1237(07)80017-7

20. Wallington, T. J. (2006). Automotive fuels and internal combustion engines: a chemical perspective. Chemical Society Reviews, 35(4), 335–347. https://doi.org/10.1039/B410469M

21. Ramli, N. A. (2020). Chemical and Biological Compositions Associated with Ambient Respirable Particulate Matter: a Review. Water Air and Soil Pollution, 231(3), 1–14. https://doi.org/10.1007/S11270-020-04490-5

22. Kim, Y. S. (2007). Gas sensor measurement system capable of sampling volatile organic compounds (VOCs) in wide concentration range. Sensors and Actuators B-Chemical, 122(1), 211–218. https://doi.org/10.1016/J.SNB.2006.05.023

23. Rumbeiha, W. K. (2012). Toxicology and "One Health": Opportunities for Multidisciplinary Collaborations. Journal of Medical Toxicology, 8(2), 91–93. https://doi.org/10.1007/S13181-012-0224-4

24. Sassi, M. (2008). Sulfur Recovery from Acid Gas Using the Claus Process and High Temperature Air Combustion (HiTAC) Technology. American Journal of Environmental Sciences, 4(5), 502–511. https://doi.org/10.3844/AJESSP.2008.502.511

25. Mamalis, A. G. (2013). The impact of automotive industry and its supply chain to climate change: Somme techno-economic aspects. European Transport Research Review, 5(1), 1–10. https://doi.org/10.1007/S12544-013-0089-X

26. Guan, B. (2015). Review of the state-of-the-art of exhaust particulate filter technology in internal combustion engines. Journal of Environmental Management, 154, 225–258. https://doi.org/10.1016/J.JENVMAN.2015.02.027

27. Guan, B. (2015). Review of the state-of-the-art of exhaust particulate filter technology in internal combustion engines. Journal of Environmental Management, 154, 225–258. https://doi.org/10.1016/J.JENVMAN.2015.02.027

28. Chamberlain, O. (2016). Carbon-Monoxide (CO): A Poisonous Gas Emitted from Automobiles, Its Effect on Human Health. Advances in Automobile Engineering, 5(2), 1–7. https://doi.org/10.4172/2167-7670.1000151

29. Chamberlain, O. (2016). Carbon-Monoxide (CO): A Poisonous Gas Emitted from Automobiles, Its Effect on Human Health. Advances in Automobile Engineering, 5(2), 1–7. https://doi.org/10.4172/2167-7670.1000151

30. Chen, X. (2017). Sulfur Dioxide and Nitrogen Dioxide Gas Sensor Based on Arsenene: A First-Principle Study. IEEE Electron Device Letters, 38(5), 661–664. https://doi.org/10.1109/LED.2017.2684239

31. Roy, P. (2015). SO_2 Emission Control and Finding a Way Out to Produce Sulphuric Acidfrom Industrial SO_2 Emission. Journal of Chemical Engineering & Process Technology, 6(2), 1–7. https://doi.org/10.4172/2157-7048.1000230

32. Travis, C. C. (1983). Potential Health Effects of Light-Duty Diesel Exhaust. Risk Analysis, 3(2), 147–155. https://doi.org/10.1111/J.1539-6924.1983.TB00116.X

33. Ilyas, S. Z. (2010). Air pollution assessment in urban areas and its impact on human health in the city of Quetta, Pakistan. Clean Technologies and Environmental Policy, 12(3), 291–299. https://doi.org/10.1007/S10098-009-0209-4

34. Shuangchen, M. (2017). Environmental influence and countermeasures for high humidity flue gas discharging from power plants. Renewable & Sustainable Energy Reviews, 73, 225–235. https://doi.org/10.1016/J.RSER.2017.01.143

35. Kim, S. (2016). The comparison of fossil carbon fraction and greenhouse gas emissions through an analysis of exhaust gases from urban solid waste incineration facilities. Journal of The Air & Waste Management Association, 66(10), 978–987. https://doi.org/10.1080/10962247.2016.1192070

36. Twigg, M. V. (2007). Progress and future challenges in controlling automotive exhaust gas emissions. Applied Catalysis B-Environmental, 70(70), 2–15. https://doi.org/10.1016/J.APCATB.2006.02.029

37. Timko, M. T. (2010). Gas Turbine Engine Emissions—Part I: Volatile Organic Compounds and Nitrogen Oxides. Journal of Engineering for Gas Turbines and Power-Transactions of The Asme, 132(6), 6. https://doi.org/10.1115/1.4000131

38. Zhang, Q. (2016). Characteristics of gaseous and particulate pollutants exhaust from logistics transportation vehicle on real-world conditions. Transportation Research Part D-Transport and Environment, 43, 40–48. https://doi.org/10.1016/J.TRD.2015.09.005

39. Wang, C.-T. (2010). Vanadium-promoted tin oxide semiconductor carbon monoxide gas sensors. Sensors and Actuators B-Chemical, 150(1), 360–366. https://doi.org/10.1016/J.SNB.2010.06.060

40. Guillet, N. (2004). Oxygen and carbon monoxide role on the electrical response of a non-Nernstian potentiometric gas sensor; proposition of a model. Sensors and Actuators B-Chemical, 98(2), 130–139. https://doi.org/10.1016/J.SNB.2003.10.001

41. Kwon, S. (2021). Room Temperature Gas Sensor Application of Carbon Nanowalls using Electrical Resistance Change by Surface Adsorption of Toxic Gases. Materials Research Bulletin, 141, 0. https://doi.org/10.1016/J.MATERRESBULL.2021.111377

42. Kwon, S. (2021). Room Temperature Gas Sensor Application of Carbon Nanowalls using Electrical Resistance Change by Surface Adsorption of Toxic Gases. Materials Research Bulletin, 141, 0. https://doi.org/10.1016/J.MATERRESBULL.2021.111377

43. Elakia, M. (2020). Investigation on visible light assisted gas sensing ability of multi-walled carbon nanotubes coated with pyrene based organic molecules. Physica E-Low-Dimensional Systems & Nanostructures, 124, 0. https://doi.org/10.1016/J.PHYSE.2020.114232

44. de la Torre, A. (2003). A Relationship Between Skin Thermal Conductivity and Gas Polytropic Index in an Open Atmospheric Balloon. Journal of Applied Meteorology, 42(2), 325–330. https://doi.org/10.1175/1520-0450(2003)042<0325:ARBSTC>2.0.CO;2

45. Fauzi, F. (2021). Gas and humidity sensing with quartz crystal microbalance (QCM) coated with graphene-based materials – A mini review. Sensors and Actuators A-Physical, 330, 0. https://doi.org/10.1016/J.SNA.2021.112837

46. Waghmare, S. D. (2020). Pristine and palladium-doped perovskite bismuth ferrites and their nitrogen dioxide gas sensor studies. Journal of King Saud University - Science, 32(7), 3125–3130. https://doi.org/10.1016/J.JKSUS.2020.08.024

47. Rossi, M. (2012). Ultra low power Wireless Gas Sensor Network for environmental monitoring applications. Workshop on Environmental Energy and Structural Monitoring Systems, 75–81. https://doi.org/10.1109/EESMS.2012.6348397

48. Ohodnicki, P. R. (2012). In-situ and ex-situ characterization of TiO2 and Au nanoparticle incorporated TiO2 thin films for optical gas sensing at extreme temperatures. Journal of Applied Physics, 111(6), 6. https://doi.org/10.1063/1.3695380

Advances in Chemiresistive Gas Sensing: A Decade of Progress and Emerging Trends

2.1 Overview of Chemiresistive Gas Sensing in the Last Decade

Chemiresistive gas sensing has emerged as one of the most promising and versatile approaches for detecting a wide range of gaseous pollutants. The fundamental principle of this technique lies in the change in electrical resistance of a sensing material when it interacts with target gas molecules. Due to its simplicity, cost-effectiveness, and compatibility with miniaturized devices, chemiresistive sensing has become a dominant technology in both industrial and environmental monitoring applications.

Over the past decade, extensive research and development have led to significant advancements in chemiresistive gas sensing materials, device design, and data interpretation methods. These advancements have collectively improved sensitivity, selectivity, response time, and stability, while also enabling integration with modern digital systems. The major trends in chemiresistive gas sensing over the last decade can be summarized as follows:

2.1.1 Development of New Sensing Materials

Considerable effort has been devoted to discovering and synthesizing new sensing materials with enhanced gas-sensing performance. Metal oxide semiconductors (MOS), such as SnO_2, ZnO, TiO_2, and Fe_2O_3, have continued to dominate due to their high chemical stability, tunable surface properties, and strong response to gases like CO, NO_x, and volatile organic compounds (VOCs) [1]. Furthermore, the introduction of dopants, heterojunctions, and composite nanostructures has significantly improved selectivity and reduced cross-sensitivity.

2.1.2 Miniaturization and Device Integration

In recent years, the miniaturization of gas sensors has become a major focus. Microelectromechanical systems (MEMS) and nanofabrication technologies have enabled the development of portable, low-cost, and energy-efficient sensors that can be integrated into compact platforms such as smartphones, wearables, and handheld detectors [2]. This has expanded the application scope of gas sensing from industrial systems to personal and environmental monitoring.

2.1.3 Integration with the Internet of Things (IoT)

The convergence of chemiresistive gas sensing with the Internet of Things (IoT) has transformed the landscape of environmental monitoring. Modern IoT-enabled systems utilize networks of interconnected sensors to provide real-time data on air quality, pollutant levels, and safety conditions. Such integration has driven the emergence of smart cities, smart homes, and intelligent transportation systems, where sensor networks communicate continuously with cloud-based platforms for analysis and decision-making [3].

2.1.4 Advancements in Pattern Recognition and Machine Learning

One of the most remarkable developments in the past decade has been the application of machine learning (ML) and artificial intelligence (AI) techniques to gas sensing. These methods enable the interpretation of complex response patterns from sensor arrays—often termed electronic noses (e-noses)—to identify multiple gases simultaneously. By employing algorithms for feature extraction, classification, and pattern recognition, these systems achieve high accuracy and discrimination even in mixed-gas environments [4].

2.1.5 Development of Perovskite-Based Sensors

The emergence of perovskite materials has opened a new frontier in chemiresistive gas sensing. Due to their tunable bandgap, high surface reactivity, and mixed ionic-electronic conductivity, perovskites such as $BiFeO_3$, $LaFeO_3$, and $BaTiO_3$ have demonstrated excellent sensitivity and selectivity toward gases like CO_2, CH_4, and VOCs [5]. Additionally, the incorporation of dopants (e.g., Ag, Pd, Pt) and nanostructuring techniques has further enhanced gas adsorption and charge transfer characteristics, making perovskite-based chemiresistors highly suitable for high-temperature and real-time exhaust monitoring applications.

2.2 Use of Binary Metal Oxides for Gas Sensing

Binary metal oxides have played a pivotal role in the advancement of chemiresistive gas sensing technology over the past several decades. These materials are composed of two different metallic elements combined with oxygen, forming compounds such as tin oxide (SnO_2), zinc oxide (ZnO), tungsten oxide (WO_3), cobalt oxide (Co_3O_4), and others. Their unique semiconducting behavior, tunable surface chemistry, and strong interaction with gas molecules make them highly suitable for gas detection applications [6].

The key sensing mechanism of binary metal oxides relies on the variation of electrical resistance upon exposure to oxidizing or reducing gases. When the gas interacts with the sensor surface, adsorption and reaction processes alter the charge carrier concentration in the semiconductor material, resulting in a measurable change in resistance. This fundamental property, combined with their robustness and low cost, has made binary metal oxides a cornerstone of modern gas sensor development.

Binary metal oxides offer several distinct advantages as sensing materials:

- High sensitivity and selectivity toward specific target gases;
- Excellent thermal and chemical stability under harsh environmental conditions;
- Low manufacturing cost and compatibility with large-scale fabrication techniques;
- Good performance consistency across a wide range of temperatures and humidity levels [7].

Some of the most widely studied and utilized binary metal oxides for gas sensing are described below.

(a) Tin Oxide (SnO_2)

Tin oxide is one of the most extensively used materials for chemiresistive gas sensing. It exhibits n-type semiconducting behavior and demonstrates excellent sensitivity to gases such as hydrogen (H_2), carbon monoxide (CO), and ethanol vapors. SnO_2-based sensors are widely employed due to their high surface reactivity, fast response and recovery times, and thermal stability across a broad range of operating temperatures [8]. Moreover, surface modification through catalytic doping (e.g., with Pd or Pt) further enhances its selectivity and detection limits.

(b) Zinc Oxide (ZnO)

Zinc oxide, another important n-type semiconductor, has garnered significant attention for gas detection due to its wide bandgap (3.37 eV), large exciton binding energy, and chemical robustness. ZnO-based sensors are known for their high sensitivity to gases such as hydrogen, ammonia (NH_3), and carbon monoxide [9]. The nanostructured forms of ZnO—such as nanorods, nanowires, and nanosheets—exhibit improved surface-to-volume ratios, enhancing adsorption and charge transfer processes. Its simple synthesis routes and compatibility with flexible substrates also make it attractive for next-generation portable gas sensors.

(c) Tungsten Oxide (WO_3)

Tungsten oxide (WO_3) is a versatile n-type semiconductor used for detecting oxidizing gases such as ozone (O_3) and nitrogen dioxide (NO_2), as well as reducing gases like hydrogen and carbon monoxide. It demonstrates excellent gas–solid interaction capability, good thermal stability, and strong photoactivity, which makes it suitable for optical and photo-assisted gas sensing [10]. Doping WO_3 with noble metals such as Au, Pt, or Pd can further enhance its selectivity and lower its optimal operating temperature.

(d) Cobalt Oxide (Co_3O_4)

Cobalt oxide is a p-type semiconductor known for its effective sensing performance toward gases such as hydrogen, carbon monoxide, and methane (CH_4). It offers high chemical reactivity, excellent repeatability, and stability under varying temperature and humidity conditions. Due to its mixed oxidation states (Co^{2+}/Co^{3+}), Co_3O_4 exhibits enhanced catalytic activity, which facilitates rapid charge transfer during gas adsorption and desorption processes. It has also been explored as a component in composite and heterostructure systems to improve selectivity and sensitivity.

Binary metal oxides have served as the foundation of chemiresistive gas sensing technology for decades due to their reliability, availability, and high performance. Materials such as SnO_2, ZnO, WO_3, and Co_3O_4 have demonstrated strong sensing responses toward various toxic and flammable gases. However, challenges such as high operating temperature, limited selectivity, and cross-sensitivity have driven researchers to explore new material systems—including mixed oxides, doped nanostructures, and perovskite-based materials—to achieve improved sensing characteristics. These next-generation materials form the focus of the following sections.

2.3 Use of Complex Metal Oxides and Composites for Gas Sensing

In recent years, complex metal oxides and composite materials have gained considerable attention as advanced gas-sensing materials owing to their tunable electronic, catalytic, and structural properties. Unlike binary metal oxides, which consist of two elements combined with oxygen, complex metal oxides contain more than two metallic elements, enabling greater flexibility in chemical composition, defect engineering, and electronic band modulation. Common examples include perovskite-type oxides, spinels, and other multicomponent oxides. Similarly, composite materials—typically combinations of metal oxides with polymers, carbon nanostructures, or other functional materials—offer synergistic effects that enhance sensing performance beyond that of their individual components [12].

These materials have several advantages compared to conventional binary oxides. Complex oxides and composites can exhibit higher selectivity, greater thermal and chemical stability, and enhanced sensitivity at low gas concentrations. Their performance arises from multiple concurrent mechanisms such as

heterojunction formation, enhanced surface reactivity, and improved charge transport, all of which contribute to better sensor performance under diverse environmental conditions.
Some of the most commonly studied and effective complex metal oxides and composite materials for gas sensing applications are discussed below.

(a) Perovskite-Type Oxides
Perovskite-type oxides represent one of the most significant classes of complex metal oxides used in gas sensing. These materials have the general formula ABO_3, where *A* and *B* are metal cations of different sizes, resulting in a versatile crystal structure that allows for extensive elemental substitution and defect tuning. Among these, lanthanum ferrite ($LaFeO_3$) and its doped derivatives have shown excellent sensitivity and selectivity toward gases such as carbon dioxide (CO_2), methane (CH_4), and volatile organic compounds (VOCs) [13]. Their superior performance is attributed to their mixed ionic-electronic conductivity, high oxygen vacancy concentration, and thermochemical stability. Furthermore, perovskite oxides can operate effectively over a wide range of temperatures and humidity levels, making them ideal for automotive exhaust and environmental monitoring applications.

(b) Metal Oxide–Polymer Composites
Hybrid composites formed by combining metal oxides with conducting polymers—such as polyaniline (PANI), polypyrrole (PPy), or polythiophene (PTh)—have demonstrated remarkable improvements in gas-sensing performance. These materials exploit the high surface area and conductivity of polymers and the gas-reactive surface chemistry of metal oxides. For example, ZnO–PANI composites have shown excellent sensitivity toward hydrogen (H_2), carbon monoxide (CO), and ammonia (NH_3) due to the formation of heterointerfaces that facilitate charge transfer between the oxide and polymer phases [14]. Such composites often operate efficiently at room temperature, unlike many metal oxide sensors that require elevated operating temperatures, making them particularly attractive for portable and low-power sensing systems.

(c) Metal Oxide–Carbon Composites
Another promising category involves metal oxide–carbon composites, where carbon-based nanomaterials such as graphene, reduced graphene oxide (rGO), or carbon nanotubes (CNTs) are incorporated into metal oxide matrices. These composites combine the excellent electrical conductivity and high surface area of carbon materials with the chemical reactivity and selectivity of metal oxides. For instance, SnO_2–graphene composites have been widely studied for detecting hydrogen, carbon monoxide, and various VOCs [15]. The presence of graphene not only enhances charge transport and signal stability but also reduces the sensor's response and recovery times by facilitating rapid adsorption and desorption of gas molecules. These hybrid systems also exhibit excellent environmental stability and mechanical flexibility, expanding their applicability to wearable and flexible sensing platforms.

Complex metal oxides and composite-based gas sensors represent a major advancement in the evolution of chemiresistive gas sensing materials. Compared to traditional binary oxides, these materials exhibit superior selectivity, higher sensitivity at low gas concentrations, and better long-term stability. The ability to tailor their composition and microstructure offers immense potential for designing next-generation gas sensors capable of reliable operation under real-world conditions.

In particular, perovskite-type oxides have emerged as highly promising candidates due to their tunable structure, high-temperature resilience, and adaptability for doping and nanostructuring—features that make

them ideal for detecting automotive exhaust gases. The next section explores these perovskite-based sensing materials in greater depth, focusing on their structural attributes, operating principles, and recent research progress.

2.4 Comparison of Gas Sensing Materials

A wide variety of materials have been explored for gas sensing applications, each possessing unique physical, chemical, and electronic properties that determine its performance characteristics. The choice of material depends largely on the target gas**,** desired sensitivity**,** operating environment, and fabrication cost. A comparative overview of the most commonly studied categories of gas sensing materials is presented below.

2.4.1 Metal Oxides

Metal oxides such as tin oxide (SnO_2)**,** zinc oxide (ZnO), and tungsten oxide (WO_3) are among the most widely used gas sensing materials. These semiconductors exhibit changes in electrical resistance upon interaction with oxidizing or reducing gases. They are known for their high sensitivity**,** thermal and chemical stability, and low production cost, making them ideal for large-scale sensing applications. However, many metal oxide sensors require elevated operating temperatures to achieve optimal performance [16].

2.4.2 Complex Metal Oxides

Complex metal oxides, including perovskite-type materials such as $LaFeO_3$ and $SrTiO_3$, have gained increasing attention due to their tunable electronic structure**,** oxygen vacancy control, and multi-element substitutional flexibility. These materials offer higher selectivity and stability under variable humidity and temperature conditions compared to binary oxides, and they demonstrate strong responses even at low gas concentrations [17].

2.4.3 Composites

Composite sensing materials combine two or more components—such as metal oxides with polymers**,** carbon nanostructures, or noble metals—to create synergistic properties that enhance overall performance. For instance, metal oxide–polymer composites (e.g., ZnO–PANI) enable room-temperature operation, while metal oxide–carbon composites (e.g., SnO_2–graphene) improve conductivity and response speed. These systems typically exhibit enhanced selectivity, improved environmental stability, and high sensitivity, especially at trace gas levels [18].

2.4.4 Organic Materials

Organic materials—including conducting polymers**,** organic dyes, and biomolecules—have emerged as promising candidates for flexible and wearable gas sensing platforms. They offer low fabrication cost, lightweight structure, and room-temperature operation, while maintaining reasonable sensitivity and selectivity toward specific gases. However, their long-term stability and reproducibility under varying humidity or temperature conditions remain challenging [19].

2.4.5 Inorganic Materials

Inorganic materials such as noble metals (e.g., Pt, Pd, Au) and semiconductors (e.g., Si, GaN) have been utilized for high-precision gas detection. These materials exhibit excellent sensitivity and selectivity**,** but are often limited by high fabrication cost and the requirement of elevated temperatures for stable operation. As a result, they are typically used in specialized industrial or research-grade gas sensing applications [20].

Material Type	**Examples**	**Typical Target Gases**	**Key Advantages**	**Limitations**
Metal Oxides	SnO_2, ZnO, WO_3	CO, H_2, CH_4, NH_3, VOCs	High sensitivity, stability, low cost	Requires high temperature, moderate selectivity
Complex Metal Oxides	$LaFeO_3$, $SrTiO_3$, $BaSnO_3$	CO_2, CH_4, NO_2, VOCs	Tunable structure, high selectivity, low detection limit	Complex synthesis, sometimes slower response
Composites	ZnO–PANI, SnO_2–graphene, WO_3–Au	H_2, CO, NH_3, VOCs	Synergistic enhancement, room-temperature operation, high sensitivity	Fabrication complexity, long-term stability issues
Organic Materials	Polyaniline, Polypyrrole, Phthalocyanine dyes	NH_3, CO_2, ethanol vapors	Low cost, flexible, low power consumption	Poor durability and humidity interference
Inorganic (Noble Metals/ Semiconductors)	Pt, Pd, Au, Si, GaN	H_2, O_2, NO_x	Excellent selectivity, fast response	High cost, requires elevated temperature

Table 2.2 Comparative Overview of Common Gas Sensing Materials

Metal oxides and their derivatives remain the most widely utilized materials for gas sensing due to their reliability and versatility. Complex oxides and composite materials offer enhanced performance through structural tunability and synergistic effects, while organic materials enable flexible, low-cost sensing solutions. Inorganic noble metals and semiconductor systems continue to serve specialized roles where high precision is required.

The selection of a suitable sensing material thus depends on a balance between sensitivity, selectivity, stability, operating temperature, and fabrication cost. These considerations form the foundation for the ongoing transition toward perovskite-based and nanostructured composite sensors, which promise superior performance for real-time monitoring of automotive exhaust gases and other environmental pollutants.

2.5 Selection of Material for a Particular Gas Analyte

The selection of an appropriate gas sensing material is a critical step in the design and development of an efficient and reliable gas sensor. The ideal sensing material should exhibit strong and reversible interaction with the target gas, while maintaining stability and reproducibility under varying environmental conditions. The choice of material depends on both intrinsic properties—such as electronic structure, surface reactivity,

and defect concentration—and extrinsic factors like temperature, humidity, fabrication cost, and compatibility with the sensing device.
Several key criteria govern the selection of a suitable sensing material for a particular gas analyte:

2.5.1 Sensitivity

Sensitivity refers to the material's ability to detect small concentrations of the target gas. High sensitivity ensures that even trace levels of the gas can produce a measurable and reproducible signal. The sensitivity of a chemiresistive material depends on its surface-to-volume ratio, defect density, and adsorption kinetics. Nanostructured materials, such as nanowires, nanotubes, and nanoparticles, typically exhibit enhanced sensitivity due to their large active surface area.

2.5.2 Selectivity

Selectivity is the ability of a sensing material to discriminate the target gas from other interfering species in the environment. High selectivity is crucial for accurate detection, especially in complex gas mixtures such as automotive exhaust. Selectivity can be improved by surface functionalization**,** doping with catalytic metals (e.g., Pt, Pd, Ag)**,** or heterostructure formation that promotes specific surface reactions with the target analyte.

2.5.3 Response Time

The response time is the duration required for the sensor signal to reach a defined percentage (typically 90%) of its steady-state value upon exposure to the target gas. A shorter response time indicates faster surface reactions and electron exchange processes between the gas and sensing material. For applications such as automotive exhaust monitoring or industrial safety**,** rapid response is essential for real-time detection.

2.5.4 Recovery Time

Recovery time is the period required for the sensor to return to its baseline resistance once the gas is removed. A short recovery time enables the sensor to track fluctuating gas concentrations more effectively. Recovery characteristics depend on the strength of gas adsorption and desorption processes and can be improved through thermal activation**,** UV illumination, or catalytic surface modification.

2.5.5 Stability

Stability reflects the material's ability to maintain consistent sensing performance over time and repeated cycles of operation. A stable sensor should exhibit minimal signal drift and maintain structural integrity under prolonged exposure to gases and environmental variations. Stability can be enhanced by using thermally robust materials (e.g., metal oxides, perovskites) and protective surface coatings to prevent contamination or degradation.

2.5.6 Operating Temperature and Humidity Range

The operating temperature and humidity range defines the environmental conditions under which the sensor can function reliably. Many gas sensing reactions require activation at elevated temperatures (200–400 °C), but high humidity can interfere with adsorption sites and alter response behavior. Therefore, selecting materials with low temperature dependence and moisture-tolerant surfaces is crucial for field applications.

2.5.7 Cost and Availability

From a practical standpoint, the cost and availability of the sensing material significantly influence its commercial viability. Materials that are inexpensive, abundant, and easily processable (e.g., SnO_2, ZnO, or

$LaFeO_3$) are preferred for large-scale manufacturing, whereas exotic or rare compounds may be reserved for niche, high-performance applications.

2.5.8 Compatibility with the Sensing Device

Compatibility refers to the ability of the material to integrate with the sensor's architecture, such as substrate type, electrode material, and device fabrication process. The chosen material must exhibit good adhesion, mechanical stability, and processability to ensure efficient electrical contact and long-term operation. This factor becomes particularly important for miniaturized MEMS-based or flexible sensors, where structural and mechanical compatibility determines overall device reliability.

Selecting a gas sensing material for a particular analyte involves a multi-parameter optimization process that balances sensitivity, selectivity, response speed, stability, and environmental tolerance with practical considerations such as cost and manufacturability. The ideal sensing material should:

- Exhibit high sensitivity and selectivity toward the target gas;
- Possess fast response and recovery characteristics;
- Maintain stability and repeatability over extended operation;
- Operate effectively across a wide range of temperatures and humidity levels; and
- Be cost-effective and compatible with sensor integration technologies.

The pursuit of materials that meet all these criteria has led to growing interest in nanostructured and perovskite-based chemiresistive materials, which combine high reactivity, tunable composition, and superior thermal stability—making them particularly suitable for automotive exhaust gas sensing and real-time environmental monitoring applications.

2.6 Gas Sensing Parameter Improvement through Material Optimization

The performance of a gas sensor depends critically on the structural, morphological, and electronic characteristics of the sensing material. Recent research has demonstrated that material optimization through nanostructuring and surface functionalization can substantially enhance sensing parameters such as sensitivity, selectivity, response and recovery times, and long-term stability.

Functionalization of nanomaterials refers to the intentional modification of their surface or bulk properties to improve gas–surface interactions and charge transfer efficiency [21]. Such functionalization enhances the number of active sites available for adsorption, promotes catalytic activity, and stabilizes the material under harsh environmental conditions. Various approaches have been employed to optimize gas-sensing materials, including surface modification, coating, encapsulation, hybridization, and doping.

(a) Surface Modification

Surface modification involves altering the chemical or physical characteristics of a nanomaterial's surface to improve its reactivity toward target gases. Chemical treatments such as oxidation, reduction, or the attachment of functional chemical groups can modify the surface energy and enhance gas adsorption [22]. Physical modification techniques—such as plasma treatment**,** UV irradiation, or ion etching—are often employed to clean, activate, or restructure the surface, thereby increasing the density of reactive sites. These modifications can significantly improve the sensor's response and recovery characteristics by promoting faster gas–surface reactions.

(b) Coating

Coating entails the deposition of a thin, uniform film of another material onto the nanostructured sensing layer. This technique can be realized through chemical methods such as chemical vapor deposition (CVD) or atomic layer deposition (ALD), and physical methods including sputtering or thermal evaporation [23]. Coating serves multiple purposes—it can protect the sensing material from environmental degradation, enhance selectivity by introducing catalytic layers (e.g., Pd, Pt), and improve stability by reducing surface contamination.

(c) Encapsulation

Encapsulation refers to embedding the sensing material within a protective or functional matrix, often to improve environmental stability and mechanical integrity. Techniques such as electrospinning**,** sol–gel processing, or in-situ polymerization are commonly employed for encapsulation [24]. This approach helps prevent particle agglomeration, minimizes humidity interference, and can enhance reproducibility. Encapsulation is particularly advantageous for flexible and wearable sensors, where mechanical robustness is crucial.

(d) Hybridization

Hybridization involves combining different materials to form composite or heterostructured systems, which can exhibit synergistic effects between the components. Common synthesis techniques include co-precipitation, sol–gel synthesis, and in-situ polymerization [25]. Hybrid materials—such as metal oxide–polymer, metal oxide–carbon, or metal oxide–noble metal composites—often demonstrate superior performance by combining high conductivity, catalytic activity, and surface reactivity. For instance, the hybridization of SnO_2 with graphene can improve charge transport and lower operating temperature, while ZnO–PANI composites enable room-temperature operation with enhanced selectivity.

(e) Doping

Doping is the deliberate incorporation of impurity atoms or ions into a host material to alter its electronic, catalytic, or structural properties [26]. Doping can be achieved through various methods such as ion implantation, chemical vapor deposition, or sol–gel synthesis. The introduction of dopants—such as Ag, Pt, Pd, Cu, or Fe—can modify the band structure, create additional charge carriers, and introduce catalytic sites that enhance surface reactions. For example, Ag-doped $BiFeO_3$ has been reported to exhibit improved sensitivity and faster response due to enhanced electron mobility and surface oxygen vacancies.

Material optimization through functionalization and nanostructural modification is one of the most effective strategies for enhancing gas-sensing performance. Each technique—whether surface modification, coating, encapsulation, hybridization, or doping—addresses specific challenges such as low sensitivity, slow response, or environmental instability.

Through controlled material design, it is possible to:

- Increase sensitivity by enlarging active surface area and tuning electronic states,
- Enhance selectivity via catalytic or functional surface modification,
- Reduce response and recovery times through improved charge transfer pathways, and
- Improve stability under varying temperature and humidity conditions.

These optimization strategies collectively enable the design of high-performance, robust chemiresistive gas

sensors, particularly when applied to nanostructured and perovskite-based materials, which will be discussed in the following section.

2.7 Metal Oxide Semiconductor (MOS) Gas Sensors

Metal Oxide Semiconductor (MOS) gas sensors represent one of the most widely used and studied classes of chemiresistive gas sensors. Their operation is based on the variation of the electrical resistance of a metal oxide semiconductor material upon exposure to a target gas [27]. This simple yet powerful principle has made MOS sensors the backbone of modern gas detection technologies used in industrial safety, environmental monitoring, and automotive exhaust analysis.

Working Principle

The fundamental operating mechanism of a MOS gas sensor relies on surface-controlled charge transfer processes. The sensing element typically consists of a thin or thick film of a metal oxide material—commonly tin oxide (SnO_2), zinc oxide (ZnO), or titanium dioxide (TiO_2)—deposited onto an insulating substrate such as alumina, silicon, or ceramic [28]. The film is equipped with interdigitated electrodes for resistance measurement and often includes a micro-heater to maintain the optimal operating temperature.

When the sensor is exposed to air, oxygen molecules adsorb onto the surface of the metal oxide and capture free electrons from the conduction band, forming oxygen ions (O_2^-, O^-, or O^{2-}) depending on the temperature. This process creates a depletion layer, increasing the material's resistance. Upon introduction of a target gas, such as a reducing gas (e.g., CO, H_2, CH_4), the gas reacts with the adsorbed oxygen species, releasing trapped electrons back into the conduction band. This leads to a measurable decrease in resistance, which is proportional to the gas concentration [29].

For oxidizing gases (e.g., NO_2, O_3), the opposite behavior is observed—the gas molecules extract electrons from the semiconductor, resulting in an increase in resistance. The relationship between gas concentration and resistance change forms the basis of quantitative gas detection in MOS sensors.

Sensor Construction and Materials

A typical MOS gas sensor comprises the following key components:

1. **Sensing Layer:** A thin film or porous layer of a metal oxide semiconductor such as SnO_2, TiO_2, ZnO, or WO_3 serves as the active sensing element.
2. **Substrate:** Common substrates include alumina (Al_2O_3) or silicon (Si), chosen for their thermal stability and compatibility with thin-film deposition techniques.
3. **Electrodes:** Metallic interdigitated electrodes (commonly Pt, Au, or Ag) are deposited onto the substrate to measure resistance changes.
4. **Heater Element:** A built-in micro-heater maintains the sensor at a specific operating temperature (typically between 200–400 °C) to facilitate surface reactions and enhance sensitivity [28].

Various deposition techniques are used to fabricate the sensing layer, including chemical vapor deposition (CVD), sol–gel processing, screen printing, sputtering, and spray pyrolysis, depending on the desired microstructure and application.

Applications

MOS gas sensors have been extensively applied across diverse sectors due to their versatility, low cost, and high reproducibility. They are used for detecting toxic and combustible gases such as carbon monoxide (CO), methane (CH_4), hydrogen (H_2), ammonia (NH_3), and volatile organic compounds (VOCs).

In automotive applications, MOS sensors are integrated into exhaust monitoring systems to ensure compliance with emission standards and optimize combustion efficiency. In industrial environments, they are employed for leakage detection and workplace safety monitoring. Additionally, MOS-based modules are widely used in air quality monitoring and smart home systems, where they help maintain indoor environmental safety [30].

Advantages and Limitations

MOS gas sensors offer several notable advantages:

- **High sensitivity and fast response time**, enabling real-time gas detection;
- **Robustness and long operational life**, suitable for continuous monitoring;
- **Low manufacturing cost** and compatibility with large-scale production;
- **Ease of integration** with microelectronic systems and MEMS architectures.

However, these sensors also exhibit some limitations:

- **Dependence on high operating temperatures**, which increases power consumption;
- **Limited selectivity**, as multiple gases can cause similar resistance changes;
- **Performance degradation** under varying humidity and environmental conditions [31].

Ongoing research aims to overcome these drawbacks through material engineering and surface modification, such as doping with catalytic metals, forming heterostructures, and integrating MOS sensors with advanced signal-processing algorithms for improved discrimination.

MOS gas sensors remain a cornerstone of chemiresistive gas-sensing technology. Their well-understood mechanism, ease of fabrication, and reliable operation have made them indispensable in applications ranging from industrial gas monitoring to automotive exhaust management. Advances in nanostructuring, doping, and composite formation have significantly enhanced their performance, paving the way for the development of next-generation perovskite-based and hybrid MOS sensors that combine the stability of metal oxides with the tunable properties of complex oxides.

2.8 MOS Gas Sensor Classification

Metal Oxide Semiconductor (MOS) gas sensors form one of the most versatile and widely utilized families of gas detection devices. Due to their adaptability, robustness, and broad range of detectable gases, MOS gas sensors can be categorized in several ways depending on their material composition, output type, operating conditions, and target gas specificity. Understanding these classifications provides insight into their diverse applications and performance characteristics.

(a) Classification Based on Metal Oxide Semiconductor Material

MOS gas sensors can be fabricated using a variety of metal oxide semiconductors, each with distinct electronic, chemical, and structural properties that determine gas sensitivity and selectivity [32]. Common materials include:

- **Tin oxide (SnO_2):** Highly sensitive to reducing gases such as CO, CH_4, and H_2.
- **Titanium dioxide (TiO_2):** Exhibits strong response to oxidizing gases such as NO_2 and O_3.
- **Zinc oxide (ZnO):** Sensitive to CO, NH_3, and H_2 due to its large bandgap and high surface activity.
- **Copper oxide (CuO):** A p-type semiconductor that detects reducing gases such as H_2S and CH_4.
- **Tungsten oxide (WO_3):** Commonly used for detection of NO_2, O_3, and VOCs.

Each metal oxide offers unique advantages in terms of sensitivity, response speed, and thermal stability, enabling their tailored use in specific sensing applications.

(b) Classification Based on Type of Output Signal

MOS gas sensors can generate different types of electrical outputs depending on their circuit design and application requirements [33]:

- **Resistance-based sensors:** Measure the change in resistance of the sensing layer as the gas concentration varies (most common type).
- **Voltage-based sensors:** Output a voltage signal corresponding to the change in surface potential caused by gas adsorption.
- **Current-based sensors:** Monitor the variation in current flow through the semiconductor under constant bias conditions.
- **Digital-output sensors:** Use integrated electronics to convert analog signals into digital data, compatible with **microcontrollers or IoT systems** for real-time monitoring.

The choice of output type depends on the desired precision, power consumption, and interface compatibility with the sensing system.

(c) Classification Based on Operating Conditions

MOS gas sensors can also be classified according to their **operating temperature, humidity, and pressure** ranges [34].

- **High-temperature sensors (200–500 °C):** Designed for exhaust gas analysis, industrial monitoring, and combustion systems; high temperature facilitates fast surface reactions.
- **Low-temperature sensors (room temperature to 100 °C):** Utilized in portable and wearable applications; often achieved through nanostructuring, doping, or hybridization with conductive polymers.
- **Humidity-resistant sensors:** Engineered with hydrophobic coatings or encapsulation layers to maintain stability in high-humidity environments.
- **Pressure-dependent sensors:** Adapted for specific environmental or process conditions where gas density affects sensor response.

Operating condition optimization ensures reliable performance across diverse real-world scenarios.

(d) Classification Based on Target Gas

MOS gas sensors can be **selective or broad-spectrum** depending on the design and functionalization of the sensing material [35].

- **Selective sensors:** Designed to detect specific gases such as carbon monoxide (CO), nitrogen dioxide (NO_2), or hydrogen (H_2). Selectivity is typically enhanced through dopants (e.g., Pd, Pt, Ag) or surface catalysts.

- **Multi-gas or wide-spectrum sensors:** Capable of detecting multiple gases such as volatile organic compounds (VOCs), hydrocarbons, and air pollutants. These are commonly used in environmental and air quality monitoring systems.

The target gas classification allows sensors to be optimized for particular industrial, automotive, or safety-related applications.

(e) Classification Based on Detection Method

Although MOS sensors are primarily chemiresistive in nature, they can be integrated with other detection mechanisms, leading to a broader classification based on detection principles [36]:

- **Catalytic combustion:** Detects combustible gases through exothermic oxidation reactions on the sensor surface.
- **Electrochemical detection:** Measures current generated by oxidation–reduction reactions involving the target gas.
- **Infrared absorption:** Utilizes the absorption of infrared light by specific gas molecules for concentration measurement.
- **Semiconductor detection:** Relies on changes in electrical conductivity of the semiconductor layer upon gas adsorption (classical MOS principle).

This multi-principle approach allows designers to combine the benefits of different mechanisms for enhanced accuracy and selectivity.

MOS gas sensors can be systematically classified according to their semiconducting material composition, signal output type, operating environment, target gas specificity, and detection mechanism. This classification framework highlights the diversity and adaptability of MOS technology across various sensing applications.

By selecting appropriate materials, optimizing operating conditions, and integrating advanced detection methods, it is possible to tailor MOS sensors for applications ranging from automotive exhaust monitoring to ambient air quality assessment and industrial safety systems.

The next section will explore the extension of these principles to MOS gas sensors, which combine the structural flexibility of complex oxides with the chemiresistive advantages of traditional metal oxide systems

2.9 Metal Oxides for Gas Sensors

Metal oxides have been extensively employed as active sensing materials in chemiresistive gas sensors due to their tunable electrical properties, chemical stability, and strong interaction with various gas species. Their sensing behavior is primarily governed by surface adsorption and charge transfer mechanisms, which cause measurable changes in the electrical resistance of the material upon exposure to target gases.

Among the large family of metal oxides, tin oxide (SnO_2), titanium dioxide (TiO_2), zinc oxide (ZnO), and copper oxide (CuO) are the most commonly used materials, each offering unique advantages in terms of sensitivity, selectivity, and operating conditions. Other oxides such as nickel oxide (NiO) and iron oxide (Fe_2O_3) are also widely investigated for specific gas detection applications.

(a) Tin Oxide (SnO_2)

Tin oxide is one of the most extensively used n-type semiconducting metal oxides in gas sensing applications. It exhibits high sensitivity toward a wide range of reducing gases such as hydrogen (H_2), carbon monoxide (CO), and alcohol vapors [37]. SnO_2-based sensors operate efficiently at high temperatures (400–600 °C), where gas–surface interactions are maximized, leading to rapid response and recovery characteristics. The high surface reactivity of SnO_2 arises from its ability to adsorb oxygen species that participate in charge exchange reactions with the target gases.

Furthermore, the sensitivity and selectivity of SnO_2 can be enhanced by doping with noble metals such as palladium (Pd), platinum (Pt), or silver (Ag), which act as catalytic promoters for surface reactions. SnO_2 sensors are commonly used in automotive exhaust monitoring, industrial gas detection, and domestic safety devices (e.g., CO alarms).

(b) Titanium Dioxide (TiO_2)

Titanium dioxide is a wide-bandgap semiconductor (≈3.2 eV) with excellent chemical stability and photocatalytic activity. TiO_2-based gas sensors are sensitive to oxygen (O_2), nitrogen oxides (NO_x), and volatile organic compounds (VOCs) [38]. These sensors typically operate at moderate temperatures (200–400 °C), which enables surface adsorption and desorption processes while minimizing power consumption.

The sensing mechanism of TiO_2 involves changes in surface oxygen vacancy concentration and electron transfer between adsorbed gas molecules and the conduction band. Due to its photocatalytic nature, TiO_2 can also operate under UV illumination, facilitating room-temperature sensing through photoactivation. TiO_2-based sensors are frequently applied in air quality monitoring, automotive emission control, and indoor pollutant detection systems.

(c) Zinc Oxide (ZnO)

Zinc oxide is another n-type wide-bandgap semiconductor (≈3.37 eV) that exhibits excellent gas-sensing characteristics, particularly for hydrogen (H_2), nitrogen oxides (NO_x), and carbon monoxide (CO) [39]. ZnO's high surface-to-volume ratio, especially in its nanostructured forms such as nanowires, nanorods, and nanoflowers, allows for rapid gas adsorption and desorption, resulting in high sensitivity and fast response times.

ZnO gas sensors are known for their ability to function at relatively low operating temperatures, sometimes near room temperature, making them energy-efficient and suitable for portable or wearable applications. Doping and hybridization with other materials, such as polymers or graphene, further improve ZnO's selectivity and environmental stability.

(d) Copper Oxide (CuO)

Copper oxide is a p-type semiconducting material with notable sensitivity to methane (CH_4), propane (C_3H_8), ethane (C_2H_6), and hydrogen sulfide (H_2S) gases [40]. CuO-based gas sensors typically operate at low to moderate temperatures, often near room temperature, depending on the gas species.

The sensing mechanism in CuO is dominated by changes in hole concentration upon interaction with reducing gases, leading to variations in conductivity. CuO's strong catalytic properties, low cost, and good environmental stability make it attractive for flammable gas detection and industrial monitoring.

Additionally, CuO–Cu_2O composites have shown enhanced sensing performance due to the formation of p–p heterojunctions that improve charge separation and gas reactivity.

(e) Other Metal Oxides

In addition to the common oxides mentioned above, several other metal oxides have shown potential for gas sensing applications:

- **Nickel oxide (NiO):** A **p-type semiconductor** with high sensitivity to gases such as hydrogen (H_2), carbon monoxide (CO), and ethanol. NiO sensors are known for their fast response and good selectivity [41].
- **Iron oxide (Fe_2O_3):** Exhibits good thermal stability and reactivity toward oxidizing and reducing gases, making it useful for high-temperature sensing applications. Fe_2O_3 is often incorporated into **composite or doped systems** to improve response behavior.

Metal oxides remain the cornerstone of chemiresistive gas sensing due to their versatility, availability, and adaptability. Each oxide offers specific advantages—SnO_2 for high-temperature CO and H_2 detection, TiO_2 for NO_x and VOC sensing, ZnO for low-temperature operation, and CuO for hydrocarbon detection.

The ongoing development of doped, hybrid, and nanostructured metal oxides has further enhanced sensitivity, selectivity, and stability, allowing these materials to meet the increasing demands of automotive exhaust monitoring, industrial safety, and environmental sensing applications.

The next section will discuss perovskite-based materials, a class of complex metal oxides that offer improved tunability and high-temperature stability, making them ideal candidates for advanced gas sensing applications.

2.10 Classification of Perovskites

Perovskites are a class of complex oxide materials characterized by their distinctive crystal structure, which is derived from the natural mineral calcium titanate ($CaTiO_3$). The versatility of the perovskite structure allows for extensive chemical substitution and structural modification, making it a highly adaptable platform for applications in gas sensing, catalysis, photovoltaics, and energy storage.

The general perovskite structure can be represented by the formula ABO_3, where:

- **A** is a larger cation (typically an alkali, alkaline earth, or rare-earth element),
- **B** is a smaller cation (usually a transition metal), and
- **O** denotes the oxygen anions that form an octahedral coordination around the B-site cation.

Depending on the cation arrangement, dimensionality, and structural complexity, perovskites can be classified into several major categories, as described below.

(a) ABO_3 Perovskites

The ABO_3-type perovskites represent the most fundamental and widely studied form of perovskite materials. In this structure, the A-site cations occupy the corners of the cubic lattice, the B-site cations reside at the center of the octahedra, and the oxygen anions are located at the face centers [42].

Examples of classical ABO_3 perovskites include lanthanum ferrite ($LaFeO_3$), strontium titanate ($SrTiO_3$), and barium titanate ($BaTiO_3$). These materials exhibit tunable electrical conductivity, magnetic ordering, and oxygen vacancy concentration, all of which can be tailored by doping or partial substitution at the A or B sites. Such flexibility makes ABO_3 perovskites highly suitable for gas sensing, where controlled defect chemistry directly influences sensitivity and selectivity.

(b) Double Perovskites

Double perovskites are an extension of the ABO_3 structure in which two different cations occupy the B-site positions in an ordered manner. They follow the general formula $A_2BB'O_6$, where A is an alkali or rare-earth metal and B/B′ are transition metal cations [43].

This ordered configuration provides enhanced control over the electronic structure, magnetic properties, and oxygen ion mobility. Examples include La_2CoMnO_6, Ba_2YCrO_6, and Sr_2FeMoO_6, which exhibit mixed-valence states and improved electronic conductivity. The ability to tune the B-site composition makes double perovskites attractive candidates for selective gas sensing, oxygen permeation membranes, and catalytic oxidation processes.

(c) Single-Layer Perovskites

Single-layer perovskites consist of one perovskite block layer separated by a simple oxide or vacuum layer. They retain the general formula ABO_3 but often display slightly distorted or strained structures that affect their electronic and ionic behavior [44].

Typical examples include strontium cobaltite ($SrCoO_3$) and barium cobaltite ($BaCoO_3$), both of which exhibit excellent oxygen mobility and surface reactivity. These materials are often utilized in gas sensing, solid oxide fuel cells (SOFCs), and oxygen evolution reaction (OER) catalysts, where their single-layered configuration facilitates rapid surface–gas interactions.

(d) Hybrid Organic–Inorganic Perovskites

Hybrid perovskites combine inorganic frameworks with organic cations, creating a new class of materials with both ionic and molecular characteristics. Their general chemical formula is $CH_3NH_3PbX_3$ (where X = Cl, Br, or I), featuring methylammonium ($CH_3NH_3^+$) as the A-site cation, lead (Pb^{2+}) as the B-site cation, and halides as the anionic framework [45].

These materials have gained enormous attention in the field of photovoltaics and optoelectronics due to their high absorption coefficients, tunable bandgaps, and excellent carrier transport properties. Although their use in gas sensing is still emerging, their hybrid nature allows for flexible device integration and room-temperature operation, which may be advantageous for future sensor applications.

(e) Ruddlesden–Popper Perovskites

Ruddlesden–Popper (RP) perovskites represent a class of layered perovskite structures consisting of alternating perovskite and rock-salt-type layers. Their general formula is $A_{2+n}B_nO_{3n+1}$, where A is an alkali or rare-earth element, B is a transition metal cation, and n defines the number of perovskite layers within a stack [46].

These materials exhibit a quasi-two-dimensional (2D) structure, which leads to anisotropic electrical and ionic transport properties. The controlled layering in RP perovskites allows for fine-tuning of electronic band structure, oxygen diffusion pathways, and surface reactivity, making them suitable for gas sensors, membranes, and energy conversion devices.

Perovskite materials can be broadly classified into ABO_3-type, double perovskites, single-layer perovskites, hybrid organic–inorganic perovskites, and Ruddlesden–Popper phases. Each category exhibits distinct structural and electronic characteristics that influence their chemical reactivity and sensing performance.

Among these, ABO_3-type and double perovskites—especially those based on transition metal cations (e.g., Fe, Co, Ni)—have demonstrated excellent potential for chemiresistive gas sensing, owing to their tunable oxygen vacancies, high thermal stability, and flexible compositional design.

The next section will focus on the structural, electronic, and gas-sensing mechanisms of perovskite-based materials, particularly emphasizing bismuth ferrite ($BiFeO_3$) and its Ag-doped nanostructured variants, which have shown exceptional promise for high-temperature automotive exhaust gas detection.

2.11 Perovskites for Gas Sensing Applications

Perovskite materials have emerged as a highly promising class of functional materials for gas sensing applications owing to their unique electronic, optical, and structural properties. Their tunable bandgap, high carrier mobility, and abundant surface oxygen vacancies enable strong interaction with gas molecules, making them excellent candidates for the detection of a wide range of gaseous species such as volatile organic compounds (VOCs), nitrogen dioxide (NO_2), carbon monoxide (CO), and ammonia (NH_3) [47].

The flexibility of the perovskite crystal structure allows for extensive compositional engineering through A-site or B-site cation substitution, which can be used to tailor parameters such as bandgap energy, defect concentration, and surface reactivity. This tunability makes perovskites versatile materials capable of operating under diverse environmental conditions, including the harsh, high-temperature environments typical of automotive exhaust systems.

(a) Sensing Mechanism

The fundamental gas sensing mechanism in perovskite-based materials is governed by changes in their electrical and optical properties resulting from the adsorption of gas molecules on the material's surface.

When a perovskite sensor is exposed to a target gas, adsorption and redox reactions occur on its surface, leading to charge transfer between the adsorbed species and the semiconductor. This interaction alters the electrical conductivity, resistance, or capacitance of the material, which can be measured as the sensor's output signal [48].

For reducing gases (e.g., CO, NH_3, CH_4), electron donation to the perovskite's conduction band typically causes a decrease in resistance, whereas for oxidizing gases (e.g., NO_2, O_3), electron withdrawal leads to an increase in resistance. The magnitude and direction of this change depend on factors such as the type of charge carrier (n-type or p-type), the operating temperature, and the nature of surface defects and dopants.

In addition to electrical responses, perovskite materials can also exhibit optical modulation upon gas adsorption. Parameters such as absorption spectra, photoluminescence intensity, and reflectivity may vary depending on the gas–solid interactions, enabling optical gas sensing based on changes in the material's light absorption or emission properties.

(b) Composites and Hybrid Systems

Recent research has demonstrated that the combination of perovskite materials with other functional materials—such as metal oxides, conducting polymers, and carbon-based nanostructures—can substantially enhance sensing performance.

- **Perovskite–metal oxide composites** (e.g., $LaFeO_3$–SnO_2, $BiFeO_3$–ZnO) benefit from synergistic effects such as increased surface area, improved catalytic activity, and enhanced charge separation, leading to improved sensitivity and selectivity.
- **Perovskite–polymer hybrids** (e.g., $LaFeO_3$–PANI) can operate effectively at lower temperatures, owing to the polymer's ability to facilitate charge transport and maintain flexibility.
- **Perovskite–carbon composites** (e.g., $BiFeO_3$–graphene or $BiFeO_3$–carbon nanotubes) exhibit enhanced electron mobility, rapid response and recovery times, and improved signal stability due to the conductive carbon network that promotes efficient charge transfer.

Such hybrid systems demonstrate the potential of perovskites to be integrated into next-generation smart sensors, particularly those designed for real-time environmental monitoring and automotive emission control.

(c) Advantages of Perovskite-Based Gas Sensors

Perovskite-based gas sensors offer several advantages over traditional binary and complex metal oxide sensors:

- **High sensitivity and tunability:** Owing to controllable defect chemistry and variable oxidation states of transition metal ions.
- **Enhanced selectivity:** Achieved through compositional flexibility and heterostructure formation.
- **Thermal and chemical stability:** Suitable for operation in harsh and high-temperature environments.
- **Optoelectronic versatility:** Capability to sense gases via electrical or optical transduction mechanisms.
- **Scalability and low-cost synthesis:** Feasible through chemical routes such as sol–gel, hydrothermal, or combustion methods.

These attributes make perovskite materials especially promising for chemiresistive gas sensors in automotive, industrial, and environmental applications.

Perovskite materials represent a rapidly advancing class of sensing materials with remarkable electronic tunability, chemical adaptability, and multifunctional behavior. Their sensing mechanism is primarily governed by surface adsorption and charge transfer, resulting in measurable variations in electrical and optical responses.

Furthermore, the integration of perovskites with other materials—such as metal oxides, polymers, or carbon nanostructures—has been shown to significantly enhance sensor performance by improving sensitivity, selectivity, stability, and response speed.

2.12 Perovskite vs. Metal Oxide for Gas Sensors

Both perovskite and metal oxide materials have been extensively explored as active sensing elements in chemiresistive gas sensors. While metal oxides have a long-established record of use due to their simplicity and robustness, perovskite materials have emerged more recently as a versatile alternative, offering enhanced tunability and multifunctionality. Understanding the comparative features of these two material systems is essential for selecting the most appropriate sensing platform for specific environmental or industrial applications.

(a) Metal Oxide–Based Gas Sensors

Metal oxide semiconductors (MOS) such as tin oxide (SnO_2), titanium dioxide (TiO_2), zinc oxide (ZnO), and copper oxide (CuO) have been widely used for decades as gas sensing materials due to their stability, low cost, and ease of fabrication [51].

These materials detect gases primarily through surface adsorption and charge transfer processes that cause measurable changes in resistance or conductivity. They exhibit fast response and recovery times and can reliably detect a wide variety of gases, including CO, H_2, CH_4, NO_x, and VOCs.

However, traditional metal oxide sensors generally require elevated operating temperatures (200–500 °C) to achieve optimal surface reactivity, leading to higher energy consumption. Moreover, they often suffer from cross-sensitivity to multiple gases and drift under varying humidity conditions, which can reduce long-term reliability.

(b) Perovskite-Based Gas Sensors

Perovskite materials, with the general formula ABX_3, where A and B are cations and X is an anion (often oxygen or a halide), have recently gained attention as promising alternatives to conventional metal oxides [49].

Their highly flexible crystal structure allows for extensive compositional modification, which can tailor bandgap, carrier concentration, defect density, and surface reactivity. These properties translate into enhanced sensitivity and selectivity for specific gases such as methane (CH_4), carbon monoxide (CO), and volatile organic compounds (VOCs).

Perovskite-based sensors can be fabricated through low-temperature, solution-based synthesis routes, which are cost-effective and compatible with flexible or miniaturized devices. Furthermore, their ability to operate via both electrical and optical transduction mechanisms makes them suitable for multifunctional sensor architectures.

Despite these advantages, perovskite gas sensors remain primarily in the research and prototype phase. Their stability, particularly under high humidity and thermal cycling conditions, requires further improvement before large-scale commercialization can be realized [52].

(c) Comparative Evaluation

A detailed comparison of perovskite-based and metal oxide–based gas sensors is presented in Table 2.2. This comparison highlights their respective strengths and current challenges in gas sensing applications.

Parameter	**Metal Oxide Gas Sensors**	**Perovskite Gas Sensors**
Typical Formula	MO, M_2O_3, or MO_2 (e.g., SnO_2, ZnO, TiO_2, CuO)	ABO_3 or ABX_3 (e.g., $LaFeO_3$, $BiFeO_3$, $CH_3NH_3PbI_3$)
Crystal Structure	Simple oxide or rutile-type	Cubic or distorted perovskite (ABO_3 framework)
Charge Carrier Type	n-type or p-type semiconductor	n-type or p-type, tunable by A/B-site substitution
Operating Temperature	Typically 200–500 °C	Can operate from room temperature to 400 °C depending on composition
Synthesis Method	Sol–gel, sputtering, CVD, screen printing	Sol–gel, hydrothermal, solution processing, spin coating
Sensitivity	High (requires heating element)	Very high (even at low temperatures)
Selectivity	Moderate; improved by doping or surface catalysts	High; tunable through compositional modification
Response/Recovery Time	Fast (seconds)	Moderate to fast (depends on microstructure and gas)
Stability	Excellent under harsh environments	Needs improvement (sensitive to humidity and temperature cycling)
Fabrication Cost	Low	Low to moderate
Mechanism	Surface adsorption/desorption of gas molecules altering resistance	Surface adsorption causing change in resistance, capacitance, or optical properties
Applications	Industrial gas detection, automotive exhaust monitoring, air quality sensing	Advanced chemiresistive, optical, and hybrid sensors; emerging for automotive and environmental use
Commercialization Status	Mature and widely commercialized	Under research and early prototyping stage

Metal oxide and perovskite materials possess distinct advantages for gas sensing applications. Metal oxides offer proven reliability, thermal stability, and commercial viability, whereas perovskites provide superior tunability, higher sensitivity, and multifunctional sensing capabilities.

The key challenge for perovskite materials remains improving their long-term stability and reproducibility, particularly under real-world operating conditions. Once these issues are addressed, perovskite-based gas

sensors—especially those based on transition-metal oxides like $BiFeO_3$ and Ag-doped $BiFeO_3$—have the potential to surpass traditional MOS technologies in both performance and adaptability for automotive exhaust monitoring and environmental pollution control applications.

2.13 Perovskite-Based Gas Sensors

Perovskite-based gas sensors represent a new generation of chemiresistive and optoelectronic sensors that utilize perovskite materials as their active sensing elements. Perovskites are crystalline materials with the general formula ABX_3, where A and B are cations of different sizes, and X is an anion, typically oxygen or a halide. The perovskite crystal structure provides exceptional flexibility for chemical substitution and structural modification, enabling fine-tuning of physical and electronic properties to suit specific sensing requirements [53].

These materials have attracted significant attention in recent years due to their high sensitivity and selectivity toward target gases, as well as their low fabrication cost, scalable synthesis routes, and compatibility with flexible and miniaturized devices.

(a) Preparation Methods

Perovskite-based gas sensors can be synthesized and fabricated using various solution-based and vapor-phase deposition techniques, depending on the desired film morphology, crystallinity, and device architecture.

Common preparation routes include:

- Solution-processed methods, such as sol–gel, spin coating, dip coating, and hydrothermal synthesis, which offer simple and low-cost fabrication with good compositional control;
- Vapor-deposited techniques, including chemical vapor deposition (CVD), physical vapor deposition (PVD), and thermal evaporation, which yield highly crystalline and uniform thin films suitable for microelectronic integration [54].

The choice of synthesis method strongly influences the microstructure, surface area, and defect density of the resulting perovskite film, all of which are critical parameters governing gas adsorption and charge transport behavior.

(b) Gas Sensing Mechanism

The sensing mechanism of perovskite-based gas sensors is primarily governed by changes in the electrical properties (such as resistance, conductivity, or capacitance) upon exposure to the target gas. When gas molecules interact with the perovskite surface, adsorption and redox reactions occur, leading to charge transfer between the gas species and the semiconductor lattice. This alters the carrier concentration within the perovskite layer, resulting in measurable changes in electrical resistance.

For reducing gases (e.g., CO, CH_4, NH_3), electrons are released to the conduction band, typically causing a decrease in resistance. Conversely, oxidizing gases (e.g., NO_2, O_3) extract electrons, leading to an increase in resistance.

In addition to chemiresistive behavior, some perovskite-based sensors also exhibit optical responses, where gas adsorption affects parameters such as absorption spectra, photoluminescence intensity, or reflectivity, allowing dual-mode (electrical and optical) detection.

(c) Performance and Advantages

Perovskite-based gas sensors have demonstrated high sensitivity and selectivity toward a range of gases including methane (CH_4), carbon monoxide (CO), nitrogen dioxide (NO_2), and volatile organic compounds (VOCs). Their outstanding performance arises from several key attributes:

- Defect-tolerant crystal structure, allowing controlled oxygen vacancy formation and charge compensation;
- Tunable bandgap and electronic structure, enabling response optimization for specific gases;
- Low-temperature fabrication, which reduces energy and processing costs;
- Compatibility with hybrid systems, allowing integration with polymers, carbon materials, or other oxides for enhanced sensing performance.

These features make perovskite-based sensors promising candidates for automotive exhaust monitoring, environmental pollution detection, and industrial gas safety systems.

(d) Challenges and Future Prospects

Despite their potential, perovskite-based gas sensors are still in the research and developmental stage. Several challenges must be addressed before widespread commercialization can be achieved [55]:

- Stability issues: Many perovskites are sensitive to moisture, oxygen, and thermal cycling, which can degrade their performance over time.
- Reproducibility: Variations in synthesis and processing conditions can cause inconsistencies in sensor behavior.
- Mass production scalability: Developing uniform, reproducible thin films at industrial scale remains challenging.
- Optimization of selectivity: Tailoring perovskite compositions for specific gas detection requires further material-level and interface engineering.

Ongoing research focuses on improving the chemical and environmental stability of perovskites through doping, composite formation, and surface passivation, as well as integrating them into microelectromechanical systems (MEMS) for practical applications.

Perovskite-based gas sensors combine the advantages of high sensitivity, low fabrication cost, and tunable functionality. Their ability to detect a variety of gases at low concentrations—coupled with their structural and electronic flexibility—positions them as a promising next-generation sensing technology.

However, to transition from laboratory prototypes to real-world applications, further research is required to enhance their long-term stability, reproducibility, and environmental tolerance. These advancements will pave the way for practical deployment in automotive exhaust analysis, industrial safety monitoring, and ambient air quality management.

The next section discusses one of the most promising members of the perovskite family, bismuth ferrite ($BiFeO_3$), and its Ag-doped variants (Ag–BFO), which exhibit excellent potential for high-temperature, high-selectivity gas sensing in automotive exhaust environments.

2.14 Bismuth Ferrite Oxide ($BiFeO_3$)

Bismuth Ferrite Oxide ($BiFeO_3$) is a multifunctional perovskite-type complex oxide composed of bismuth (Bi), iron (Fe), and oxygen (O). It crystallizes in a distorted rhombohedral perovskite structure belonging to the *R3c* space group and is one of the most studied multiferroic materials, exhibiting simultaneous ferroelectric and antiferromagnetic ordering at room temperature [56].

These coupled electric and magnetic properties—combined with semiconducting behavior—make $BiFeO_3$ an attractive candidate for a wide range of applications including non-volatile memories, spintronics, photocatalysis, and gas sensing. Its strong coupling between electrical, magnetic, and structural properties allows for efficient modulation of charge transport processes, which is particularly beneficial for gas sensing applications.

(a) Structural and Electronic Properties

The crystal structure of $BiFeO_3$ follows the general perovskite formula ABO_3, where A = Bi^{3+} and B = Fe^{3+}. The Bi^{3+} ions occupy the corners of the unit cell, Fe^{3+} ions are located at the center of oxygen octahedra, and O^{2-} ions form the framework of the structure.

The stereochemically active $6s^2$ lone pair of Bi^{3+} induces lattice distortion, giving rise to spontaneous polarization, while Fe^{3+} contributes to the magnetic ordering through superexchange interactions. The coexistence of ferroelectricity, antiferromagnetism, and semiconducting behavior enables efficient charge modulation upon gas adsorption—an essential feature for chemiresistive gas sensing [56].

(b) Gas Sensing Mechanism

The gas sensing mechanism of $BiFeO_3$ is primarily governed by surface adsorption and charge transfer between the gas molecules and the semiconductor. When exposed to air, oxygen molecules are adsorbed on the $BiFeO_3$ surface, capturing free electrons from the conduction band and forming oxygen ions (O_2^-, O^-, or O^{2-}) depending on the operating temperature.

Upon exposure to a reducing gas such as H_2 or CO, these oxygen ions react with the target gas, releasing trapped electrons back into the conduction band. This process decreases the depletion layer width, thereby reducing the sensor resistance. Conversely, when exposed to an oxidizing gas such as NO_2, additional electrons are withdrawn from the conduction band, leading to an increase in resistance [57].

The change in resistance is directly proportional to the gas concentration, allowing $BiFeO_3$-based sensors to detect gases at very low parts-per-million (ppm) levels with fast response and recovery times.

(c) Sensing Performance and Advantages

$BiFeO_3$ has demonstrated promising performance in detecting gases such as hydrogen (H_2), carbon monoxide (CO), and nitrogen dioxide (NO_2). The material exhibits high sensitivity, excellent selectivity, and fast dynamic response under variable temperature and humidity conditions.

Key advantages of $BiFeO_3$ for gas sensing include [58]:

- High sensitivity and selectivity to both oxidizing and reducing gases;
- Fast response and recovery times, attributed to efficient charge transfer at the surface;

- Thermal and chemical stability, enabling operation over a wide temperature and humidity range;
- Low fabrication cost and compatibility with various deposition techniques;
- Multiferroic and semiconducting nature, which allows coupling of electrical and magnetic responses for potential multi-modal sensing applications.

These characteristics make $BiFeO_3$ a highly versatile material for automotive exhaust gas monitoring, environmental air quality analysis, and industrial safety sensors.

(d) Research and Development Trends

Research on $BiFeO_3$-based gas sensors is an active and rapidly evolving field. Recent studies have focused on strategies to enhance the material's sensing performance through doping, nanostructuring, and composite formation.

- Doping with noble metals (Ag, Pt, Pd) or transition metals (Co, Mn, Cu) has been shown to increase surface catalytic activity and oxygen vacancy concentration.
- Nanostructuring $BiFeO_3$ into forms such as nanoparticles, nanorods, and thin films enhances the active surface area and accelerates gas diffusion.
- Hybrid composites, such as $BiFeO_3$–graphene and $BiFeO_3$–ZnO, have demonstrated improved electrical conductivity and selectivity.

These advancements highlight $BiFeO_3$'s potential as a robust, high-temperature, and cost-effective sensing material, especially suitable for automotive exhaust gas detection, where stability and sensitivity are critical.

Bismuth Ferrite Oxide ($BiFeO_3$) is a multifunctional perovskite with intrinsic ferroelectric and magnetic characteristics that make it uniquely suited for gas sensing applications. Its semiconducting nature, combined with excellent thermal and environmental stability, enables effective detection of both oxidizing and reducing gases at low concentrations.

Continued research in doping, nanostructural engineering, and composite development is expected to further enhance $BiFeO_3$'s sensing performance, paving the way for its integration into next-generation high-temperature gas sensors for automotive exhaust and industrial emission monitoring.

2.15 Ag-Doped Bismuth Ferrite (Ag–$BiFeO_3$) Nanostructured Perovskite Gas Sensors

Ag-doped Bismuth Ferrite (Ag–$BiFeO_3$) is an advanced perovskite-based material that has recently garnered significant attention in the field of chemiresistive gas sensing. Derived from pure Bismuth Ferrite ($BiFeO_3$), Ag–BFO combines the intrinsic multiferroic and semiconducting characteristics of $BiFeO_3$ with the catalytic activity and enhanced conductivity introduced by silver (Ag) doping [59].

The incorporation of Ag into the $BiFeO_3$ lattice leads to profound modifications in the material's crystal structure, electronic configuration, and surface chemistry, resulting in improved sensitivity, selectivity, response speed, and operating stability—particularly under high-temperature environments such as those found in automotive exhaust systems.

(a) Structural and Electronic Effects of Ag Doping

In the perovskite structure of $BiFeO_3$ (ABO_3 type), Ag^+ ions can partially substitute Bi^{3+} ions at the A-site or exist as dispersed metallic nanoparticles on the grain surface, depending on synthesis conditions and dopant concentration.

This substitution or surface dispersion induces several beneficial effects [60]:

- Enhanced Oxygen Vacancy Concentration: Partial substitution of Bi^{3+} by Ag^+ leads to charge imbalance, compensated by the formation of oxygen vacancies. These vacancies act as active adsorption sites for gas molecules, enhancing surface reactivity.
- Improved Electrical Conductivity: Ag introduces additional charge carriers, facilitating electron hopping between Fe^{3+} and Fe^{2+} ions, which improves charge transport across the sensing layer.
- Reduced Grain Size: Ag doping often promotes fine-grained microstructures with large surface-to-volume ratios, increasing the effective adsorption area.
- Catalytic Activation: Metallic Ag clusters can act as surface catalysts, accelerating oxidation–reduction reactions between adsorbed gases and surface oxygen species.

These combined effects significantly improve the gas sensing performance of $BiFeO_3$ by enhancing both surface activity and charge transfer kinetics.

(b) Gas Sensing Mechanism of Ag–$BiFeO_3$

The sensing mechanism of Ag–$BiFeO_3$ follows the general chemiresistive behavior of p-type semiconducting oxides but is notably enhanced by Ag-induced catalytic and electronic effects.

When exposed to air, oxygen molecules adsorb on the Ag–BFO surface and capture electrons, forming oxygen species (O_2^-, O^-, or O^{2-}). This adsorption depletes electrons near the surface, increasing hole concentration and thus decreasing resistance. Upon exposure to a reducing gas such as CO or H_2, the gas reacts with the adsorbed oxygen ions, releasing electrons back into the valence band. This reduces hole concentration and leads to an increase in resistance [61].

The presence of Ag facilitates this process by:

- **Lowering the activation energy** for gas–oxygen reactions;
- **Accelerating charge transfer** between the surface and the bulk; and
- **Enhancing oxygen mobility** through increased vacancy concentration.

The result is a faster response and recovery, higher sensitivity, and better selectivity compared to undoped $BiFeO_3$.

(c) Sensing Performance and Target Gases

Ag–$BiFeO_3$ has demonstrated excellent gas sensing performance toward several toxic and combustible gases, including CO, NO_2, H_2, and NH_3. Its superior sensitivity and stability at elevated temperatures make it particularly suitable for automotive exhaust gas sensing, where conventional MOS sensors may degrade.

Typical performance characteristics reported for Ag–$BiFeO_3$ sensors include:

- **Operating temperature range:** 150–400 °C
- **Response time:** 5–20 s
- **Recovery time:** 10–30 s
- **Detection limit:** as low as a few ppm
- **Enhanced selectivity:** to CO and NO_2 under mixed-gas conditions

These results demonstrate that Ag–BFO can efficiently operate under high-temperature and high-humidity environments, maintaining consistent output and long-term durability.

(d) Advantages of Ag Doping

Ag incorporation enhances $BiFeO_3$-based gas sensors through several synergistic mechanisms:

- **Increased catalytic activity:** Ag nanoparticles promote surface redox reactions.
- **Higher charge mobility:** Facilitates faster electron/hole transport.
- **Improved oxygen adsorption:** More active sites from oxygen vacancies.
- **Lower activation energy:** Enables low-temperature sensing operation.
- **Enhanced reproducibility:** Greater signal consistency and reduced drift.

These properties collectively make Ag–$BiFeO_3$ one of the most promising perovskite-based sensing materials for automotive exhaust analysis, environmental monitoring, and industrial safety detection.

Ag-doped $BiFeO_3$ exhibits superior gas sensing performance compared to pure $BiFeO_3$ due to synergistic effects of catalytic activation, enhanced electrical conductivity, and oxygen vacancy engineering. The combination of high thermal stability, rapid response, low detection limits, and broad gas selectivity makes Ag–BFO highly suitable for real-time automotive exhaust gas sensing applications.

Future research should focus on optimizing dopant concentration, nanostructural morphology, and sensor device integration to achieve large-scale, stable, and reproducible perovskite-based gas sensors for industrial deployment.

Summary

This chapter provided a comprehensive review of the recent developments, classifications, and advancements in chemiresistive gas sensing materials, with a special focus on metal oxide and perovskite-based systems. The discussion highlighted how material selection, structural engineering, and functionalization play a crucial role in determining gas sensing performance parameters such as sensitivity, selectivity, response time, recovery time, and stability.

Initially, the chapter outlined the evolution of chemiresistive gas sensing technology over the past decade, emphasizing progress in nanostructured metal oxides, composite systems, and hybrid functional materials. The emergence of the Internet of Things (IoT), machine learning-assisted signal processing, and low-cost fabrication techniques has further accelerated the deployment of these sensors in industrial, environmental, and automotive applications.

Metal oxide semiconductors such as SnO_2, TiO_2, ZnO, CuO, NiO, and Fe_2O_3 have historically been the cornerstone of gas sensing due to their robustness, affordability, and reliable performance. However, their dependence on high operating temperatures and limited selectivity under complex gas mixtures motivated researchers to explore more tunable alternatives. Strategies such as doping, surface modification, coating, encapsulation, and hybridization were discussed as effective ways to optimize material performance by introducing active sites, modifying band structures, and stabilizing surface chemistry.

The chapter then transitioned to complex metal oxides and perovskite-type structures, which offer higher tunability, enhanced electronic mobility, and superior structural stability. Perovskite oxides (ABO_3-type), including $LaFeO_3$, $SrTiO_3$, and $BiFeO_3$, exhibit adjustable defect chemistry and oxygen vacancy concentrations that significantly improve gas adsorption and charge transfer processes. The classification of perovskites—such as ABO_3, double perovskites ($A_2BB'O_6$), Ruddlesden–Popper phases, and hybrid organic–inorganic perovskites—was detailed to show the diversity of possible structures and compositions available for targeted sensing applications.

Comparative analyses between metal oxide and perovskite-based gas sensors demonstrated that perovskites outperform traditional oxides in terms of sensitivity, selectivity, and tunability, while maintaining a relatively low fabrication cost. Nonetheless, challenges such as stability under humidity, reproducibility, and scalability remain barriers to full commercialization.

Among perovskite materials, Bismuth Ferrite ($BiFeO_3$) emerged as a particularly promising candidate owing to its multiferroic nature, p-type semiconducting behavior, and high thermal and chemical stability. Its perovskite-like structure enables efficient modulation of charge transport during gas adsorption, resulting in excellent detection capabilities for gases such as H_2, CO, and NO_2. The material's ability to operate under wide temperature and humidity ranges further reinforces its suitability for automotive exhaust gas monitoring.

Building upon this, Ag-doped $BiFeO_3$ (Ag–BFO) nanostructures were reviewed as next-generation materials that leverage the synergistic effects of silver doping. Ag incorporation enhances oxygen vacancy density, catalytic surface activity, and charge carrier mobility, thereby leading to superior response characteristics and lower operating temperatures. Comparative studies have shown that Ag–BFO sensors exhibit faster response and recovery times, higher sensitivity, and greater selectivity than undoped $BiFeO_3$. These improvements make Ag–BFO highly suitable for high-temperature, real-time automotive exhaust gas detection, addressing key industrial and environmental monitoring challenges.

References:

1. Oleksenko, L. P. (2013). Nanosized Semiconductor CoxOy/SNO_2 Materials for Carbon Monoxide Sensors. *Theoretical and Experimental Chemistry*, *49*(5), 310–314. https://doi.org/10.1007/S11237-013-9330-X

2. Baschirotto, A. (2008). A portable integrated wide-range gas sensing system with smart A/D front-end. *Sensors and Actuators B-Chemical*, *130*(1), 164–174. https://doi.org/10.1016/J.SNB.2007.07.144

3. Degner, M. (2008). Real time exhaust gas sensor with high resolution for onboard sensing of harmful components. *IEEE Sensors*, 973–976. https://doi.org/10.1109/ICSENS.2008.4716604

4. Acharyya, S. (2020). Single resistive sensor for selective detection of multiple VOCs employing SNO_2 hollowspheres and machine learning algorithm: A proof of concept. *Sensors and Actuators B-Chemical*, *321*, 0. https://doi.org/10.1016/J.SNB.2020.128484

5. Zhang, S. (2019). Highly-sensitivity acetone sensors based on spinel-type oxide (NiFe2O4) through optimization of porous structure. *Sensors and Actuators B-Chemical*, *291*, 266–274. https://doi.org/10.1016/J.SNB.2019.04.090

6. Ngamou, P. H. T. (2015). Tailoring the structure and gas permeation properties of silica membranes via binary metal oxides doping. *RSC Advances*, *5*(101), 82717–82725. https://doi.org/10.1039/C5RA15783H

7. Sathitwitayakul, T. (2012). The gas sensing properties of some complex metal oxides prepared by self-propagating high-temperature synthesis. *Materials Letters*, *75*, 36–38. https://doi.org/10.1016/J.MATLET.2012.02.003

8. Durrani, S. M. A. (2012). Investigation of the carbon monoxide gas sensing characteristics of tin oxide mixed cerium oxide thin films. *Sensors*, *12*(3), 2598–2609. https://doi.org/10.3390/S120302598

9. Muchtar, A. R. (2018). Preparation of Graphene–Zinc Oxide Nanostructure Composite for Carbon Monoxide Gas Sensing. *Journal of Electronic Materials*, *47*(7), 3647–3656. https://doi.org/10.1007/S11664-018-6213-X

10. Mahajan, S. (2020). Metal-oxide semiconductors for carbon monoxide (CO) gas sensing: A review. *Applied Materials Today*, *18*, 0. https://doi.org/10.1016/J.APMT.2019.100483

11. Zhang, D. (2019). Cobalt-doped indium oxide/molybdenum disulfide ternary nanocomposite toward carbon monoxide gas sensing. *Journal of Alloys and Compounds*, *777*, 443–453. https://doi.org/10.1016/J.JALLCOM.2018.10.365

12. Zhang, D. (2019). Cobalt-doped indium oxide/molybdenum disulfide ternary nanocomposite toward carbon monoxide gas sensing. *Journal of Alloys and Compounds*, *777*, 443–453. https://doi.org/10.1016/J.JALLCOM.2018.10.365

13. Liu, X. (2008). Acetone gas sensing properties of Smfe1-xMgxO3 perovskite oxides. *Sensors and Actuators B-Chemical*, *134*(2), 483–487. https://doi.org/10.1016/J.SNB.2008.05.024

14. Nagaraju, S. C. (2014). Humidity Sensing Properties of Surface Modified Polyaniline Metal Oxide Composites. *The Journal of Engineering*, *2014*, 1–8. https://doi.org/10.1155/2014/925020

15. Mahajan, S. (2020). Metal-oxide semiconductors for carbon monoxide (CO) gas sensing: A review. *Applied Materials Today*, *18*, 0. https://doi.org/10.1016/J.APMT.2019.100483

16. Alizadeh, T. (2015). A new strategy for low temperature gas sensing by nano-sized metal oxides: Development a new nerve agent simulant sensor. *Materials Chemistry and Physics*, *168*, 180–186. https://doi.org/10.1016/J.MATCHEMPHYS.2015.11.019

17. Jain, S. (2019). Development of Ni doped ZnO/polyaniline nanocomposites as high response room temperature NO_2 sensor. *Materials Science and Engineering B-Advanced Functional Solid-State Materials*, *247*, 0. https://doi.org/10.1016/J.MSEB.2019.114381

18. Ranga, R. (2021). Ferrite application as an electrochemical sensor: A review. *Materials Characterization*, *178*, 0. https://doi.org/10.1016/J.MATCHAR.2021.111269

19. Belle, C. J. (2013). High-throughput experimentation in resistive gas sensor materials development. *Journal of Materials Research*, *28*(4), 574–588. https://doi.org/10.1557/JMR.2012.344

20. Hagedorn, K. (2016). Catalytically Doped Semiconductors for Chemical Gas Sensing : Aerogel-Like Aluminum-Containing Zinc Oxide Materials Prepared in the Gas Phase. *Advanced Functional Materials*, *26*(20), 3424–3437. https://doi.org/10.1002/ADFM.201505355

21. Susanti, D. (2015). Preparation of CO Gas Sensor from ZnO Material Synthesized via Thermo-Oxidation Process. *Modern Applied Science*, *9*(7), 7. https://doi.org/10.5539/MAS.V9N7P127

22. Zhao, X. (2020). Chemical vapor deposition and its application in surface modification of nanoparticles. *Chemical Papers*, *74*(3), 767–778. https://doi.org/10.1007/S11696-019-00963-Y

23. Doll, G. L. (2010). Chemical Vapor Deposition and Atomic Layer Deposition of Coatings for Mechanical Applications. *Journal of Thermal Spray Technology*, *19*(1), 510–516. https://doi.org/10.1007/S11666-009-9364-8

24. Oh, J.-S. (2017). Facile in situ formation of hybrid gels for direct-forming tissue engineering. *Materials Science and Engineering: C*, *78*, 796–805. https://doi.org/10.1016/J.MSEC.2017.04.111

25. Oh, J.-S. (2017). Facile in situ formation of hybrid gels for direct-forming tissue engineering. *Materials Science and Engineering: C*, *78*, 796–805. https://doi.org/10.1016/J.MSEC.2017.04.111

26. Rao, S. K. (2020). Unequivocal evidence of enhanced room temperature sensing properties of clad modified Nd doped mullite Bi2Fe4O9 in fiber optic gas sensor. *Journal of Alloys and Compounds*, *838*, 0. https://doi.org/10.1016/J.JALLCOM.2020.155603

27. Graf, M. (2004). Metal Oxide-Based Monolithic Complementary Metal Oxide Semiconductor Gas Sensor Microsystem. *Analytical Chemistry*, *76*(15), 4437–4445. https://doi.org/10.1021/AC035432H

28. Bora, A. (2015). A Temperature Modulation Circuit for Metal Oxide Semiconductor Gas Sensor. *Indian Journal of Science and Technology*, *8*(13), 1–7. https://doi.org/10.17485/IJST/2015/V8I13/52888

29. Pitcher, S. (2003). Current/voltage characteristics of a semiconductor metal oxide gas sensor. *Sensors and Actuators B-Chemical*, *93*(1), 454–462. https://doi.org/10.1016/S0925-4005(03)00166-7

30. Lackner, E. (2017). Carbon monoxide detection with CMOS integrated thin film SNO_2 gas sensor. *Materials Today: Proceedings*, *4*(7), 7128–7131. https://doi.org/10.1016/J.MATPR.2017.08.007

31. Li, C. (2019). Ordered porous BiVO4 based gas sensors with high selectivity and fast-response towards H2S. *Chemical Engineering Journal*, *375*, 0. https://doi.org/10.1016/J.CEJ.2019.121924

32. Bora, A. (2015). A Temperature Modulation Circuit for Metal Oxide Semiconductor Gas Sensor. *Indian Journal of Science and Technology*, *8*(13), 1–7. https://doi.org/10.17485/IJST/2015/V8I13/52888

33. En-on, J. (2017). Flexible alternating current electroluminescent ammonia gas sensor. *RSC Advances*, *7*(27), 16885–16889. https://doi.org/10.1039/C7RA01318C

34. Yuan, Z. (2021). High Response Formic Acid Gas Sensor Based on MoS 2 Nanosheets. *IEEE Transactions on Nanotechnology*, *20*, 177–184. https://doi.org/10.1109/TNANO.2021.3059622

35. Pasha, A. (2019). Fabrication of gas sensor device using poly (3, 4-ethylenedioxythiophene)-poly (styrenesulfonate)-doped reduced graphene oxide organic thin films for detection of ammonia gas at room temperature. *Iranian Polymer Journal*, *28*(3), 183–192. https://doi.org/10.1007/S13726-019-00689-4

36. Liu, X. (2013). Micromachined catalytic combustion type gas sensor for hydrogen detection. *Micro & Nano Letters*, *8*(10), 668–671. https://doi.org/10.1049/MNL.2013.0468

37. Absalan, S. (2019). High-performance carbon monoxide gas sensor based on palladium/tin oxide/porous graphitic carbon nitride nanocomposite. *Journal of Alloys and Compounds*, *795*, 79–90. https://doi.org/10.1016/J.JALLCOM.2019.04.187

38. Yamazoe, N. (2013). Gas reception and signal transduction of neat tin oxide semiconductor sensor for response to oxygen. *Thin Solid Films*, *548*, 695–702. https://doi.org/10.1016/J.TSF.2013.03.139

39. Faisal, A. D. (2017). Synthesis of ZnO comb-like nanostructures for high sensitivity $$\\hbox {H}_{2}$$S gas sensor fabrication at room temperature. *Bulletin of Materials Science*, *40*(6), 1061–1068. https://doi.org/10.1007/S12034-017-1461-6

40. Patil, L. A. (2006). Heterocontact type CuO-modified SNO_2 sensor for the detection of a ppm level H2S gas at room temperature. *Sensors and Actuators B-Chemical*, *120*(1), 316–323. https://doi.org/10.1016/J.SNB.2006.02.022

41. Moon, Y. K. (2019). Metal Oxide Gas Sensors with Au Nanocluster Catalytic Overlayer: Toward Tuning Gas Selectivity and Response Using a Novel Bilayer Sensor Design. *ACS Applied Materials & Interfaces*, *11*(35), 32169–32177. https://doi.org/10.1021/ACSAMI.9B11079

42. Rhodes, C. J. (2014). Perovskites and their potential use in solar energy applications. *Science Progress*, *97*(3), 279–287. https://doi.org/10.3184/003685014X14098307810589

43. André, L. (2018). Investigation of metal oxides, mixed oxides, perovskites and alkaline earth carbonates/hydroxides as suitable candidate materials for high-temperature thermochemical energy storage using reversible solid-gas reactions. *Materials Today Energy*, *10*, 48–61. https://doi.org/10.1016/J.MTENER.2018.08.007

44. Ramírez, J. L. (2015). Single Layer Gold Hotplate, Printed on Polyimide, with Heater Used as Sensing Current Drain for Metal-oxide Gas Sensor. *Procedia Engineering*, *120*, 707–710. https://doi.org/10.1016/J.PROENG.2015.08.764

45. Li, X. (2019). Two-Dimensional Dion-Jacobson Hybrid Lead Iodide Perovskites with Aromatic Diammonium Cations. *Journal of the American Chemical Society*, *141*(32), 12880–12890. https://doi.org/10.1021/JACS.9B06398

46. Worley, C. (2019). (CH3NH3)AuX4·H2O (X=Cl, Br) and (CH3NH3)AuCl4: Low-Band Gap Lead-Free Layered Gold Halide Perovskite Materials. *Chemistry: A European Journal*, *25*(42), 9875–9884. https://doi.org/10.1002/CHEM.201901112

47. Sharma, N. (2020). Fabrication of LaFeO3 and rGO-LaFeO3 microspheres based gas sensors for detection of NO_2 and CO. *RSC Advances*, *10*(3), 1297–1308. https://doi.org/10.1039/C9RA09460A

48. Sharma, N. (2020). Fabrication of LaFeO3 and rGO-LaFeO3 microspheres based gas sensors for detection of NO_2 and CO. *RSC Advances*, *10*(3), 1297–1308. https://doi.org/10.1039/C9RA09460A

49. Hsu, K.-C. (2019). Gas sensitivity and sensing mechanism studies on ZnO/La0.8Sr0.2Co0.5Ni0.5O3 heterojunction structure. *Ceramics International*, *45*(7), 8744–8749. https://doi.org/10.1016/J.CERAMINT.2019.01.198

50. Pargoletti, E. (2020). Breakthroughs in the Design of Novel Carbon-Based Metal Oxides Nanocomposites for VOCs Gas Sensing. *Nanomaterials*, *10*(8), 8. https://doi.org/10.3390/NANO10081485

51. Moalaghi, M. (2020). Tin oxide gas sensor on tin oxide microheater for high-temperature methane sensing. *Materials Letters*, *263*, 0. https://doi.org/10.1016/J.MATLET.2019.127196

52. Kim, B. J. (2014). In2O3-based micro gas sensor for detecting NOx gases. *Electronic Materials Letters*, *10*(2), 509–513. https://doi.org/10.1007/S13391-013-3133-Z

53. Chaudhari, G. N. (2006). Structural and gas sensing behavior of nanocrystalline BaTiO3 based liquid petroleum gas sensors. *Vacuum*, *81*(3), 251–256. https://doi.org/10.1016/J.VACUUM.2006.03.026

54. Maity, A. (2019). High sensitivity NH 3 gas sensor with electrical readout made on paper with perovskite halide as sensor material. *Scientific Reports*, *9*(1), 1. https://doi.org/10.1038/S41598-019-43961-6

55. Zhuang, Y. (2017). High-performance gas sensors based on a thiocyanate ion-doped organometal halide perovskite. *Physical Chemistry Chemical Physics*, *19*(20), 12876–12881. https://doi.org/10.1039/C7CP01646H

56. Li, Q. (2018). Ag modified bismuth ferrite nanospheres as a chlorine gas sensor. *RSC Advances*, *8*(58), 33156–33163. https://doi.org/10.1039/C8RA06247A

57. Li, Q. (2018). Ag modified bismuth ferrite nanospheres as a chlorine gas sensor. *RSC Advances*, *8*(58), 33156–33163. https://doi.org/10.1039/C8RA06247A

58. Waghmare, S. D. (2020). Pristine and palladium-doped perovskite bismuth ferrites and their nitrogen dioxide gas sensor studies. *Journal of King Saud University - Science*, *32*(7), 3125–3130. https://doi.org/10.1016/J.JKSUS.2020.08.024

Towards Robust High-Temperature Gas Sensors for Automotive Exhaust Monitoring: Motivation, Framework, and Research Strategy

The rapid growth of motorized transport has created a pressing environmental challenge. Automotive exhausts remain a major source of air pollutants such as CO, NO_x, hydrocarbons, and particulate matter. While the global transition toward electric vehicles offers a promising long-term solution, full electrification is not yet practical for heavy-duty vehicles and long-haul applications. These vehicles continue to depend on hydrocarbon fuels, generating significant exhaust emissions that threaten both environmental quality and human health.

To manage these emissions, continuous monitoring of exhaust composition is essential. However, existing approaches — such as periodic emission testing (PUC) — suffer from calibration issues, cost constraints, and poor correlation with real driving conditions. Conventional analytical systems (FTIR, NDIR, FID) deliver excellent precision but are bulky, expensive, and unsuitable for in-vehicle integration.

This challenge motivates the development of compact, low-cost, thermally stable gas sensors capable of real-time monitoring in exhaust environments. Among various sensing approaches, chemiresistive sensors are particularly attractive because they combine simplicity, miniaturization potential, and compatibility with electronic systems. To function effectively within exhaust lines, such sensors must operate reliably around 200–250 °C, withstand high humidity and vibrations, and selectively detect individual gases within complex mixtures.

3.2 Scientific and Technological Context

Semiconducting metal oxides (SMOs) are well established as active materials for chemiresistive sensors. However, their optimum sensing temperature (≈350–450 °C) is significantly higher than the actual exhaust temperature range (≈190–240 °C). Bridging this temperature gap has become a major engineering and materials science challenge. Two strategies are possible:

1. **Thermal activation:** externally heat the sensor or gas stream to the desired temperature — effective but power-intensive and costly.
2. **Material modification:** tailor the semiconductor's electronic and catalytic properties (through doping, heterostructuring, or compositing) to reduce its optimal operating temperature.

The latter approach is more promising for vehicular applications. Doping with noble metals such as Ag, Au, or Pt introduces catalytic activity and oxygen vacancies that enhance surface reactions at lower temperatures. Yet even with improved sensitivity, another key challenge persists: selectivity — the ability to distinguish one analyte in a multicomponent gas mixture.

Recent advances in Density Functional Theory (DFT) and pattern recognition algorithms enable a combined materials–data approach: DFT provides atomic-level understanding of adsorption phenomena, while pattern recognition techniques (e.g., PCA, ANN) enable discrimination among gas responses in complex exhaust mixtures. Integrating these tools offers a route toward both fundamental understanding and practical sensor design.

3.3 Knowledge Gaps and Scientific Opportunities

Despite substantial progress, several critical knowledge gaps remain in the field:

- Limited cross-selectivity data under realistic exhaust conditions.
- High operating temperatures required for SMOs, leading to energy inefficiency.
- Insufficient atomic-level insight into how dopants (such as Ag) influence gas adsorption and charge transfer in perovskite lattices.
- Lack of integrated frameworks combining DFT-guided material design, synthesis, and experimental validation.
- Minimal use of sensor arrays and machine-learning algorithms to handle complex gas mixtures typical of exhausts.

Addressing these gaps requires a comprehensive approach that couples theoretical prediction with material innovation and advanced data analysis.

3.4 Research Focus and Conceptual Framework

This book section explores the design and development of Ag-doped $BiFeO_3$ (Ag–BFO) as a robust, selective, and thermally stable sensing material for automotive exhaust gas monitoring. The research framework integrates computational, experimental, and data-driven components:

I. **Atomic-Scale Modelling (DFT):**

Investigate gas adsorption energetics and electronic structure changes in undoped and Ag-doped $BiFeO_3$ for exhaust-relevant gases (CO, CO_2, NO, NO_2, CH_4).

II. **Material Synthesis and Characterization:**

Prepare and characterize Ag–BFO nanostructures using sol–gel and hydrothermal methods; evaluate structure, morphology, and defect states.

III. **Sensor Fabrication and Testing:**

Develop chemiresistive sensors, test them under controlled gas exposure at 190–250 °C, and analyze dynamic parameters such as sensitivity, selectivity, and response/recovery times.

IV. **Data Analytics and Pattern Recognition:**

Employ multivariate analysis (PCA, LDA, ANN) to classify gas responses and improve selectivity in mixed-gas conditions.

V. **Theoretical–Experimental Correlation:**
Correlate DFT predictions with laboratory results to validate adsorption mechanisms and optimize sensor performance.

3.5 Scientific and Societal Significance

The work described in this chapter contributes to both sensor science and environmental technology:

- **Scientific relevance:** Provides an integrated understanding of how noble-metal doping affects adsorption energetics, electronic structure, and macroscopic sensing behavior in perovskite oxides.
- **Technological impact:** Demonstrates a pathway to low-cost, high-temperature-stable sensors suitable for continuous automotive exhaust monitoring.
- **Societal benefit:** Enables improved emission control and policy enforcement through real-time, in-vehicle pollutant monitoring systems.
- **Interdisciplinary significance:** Combines materials design, computational chemistry, and artificial intelligence for next-generation sensing platforms.

3.6 Conceptual Research Design

The adopted research strategy unfolds through three interconnected stages (Figure 3.1):

1. **Computational Design (DFT):** Surface modelling, adsorption energy calculations, charge density mapping.
2. **Experimental Validation:** Synthesis, characterization, and fabrication of chemiresistive devices.
3. **Performance Optimization:** Pattern-recognition-enabled multi-gas sensing and data interpretation.

This integrated workflow ensures a consistent feedback loop between theory and experiment, enabling rational material optimization.

3.7 Scope of the Book Section

The material presented here establishes the scientific rationale and design principles for developing Ag-doped $BiFeO_3$ as an advanced chemiresistive sensing material. It provides the conceptual foundation for subsequent chapters that cover:

- Computational methodology and adsorption modelling (DFT) and Experimental synthesis and characterization of Ag–BFO.

This chapter presented the motivation, conceptual framework, and strategic approach underlying the development of Ag-doped $BiFeO_3$ gas sensors for automotive exhaust monitoring. By combining atomic-level modelling, targeted synthesis, and data-driven analysis, the work aims to advance the field toward compact, energy-efficient, and selective sensor technologies capable of operating in demanding exhaust automotive emissions.

Density Functional Theory (DFT) Framework and Experimental Validation of Gas Sensing Materials

The development of efficient and selective gas sensors requires a deep understanding of material behavior at both the atomic and macroscopic levels. This chapter integrates two complementary aspects — theoretical modeling using Density Functional Theory (DFT) and experimental validation through laboratory-based characterization — to provide a comprehensive framework for gas sensing research. The DFT approach is employed to study the electronic structure, adsorption behavior, and surface reactivity of gas-sensing materials, enabling the prediction of how gases interact with functionalized surfaces such as doped Bismuth Ferrite Oxide ($BiFeO_3$). These theoretical insights form the basis for designing materials with improved sensitivity, selectivity, and stability. The experimental section details the fabrication of thin and thick film sensors, measurement configurations, and analytical techniques such as X-ray diffraction (XRD), scanning electron microscopy (SEM), and energy dispersive X-ray analysis (EDX). Together, these methods bridge the gap between computational predictions and real-world sensor performance, offering a systematic pathway for the design and optimization of next-generation gas sensing systems.

Theoretical modelling has become an indispensable tool in modern materials science, enabling researchers to understand and predict the behavior of materials at the atomic and electronic levels. In the context of gas sensing, computational approaches provide crucial insight into the interaction mechanisms between gas molecules and sensing materials—insights that are often difficult to capture experimentally.

This chapter presents the theoretical framework adopted in the present work, focusing on Density Functional Theory (DFT) as the principal computational approach. DFT serves as the foundation for understanding adsorption phenomena, charge transfer, and electronic property modulation that occur when gas molecules interact with active sensing materials such as Bismuth Ferrite ($BiFeO_3$) and its Ag-doped variants.

By simulating these interactions at the atomic scale, DFT allows for the prediction of key parameters such as adsorption energy, charge redistribution, and density of states, which directly correlate with measurable macroscopic sensor performance (e.g., sensitivity and selectivity). The theoretical insights obtained form the basis for experimental material design and optimization discussed in later chapters.

4.1 Theoretical Investigation

The theoretical component of this study aims to establish a detailed understanding of how gas molecules—specifically CO, CO_2, NO, NO_2, and CH_4—interact with pristine and Ag-doped $BiFeO_3$ surfaces. Through first-principles simulations, the adsorption sites, energetics, and charge transfer mechanisms are analyzed to explain and predict the sensing behavior of these materials.

Such theoretical investigations provide a microscopic interpretation of the gas-sensing mechanism. They not only reveal how dopants like Ag influence the surface electronic structure and defect states of $BiFeO_3$, but

also explain why certain gases exhibit stronger binding affinity or charge exchange with specific surface configurations.
In essence, the theoretical framework bridges the gap between fundamental material properties and practical sensor performance, enabling the rational design of efficient, selective, and thermally stable gas-sensing materials.

4.2 Density Functional Theory for Gas Sensing Applications

Density Functional Theory (DFT) is a quantum mechanical computational approach used extensively in physics, chemistry, and materials science to determine the electronic structure of atoms, molecules, and solids. It is based on the principle that all ground-state properties of a many-electron system can be described as a functional of its electron density rather than its many-body wavefunction [1].
For gas sensing research, DFT provides a microscopic picture of the adsorption process, describing how gas molecules interact with sensor surfaces at the electronic level. Key quantities such as adsorption energy (E_ad), charge transfer (ΔQ), and density of states (DOS) are derived from these simulations, helping to interpret and predict the material's response to different analytes [2].

By modelling both the gas molecules and the sensing material surface, DFT enables:

- Prediction of binding energies and adsorption sites, revealing how strongly a gas adheres to the sensor surface.
- Calculation of electron density distributions, offering insights into charge exchange mechanisms during adsorption.
- Evaluation of electronic band structure modifications, which indicate how gas adsorption affects material conductivity.
- Understanding of dopant effects, such as how Ag incorporation modifies the electronic landscape, increases oxygen vacancies, or enhances catalytic activity.

Through these analyses, DFT helps identify materials with optimal gas–surface interactions, allowing researchers to design sensors with enhanced sensitivity, selectivity, and stability for specific target gases.

In the present work, DFT simulations are used to:

1. Examine the adsorption characteristics of CO, CO_2, NO, NO_2, and CH_4 on both pristine and Ag-doped $BiFeO_3$ surfaces.
2. Quantify adsorption energies to determine thermodynamic favorability of each gas–surface interaction.
3. Analyze the charge density difference maps to visualize charge redistribution upon gas adsorption.
4. Evaluate changes in the electronic structure (band gap, DOS) to understand the material's sensing response.

These theoretical results provide an atomic-level foundation for interpreting experimental observations of gas sensing performance and guide the optimization of Ag-doping levels in $BiFeO_3$ for superior chemiresistive behavior.

4.3 Fundamentals of Density Functional Theory

Understanding the interaction between gas molecules and sensing materials requires a detailed description of their electronic structure. Among the various quantum mechanical frameworks available, Density Functional Theory (DFT) has emerged as one of the most powerful and widely used tools for this purpose. DFT provides a practical yet rigorous approach for predicting the ground-state properties of atoms, molecules, and solids by focusing on electron density rather than complex many-electron wavefunctions.

4.3.1 Conceptual Foundation

In quantum mechanics, the behaviour of electrons in a system is governed by the Schrödinger equation, which expresses the relationship between the system's total energy and the wavefunction of its electrons. The wavefunction contains complete information about the system but depends on the coordinates of all electrons—making it computationally expensive for large systems such as solids or nanostructured materials [3,4].

Density Functional Theory simplifies this complexity by shifting the focus from the many-body wavefunction to a more manageable quantity: the electron density (ρ). Electron density represents the probability of finding an electron at a particular position in space, and it varies with the spatial distribution of atoms in the system. Since electron density is a measurable and physically meaningful property, it serves as the fundamental variable in DFT [5].

4.3.2 The Hohenberg–Kohn Theorems

The theoretical foundation of DFT is built upon two landmark theorems proposed by Hohenberg and Kohn (1964) [6]:

1. **First Theorem (Uniqueness Theorem):**
   The ground-state properties of a many-electron system are uniquely determined by its electron density. This means that all observables—including total energy—are functionals of the electron density, not of the wavefunction.
2. **Second Theorem (Variational Principle):**
   The ground-state electron density minimizes the total energy functional. The correct ground-state energy is obtained when the true electron density is used in the functional.

These theorems provide the conceptual justification for replacing the many-electron wavefunction with a simpler three-dimensional function, ρ(r), thereby transforming the quantum many-body problem into a more tractable form.

In the study of quantum systems with many electrons, one of the most profound breakthroughs came in the 1960s with the development of Density Functional Theory (DFT). The foundation of DFT lies in the Hohenberg–Kohn (HK) theorem, proposed by Pierre Hohenberg and Walter Kohn in 1964. This theorem revolutionized quantum chemistry by showing that the complex wavefunction of a many-electron system can be replaced by a much simpler quantity — the electron density (ρ).

4.3.2.1 Understanding the Concept

In earlier approaches, such as the Schrödinger or Hartree–Fock methods, the system's properties were described using a wavefunction that depends on the coordinates of all electrons — an extremely complicated

object for large systems. The Hohenberg–Kohn theorem simplified this picture dramatically. It states that the ground-state electron density uniquely determines the external potential of the system. In simpler terms, if you know how the electrons are distributed in space (their density), you can, in principle, determine everything else — including the total energy and all observable properties of the system.

- V_ext(r) ↔ ρ(r)

This means that the external potential and the ground-state electron density are uniquely related.

4.3.2.2 Two Key Theorems

Hohenberg and Kohn proposed two central theorems that form the basis of DFT:

Theorem 1: The external potential V_ext(r) and the total ground-state energy E_total are unique functionals of the electron density ρ(r). In other words, the energy of a system can be written entirely in terms of its electron density.

Theorem 2: For the correct, or ground-state, electron density, the system's total energy reaches its minimum value. Any other (incorrect) density will always give a higher energy value. This can be expressed as:

$$E_{G\,s}[\rho(\mathrm{r})] \geq E_{\mathrm{GS}}\ \ [\rho_{\mathrm{GS}}(r)]$$

The subscript GS is the abbreviation of the ground state; $E_{GS}[\rho(\mathrm{r})]$ is system energy calculated by random density; while $E_{GS}[\rho_{GS}(r)]$ is the minimum energy due to the density state reaching ground state.

4.3.2.3 Mathematical Formulation

The total energy of a system can therefore be written as a functional (a mathematical function of another function) of electron density ρ(r):

$$E[\rho(\mathrm{I})] = T[\rho(\mathrm{r})] + V_{ee}[\rho(\mathrm{r})] + \mathrm{V}_{en}[\rho(\mathrm{I})]$$
$$\mathrm{E}[\rho(\mathrm{r})] = \mathrm{T}[\rho(\mathrm{r})] + \mathrm{V\_ee}[\rho(\mathrm{r})] + \mathrm{V\_en}[\rho(\mathrm{r})]$$

Where $T[\rho(\mathrm{I})], V_{ee}[\rho(\mathrm{I})]$ and $V_{en}[\rho(\mathrm{I})]$ represent kinetic, electron-electron and electron-nuclear energies respectively. If we separate out the energy intrigued by interaction between electrons and external potential, total energy is shown below as a function of electron density:

If we separate the part of the energy that arises from interactions with the external potential V_ext(r), we can rewrite it as:

$$E[\rho(\mathrm{r})] = F_{HK}[\rho(\mathrm{r})] + \int \rho(\mathrm{r})\mathrm{V}_{ext}(r)dr$$
$$= T[\rho(\mathrm{r})] + V_{ee}[\rho(\mathrm{r})] + \int \rho(\mathrm{r})\mathrm{V}_{ext}(r)dr$$

4.3.2.4 Physical Interpretation

The power of the Hohenberg–Kohn theorem lies in its simplicity. Instead of tracking the motion of each electron individually (as required by wavefunction-based methods), DFT focuses only on the electron density, which depends on three spatial variables — regardless of how many electrons are in the system.

This shift from wavefunction to density dramatically reduces computational complexity, allowing scientists to model atoms, molecules, and solids with far greater efficiency.

4.3.2.5 An Analogy

Imagine you're studying a city at night. Instead of keeping track of every person's position and motion (like in wavefunction methods), you only measure the brightness map of the city — how many lights are on at each location. From this brightness map (the electron density), you can infer where people live, how dense certain areas are, and even estimate total energy use. That's what the Hohenberg–Kohn theorem allows for electrons in a material.

The Hohenberg–Kohn theorem is the cornerstone of Density Functional Theory (DFT). It states that the ground-state electron density of a system uniquely determines its external potential and total energy. This means that all properties of a quantum system can, in principle, be derived from its electron density alone. By shifting the focus from wavefunctions to density, DFT makes it possible to compute electronic properties of complex materials with far greater simplicity and efficiency.

4.3.3 The Kohn–Sham Formalism

In the 1960s, Walter Kohn and Lu Jeu Sham created the Kohn-Sham technique [10], a particular application of Density Functional Theory. Computational chemistry and materials science utilise it often to investigate molecular and atomic electrical structure.

The Kohn-Sham approach involves substituting a set of non-interacting "pseudo-particles" (also known as Kohn-Sham orbitals) for the interacting electrons in a system in the Schrödinger equation. Hence, faster computing approaches may be used to solve the Schrödinger equation.

The electron density of a system, in turn used to compute the system's total energy using the Kohn-Sham orbitals. Total energy is found by adding the energies of individual electrons, the energy of interactions between electrons, and the potential energy of the electrons owing to the nucleus.

The Kohn-Sham approach relies on the creation of a second, non-interacting system with the same electron density as the real interacting system. The energy used in the process of exchanging and correlating electrons in the system is known as the exchange-correlation energy, and it is determined with the help of this auxiliary system.

For investigating the electronic structure of molecules or materials, the Kohn-Sham approach is often employed in computational chemistry and materials research. Whether you're interested in atoms, molecules, or solids, this potent computational tool may help you learn more about their electrical characteristics [11].
The Hohenberg-Kohn Theorems indicate that in order to calculate the system's total energy, we must first learn what its ground state density is, but the exact nature of the link between density and energy is still a mystery. Using the one-electron Schrödinger equation with self-consistent equations that include exchange and correlation effects, KohnSham presented a technique to calculate density in 1965 [41]. The Hohenberg-Kohn Theorems indicate that we need to know the density of the system in its ground state before we can calculate its total energy, although the nature of that connection has yet to be established. In 1965 [41], KohnSham suggested an approach to calculating density based on the one-electron Schrödinger equation, which involves self-consistent equations that take into account exchange and correlation effects.

$$\left(-\frac{\hbar^2}{2m}\nabla^2 + v_{\text{eff}}(r)\varphi_i(r) = \varepsilon_i\varphi_i(r)\right.$$

Where $v_{eff}(r)$ denotes the Kohn-Sham potential, which represents the effective external potential in which no-interacting particles move. φ_i(r)is the Kohn-Sham orbital function, and the value ε_i is the eigenvalue of the corresponding Kohn-Sham orbital, representing its energy.

The following equation can be used to calculate the electron density:

$$\rho(r) = \sum_{i=1}^{N} |\rho_i(r)|$$

N is electron number in the system. And $v_{\text{eff}}(r)$ expression can be written as:

$$v_{\text{eff}}(r) = E_{\text{eff}}(r) + \text{e}^2 \int \frac{\rho(\text{r}')}{|r - r|} dr' + V_{xc}(\text{r})$$

The total energy with Kohn-Sham external potential is written as

$$\text{E}(\rho) = \text{T}(\rho) + \text{E}_{ee}(\rho) + \int v_{\text{eff}}(r)\rho(r)ar + V_{xc}(\rho)$$

In that formula, $T(\rho)$ is the kinetic energy of non-interactive electrons, $\text{E}_{ee}(\rho)$ is the interaction energy between electrons, and $v_{\text{eff}}(r)$ is the previously established external potential. $V_{xc}(\rho)$ denotes the exchange-correlation potential, which is written as:

$$V_{xc} = \frac{\delta E_{xc}(\rho)}{\delta\rho(r)}$$

The Coulomb functional, the Exchange functional, the Correlation functional, and the Kinetic functional make up $E_{xc}(\rho)$. Because some components of DFT can never be understood precisely, approximation is unavoidable.

As a result, a good estimate of the $E_{xc}(\rho)$. component leads to an accurate and efficient technique, such as Local Density Approximation (L(S)DA) and Generalized Gradient Approximation (GGA), both of which are generally recognised in present DFT research.

4.3.4 Energy and Electronic Properties

Once the total energy of the system is minimized with respect to electron density, various electronic properties can be derived, including:

- Total energy and formation energy of the material,
- Band structure and density of states (DOS),
- Charge density distribution,
- Adsorption energy and charge transfer during gas–surface interactions.

These quantities form the basis for interpreting gas adsorption mechanisms in sensing materials. For instance, changes in the band gap or charge redistribution upon gas adsorption directly correspond to variations in the sensor's resistance—providing a microscopic understanding of macroscopic sensing behaviour.

In essence, Density Functional Theory provides a rigorous yet computationally efficient framework for studying the electronic structure of materials. By focusing on electron density, DFT circumvents the complexity of many-electron wavefunctions while retaining sufficient accuracy to predict key physical and chemical properties.

For gas sensing applications, DFT enables detailed examination of adsorption phenomena, charge transfer, and surface reactivity—parameters that determine sensitivity, selectivity, and response kinetics. In the subsequent sections, the application of DFT to $BiFeO_3$ and Ag-doped $BiFeO_3$ systems will be discussed, elucidating how electronic structure modifications influence gas-sensing performance.

4.4 The Schrödinger Equation and the Many-Body Problem

The Schrödinger equation is one of the foundational equations in quantum mechanics. It describes the behavior of electrons in a physical system such as an atom, molecule, or solid. This equation, formulated by Erwin Schrödinger in 1925–1926, fundamentally transformed our understanding of matter at the atomic and subatomic scales. It provides the theoretical basis for determining the electronic structure of materials and serves as the starting point for Density Functional Theory (DFT) and many other quantum mechanical methods [8].

The Schrödinger equation defines the wavefunction (ψ) of a system, which represents the probability amplitude of finding an electron at a particular position in space. The absolute square of this wavefunction, $|\psi|^2$, gives the probability density of locating the electron at that point. Mathematically, the time-dependent Schrödinger equation can be written as:

$$i\hbar\, \partial\psi/\partial t \;=\; H\psi$$

where:

- ψ – wavefunction describing the quantum state of the system.
- i – imaginary unit, where $i^2 = -1$.
- $\hbar$ – reduced Planck's constant ($h / 2\pi$).
- H – Hamiltonian operator representing total energy (kinetic + potential).

The Hamiltonian operator (H) for an electron in a potential field is expressed as:

$$H \;=\; -(h^2 / 2m)\, \nabla^2 \;+\; V$$

where:

- h is Planck's constant,
- m is the electron mass,
- V is the potential energy function,
- ∇^2 (Laplacian operator) is defined as:

$$\nabla^2 = \left(\frac{\partial^2}{\partial x^2}\right) + \left(\frac{\partial^2}{\partial y^2}\right) + \left(\frac{\partial^2}{\partial z^2}\right)$$

Here, *x*, *y*, and *z* represent the spatial coordinates in a three-dimensional Cartesian coordinate system.
In many applications, the time-independent Schrödinger equation is more relevant, as it focuses on stationary states of the system:

$$H\psi = E\psi$$

where E represents the energy eigenvalue associated with the wavefunction ψ.
This equation describes the quantized energy levels of electrons in atoms, molecules, or solids.

The Schrödinger equation can be solved analytically only for very simple systems, such as the hydrogen atom or the H_2^+ molecular ion, because of the complexity of electron–electron interactions in multi-electron systems. For more complex systems, numerical and approximate methods—such as Density Functional Theory (DFT), Hartree–Fock, and post-Hartree–Fock methods—are employed to obtain electronic properties.

By solving the Schrödinger equation, one can determine key quantities such as electron energy levels, charge densities, and wavefunctions, which form the foundation for computing derived properties like bond strength, electron density distribution, and chemical reactivity. These properties are essential for understanding the physical and chemical behavior of materials.

In summary, the Schrödinger equation provides the fundamental framework for describing the quantum mechanical behavior of electrons. It serves as the cornerstone of theoretical approaches used to explore the electronic structure of atoms, molecules, and solids—thereby forming the theoretical basis for advanced methods such as Density Functional Theory that are employed in gas-sensing material investigations.

When we study materials at the atomic scale, we deal with a huge number of interacting particles — mainly electrons and atomic nuclei. Each electron feels the attraction of all nuclei and the repulsion of all other electrons, while each nucleus interacts with every other nucleus. This web of interactions is known as the many-body problem in quantum mechanics.

In principle, we could describe this system exactly using the Schrödinger equation, which governs the motion of all particles. However, solving it directly for such a large number of interactions is nearly impossible because of the enormous computational complexity. To make progress, physicists use a clever simplification known as the Born–Oppenheimer approximation.

4.4.1 The Born–Oppenheimer Approximation

Electrons are much lighter than atomic nuclei — in fact, nearly 2000 times lighter. Because of this, electrons move extremely fast compared to the heavy nuclei. Therefore, while electrons rapidly adjust their motion, the nuclei can be considered almost stationary during the electron movement.

This assumption allows us to treat the electronic and nuclear motions separately, greatly simplifying the problem. Mathematically, the total Hamiltonian (which represents the total energy of the system) can be written as:

$$H = T_n + T_e + V_{en} + V_{nn} + V_{ee}$$

where:
• T_n: kinetic energy of the nuclei

• T_e: kinetic energy of the electrons
• V_{en}: potential energy between electrons and nuclei
• V_{nn}: repulsive potential between nuclei
• V_{ee}: repulsive potential between electrons

In this approach, the wavefunction (Ψ), which describes the behavior of the entire system, can be expressed as the product of two parts:

$\Psi(r, R) = \Psi_e(r; R)\, \Psi_n(R)$

where:

$\Psi_e(r; R)$ describes the electronic motion for fixed nuclear positions (R),

$\Psi_n(R)$ describes the nuclear motion based on the potential energy landscape defined by the electrons.

The Born–Oppenheimer approximation allows us to split the total Schrödinger equation into two simpler equations:

Electronic part: $H_e(r, R)\, \Psi_e(r, R) = E_e(R)\, \Psi_e(r, R)$
Nuclear part: $H_n(R)\, \Psi_n(R) = E_n\, \Psi_n(R)$

Hence, the total energy of the system can be written as:

E_total = E_electronic + E_nuclear-nuclear

4.4.2 The Hartree–Fock Approximation

Even after using the Born–Oppenheimer approximation to separate the motion of nuclei and electrons, solving the Schrödinger equation for systems with many electrons remains extremely difficult. The reason is that each electron interacts not only with the nucleus but also with every other electron — creating a complex web of mutual forces that cannot be calculated directly.

To deal with this complexity, the physicist Douglas Hartree proposed in 1928 a simplified approach known as the self-consistent field (SCF) method. His idea was elegant: instead of treating all electrons at once, we imagine that each electron moves independently in an average electric field created by the nucleus and all the other electrons.

This means that the total behavior of an atom or molecule can be built up by combining several single-electron wavefunctions. If there are n electrons, the total wavefunction (Ψ) can be written approximately as a product of n individual single-electron wavefunctions (ψ):

- $\Psi(r_1, r_2, \ldots, r_n) \approx \psi_1(r_1)\, \psi_2(r_2) \ldots \psi_n(r_n)$

This simplification drastically reduces the computational difficulty — but it ignores an important quantum principle: electrons are indistinguishable fermions, and no two electrons can occupy the same quantum state

(the Pauli exclusion principle).

4.4.2.1 Inclusion of Spin and Anti-Symmetry

In 1930, John Slater and Vladimir Fock improved Hartree's idea by including the spin of electrons and the rule of wavefunction anti-symmetry. This gave rise to the Hartree–Fock (HF) method — the foundation of most modern quantum chemistry.

Electrons come in two spin states — spin-up (α) and spin-down (β). If two electrons occupy the same spatial orbital, they must have opposite spins. To ensure that the total wavefunction changes sign whenever two electrons are swapped, Slater introduced a mathematical form known as the Slater Determinant:

$$\Psi_m = \frac{1}{\sqrt{N!}} \begin{vmatrix} \Psi_{1,\alpha}(1) & \Psi_{1,A}(1) & \dots & \Psi_{\mathrm{N},\beta}(1) \\ \Psi_{1,\alpha}(2) & \Psi_{1,\phi}(2) & \cdots & \Psi_{\mathrm{N},\beta}(2) \\ \vdots & \vdots & \vdots & \vdots \\ \Psi_{1,\alpha}(\mathrm{N}) & \Psi_{1,G}(\mathrm{N}) & \cdots & \Psi_{\mathrm{K_a}}(\mathrm{N}) \end{vmatrix}$$

Each column represents a single-electron wavefunction, and each row represents a different electron. If any two rows or columns are identical — meaning two electrons are in the same state — the determinant becomes zero. This automatically enforces the Pauli exclusion principle.

4.4.2.2 Simplifications Behind the Hartree–Fock Method

To make calculations possible, several key assumptions are made in the Hartree–Fock approach:

- Born–Oppenheimer approximation: Electrons move much faster than nuclei, so the nuclei are considered fixed.
- Non-relativistic treatment: The effects of Einstein's relativity are neglected because electrons move slower than light.
- Wavefunction as a linear combination: Each electron's wavefunction is expressed as a combination of simple basis functions.
- Antisymmetry requirement: The total wavefunction must obey the Pauli exclusion principle, handled by the Slater determinant.
- Mean-field approximation: Each electron feels only an average field due to all others — direct electron–electron correlations are ignored.

4.4.2.3 Limitations and the Need for Improvement

While the Hartree–Fock method provides a major simplification, it is still an approximation. By ignoring the instantaneous correlations between electrons (how one electron's motion affects another's at a given moment), it introduces a small but important error known as the correlation energy, defined as:

$$E_{\text{exact}} - E_{HF} = E_{\text{correlation}}$$

This difference explains why Hartree–Fock often predicts slightly higher energies (less stable systems) than experiments show.

To overcome this limitation, modern computational methods such as Density Functional Theory (DFT) include both exchange (arising from electron indistinguishability) and correlation (arising from electron

motion coupling) effects. Thus, DFT is often considered a more complete successor to the Hartree–Fock method.

You can think of the Hartree–Fock approach as a "teamwork model" for electrons: each electron moves independently, responding to the average influence of its teammates rather than tracking every small interaction in real-time. This saves enormous computation time, though some fine details — like the tiny adjustments electrons make to avoid each other — are left out.

4.5 DFT Approximations and Implementation

4.5.1 Local (Spin) Density Approximation (L(S)DA)

One of the simplest approximations that may provide a reliable exchange-correlation function is the local spin density approximation (L(S)DA). Despite the fact that this method was first introduced in Kohn and Sham's publication, it has been traced back to the Thomas-Fermi theory.

In order to calculate a L(S)DA, it is assumed that the density is constant throughout. Hence, the energy exchange correlation between LSDA and LDA may be written as:

$$E_{xc}^{\mathrm{LSDA}}(\rho(r)) = \int \rho(r)\varepsilon_{xc}\Big(\rho(r_{\uparrow}, r_{\downarrow})\Big)\mathrm{dr},$$
$$E_{xc}^{LDA}(\rho(r)) = \int \rho(r)\varepsilon_{xc}(\rho(r))\mathrm{dr}$$

Where $\varepsilon_{xc}(\rho(r))$denotes each particle's exchange-correlation energy. As a result, while this method accurately defines molecules, geometries, and vibration frequencies, it is ineffective at predicting bonding energies (more than 10 percent). Furthermore, it may be divided into two components for easier comprehension: exchange term and correlation term.

$$E_x = E_x + E_c$$

E_x is less difficult to solve than E_c. The exchange energy, commonly known as Dirac exchange, may be stated as follows:

$$E_{\mathrm{x}}(\rho(r)) = -\frac{3}{4}\left(\frac{3}{\pi}\right)^{\frac{1}{3}}\int \rho(r)^{\frac{4}{3}}dr$$

However, until recently, no precise equation for describing correlation energy has been presented. E_c is derived from Jianmin's group's quantum Monte Carlo (QMC) simulations.

4.5.2 Generalized Gradient Approximation (GGA)

The exchange energy is often underestimated and the correlation energy typically overestimated in L(S)DA because of the homogeneous density assumption. By accounting for the genuine electronic density's inhomogeneity, the density gradient may rectify any errors that may arise. Better findings for molecular geometries and ground-state energy may be obtained by using the Generalized Gradient Approximation (GGA) to describe the E_s, which incorporates not just density but also gradient density.
The expression is alluded to with spin:

$$E_{xc}^{GGA}(\rho(r)) = \int \rho(r)\varepsilon_{xc}\left(\rho(r_{\uparrow}, r_{\downarrow}, \nabla r_1 \uparrow, \nabla r_{\downarrow})\right) dr$$

As theoretical knowledge has progressed, a number of other GGA-functions have been devised to cut down on error, including PBE and PW91[44]. The underestimations may be corrected to some degree using GGA. Unfortunately, there are a few problems, including an exaggeration of the band gap and an overestimation of the lattice constant of the heaviest element. Perdew-Burke-Ernzerhof (PBE) method with GGA-functional is regarded as the most acceptable electronic structure calculation function approach, and it has been employed throughout the thesis projects due to its balance of CPU time cost and correctness of discoveries.

4.5.3 Advantages and Disadvantages of DFT

Advantages:

(1) We utilise DFT to build and enhance more complex simulation methods like molecular dynamics and umbrella sampling simulations because it provides a basis for first-principles theory or ab initio calculations.

(2) Moreover, even on transition metal complexes, where Ab initio calculation is challenging owing to the enormous number of electrons in the system, DFT is more effective in exploring geometries, calculating vibration frequencies, and computing energies.

(3) The DFT method, which is grounded in the concept of electronic density, is preferable to the wavefunction method in terms of conveying a precise physical meaning.

Disadvantages:

(1) The exchange-correlation function $E_{xc}(\rho(r))$ is still unknown, and no mathematical solution can improve on the current method.

(2) The bandgap calculated by DFT is usually underestimated because the ground state theory makes it less suited for the higher energy unoccupied excited state.

(3) In order to enhance the approximation, certain functions are connected to experimental data in order to better suit the computation and experiment, which, to some extent, makes DFT semi-empirical.

(4) The limitations of large systems, such as nanomaterials and biological systems, need the development of novel auxiliary methods to aid in computation.

4.6 Computational Methods and Simulation Framework

The Kohn-Sham equations provide us a broad understanding of a system with many electrons. While it is possible to describe simple systems with a large number of electrons in a limited space, it is still not possible to account for the motion of an infinite number of electrons that are not interacting with one another in a fixed potential. Hence, limitless large-scale space, which is hypothesised to be the composite of innumerable periodically repeating unicells in three-dimensional space, can only be represented by a finite presentative basis set.

4.6.1 Basis Sets

The electronic wavefunction is represented by a set of functions (sometimes called basis functions) in the Hartree-Fock method and density functional theory. Atomic orbitals, like the well-known linear combination of atomic orbitals (LCAO), or plane waves make up the basis set (often applied in solid-state). As plane-wave basis functions are guaranteed to converge to the required wavefunction in a smooth, monotonic fashion and are much simpler to design and carry out than their localised counterparts, I employed them in my

investigation. The kinetic energy operator, for instance, has a diagonal form in reciprocal space. Fast Fourier transformations, which have a general formulation as Equation, allow for the speedy computation of integrals over real-space operators.

$$\Psi_{i,k}(r) = \sum_{G}^{|G|<G_{\max}} c_{i\mathbf{k}}, G e^{i((k+G),r)}$$

Here, $\Psi_{i,k}(r)$denotes the Fourier Series expansion expression; c_{ik} denotes the Fourier coefficients, which are stored on the regular grid of G; extremely fast FFT algorithms can quickly transition between r-space and G-space representations.

4.6.2 The Supercell Approach

In a real system, many electrons move across the surface and the interface. Yet, it is quite difficult to calculate such a large number of electrons using the available wavefunction.

According to Bloch's theorem [66], a huge system may be broken down into a large number of tiny unit cells and then replaced in three dimensions by that finite cell unity. The periodic issue may alternatively be solved by using Bloch's Theorem.

$$\Psi(r) = e^{ik\cdot r}u(\mathrm{r})$$
$$u(\mathrm{r}) = u(\mathrm{r} + l)$$

Where r is the location; Ψ is the Bloch wave; $u(r)$ is a periodic function; l is the unit cell length; k is the crystal momentum vector in the reciprocal lattice's first Brillouin zone (BZ); e is Euler's number; and I is the imaginary number. When we use the Fourier series to extend the periodic function, we get:

$$u(\mathrm{r}) = \sum_{G} C_{i,G} e^{i(G)r}$$

where G is the reciprocal lattice vector. Hence, the electronic wave functions can finally be written as:

$$u(\mathrm{I}) = \sum_{G} C_{i,k+G} e^{(k+\mathrm{G})r}$$

The plane-wave basis set is formed as a result of the deformation of multiple trigonometric functions $(e^{\mathrm{x}} = \cos x + i\sin x)$, This type of plan wavefunction may be used in a periodic system with the use of fast Fourier transformation (FFT) to simply depict a periodic solid from real space to reciprocal space. To enhance the precision of the reciprocal space calculation, we may increase the size of the Kpoint sample in the DFT calculation, albeit this would lead to a greater demand on computational resources.

As the calculation of vacuum is equally costly as the calculation of atoms, it is necessary to choose a supercell that is big enough to prevent lateral contact without being so huge that unnecessary calculations are avoided. The K-point count may also change using the smearing technique. Common practise in this field is a grid layout based on the Monkhorst-Pack method.

The Material Studio software is used to calculate K-points for the thesis, and the results of the test are considered to be good. It's wise to find a happy medium between absolute perfection and manageable workloads.

4.6.3 The Approximation of Pseudopotentials

Bloch's theorem states that plane waves can be used to increase the wavefunction. This rapid and frequent fluctuation of the valence electron wavefunctions towards the core region is a result of the high ionic potential. Characterizing the tightly bound core orbitals requires a large number of plane waves (perhaps over 10,000), which is quite expensive, but yields a more precise result. The pseudopotential approximation is studied as a means to reduce costs and improve computation accuracy while dealing with this challenging problem. Instead of core electrons, it is valence electrons that are crucial to the material's properties. By substituting valence electrons (frozen core electrons) that reflect the pseudo-wavefunction for the atomic all-electron potential (full-potential), the pseudopotential serves as an effective potential. The number of nodes in the wavefunction is greatly reduced by this approximation. When the radius is larger than the core cutoff radius I_{oul}, the potentials for the pseudo-wavefunction and the all-electron wavefunction, as shown in A diagram depicting the genuine wave function (solid line) and the pseudopotential wave function (dashed line), are the same.

An important factor in striking a balance between computing costs and correctness of results is the size of the basis set and the number of electrons involved in the calculation, and pseudopotential approximation does this by reducing both.

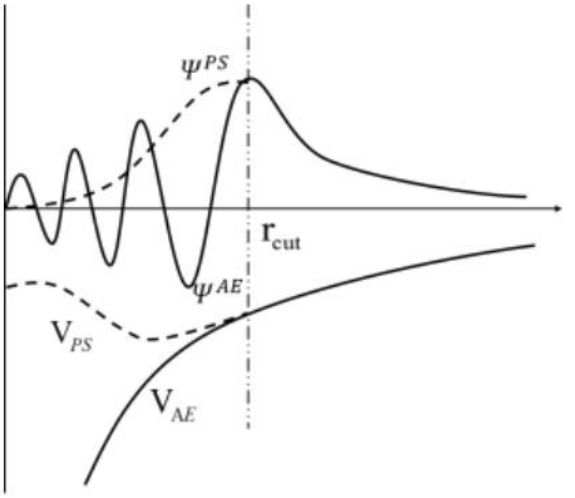

Figure 4. 1 A diagram depicting the genuine wave function (solid line) and the pseudopotential wave function (dash line), as well as their potential and pseudopotential.[41]

The radius is the boundary beyond which the all-electron potential and the pseudo-electron potential are in good agreement with one another. An important factor in DFT calculations, the planewave cutoff energy may be traced back to the atom type in question. The shut off energy value is calculated based on the maximum value inquired over the whole system. For reliable calculations, an electrical static calculation cutoff energy of 450eV and an MD simulation cutoff energy of 380eV must be used.

4.6.4 The Method of Projector Augmented Waves:

The projector augmented wave technique (PAW) is used in electron structure computations in ab initio calculations. This methodology is an extension of the pseudopotential and liner augmented-plane-wave-methods, which improves DFT calculation efficiency. The downside of the valence wavefunction is the fast oscillation around the ion core, which necessitates the use of numerous Fourier components (or a very fine mesh using grid-based technique) to adequately represent the wavefunctions.

The PAW approach solves this problem by converting the fast oscillation wavefunction to a smooth wavefunction, which is significantly easier to solve.

4.6.5 Geometry Optimization

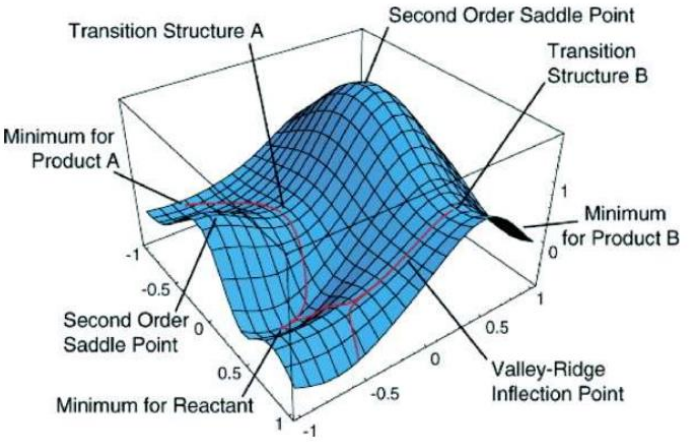

Figure 4. 2 :The potential energy surface is introduced simply. On the PES figure, it denotes minima (such as resctant and product), transilion states, a second-order saddle point, reaction paths, and a valley-ridge inflexion point. Reprint of previously published [41]

When a computer model of chemical bonds assumes that the net inter-atomic force on each atom is zero, the model seeks a stationary point on the potential energy surface (PES) known as geometry optimization.

The structures with the lowest energy in the PES usually correspond to natural substances; some of them may be used practically and theoretically in other fields such as thermodynamics, chemical kinetics, spectroscopy, and so on. Both the quasi-Newton algorithm and the Conjugate gradient (CG) algorithm, two optimization methods, have seen widespread application in recent theoretical calculations.

The quasi-Newton method works better for optimizing near-local lowest energy structures. We still recommend the conjugate-gradient method when the geometry is near to the local minimum and we lack confidence in the underlying structures.

4.6.6 The Constrained Minimization Method and Transition States

An individual structure along the reaction coordination of a chemical process, known as a transition state. As seen in Figure 4.2 its potential energy is highest along the reaction channel and lowest in all other directions.

In other words, it's a possible energy saddle point. Because of this, the transition state may be identified by searching for saddle points on the potential energy surface of the target chemical species. With the 2D snapshot generated by the 3DPES, we can better see and locate the transition state along the reaction pathway. As can be seen in the diagram below, the transition state occupies the extreme endpoint of the reaction coordination.

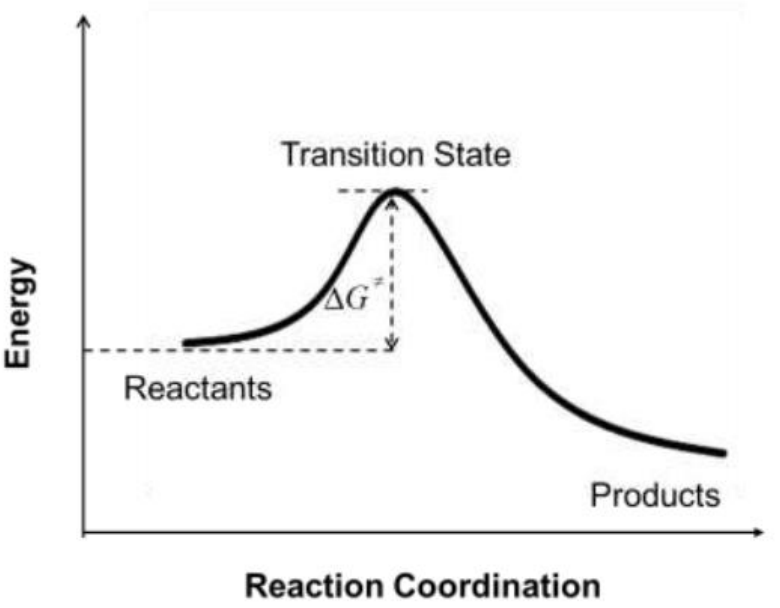

Figure 4. 3 : A schematic graph of a 2D energy profile of a chemical process. [41]

ΔG^z denotes the activation energy, which is the difference in energy between the reactants and the transition state.

Transition state theory (TST) may be used to calculate the reaction rate constant k with ΔG^{x}:

$$k = \frac{k_B \, \mathrm{T}}{h} e^{\frac{-\Delta G^{*}}{k_B T}}$$

Where k_B is Boltzmann constant; h is the Planck constant, and T is temperature, respectively. ΔG^{z} is the standard Gibbs free energy difference between TS and reactants. Local searchers, the dimer approach, nudged elastic bands, and other strategies have all been used so far in the hunt for the transition state. In this thesis, the saddle point is located using the constrained minimization method instead of the more common iterative technique. Although these techniques provide total energies, the Gibbs free energy requires further modifications. This method, also known as "constrained minimization," functions by minimizing a set of constraints.

i) all structures derived from intelligent assumptions; often, transition states either close to the beginning or end state, or structures between the IS and FS configurations; optimize all of these representative candidates to establish the likely target structures.

ii) If these candidates are chosen, we will constrain the distance between their reactive atoms and optimize their structural flexibility using a quasi-Newton approach.

iii) After implementing the command code, the distance will be shifted closer to the transition point.

iv) Several distance updates reveal an exact transition state, in which the energy is highest along the reaction path while being lowest for the other degrees of freedom. Simultaneously, the atomic forces vanish.

v) To verify that the optimised structure satisfies the target TS, it must be checked using vibration frequency analysis to see whether it has a single imaginary eigenvalue. This limited optimization strategy.

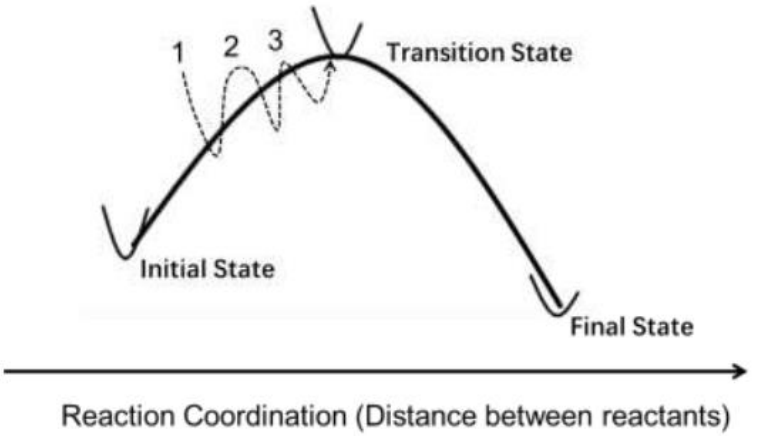

Figure 4. 4: A schematic depiction of the constrained optimization approach used to find a transition state.The entire solid curve represents the reaction route with the lowest energy on the PES from the starting to final states. [41]

The peak of this curve stands for the transition stage, a route saddle point. The optimization procedure is seen by the dotted line, and it consists of a series of upward iterations during which the structure is forced into the transition state by constrained reduction.

4.6.7 Chemisorption Energies

The process of adsorption on a surface causes the adsorbate to undergo a chemical reaction, known as chemisorption. In other words, a chemical bond is broken and a new one created just at the surface. Thus, we use the idea of chemisorption energy to characterize the process of energy conversion:

$$E_{\text{chem}} = E_{\text{A/surface}} - (E_{\text{A}} + E_{\text{surface}})$$

Where E_{chem}, $E_{\text{A/surface}}$ and E_{surface}represent the total energy of the chemisorption system, species A in the gas phase, and the clean surface, respectively. According to the definition, a negative value of E_{chem}indicates that the process is exothermic; the greater negative, the more energy released.

4.6.8 Free Energy and Thermodynamic Corrections

When some initial estimates have been made, we may proceed to more precise calculations of reaction energy and reaction barriers. In contrast, the total of the energies computed at zero temperature is what is used to obtain the energies from DFT calculations. All of the energies presented in this dissertation are free energies; some were calculated directly using cutting-edge molecular dynamic techniques, while others were corrected for thermodynamics to provide a fair comparison with experimental data. The thermodynamic correction

consists of the zero-point energy (ZPE), thermal energy, and entropy energy. Only vibrational motion, leading to zero point energy, thermal energy, and entropy, can correct the most frequent species, surface adsorbates.

The ZPE formula is as follows:

$$E_{ZPE:} = \sum_i \frac{hv_i}{2}$$

Where h is Plank's constant and v_1 is vibrational frequency calculated based on the harmonic oscillator approximation. The standard molar vibrational thermal energy is expressed as:

$$\mathrm{U}_{\mathrm{vib}}^{0} = \mathrm{RT} \sum_i \frac{\frac{\mathrm{hv_i}}{k_B}}{e^{\frac{\mathrm{hvi}}{\mathrm{kBT}}} - 1}$$

Where $\mathbb{R}$ presents the gas constant and k_B represents Boltzmann's constant. The standard molar vibrational entropy is determined using the formula:

The typical molar Gibbs free energy of adsorbate on the surface may be stated using the three terms above as:

$$G^0 = E_{\text{total}} + E_{zPE} + U^0 - TS^0$$

Where E_{Total} represents the total energy calculated by DFT method. As for gaseous species, Gibbs free energies are calculated by GAUSSIAN 09.

4.7 Importance Of Surfaces:

Catalysis, interfaces, gas separation membranes, and semiconductor manufacturing all use surfaces. Understanding surface geometry and electrical structure is important because surface structure strongly affects catalytic activity. DFT has helped improve technologies, lower catalysis costs, and create three-way catalysts that reduce automobile CO, NOx, and SOx emissions. These catalysts can oxidise hydrocarbons, carbon monoxide, and nitrogen oxide, among other high-stakes targets. They are often constructed of platinum and poisoned.

DFT techniques to clarify important reactions on catalytic metals, zeolites, and oxides have improved catalytic converter design, increasing efficiency and lowering cost. Surface science DFT tandem efforts have succeeded. STM, temperature-programmed desorption, X-ray diffraction, and X-ray photoelectron spectroscopy have been utilised with DFT to analyse the surface structure of metals, metal oxides, nanoparticles, carbides, and sulphides in ultra-high vacuum.

.

4.8 Periodic Boundary Conditions and Slab Models

A two-dimensional slice of material, infinite in two dimensions but finite along the surface normal, is the ideal model for studying a surface. If you're doing this in two dimensions, using periodic boundary conditions would seem like a good idea, but in three dimensions, this isn't the case. Although there are programmes that use this approach, it is more common to inspect a surface using a code that applies periodic boundary conditions in all three dimensions, as we will show.

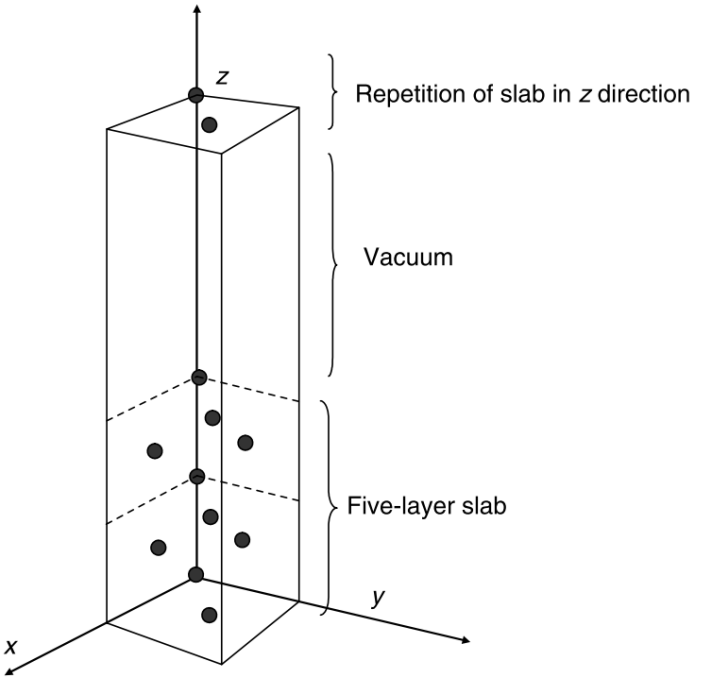

Figure 4. 5: Supercell Approach[41]

A solid surface may be specified by using a supercell with periodic boundary conditions in all three dimensions. The idea is best shown by looking at Figure 4.5, in which the supercell contains atoms exclusively along a subset of the vertical axis. Atoms in the bottom half of the supercell fill the whole supercell in x and y, but there is free space above the atoms in the top half. A three-dimensional copy of the supercell results in a stack of solid slabs separated by voids, as seen in Fig. 2.6. Vacant regions between the periodic images of the slab along the z axis are called vacuum space. Vacuum space sufficient for the electron density of the material to drop to zero in the vacuum and for the top of one slab to have no impact on the bottom of the next is required for this concept to work. Figure 2.7 shows an alternative view of the atoms in such a material, from the vacuum itself. From this vantage point, we can see that the supercell has two distinct surfaces—an upper and a lower one. Let's pretend we need to do some math on the outside of a copper or other fcc metal. Please advise on how we may go about constructing a model slab similar to that in Fig. 2.8. A supercell may be constructed more easily when its vectors are aligned with the Cartesian x, y, and z axes, with the z axis of the supercell coincident with the surface normal.

It is important to keep in mind that the lattice constant for fcc metals is equal to the length of the average cell's side. At that point, the supercell vectors might be put to use.

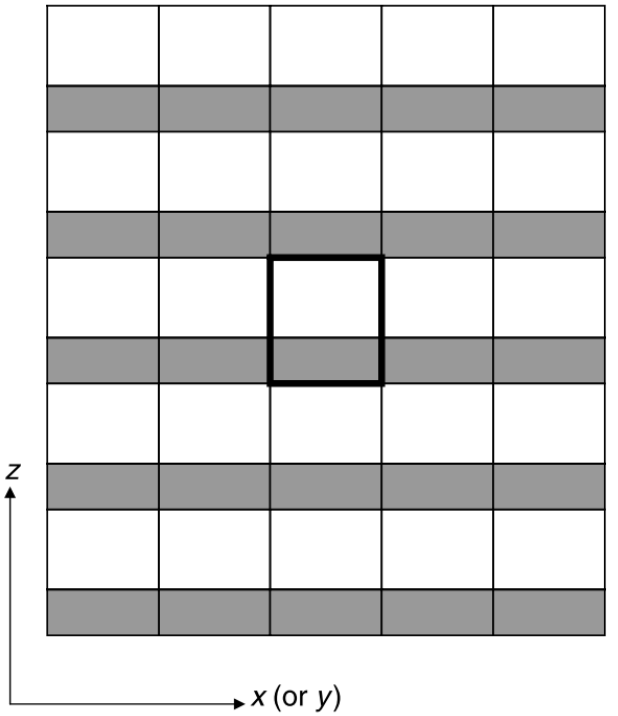

Figure 4. 6: A two-dimensional schematic depiction of the material specified by the supercell in Figure 4. 5, with 25 clones of the supercell denoted by thick lines.

The darkened (white) areas represent atoms' positions in space (vacuum) [41]

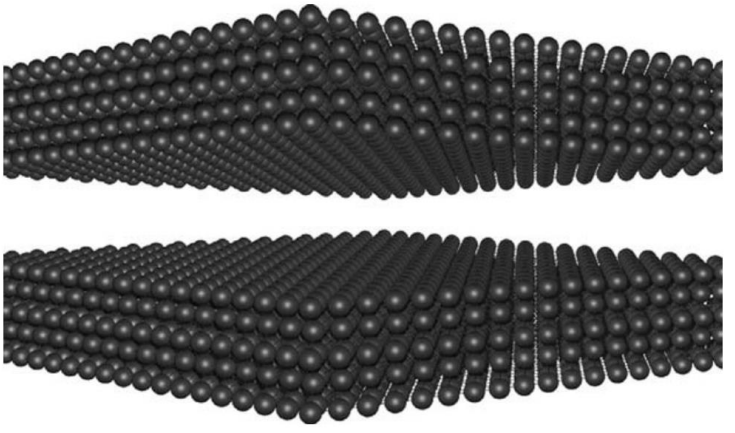

Figure 4. 7: Illustration of a five-layer slab model of a surface utilised in a completely periodic computation. [41]

The supercell in this picture is identical to the one in Figure 4. 5and is replicated 20 times in the x and y directions and twice in the z direction. a denotes the lattice constant.

The fractional coordinates of the atoms in Figure 4. 5 are as follows:
0.0, 0.0, 0.0
0.5, 0.5, 0.2
0.5, 0.5, 0.5
0.5, 0.5, 0.5
0.5, 0.5, 0.5
0.5, 0.5, 0.5
0.5, 0.5, 0.5

These choices specify a slab with a thickness of 3a and a vacuum gap of a/2 in the z direction. Each layer of this slab has two different atoms inside the supercell. The number 5 used in the definition of a3 seems quite random. Supercell vacuum space necessitates a sufficiently big value for this vector, however increasing the vacuum spacing necessitates additional computation. A practical method for estimating how much vacuum is "enough" is to compare the charge density in the vacuum space of many models with varied amounts of vacuum spacing. The charge density in empty space should be close to zero in a perfect universe.

If you decide to give it a go, bear in mind that maintaining the correct physical distance between the layers of the material will need adjusting the z components of the atoms' fractional coordinates if you change the length of a3. (If you find this puzzling, now is a great time to learn about fractional coordinates.) As far as possible, we'd want our slab model to accurately represent the fundamental characteristics of a real surface. The aforementioned slab kind is composed of five fcc metal layers.

Unless in exceptional circumstances, a real surface is the cutting edge of a material at least a few microns thick; this is quite different from our five-layer concept. The issue this raises is, "How many layers are enough?" Additional layers are almost always better, but using them takes more processing power. How many layers are needed to achieve convergence is based on the specifics of the material and the characteristic being studied. Calculations showing the variation of a parameter (such as surface energy or adsorption energy) with increasing number of layers may provide a solution, as they did with the issue of the vacuum spacing. Many illustrations of this idea are provided below. The trade-off between computational cost and physical accuracy in our model is typically reflected in the number of layers it has.

4.8.1 Selection Of K Points For Surface Calculations

Selecting k locations for Brillouin zone integration was discussed. Many of the same concerns arise whether doing the computation on a slab or a mass of material, and the Monkhorst-Pack method for calculating k points may be utilised for either. One way to get a feel for this endeavour is to look at the reciprocal lattice vectors that map to the supercell described in the previous section. The supercell is approaching, and we must be ready. Currently being discussed is the use of an M1XM1XM2 k-point mesh, where M1>M2 would appear to be appropriate in light of this geometric reasoning.

Another important discovery for finding k points is the existence of a vacuum zone in the long dimension of the supercell. At the edge of the slab, the electron density goes to zero if the vacuum zone is big enough. As a result, a MXNX1 k-point mesh is commonly used in slab computations, where M and N are selected to appropriately sample k space in the plane of the surface. To meet the symmetry of the supercell, $|b_1|=|b_2|$, M, and N should be equal in the case we outlined before.

4.8.2 Surfaces Classification By Miller Indices

Returning to Figure 4. 7, we might speculate that the surfaces shown there could be produced by physically breaking a bulk crystal. Doing this with a real crystal reveals the many distinct planes along which it may be broken, each of which is likely to disclose a different kind of surface in terms of the arrangement of atoms on the surface. To this end, we'll need to devise a system of notation for specifying the precise kind of surface we're examining.

For instance, Figure 4.8 depicts a Cu surface from an alternative perspective, one that places more emphasis on the surface plane's location in relation to the bulk crystal structure. It is possible to ascertain the orientation of a plane by tracking the movement of a vector that is perpendicular to the plane's surface. Instead, [0,0,1] might work for this vector, as seen in Fig. 4.8. All of these vectors are parallel, therefore [0,0,2], [0,0,7], and so on are also valid alternatives.

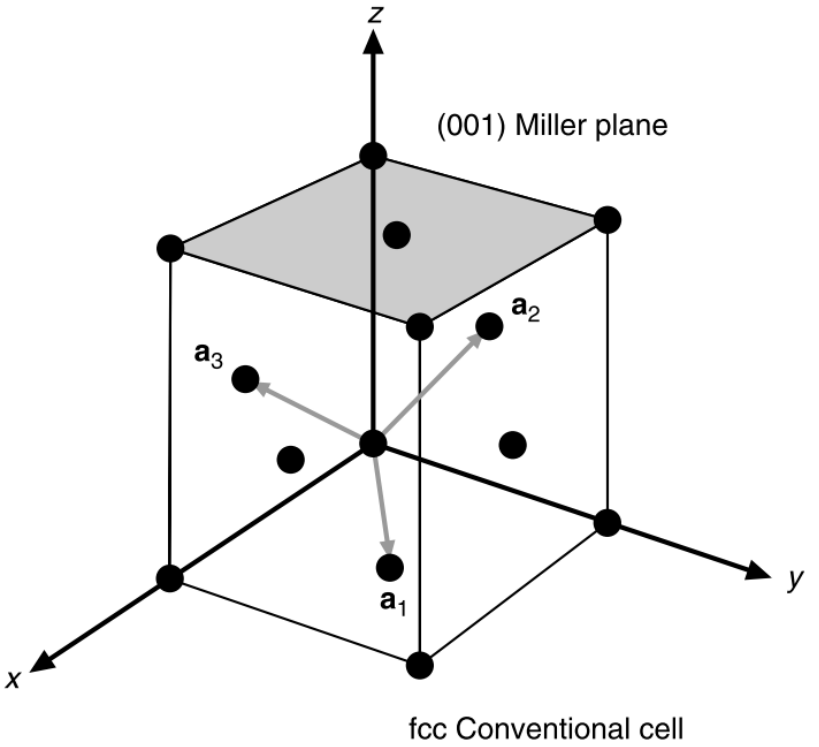

Figure 4. 8: The (001) Miller plane is indicated in a conventional cell of a fcc metal. [41]

Common practise requires limiting the number of potential vectors by specifying the angles at which the plane contacts the three axes of the primitive cell or conventional cell of the material in issue (either may be used). In order to make the reciprocals of these intercepts as small as feasible while still rounding to integers, a scaling factor is applied to them. Miller surface index is defined as the values acquired in this way.

In the case shown in Figure 4. 8, the plane contacts the z axis of the typical cell at 1 (in units of the lattice constant) but not the x or y axes. These intercepts' reciprocals are (1/ ∞, 1/∞,1/∞), hence the surface is designated by (001). Because no scaling is required for this set of indices, the surface depicted in the image

is referred to as the (001) surface. If the vector describing the surface normal requires a negative sign, an overbar denotes that component of the Miller index.

By looking up at the bottom face of the cube in Figure 4, we may identify the (001) surface using this notation. It's important to make sure that the other four cube sides in Figure 4. 8 are also (100), (010), (100), and (010). Due to the symmetry of the bulk crystal, it is often unnecessary to differentiate between these six surfaces, since they all have the same structure.

Figure 4. 9 depicts another surface definable in a face-centered cubic material; this time, the highlighted plane intersects the x, y, and z axes at 1, 1, and 1. These intercepts' reciprocals are 1/1, 1/1, and 1/1.

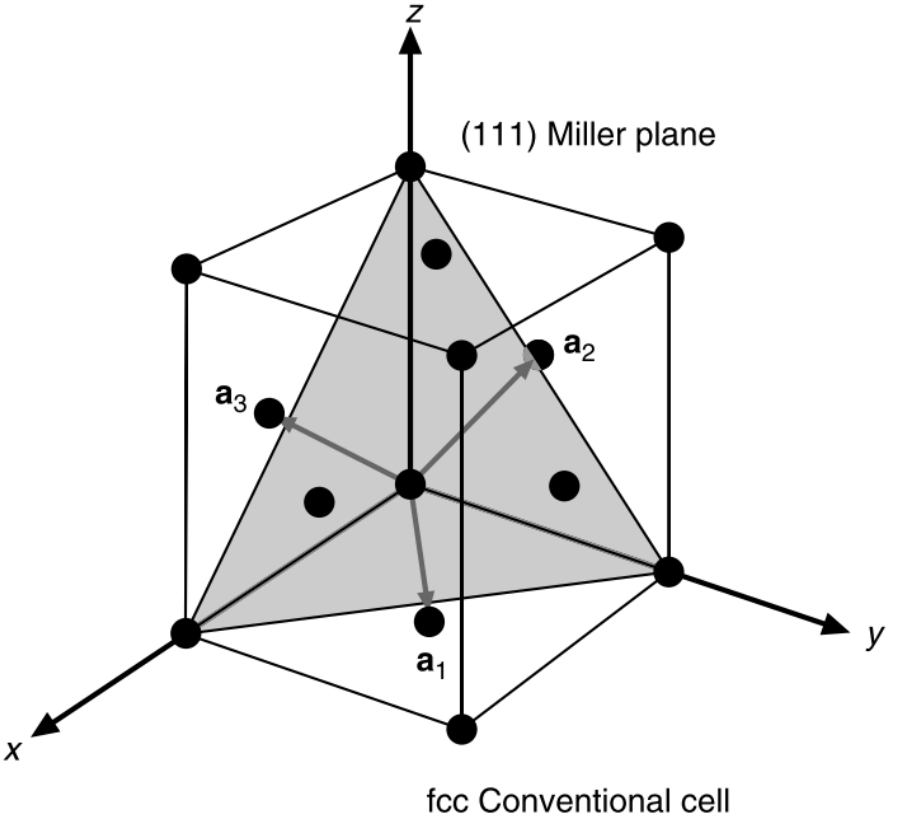

Figure 4. 9: Similar to Figure 4. 8, but with the (111) Miller plane marked. [41]

Hence, this surface is designated as (111), indicating its orientation. The Miller index surface of a fcc material is noteworthy because it has the highest possible density of atoms in the material's surface layer. For a particular crystal structure, surfaces with the highest surface atom densities tend to be the most stable, playing a pivotal role in the real crystals at equilibrium. Based on this qualitative evidence, we may assume that the Cu(111) surface makes up a significant fraction of the overall surface area of a genuine Cu polycrystal.

The plane of the (110) surface crosses the x and y axes at 1 but not the z axis at all. Because the reciprocals of these intercepts are (1/1, 1/1, 1/1), the surface is known as the (110) Miller plane. Top-down views of the

fcc (001), (111), and (110) surfaces are shown in Figure 4. 10Figure 4. 10: Views from the top of the (100), (111), and (110) surfaces of fcc metals. Only the atoms in the top layer are visible..

These images emphasise the symmetry of each surface. The surface (001) has fourfold symmetry, the surface (111) has threefold symmetry, and the surface (110) has twofold symmetry. These three fcc surfaces are all atomically flat, meaning that every atom on the surface has the same coordination and coordinate relative to the surface normal. They are referred to collectively as the low-index surfaces of fcc materials. Other crystal structures feature low-index surfaces as well, although their Miller indices may differ from those of the fcc structure. The (110) surface, for example, has the maximum density of surface atoms in bcc materials. We've only presented instances of low-index surfaces so far. Because of their stability, these surfaces are useful in the real world. They are especially useful for DFT computations since supercells defining low-index surfaces require just a small number of atoms. However, there are other additional surfaces with intriguing and essential features.

To illustrate, Figure 4. 11 depicts top and side views of the Cu(322) surface. This surface features sections that appear like the (111) surface locally, separated by one-atom-high steps. Atoms near step edges have a lower coordination number than other atoms on the surface, resulting in greater reactivity. Although the structure of Cu(322) is more sophisticated than that of low-index surfaces, it is still periodic in the plane of the surface, therefore a supercell that describes this surface may be created. As previously stated, alternative crystal structures can have different Miller indices than the fcc structure. Spheres are stacked in a single close-packed layer to form a basal plane in the hexagonal close-packed (hcp) structure, with each atom surrounded by six others. The following layer is created by inserting spheres into the basal plane's alternating threefold hollows. The hcp structure is obtained by adding a third layer so that the spheres are directly above the spheres in the basal plane. (The fcc structure is generated by inserting third layer atoms into hollows that are not exactly above the basal plane.) A sixfold symmetry axis normal to the basal plane characterises hexagonal close-packed (hcp) materials.

As shown in Figure 4. 12, using a three-axis approach to construct Miller indices for this structure is insufficient. The two planes marked in Figure 4. 12 are symmetrically equal, although their Miller indices do not reveal this connection. This is bad since analogous planes have similar indices, which is one of the reasons Miller indices are valuable. Another flaw in this example is that the [hkl] direction is not perpendicular to the (hkl) plane.

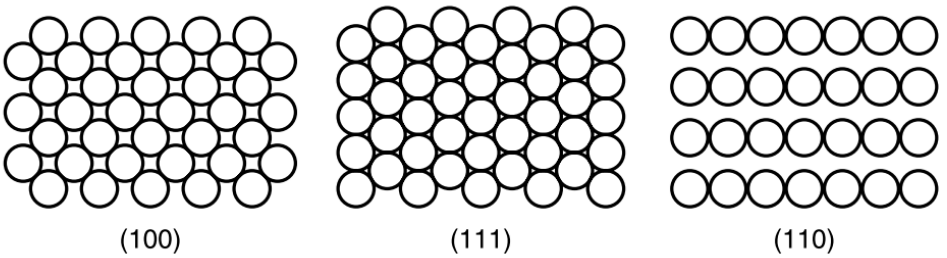

Figure 4. 10: Views from the top of the (100), (111), and (110) surfaces of fcc metals. Only the atoms in the top layer are visible. [41]

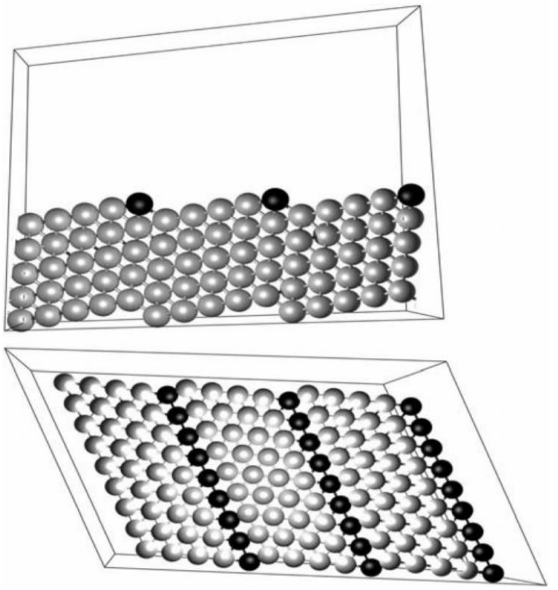

Figure 4. 11: Cu(322) top and side views (upper and lower image, respectively). [41]

Three supercells are depicted. The Cu atoms that create the step edge are dark grey in each picture.

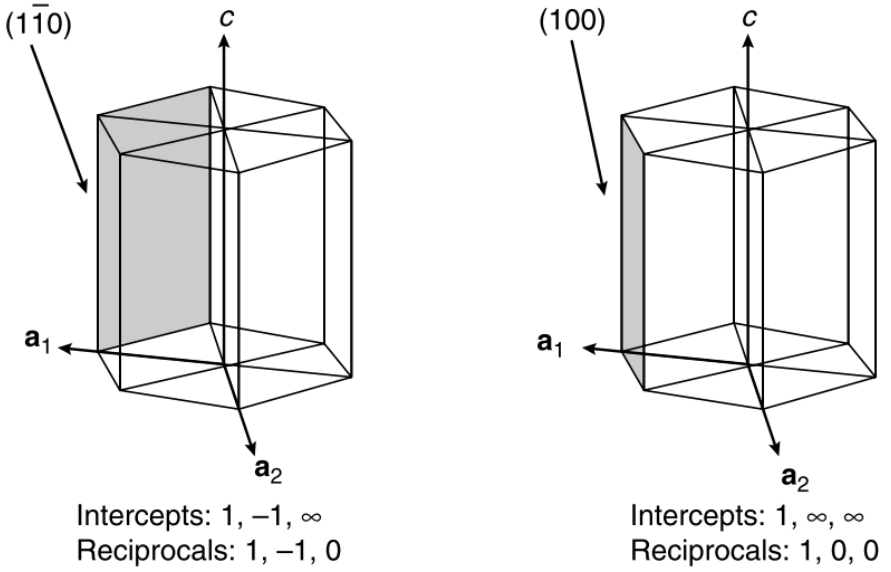

Figure 4. 12: Using a three-axis technique to label planes in a hcp solid. [41]

By symmetry, these two planes are comparable, however the indices produced using three axes are not.

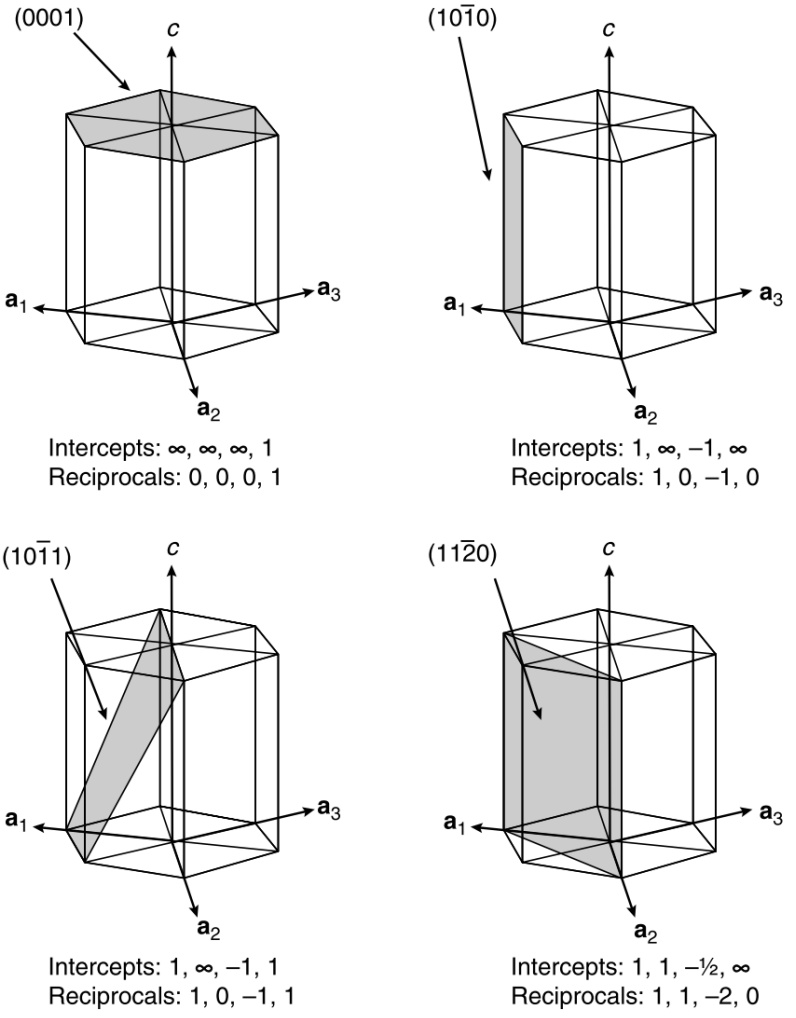

Figure 4. 13: Miller indices for hcp materials employing the four axis, four index scheme. [41]

A four-axis, four-index approach for hcp solids is a superior option. Figure 4. 13 shows a few instances. As previously, the Miller indices are calculated by calculating the reciprocals of the plane's intercepts with the four axes. The corresponding planes mentioned above become (1100) and (1100) using this method (1010). The six equivalent planes that come from the sixfold axis of symmetry are now known as the 1100 family of planes. The [hkil] direction is normal to the (hkil) plane when utilising four axes, just as it was for cubic solids while using three axes.

4.8.3 Surface Relaxation

Earlier, we demonstrated how to create a five-layer slab out of atoms by using our slab model. The atomic positions were perfect bulk positions for the fcc material. In a bulk fcc metal, the distance between any two adjacent layers must be the same. A material's layers near a surface don't have to be equally spaced, nevertheless. Therefore, it is natural to anticipate that the spacings between layers at the surface will vary from those in the bulk due to the lower coordination of atoms at the surface compared to those in the bulk.

This kind of behaviour is known as surface relaxation, and characterising it is a plausible goal of our first surface calculations. Figure 4 is a schematic depiction of the atomic positions before and after relaxation in a DFT calculation of a five-layer slab model of a surface.

At left is the original slab model with the atoms in their bulk positions, and on the right is the model after the top three layers have been relaxed. The energy of the relaxed surface is lower than that of the idealised one. By minimising energy as a function of atom positions in the supercell, we may find the outline of the relaxed surface. In this model, we consider the lowest levels of the slab to represent the material's bulk and force the atoms there to adopt their most ordered configurations for this purpose.

Next, the calculation includes minimising the overall energy of the supercell as a function of atom positions, restricting movement to just the top layers, as described in Geometry Optimization. This process yields a shape like to that seen in the right-hand side of Figure 4. 14. The real velocity of surface atoms is 0.1 A. This photograph emphasises how much the higher layers have relaxed.

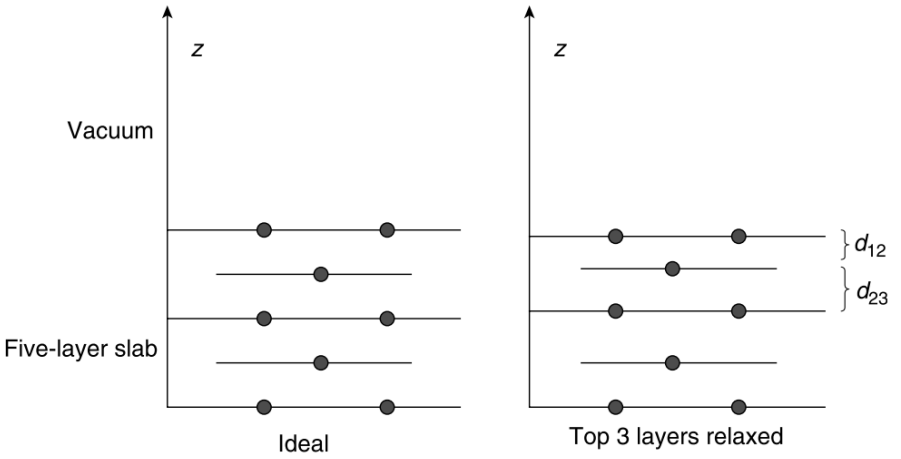

Figure 4. 14: A schematic representation of surface atom relaxation in a slab model. [41]

Two tiers of atoms were kept in their optimal, bulk shapes while the top three were allowed to relax. The atomic coordination changes significantly when a surface terminates abruptly along the surface normal. The separation between the atomic layers 1 and 2 is often reduced as a consequence. The change due to relaxation is denoted by the symbol d12, and d12 is the distance between the outermost surface layer and the second layer. The relaxation-induced shift is often expressed as a percentage of the bulk material's layer spacing, with negative values indicating layer contraction and positive values indicating layer expansion. In this article, we focused only on normal-to-the-surface relaxation in our explanation of surface relaxation. This is the correct representation of our algorithm, since the slab is perfectly symmetric in the surface plane.

So, during relaxation, the atoms are unable to move on the surface plane because the force components acting on them are exactly zero. This is not only a mathematical construct; it corresponds to the actual properties of a real surface. We can see that bulk lattice spacing is required to define our supercell if we assume that these bulk-like layers determine the supercell's dimensions in the surface plane. In this talk, we highlight a hitherto unmentioned facet of surface computations: the need to decide on a specific numerical value for the lattice constant. The most effective method makes use of the lattice constant obtained from a rigorously converged

DFT calculation for the bulk material using the identical exchange-correlation functional that will be utilised for surface calculations. Applying a different lattice constant (such as the experimental lattice constant) imparts artificial stresses into the material, leading to a physically false relaxation of the surface atoms.

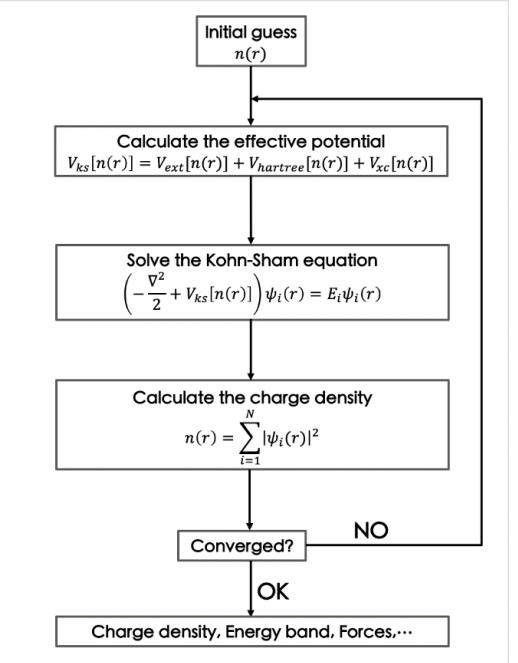

Figure 4.15 : Flowchart for DFT calculations [41]

4.9 Quantum espresso

For first-principles computations in materials science and condensed matter physics, a free and open-source software package known as Quantum ESPRESSO (Electronic Structure and Properties of Materials through a European Simulation Resource) is available. It is often used in the investigation of electronic structure and characteristics of materials [12], and it is based on Density Functional Theory (DFT) and the Kohn-Sham technique.

Quantum ESPRESSO includes a suite of programs that can be used to perform various types of calculations, such as:

- electronic structure calculations
- molecular dynamics simulations
- optimization of crystal structures
- response properties calculations
- and more.

The code is designed to be highly modular and flexible, allowing for the use of different exchange-correlation functionals, pseudopotentials, and other input parameters. It can be used to study a wide range of materials, including metals, semiconductors, insulators, and biomolecules.

Quantum ESPRESSO is a very efficient and parallelized algorithm that can be executed on a diverse set of hardware configurations, from personal computers to supercomputers [13]. It has a huge and active user community due to its widespread application in both academic and industry research.

Quantum ESPRESSO, in a nutshell, is a free and open-source programme that uses Density Functional Theory and the Kohn-Sham technique to do first-principles calculations in the fields of materials science and condensed matter physics. It has a huge, active community, is extensively used in academic and industry research, and provides a broad variety of features for things like electronic structure calculations, molecular dynamics simulations, crystal structure optimization, and response properties computations.

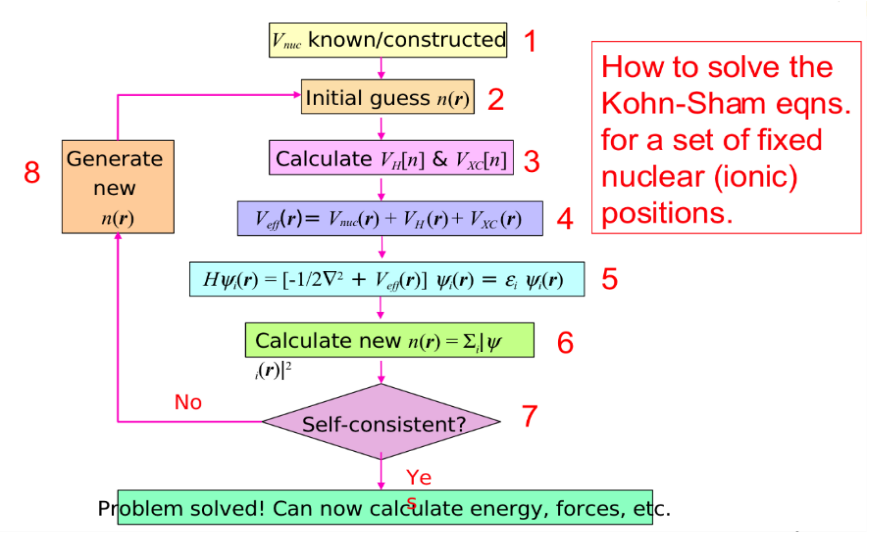

Figure 4.16: Flowchart for SCF calculation in Quantum Espresso [41]

4.10 Experimental Investigation

The purpose of conducting gas sensing experiments is to learn more about the characteristics and functionality of gas sensing materials under controlled laboratory conditions. The sensor's stability and operating range, as well as its sensitivity, selectivity, reaction time, and recovery time, may be evaluated using these methods. In the field of gas sensing, some of the most popular experimental methods include:

1. Gas sensing measurements: The effectiveness of the sensor is investigated by measuring the gas sensed. The sensor's electrical characteristics may be monitored to determine the presence or absence of the target gas after being exposed to a known concentration of the gas. This technique allows the measurement of sensitivity, selectivity, reaction time, and recovery time.
2. Temperature-dependent measurements: In order to investigate the sensor's stability throughout a broad temperature range, temperature-dependent measurements are performed. One way to do this is to monitor the sensor's temperature-dependent electrical property changes.
3. Humidity-dependent measurements: The stability of the sensor throughout a large humidity range is investigated using humidity-dependent readings. Seeing how the sensor's electrical characteristics change in response to moisture levels is one way to do this.

4. Exposure to realistic environments: Exploring the sensor's behaviour in real-world settings is essential. A gas combination that mimics the circumstances of the actual world may be used to test the sensor's performance.
5. Microscopy techniques: Scanning electron microscopy (SEM), transmission electron microscopy (TEM), and atomic force microscopy are used to examine the surface structure and chemical composition of the sensor to learn more about the processes involved in gas adsorption (AFM).
6. Spectroscopy techniques: In order to understand more about the chemical composition and bonding of the sensor, spectroscopic techniques including Raman spectroscopy, infrared spectroscopy (IR), and ultraviolet-visible spectroscopy (UV-Vis) are used.

Ultimately, gas sensing experimental investigations include the use of laboratory techniques to investigate the properties and functionality of gas sensing materials. These techniques may be used to assess the sensor's stability and operating range, as well as its sensitivity, selectivity, response time, and recovery time. Microscopy and spectroscopy may be used to examine the sensor's surface structure and chemical composition, shedding light on the underlying mechanisms of gas adsorption.

4.10.1 Sensor Testing Configuration

In order to get the most out of a gas sensor, it's important to characterise it and determine all the factors that affect its performance.

Due to the complexity of the processes involved, the operating conditions and performance characteristics of a device are intertwined. The performance testing requirements for any commercially produced sensors must be defined by the parameters tested during the development stage.

4.10.2 Measuring Techniques

Measuring the sensor's resistance or conductance in air and with a known concentration of analyte gas provides an indication of the sensor's sensitivity. The sensor's response may be studied in two different ways.

4.10.3 Method of Flow Through

When a constant stream of analyte gas is sent through the system, the resulting response curve may be recorded. Using a carrier gas (MFC), mass flow controllers are able to adjust the analyte gas concentration [14].

While taking recovery readings, the master flow controller for the analyte gas is disabled.

4.10.4 Method of the Static Environment

In this setup, the sensor element is placed within a sealed container whose volume is precisely determined. To determine the sensor's resistance in a target concentration of the analyte gas, a syringe is used to inject a known volume of gas into the housing. We keep an eye on the sensor's resistance over time to see whether it settles into a stable condition. When the sensor is taken out of its sealed environment, researchers may test whether or not it can recover [15].

4.10.5 Fabrication of Testing Systems

We constructed our own gas detecting test chamber that we customised from the ground up. With the test system we developed, we also included static measurement capabilities. Figure 4 provides a pictorial and schematic overview of the gas sensing system.

Our measurements were conducted using a stationary method, with gas concentration being established using volume ratio. The sensor's temperature is adjusted with the help of a temperature controller. A syringe is used to inject the required concentration of gas from pre-calibrated gas cylinders into the test chamber after the desired temperature has been reached. Sensor resistance variations in the presence of test gas may be measured using a digital multimeter. In this study, we use the ambient air pressure as the standard for all measurements.

We constructed our own testing apparatus, which is a stainless steel tube with a 7.5cm inside diameter and a 6.35cm inside height. Effectively, the chamber can hold 280 ml. The syringe concentration may be manually entered via an inlet.

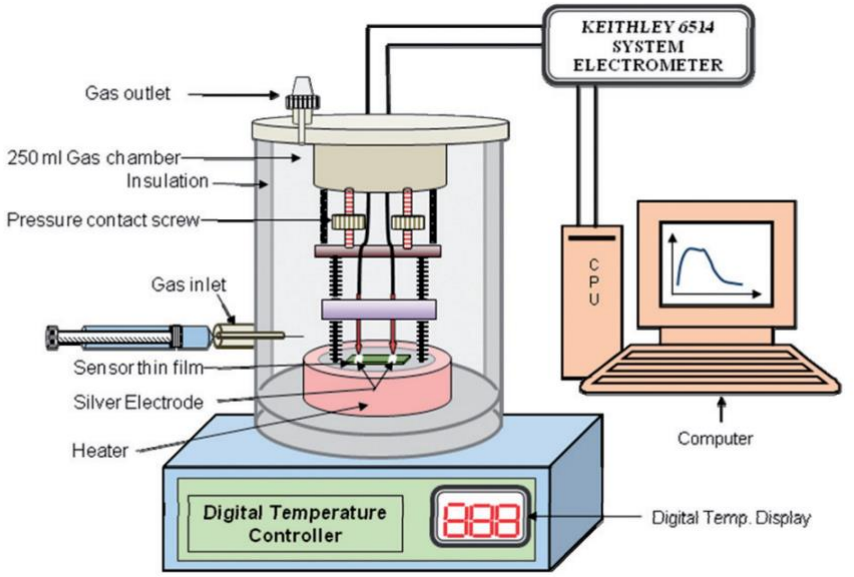

Figure 4. 15 Gas sensing set-up used for laboratory validation [30]

For gas injection, a septum is provided at the input. Two small copper wires are utilised to create electrical connections from the sensor, and they are painted silver to prevent corrosion. To find the best temperature for the sensor to operate at, its detecting abilities are tested in a wide range of temperatures. A heater is included within the chamber to bring the sample up to the ideal temperature for testing. The heater consists of a nichrome wire wrapped in mica and sandwiched between two copper plates.

4.10.6 Technology for Active Layer Deposition

Several other processing methods have been successfully tested, but only on a small scale in the lab. The right oxide composition may be achieved with the right amount of doping and the fewest number of processing steps. Sputtering, evaporation (i.e. physical vapour deposition - PVD), and chemical vapour

deposition (CVD) for films with thicknesses of 0.005-2m; screen printing, drop coating, and tape casting for films with thicknesses of >10m. Coatings of metals, ceramics, and cermets thicker than 50 m may be deposited by thermal spraying. This article summarises the numerous synthesis procedures used to create gas sensor films.

4.10.7 Thin Film Engineering

Thin-film deposition may be accomplished in a number of different ways, both chemically and physically. CVD, or chemical vapour deposition, is the method of depositing a material by diffusing reactants into a gas and then passing that gas over a heated surface. To move the reactants, scientists use a gas known as a carrier gas [16]. Films are formed during and after chemical reactions of reactants when gas passes over a heated solid surface, which is the source of the energy for the reactions. The by-products of the reactions are released into the environment. This allows for the deposition of thin films of the required composition onto the surface of the substrate. CVD techniques provide superior film-coating conformance across irregular surfaces.

Nanopowders and nanostructured thin films have been fabricated using chemical vapour deposition (CVD) methods as plasma-enhanced CVD (PECVD) and atmospheric-pressure CVD (APCVD).

Particles are deposited on a substrate using physical vapour deposition (PVD), which involves a direct impingement of particles. Vapors are physically transferred from the source to the substrate, which is the primary benefit of PVD methods. Many techniques exist for PVD implementation. Vacuum evaporation involves vaporising a solid at high temperatures and then transferring the vapour to a colder substrate, where it condenses to create a film. The atoms in the target are sputtered because the momentum of the impinging ions is transferred to them. A thin film may be formed on a substrate from the sputtered species by compressing them. Diode sputtering, bias sputtering, magnetron sputtering, and radio frequency (RF) sputtering are all types of sputtering. Producing oxide nano-particles with little aggregation is the goal of the low-pressure flame deposition (LPFD) method, which is based on the combustion flame-chemical-vapour condensation process. In pulsed laser deposition (PLD), a high-power pulsed laser beam is directed within a vacuum chamber to impact a target of the material to be deposited. PLD is a thin film deposition technology, more precisely a physical vapour deposition. A thin layer of this material is placed on a substrate (such as a silicon wafer) by evaporating it from the target and directing the plasma plume towards it [18].

As an economical substitute for chemical vapour deposition and reactive sputtering technologies, solution-based thin-film deposition techniques are receiving a lot of research and development attention. Vapour deposition techniques, on the other hand, consistently produce films of superior quality [19].

In the sol-gel method, a system goes from a liquid sol (a colloidal suspension of microscopic solid particles in a liquid) to a viscous gel, where the suspended particles are organised in a loose but definite three-dimensional shape. Spin-coating (pouring the solution onto the substrate surface and spinning to release fluid and achieve a uniform thickness), dipping the substrate surface into the solution, and spray-coating (applying the solution to the sensor surface) are all viable methods for generating gel layers [20].

Spray pyrolysis involves atomizing the chemical solution into a spray of tiny droplets using a filtered carrier gas that may or may not be engaged in the pyrolytic process, depending on the kind of film being produced (SnOX vs. CdS). Continual pressure and flow rates of the carrier gas and solution are applied prior to entering the spray nozzle. [21].

4.10.8 Thick Film Technology

Thick-film technology exists for several reasons, one of the most important being the need to combine different types of electrical components technology. Nevertheless, it is king when it comes to complex sensing applications. Although while demand is continually pushing technology developers to create such solutions and it is an active subject of research, the single chip solution is typically seen as the holy grail by designers but has seldom made sense thus far. About 30 years have passed since the invention of thick-film technology [22]. Products from GfG, OLDHAM, Industrial Scientific Company, GMI, BW technologies, Draeger Industrie, and KANE (gas detectors), B+B ThermoTechnic, and M&C Products, as well as gas sensors from Envin Scientific, Zellweger Anaalitics, Trafag, and Oliver IGD (gas sampling probes). One of the most important thick-film deposition procedures is screenprinting, which is also utilised for ceramics and textiles. One way to apply an active layer to a substrate is by using thick-film paste for painting or printing [24].

To create a printable paste, sensing materials like metal oxides are finely milled and combined with a small amount of glass frit of a similar size (for adhesion to the substrate), catalysts (if required), and an organic carrier. Screen printing powders need materials with a particle size of 0.5 m or less, however this is not a hard and fast rule. To spread the paste evenly throughout the substrate, a screen made of polyester or nylon is stretched across a metal frame. The emulsion on the screen is made to react to UV light. These regions were drawn using photography as a reference. The screen is kept at a distance of 0.5 mm from the substrate surface in the screen printing machine. A spatula is used to distribute the paste to the designated areas. After being printed onto a ceramic substrate (often alumina), the paste is cured and then fired at temperatures between 500 and 1000 degrees Celsius for an hour or longer. The substrate may have a layer of standard printed thickfilm materials for resistive heaters and conductor lines (typically noble metal pastes like Pt and Au) placed to it before or after the sensor layer [24].

Ceramics with uniform thickness and smooth surfaces may be formed using a method called tape casting.

This method was first developed to manufacture electronic ceramics (insulating substrates and packages and multilayer capacitors). To spread ceramic slurry evenly over a horizontal surface, a 'doctor blade' is utilised. The pliable 'green tape' is then cut, laminated, shaped, and sintered once it has dried. The thickness of the tape is usually 25 m to 1 mm, however tapes as thin as 5 m are possible [25].

The process of drop-coating is another thick film method. When the number of drops is adjusted, a range of thicknesses is produced. Both the viscosity and density of the solution are crucial to the success of this method. After solution deposition, solvent evaporation occurs spontaneously or with little firing [26].

The granules may also be mixed with the right liquid and brushed over the substrate. Such a covered sample may then be annealed at greater temperatures and put to good use. The substrate is dipped into a solution, removed, and the solvent is allowed to evaporate, leaving a solid coating on the substrate [27].

Several factors, including the nature of the reaction occurring at the oxide surface, the temperature, the catalytic characteristics of the surface, the electronic properties of the bulk oxide, and the microstructure, all play a role in determining the performance of gas sensors fabricated from thick layers of semiconductive oxides. Improved longevity is predicted, and one may have fine control over the material's thickness and microstructure [28].

4.10.9 Fabrication of Sensors

In this research, thick film sensors were developed by spreading nanopowder in an appropriate medium. In order to achieve a fine nanocrystalline powder, it was completely ground in a mortar. The material is then finely pulverised and dispersed with hydrochloric acid. Constant stirring with a magnetic stirrer for two to four hours ensured that the solution was well mixed. To create a substantial sensor film, it is painted onto the glass substrate. Measurements of gases were made using a spray pyrolysis-made thin-film sensor. Both thin and thick film sensors are annealed at 600 C for a whole 24 hours before any sensing measurements are taken. The surface temperature of the sample was measured and found to be within 5% of the target temperature. There were around 20 to 25 pure and doped gas sensors deposited on average. Five of each kind of sensor that was left at the lab was selected for use in the gas sensing studies. Figure 4 depicts a simplified design of the sensor. 2. In this case, a 5mm separation between electrodes is used.

Figure 4. 16 Schematic representation of sensor fabricated

4.10.10 Gases Employed for Sensor Characterisation

4.10.10.1 Carbon monoxide (CO)

This poisonous gas results from improper combustion of fuel. Symptoms such as fatigue, dizziness, and nausea may result from a lack of oxygen reaching the brain and other tissues in the body [29].

4.10.10.2 Sulfur dioxide (SO_2)

When sulfur-containing fossil fuels are burned, they release sulphur dioxide, a poisonous gas. It has been connected to acid rain and may induce breathing difficulties[30].

4.10.10.3 Nitrogen Dioxide and Nitrogen Oxide

Nitric oxide (NO) and nitrogen dioxide (NO_2) are two of the most toxicologically relevant nitrogen oxides; both are non-flammable and colourless to brown at room temperature. When both gases are kept at room temperature, the aroma of nitric oxide is fresh and pleasant, while that of nitrogen dioxide is pungent and overpowering. Vehicle exhaust, the burning of coal, oil, or natural gas, and industrial processes like arc welding, electroplating, engraving, and dynamite blasting all contribute to atmospheric nitrogen oxide levels. Nitric acid is also used commercially to produce them by interacting with metals or cellulose. Values of 3 ppm for 8 hours and 5 ppm for 10 minutes are the limits [31].

Nitric acid, lacquers, and dyes are just a few of the many chemicals that use nitrogen oxides. Rocket fuels, the nitration of organic chemicals, and the production of explosives are all industries that use nitrogen oxides. Because of their reactivity with other atmospheric molecules, nitrogen oxides swiftly deteriorate in the atmosphere. As nitrogen dioxide combines with molecules generated by sunlight, nitric acid is produced. Air pollution in the form of ozone and smog is created when nitrogen dioxide combines with sunlight. Smog's

burning eyes, choking, and coughing are all brought on by ground-level ozone, a potent irritant. Ozone is particularly harmful to children since it may damage their lungs and make existing health problems worse. Trees and crops may be negatively impacted by the increased ozone levels. When inhaled, nitrogen dioxide severely damages a human's respiratory system and nervous system. This means that exceeding the threshold levels of nitrogen oxide causes serious problems for human health and the environment. Little amounts of nitrogen oxides in water may evaporate, but the overwhelming majority will react with water to produce nitric acid. When discharged onto soil, nitrogen oxides (NOx) may be carried upward by evaporation [32].

Yet, most of it will be converted into nitric acid and other compounds.
The majority of people's exposure to nitrogen oxides comes from breathing polluted air. Certain people may be more vulnerable to the effects of nitrogen oxides if they happen to live in areas with high traffic volumes or in close proximity to combustion sources like coal-burning power stations. Nitrogen oxide levels are higher in homes where wood is burned or where kerosene or gas is used for heating or cooking. Nicotine users and passive smokers alike are at risk for nitrogen oxide exposure [33] due to the presence of nitric oxide and nitrogen dioxide in tobacco smoke.

Nitrogen oxides may be inhaled by those who work in factories producing nitric acid or specific explosives like dynamite and trinitrotoluene (TNT), or who perform metal welding [34].

4.10.11 Techniques for Analytical Characterization

For sensing applications, pure and doped samples are generated as thick and thin films. Several analytical methods are used to characterise samples prepared for sensing. Methods include chemical analysis and structural dissection. Several solid-characterization analyses include the production of secondary particles or radiation by the interaction of electromagnetic radiation, electrons, or ions with the solid, and then their assessment [35]. In this research, we used the following techniques for characterisation: X-ray diffraction, scanning electron microscopy, energy dispersive spectroscopy, and Raman spectroscopy.

4.10.11.1 Diffraction of X-rays

X-ray diffraction (XRD) is an important experimental technique that has been used to address a wide range of problems related to the crystal structure of bulk solids and thin films, including the determination of lattice constants and geometry, the naming of previously unknown materials, the determination of the preferred orientation of polycrystalline films, the detection of defects, and the measurement of stress. X-ray methods are advantageous since they are non-destructive and don't need a lot of preliminary work on the sample. This analytical method also allows for an easy quantification of the crystalline phases present in the samples and an assessment of the average grain size of the polycrystalline films [36].

This method is used to detect and analyse crystalline substances by using the diffraction phenomenon. Diffraction occurs when X-rays hit a crystal and scatter off of its many faces. Their behaviour is consistent with Bragg's Law [37].

$$n\lambda = 2d\sin(\theta)$$

Where, d is the interplanar separation
λ is the X-ray wavelength.

n is the order of diffraction

When radiation like X-rays enters a crystalline solid and is scattered by the material, a phenomenon known as diffraction occurs. The scattered (diffracted) beams' direction and intensity are determined by the orientation of the crystal lattice with regard to the incident beam. Crystal lattices have many faces, and X-rays may diffract off of them because of the parallel rows of atoms separated by a particular distance (d-spacing) [38]. For a beam to be fully diffracted, its path length between atomic rows at the angle of incidence must be an integer multiple of the wavelength of the incident beam. If the angle of incidence of the directed X-ray beam is larger than or equal to the wavelength of the X-rays, then the diffracted beam will have an intensity that is less than 100%. The analysis is shown as a sequence of peaks, with peak intensity along the Y-axis and goniometer angle along the X-axis.

If the sample is ground into a powder, it should supply all potential crystal lattice orientations; the goniometer will provide different angles of incidence; and the detector will measure the intensity of the diffracted beam [39].

The crystal structure determines the precise orientation and magnitude of a group of peaks. The powder's composition may be determined by comparing its spectra to those in reference tables, such as the JCPDS spectra maintained by the American Society for Testing and Materials. By comparing the peak position to the typical JCPDS card values of the material, we may determine the crystallites' orientation [40].

Additionally, the crystallite size of the sample may be evaluated using XRD, which is particularly useful for studying nanostructured metal oxide gas sensors. The XRD peaks calculated from an automated X-ray scan are an average of the diffraction effects of billions of nano-sized crystals. The Scherer equation and the peak width at half maximum (FWHM) provide the simplest solution.

Scherrer's formula determines the size of the crystallite.

$$D = \frac{0.9\lambda}{B\cos\theta}$$

where D is crystallite size.

λ is the wavelength of X-rays.

B is the full width half maxima in radians.

θ is the angle in degrees at which the intensity peak appears.

It's possible that the size of the particles generated from the agglomeration of these crystals is related to the size of the individual crystals in the sample. In order to learn more about the powder's crystallite structure and crystallite size, this research analysed XRD data. Cu-k radiation from a Bruker AXS D8 high-resolution X-ray diffractometer was used to get the XRD patterns of the nanopowders.

4.10.11.2 Scanning Electron Microscopy (SEM)

Significant amounts of kinetic energy are dissipated as a wide range of signals when incoming electrons are decelerated in a solid sample. Some of these signals include secondary electrons (used to create SEM images), backscattered electrons (BSE), diffracted backscattered electrons (EBSD) (used to determine crystal structures and orientations of minerals), photons (characteristic X-rays used for elemental analysis and continuum X-rays), visible light (cathodoluminescence—CL), and heat. Backscattered electrons and secondary electrons are often used for sample imaging. Backscattered electrons are ideal for revealing compositional variations in multiphase samples, whereas secondary electrons are superior for visualising surface shape and topography (i.e. for rapid phase discrimination). X-rays are produced when entering electrons collide inelastically with electrons located in different shells of atoms in the sample. X-rays of a certain wavelength are generated when excited electrons decay down to lower energy states (which is linked to the difference in energy levels of electrons in various shells of a specific element). Different X-rays are produced by the electron beam for each element in the material. As the x-rays generated by electron interactions do not result in any significant volume loss in the material, SEM analysis is considered to be non-destructive. By focusing a beam of high-energy electrons with energies between a few KeV and 50KeV on the surface of solid objects, the SEM may produce a wide variety of signals at the surface. The signals generated by electron-sample interactions reveal characteristics of the sample, such as its external appearance (texture), chemical composition, crystalline structure, and orientation of its constituent components. In most cases, information is collected across a small area of the sample's surface, and then a two-dimensional image is constructed to show the spatial variation of a given feature. Scanning electron microscopy (SEM) typically photographs regions between 1 cm and 5 microns wide (magnification range from 20X to about 30,000X, spatial resolution of 50 to 100 nm). Particularly useful for determining chemical compositions (through EDS), crystalline structure, and crystal orientations, the SEM may also be used to perform research on discrete points on the material (using EBSD).

In this study, a JEOL JSM-6390LV SEM was used for analysis. Particle morphology, film surface topography, and grain size were all analysed using the gathered images.

4.10.11.3 X-ray Energy Dispersive Analysis (EDAX)

Energy Dispersive X-ray analysis is often referred to as EDX analysis. EDS analysis, or EDAX analysis, is another name for it. It's a way to find out what kinds of elements make up a certain part of a specimen. The scanning electron microscope incorporates an EDX analysis system.

During EDX analysis, an electron beam is directed at the specimen from inside a scanning electron microscope. Electrons in the specimen atoms are knocked loose when they collide with the bombardment electrons. In the end, an electron from a higher-energy shell will replace one that was ejected from an inner shell. The outer electron must release some of its energy in the form of an X-ray in order to complete the transfer.

The electron's energy dissipation is proportional to the shell it is travelling into. And during the exchange, atoms of different elements give forth X-rays of differing energies. By analysing the amounts of energy contained in the X-rays created by a specimen during the electron beam bombardment, the atom from which the X-rays were produced may be identified.

The energy-dispersive X-ray (EDX) spectrum is simply a graph that displays the frequency distribution of X-rays received at each energy level. The highest concentrations of x-rays in an EDX spectrum tend to occur at certain energy levels. Since each atom has its own distinct peak, each element may be identified by its spectrum. When an element is present at a high enough concentration, its spectral peak becomes more prominent.

Each peak in an EDX spectrum plot not only identifies the element to which it corresponds, but also the kind of X-ray to which it is most closely related. For instance, the amount of energy carried by X-rays generated by an electron transitioning from the L-shell to the K-shell is represented as a K-Alpha peak. The transition from the M-shell to the K-shell releases X-rays, which is represented by a peak known as the K-Beta peak. You may see this in Figure 2.5.

For elemental speciation in this investigation, EDS data was gathered using a JEOL Model JED - 2300.

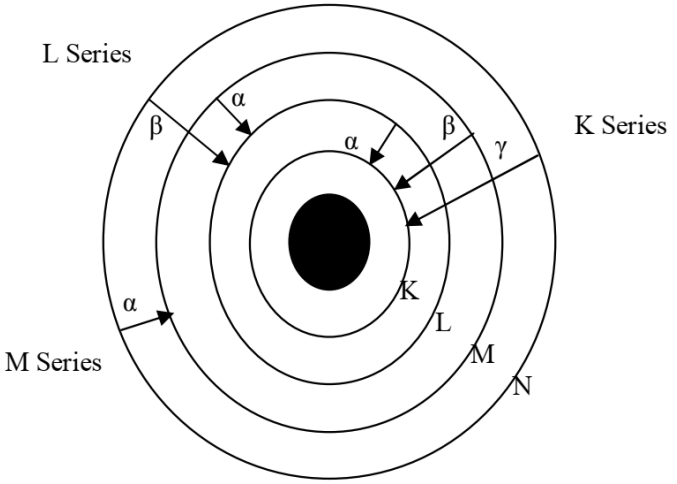

Figure 4. 17 Elements in an EDX spectrum are recognised by the energy content of the X-rays generated by their electrons as they move from a higher energy shell to a lower energy shell.[30]

Summary

Quantum chemists and materials scientists employ Density Functional Theory (DFT), a computer approach, to investigate the atomic and molecular details of the electrical structure of substances. It is predicated on the idea that the electron density, rather than the wave functions of individual electrons, is the relevant quantity for determining a system's attributes. DFT may be used to simulate the adsorption of gases on sensing materials and to compute the electronic characteristics of gas molecules and sensing materials, such as energy levels, electron densities, and charge distributions. It may also be used to forecast a sensor's reaction to various gases, leading to the creation of sensors that can detect numerous gases at once, as well as to improve the design of gas sensors by determining the most sensitive and selective sensing materials for a certain gas. Under Hohenberg-theorem, Kohn's a system's ground-state electron density is a special function of its external potential. The wave function of a system, which quantifies the probability of finding an electron at a certain place in space, is calculated using the Schrödinger equation, a mathematical equation that explains the behaviour of electrons in a system. The electronic structure of a system may be studied with the use of DFT, a sophisticated computational approach. The electron density of a many-electron system is related to its external potential by the Hohenberg-Kohn theorem, a fundamental concept in density functional theory

(DFT). It argues that the potential energy felt by the electrons in an atom because of the existence of nuclei and other electrons is what determines the electron density. The ground-state electron density, rather than individual electron wave functions, may be used as the primary variable in calculations of electronic characteristics according to this theorem. One particular use of this theory is the Kohn-Sham technique. Electronic structure of molecules and materials may be studied with the use of the potent computer tool known as the Kohn-Sham method. It swaps out the Schrödinger equation with a system of non-interacting "pseudo-particles" with the same electron density as the real, interacting electrons. In materials research and condensed matter physics, first-principles calculations are performed using Quantum ESPRESSO, an open-source software programme. Because of its modular and adaptable architecture, it can accommodate a wide variety of input parameters and exchange-correlation functionals. For first-principles computations in materials science and condensed matter physics using Density Functional Theory and the Kohn-Sham approach, an open-source software package called Quantum ESPRESSO is available for download. It has a large and vibrant user base because of its widespread adoption in both academic and commercial settings.

The sensitivity, selectivity, reaction time, recovery time, stability, and operating range of a gas sensor are all quantified by laboratory experiments. Measurements of gas sensing, measurements as a function of temperature and humidity, and exposure to realistic settings are some of the most popular forms of gas sensing experimentation. The chemical composition and surface morphology of the sensor are studied using spectroscopic methods including Raman, infrared (IR), and ultraviolet-visible (UV-Vis). In order to get the most out of a gas sensor, it is important to characterise its many different aspects. Two methodologies, flow through and static environment, are utilised to evaluate the sensor's sensitivity, selectivity, reaction time, and recovery time. The response curve is measured as a constant stream of analyte gas is passed through the system. The resistance is monitored over a period of time until equilibrium is established in a static environment. X-ray diffraction (XRD) is an essential experimental technique that has been used to address all issues concerning the crystal structure of bulk solids and thin films, including lattice constants and geometry, identification of unknown materials, orientation of single crystals and preferred orientation of polycrystalline films, defects, stress, and so on. The crystalline phases and mean grain size of materials may be simply quantified and evaluated using X-ray methods since they are non-destructive and do not need substantial sample preparation. The direction and intensity of the scattered (diffracted) beams are determined by the orientation of the crystal lattice with regard to the incoming beam during diffraction, which happens when penetrating radiation enters and is dispersed by a crystalline material. The field of nanostructured metal oxide gas sensors relies heavily on X-ray diffraction (XRD) for determining the crystallite size of a sample. To learn more about the powder's crystallite structure and crystallite size, SEM is utilised. Elemental analysis by X-ray diffraction (EDX) is a technique that uses a focused beam of high-energy electrons (often between a few KeV and 50KeV) to identify the elements present in a specimen or a small section of a larger one.

References:

1. Tezer, N. (2009). Density functional theory and ab-initio computational study of molecular structure, tautomerism, and geometrical isomerism of ethynyl-bridged dipyridinones: In the gas phase and dielectric media. *Journal of Molecular Structure-Theochem*, *895*(1), 100–106. https://doi.org/10.1016/J.THEOCHEM.2008.10.031

2. Cao, J. (2020). Sensing Behavior of Two Dimensional Al- and P-Doped WS 2 Toward NO, NO 2 , and SO 2 : an Ab Initio Study. *Nanoscale Research Letters*, *15*(1), 158–158. https://doi.org/10.1186/S11671-020-03391-0

3. Fu, H. (2017). Experimental and theoretical studies of V2O5@TiO2 core-shell hybrid composites with high gas sensing performance towards ammonia. *Sensors and Actuators B-Chemical*, *252*, 103–115. https://doi.org/10.1016/J.SNB.2017.05.027

4. Chruściński, D. (2005). Wigner function and Schrödinger equation in phase-space representation. *Physical Review A*, *71*(5), 5. https://doi.org/10.1103/PHYSREVA.71.052104

5. Goumri-Said, S. (2012). On the electronic nature of silicon and germanium based oxynitrides and their related mechanical, optical and vibrational properties as obtained from DFT and DFPT. *Computational Materials Science*, *53*(1), 158–168. https://doi.org/10.1016/J.COMMATSCI.2011.09.021

6. Sahni, V. (2012). Hohenberg-Kohn and Percus-Levy-Lieb proofs of density-functional theory. *Physical Review A*, *85*(5), 5. https://doi.org/10.1103/PHYSREVA.85.052502

7. Koppen, J. (2014). Density functional theory approach to gold-ligand interactions: Separating true effects from artifacts. *Journal of Chemical Physics*, *140*(24), 244313–244313. https://doi.org/10.1063/1.4885137

8. Nakatsuji, H. (2018). Solving the Schrödinger equation of atoms and molecules: Chemical-formula theory, free-complement chemical-formula theory, and intermediate variational theory. *Journal of Chemical Physics*, *149*(11), 114105–114105. https://doi.org/10.1063/1.5040376

9. Telnov, D. A. (1998). Generalized Floquet formulation of time-dependent current-density-functional theory. *Physical Review A*, *58*(6), 4749–4756. https://doi.org/10.1103/PHYSREVA.58.4749

10. Kaplan, A. D. (2018). Collapse of the electron gas from three to two dimensions in Kohn-Sham density functional theory. *Physical Review B*, *98*(8), 8. https://doi.org/10.1103/PHYSREVB.98.085147

11. Mosquera, M. A. (2016). Connection between Hybrid Functionals and Importance of the Local Density Approximation. *Journal of Physical Chemistry A*, *120*(9), 1605–1612. https://doi.org/10.1021/ACS.JPCA.5B10864

12. Shenton, J. K. (2017). Effects of the Hubbard U on density functional-based predictions of BiFeO3 properties. Journal of Physics: Condensed Matter, 29(44), 445501–445501. https://doi.org/10.1088/1361-648X/AA8935

13. Malcioglu, O. B. (2011). turboTDDFT – A code for the simulation of molecular spectra using the Liouville–Lanczos approach to time dependent density-functional perturbation theory☆. Computer Physics Communications, 182(8), 1744–1754. https://doi.org/10.1016/J.CPC.2011.04.020

14. Gębicki, J. (2009). Influence of Analyte Flow Rate on Signal and Response Time of the Amperometric Gas Sensor with Nafion Membrane. Electroanalysis, 21(14), 1568–1576. https://doi.org/10.1002/ELAN.200804567

15. Collings, N. (2012). Steady-state modelling of the universal exhaust gas oxygen (UEGO) sensor. Measurement Science and Technology, 23(8), 8. https://doi.org/10.1088/0957-0233/23/8/085108

16. Hassan, H. ul. (2016). Sensor based on chemical vapour deposition-grown molybdenum disulphide for gas sensing application. RSC Advances, 6(79), 75839–75843. https://doi.org/10.1039/C6RA10132A

17. Dhivya, P. (2014). Magnetron sputtered nanostructured cadmium oxide films for ammonia sensing. Journal of Solid State Chemistry, 214, 24–29. https://doi.org/10.1016/J.JSSC.2013.11.030

18. Dhivya, P. (2014). Magnetron sputtered nanostructured cadmium oxide films for ammonia sensing. Journal of Solid State Chemistry, 214, 24–29. https://doi.org/10.1016/J.JSSC.2013.11.030

19. Hassan, H. ul. (2016). Sensor based on chemical vapour deposition-grown molybdenum disulphide for gas sensing application. RSC Advances, 6(79), 75839–75843. https://doi.org/10.1039/C6RA10132A

20. Jia, H. (2018). Cu2O@PNIPAM core–shell microgels as novel inkjet materials for the preparation of CuO hollow porous nanocubes gas sensing layers. Journal of Materials Chemistry C, 6(27), 7249–7256. https://doi.org/10.1039/C8TC01995A

21. Park, Y. (2017). Effect of gas flow rates and nozzle throat width on deposition of α-alumina films of granule spray in vacuum. Journal of The European Ceramic Society, 37(7), 2667–2672. https://doi.org/10.1016/J.JEURCERAMSOC.2017.02.021

22. Park, Y. (2017). Effect of gas flow rates and nozzle throat width on deposition of α-alumina films of granule spray in vacuum. Journal of The European Ceramic Society, 37(7), 2667–2672. https://doi.org/10.1016/J.JEURCERAMSOC.2017.02.021

23. Oyabu, T. (1982). Sensing characteristics of tin oxide thick film gas sensor. Journal of Applied Physics, 53(11), 7125–7130. https://doi.org/10.1063/1.331605

24. Suematsu, K. (2018). Ultraselective Toluene-Gas Sensor: Nanosized Gold Loaded on Zinc Oxide Nanoparticles. Analytical Chemistry, 90(3), 1959–1966. https://doi.org/10.1021/ACS.ANALCHEM.7B04048

25. Geffroy, P.-M. (2007). Innovative Approach to Metal Matrix Composites Film by Tape Casting Process. Advanced Engineering Materials, 9(7), 547–553. https://doi.org/10.1002/ADEM.200700013

26. Hojamberdiev, M. (2020). Efficient NO2 sensing performance of a low-cost nanostructured sensor derived from molybdenite concentrate. Green Chemistry, 22(20), 6981–6991. https://doi.org/10.1039/D0GC02779K

27. Garje, A. D. (2008). Gas sensing properties of nano SnO 2 based thick films prepared by dip coating method with effect of molarity of PtCl 2 solution. Journal of Materials Science: Materials in Electronics, 19(6), 547–552. https://doi.org/10.1007/S10854-007-9384-4

28. Xu, K. (2014). Correlation between microstructure and gas sensing properties of hierarchical porous tin oxide topologically synthesized on coplanar sensors' surface. Sensors and Actuators B-Chemical, 205(205), 416–425. https://doi.org/10.1016/J.SNB.2014.09.015

29. Bleecker, M. L. (2015). Carbon monoxide intoxication. Handbook of Clinical Neurology, 131, 191–203. https://doi.org/10.1016/B978-0-444-62627-1.00024-X

30. Ward, P. L. (2009). Sulfur dioxide initiates global climate change in four ways. Thin Solid Films, 517(11), 3188–3203. https://doi.org/10.1016/J.TSF.2009.01.005

31. Zhou, Y. (2018). UV assisted ultrasensitive trace NO2 gas sensing based on few-layer MoS2 nanosheet–ZnO nanowire heterojunctions at room temperature. Journal of Materials Chemistry, 6(22), 10286–10296. https://doi.org/10.1039/C8TA02679C

32. Chen, H. (2020). The effects of outdoor air pollution on chronic illnesses. McGill Journal of Medicine, 12(1), 58–64. https://doi.org/10.26443/MJM.V12I1.735

33. Sonker, R. K. (2016). Low temperature study of nanostructured Fe2O3 thin films as NO2 sensor. Materials Today: Proceedings, 3(6), 2315–2320. https://doi.org/10.1016/J.MATPR.2016.04.142

34. Mishra, A. (2019). Metal oxide nanohybrids-based low-temperature sensors for NO2 detection: a short review. Journal of Materials Science: Materials in Electronics, 30(9), 8160–8170. https://doi.org/10.1007/S10854-019-01232-0

35. Newbury, D. E. (2012). Energy Dispersive Spectrometry. Characterization of Materials, 1–26. https://doi.org/10.1002/0471266965.COM087.PUB2

36. Brewer, R. T. (2003). Reflection high-energy electron diffraction experimental analysis of polycrystalline MgO films with grain size and orientation distributions. Journal of Applied Physics, 93(1), 205–210. https://doi.org/10.1063/1.1526156

37. Zhezhe, W. (2017). ZnO nanoparticles as sensing materials with high gas response for detection of n-butanol gas. Journal of Nanostructures, 7(2), 103–110. https://doi.org/10.22052/JNS.2017.02.003

38. Ristanović, Z. (2014). Breakthroughs in Hard X-ray Diffraction: Towards a Multiscale Science Approach in Heterogeneous Catalysis. Angewandte Chemie, 53(33), 8556–8558. https://doi.org/10.1002/ANIE.201404463

39. Kaplow, R. (1963). X-Ray Diffractometer for the Study of Liquid Structures. Review of Scientific Instruments, 34(5), 579–581. https://doi.org/10.1063/1.1718508

40. Jiang, H. B. (2011). Anatase TiO2 Crystals with Exposed High-Index Facets. Angewandte Chemie, 50(16), 3764–3768. https://doi.org/10.1002/ANIE.201007771

41. Sholl, D. S., & Steckel, J. A. (2009, April 13). Density Functional Theory: A Practical Introduction. Wiley-Interscience. https://doi.org/10.1604/9780470373170

Density Functional Theory (DFT) Investigation on Doped BFO for Gas Molecule Adsorption Performance

In recent years, perovskite-based gas sensors have gained growing attention due to their unique combination of electrical, magnetic, and structural properties. Among them, Bismuth Ferrite ($BiFeO_3$, or BFO) has emerged as a particularly versatile candidate — not only as a *multiferroic and spintronic material* but also as a robust gas-sensing material due to its remarkable thermal stability and long-term operational reliability. Previous studies have demonstrated that nanostructured BFO exhibits significant carbon monoxide sensitivity — achieving up to 2.12% response at 30 ppm — confirming its potential for real-time detection in automotive exhaust conditions [9–10].

One of the most effective approaches to enhance BFO's gas sensing capability is metal doping, where transition or noble metals are introduced into its lattice. Such dopants modify the material's band structure, surface energy, and charge transport behavior, thereby improving both its sensitivity and selectivity. For instance, tungsten-doped BFO prepared by spray pyrolysis exhibited higher responsivity and a lower optimal operating temperature for nitrogen oxide (NO) sensing applications [11]. The electrical and surface properties of BFO depend strongly on its crystal structure and morphology — which can be tailored through controlled synthesis methods to yield particles of different sizes, shapes, and surface areas [12]. However, despite progress in material preparation, a detailed understanding of the gas adsorption mechanism at the atomic scale, particularly for doped BFO systems, remains limited.

To bridge this gap, Density Functional Theory (DFT) provides a powerful computational framework to explore the interaction between gas molecules and sensing materials at the electronic level. DFT enables the prediction of properties such as adsorption energy, charge transfer, and electronic density of states (DOS) — key indicators of a material's sensing performance. Previous DFT-based investigations have explored similar interactions for a range of materials, including CO adsorption on doped MgO surfaces [23] and transition metal-embedded MoS_2 monolayers [16], yielding valuable insights into adsorption mechanisms and charge transfer dynamics. However, no systematic DFT-based study has yet been reported for CO, CO_2, NO, NO_2, and CH_4 adsorption on pure and Ag-doped BFO — the primary gas species found in automotive exhausts.

In this study, first-principles DFT simulations are employed to analyze the adsorption behavior of these gases on both undoped and Ag-doped BFO surfaces. The results include detailed evaluations of adsorption energy, charge transfer, charge density difference, and DOS, which collectively describe the interaction strength and electronic modulation caused by gas adsorption. This theoretical analysis provides a foundation for designing and experimentally validating Ag-doped BFO-based gas sensors with enhanced selectivity and reduced operating temperature.

5.1 Model Structures of BFO and Ag-BFO

Figure 5.1 illustrates the optimized atomic configurations of undoped and Ag-doped BFO used in this study. To minimize unwanted interatomic interactions, the primitive cell of BFO was expanded into a 2×2×1

supercell containing 42 atoms, with a vacuum spacing of 10 Å along the z-axis. The substitution of a bismuth atom with silver (Ag) near the surface modifies the local crystal field, leading to subtle changes in the bandgap and charge localization. These variations are expected to influence the gas adsorption behavior and electron transport dynamics — both crucial factors in determining sensor performance.

5.2 Computational Methodology

The computational investigation in this study was performed using first-principles Density Functional Theory (DFT) as implemented in the Quantum ESPRESSO (v6.4) software package. DFT provides an accurate yet computationally efficient approach to model the electronic structure and adsorption behavior of gas–solid systems at the atomic level. All parameters were selected based on convergence testing, literature best practices, and the physical requirements of the BFO system under study.

5.2.1Exchange–Correlation Functional

The Generalized Gradient Approximation (GGA) in the Perdew–Burke–Ernzerhof (PBE) formulation was used for the exchange–correlation energy. This functional provides a good compromise between computational cost and accuracy for transition metal oxides like BFO. However, since Fe 3d electrons are strongly correlated, the standard GGA can underestimate the bandgap, and hence a DFT+U correction was applied.

5.2.2 On-Site Coulomb Correction (DFT+U+V Method)

A Ueff of 6 eV was applied to Fe 3d orbitals using the DFT+U+V method. This correction accounts for strong electron correlation and ensures accurate electronic structure and magnetic properties, consistent with literature values for BFO.

5.2.3 Pseudopotentials

Ultrasoft pseudopotentials from the Quantum ESPRESSO library were employed to represent electron–ion interactions. These allow accurate modeling with reduced computational cost, particularly important for heavy atoms like Bi and Fe.

5.2.4Plane-Wave Cutoff Energy

A cutoff energy of 90 Ry (≈1225 eV) was chosen after convergence testing. This ensures total energy variations remain below 1 meV/atom, balancing computational cost and accuracy for stable results.

5.2.5 Brillouin Zone Sampling (K-point Grid)

A 4×4×1 Monkhorst–Pack k-point grid was used for Brillouin zone integration. This grid size provided well-converged total energies and is suitable for a large 2×2×1 supercell used in surface adsorption studies.

5.2.6 Structural Relaxation

All atomic forces were relaxed below 0.02 eV/Å with total energy convergence at 10^{-5} eV, ensuring that each configuration reached its lowest-energy geometry without residual stress or metastability.

5.2.7 Supercell and Vacuum Spacing

A 2×2×1 supercell containing 42 atoms was used with a 10 Å vacuum spacing along the z-axis. This setup minimizes interaction between periodic images and prevents spurious surface effects.

5.2.8 Adsorption Energy Calculation

Adsorption energy (E_ads) was calculated as: E_ads = E_tot − (E_surf + E_molecule), where E_tot is the total energy of the gas–surface system, E_surf the clean surface energy, and E_molecule the isolated gas energy. A negative E_ads indicates favorable adsorption.

5.2.9 Visualization and Analysis

Charge density difference and Density of States (DOS) were analyzed using XCrySDen and VESTA tools. These visualizations reveal how doping and adsorption influence electronic structure and charge redistribution.

Parameter	Chosen Value/Method	Rationale	Significance
Exchange–correlation	GGA-PBE	Accurate and validated for oxides	Reliable electronic structure
On-site correction	DFT+U+V (Ueff = 6 eV)	Corrects d-electron correlation	Accurate bandgap, magnetism
Cutoff energy	90 Ry	Converged total energy	Numerical stability and precision
K-point grid	4×4×1	Efficient sampling for supercell	Computational efficiency
Relaxation criterion	0.02 eV/Å	Ensures equilibrium geometry	Accurate adsorption behavior
Vacuum spacing	10 Å	Avoids periodic interaction	Physical adsorption accuracy

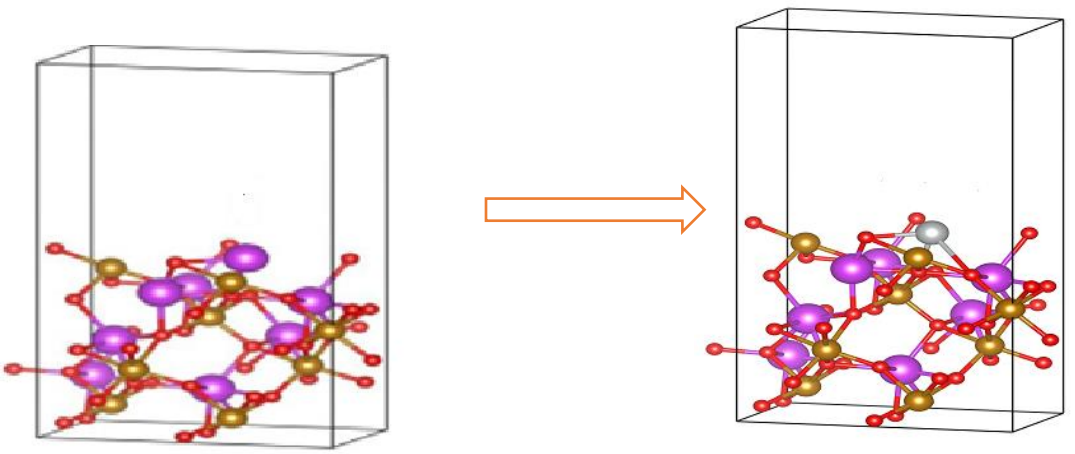

Figure 5. 1 BFO (010) Structure and Ag Doped BFO (010) Structure

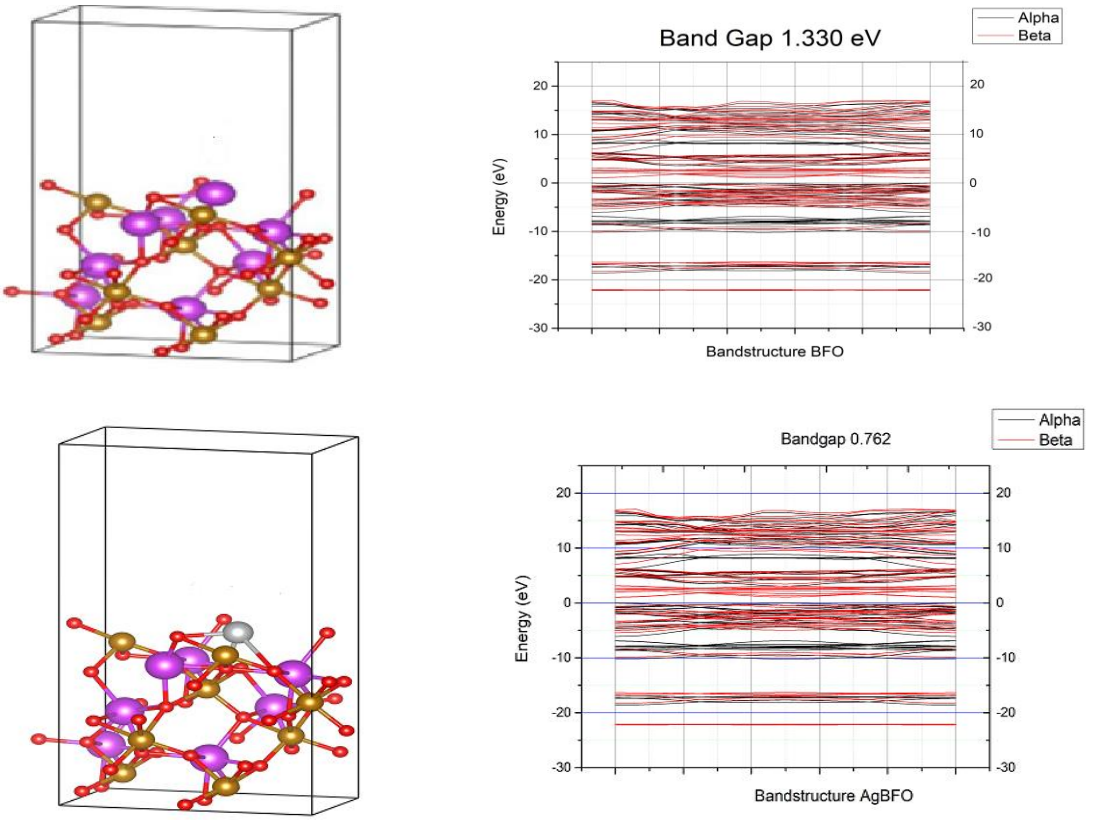

Figure 5. 2 Band gap calculation for BFO (010) and Ag-BFO(010)

5.3 Electron Configuration and CO Gas Adsorption Mechanism

Understanding how carbon monoxide (CO) interacts with the surface of Bismuth Ferrite (BFO) is fundamental to explaining its sensing behavior. To explore this, an adsorption model of CO molecules deposited on the BFO(010) surface was developed. This model allows for a detailed study of how surface characteristics influence gas adsorption and the resulting sensor response.

5.3.1 CO Adsorption on the Pure BFO(010) Surface

Figure 5.1 illustrates the modeled structure of CO adsorption on the BFO(010) surface. Using Density Functional Theory (DFT) calculations, the most stable adsorption configuration was identified, with an optimal adsorption distance of approximately 3.00 Å between the CO molecule and the surface.

After geometry optimization, the adsorption energy ($E_a$ds) was calculated to be –0.52 eV, representing a moderately exothermic process. The adsorption energy was evaluated using the expression:

Eads=Etot−(Esurf+Emolecule)

where
Etot = total energy of the combined gas–surface system, Esurf= energy of the clean BFO(010) surface, andEmolecule = energy of the isolated CO molecule.

A negative adsorption energy implies that the interaction between CO and the surface is thermodynamically favorable, though the magnitude suggests physisorption, where the bonding arises mainly from weak van der Waals and electrostatic interactions rather than strong chemical bonding.

The charge density distribution map presented in Figure 5.3 further clarifies this interaction. In this figure, yellow regions represent electron accumulation, while blue regions denote electron depletion. The visualization reveals that the electron redistribution due to CO adsorption occurs primarily on the surface layer of BFO. This localized electron reorganization confirms that the gas-sensing mechanism is surface-dominated, which is consistent with typical behavior observed in semiconductor metal oxides.

However, the limited degree of charge transfer observed between the CO molecule and the undoped BFO surface suggests that pure BFO exhibits moderate sensitivity toward CO detection. To improve this interaction, transition or noble metal doping, such as with silver (Ag), can be introduced to enhance surface reactivity and electron exchange efficiency.

5.3.2 Effect of Ag Doping on CO Adsorption

To evaluate the influence of noble metal modification, the adsorption of CO on Ag-doped BFO(010) was investigated using the same surface model. The optimized structure for Ag–BFO(010) exhibited similar geometric features to the undoped case, confirming the model's stability. The computed adsorption energy in this case was –0.51 eV, slightly lower than that of the pure surface.

This subtle reduction in adsorption energy indicates that Ag doping enhances the likelihood of adsorption, improving the overall gas-sensing efficiency. In adsorption studies, a more negative $E_a$ds value corresponds to stronger binding, hence Ag–BFO surfaces are more active toward CO molecules than pure BFO surfaces.

5.3.3 Electronic Structure and Density of States (DOS) Analysis

The Density of States (DOS) results for both bare BFO and Ag-doped BFO after CO adsorption are presented in Figure 5.5. These plots reveal how electronic states near the Fermi level (E_x) are affected by Ag incorporation and CO adsorption.

For pure BFO, the DOS around the Fermi level is relatively sparse, signifying limited electron availability for conduction. After Ag doping, however, there is a noticeable increase in the DOS near the Fermi level, indicating enhanced electronic activity. This higher electron density facilitates greater electrical conductivity changes when CO molecules adsorb, thereby increasing sensor response and sensitivity.

5.3.4 Charge Density Redistribution and Adsorption Mechanism

Further insight into the adsorption process is obtained from the charge difference density distributions (Figure 5.3). The comparison between pure and Ag-doped surfaces reveals distinct differences:

- In pure BFO(010), charge redistribution is localized mainly around surface oxygen atoms, showing weak interaction with CO.
- In Ag-doped BFO(010), pronounced electron depletion appears near the CO molecule, while electron accumulation is observed around Ag and Fe atoms.

This pattern demonstrates enhanced charge transfer between the adsorbed CO molecule and the Ag-modified surface. The Ag dopant acts as an electron bridge, facilitating stronger coupling between the adsorbed gas and the metal oxide framework.

These findings indicate that Ag doping increases both the surface reactivity and electronic conductivity of BFO, thereby improving its CO detection performance. In practical terms, Ag-doped BFO sensors can respond more rapidly and with higher sensitivity due to this efficient charge exchange process.

In simpler terms, the pure BFO surface interacts weakly with CO molecules, leading to a limited electrical response. When Ag atoms are introduced, they create new electronic pathways that allow electrons to flow more easily between the CO molecule and the surface. This improves both adsorption strength and signal sensitivity. Thus, the presence of Ag transforms BFO into a more responsive and efficient CO gas sensor, suitable for applications such as automotive exhaust monitoring and environmental pollution detection.

Parameter	Pure BFO (010)	Ag-BFO (010)	Interpretation
Adsorption distance (Å)	3.00	3.00	Optimal distance identical in both systems
Adsorption energy (eV)	–0.52	–0.51	Ag-doping slightly strengthens adsorption
Interaction type	Physisorption	Physisorption + charge enhancement	Improved electron exchange
Charge redistribution	Localized near O atoms	Extended to Ag and Fe sites	Enhanced sensitivity
DOS near Fermi level	Moderate	Higher	Better conductivity and signal response

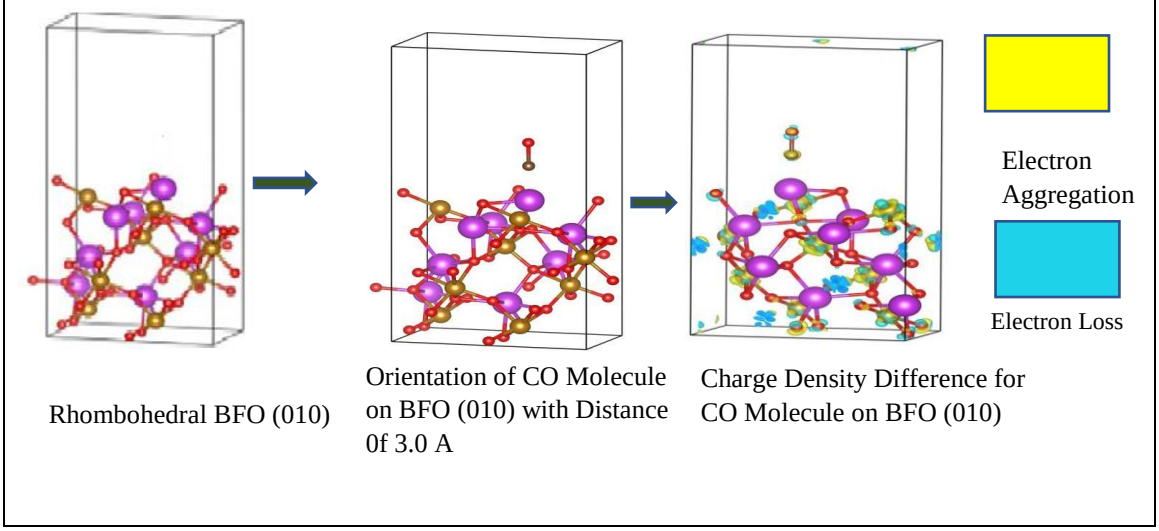

Figure 5. 3 DFT Investigation for CO Gas Adsorption Mechanism on BFO

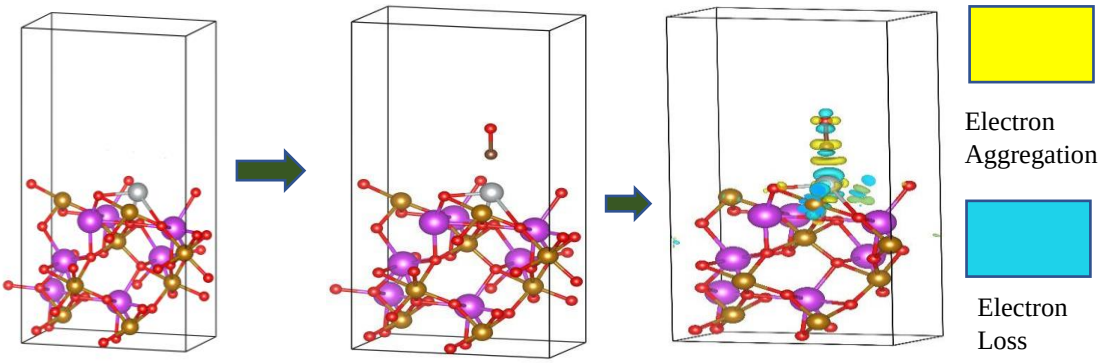

Rhombohedral Ag-BFO (010)

Orientation of CO Molecule on Ag-BFO (010) with Distance 0f 3.0 A

Charge Density Difference for CO Molecule on Ag-BFO.

Figure 5. 4 DFT Investigation for CO Gas Adsorption Mechanism on Ag Doped BFO

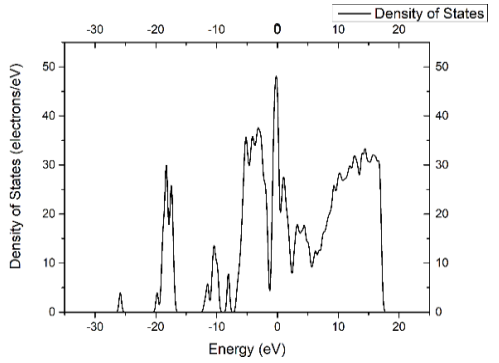

Total Density of States CO-BFO

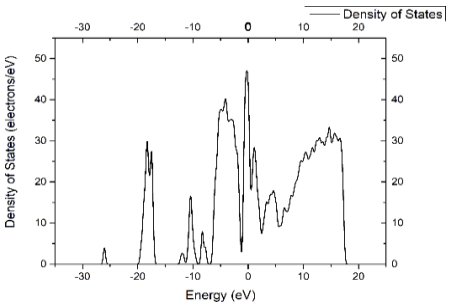

Total Density of States CO-AGBFO

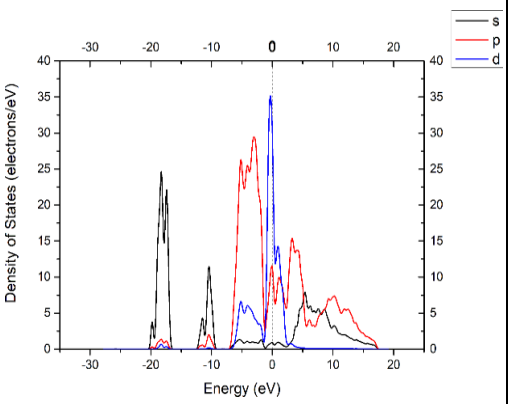

Partial Density of States BFO

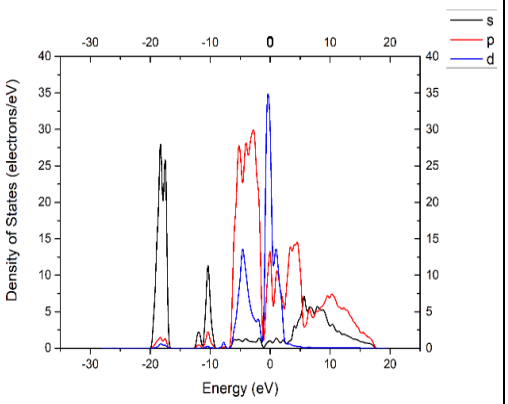

Partial Density of States AGBFO

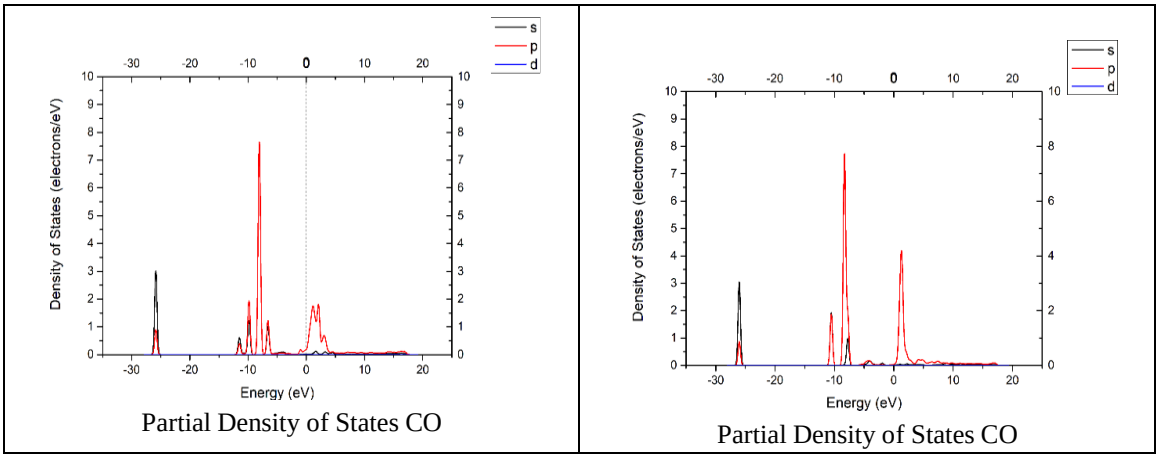

Figure 5. 5 Total Density of States Plot and Partial Density of States Plot for CO adsorption on BFO and Ag-BFO

5.4 Electron Configuration and CO_2 Gas Adsorption Mechanism

To further understand the gas-sensing properties of Bismuth Ferrite (BFO), the adsorption of carbon dioxide (CO_2) molecules on the BFO(010) surface was investigated. This study helps elucidate how CO_2 interacts with the material's electronic structure and how Ag doping influences adsorption behavior.

5.4.1 CO_2 Adsorption on Pure BFO(010) Surface

The optimized structure of CO_2 adsorption on the BFO(010) surface is shown in Figure 5.6. Using Density Functional Theory (DFT) simulations, it was found that the adsorption energy ($E_a$ds) for the CO_2–BFO(010) system is –0.78 eV, indicating that the process is exothermic and energetically favorable. For comparison, this adsorption energy is slightly higher in magnitude than that of the CO–BFO(010) system (–0.72 eV), implying that CO_2 binds more strongly than CO on the same BFO surface.

The adsorption energy was calculated using the standard relation:

$$E_{ads}=E_{tot}-(E_{surf}+E_{molecule})$$

where

- E_{tot} = total energy of the combined system (surface + gas molecule),
- E_{surf} = total energy of the pristine BFO(010) surface, and
- $E_{molecule}$ = total energy of the isolated CO_2 molecule.

The negative sign of E_{ads} confirms that the process is thermodynamically favorable. The relatively moderate adsorption energy suggests that physisorption dominates, characterized by weak electrostatic interactions rather than strong chemical bonding.

This adsorption strength is appropriate for gas-sensing applications since it allows CO_2 molecules to attach and detach rapidly from the surface, enabling quick sensor response and recovery.

5.4.2 Effect of Ag Doping on CO_2 Adsorption

To evaluate the effect of noble metal modification, one silver (Ag) atom was introduced into the BFO lattice near the surface. The addition of this dopant altered the local electronic environment and the way CO_2 molecules interact with the surface atoms.

After doping, the calculated adsorption energy for CO_2 decreased significantly to –0.16 eV, implying a weaker interaction between the gas molecule and the doped surface. This reduction in adsorption energy means that Ag doping lowers the surface's affinity for CO_2, reducing the likelihood of strong attachment and indicating that Ag–BFO is less effective for CO_2 detection compared to the undoped system.

In simple terms, the presence of silver atoms changes the charge distribution in such a way that CO_2 molecules find it more difficult to adhere strongly to the surface.

5.4.3 Density of States (DOS) Analysis

To gain deeper insight into the electronic behavior during adsorption, the Total Density of States (TDOS) of the system was analyzed for both undoped and Ag-doped configurations (see Figure 5.8). The TDOS reflects the distribution of available electronic states and their energy levels relative to the Fermi energy (E_F) — the level at which electrons can move freely and contribute to conduction.

For the undoped BFO(010) surface, the CO_2 adsorption peak is located around –4.3 eV, relatively close to the Fermi level. This indicates that the adsorbed CO_2 molecules interact moderately with the surface electrons, causing detectable but limited changes in the material's electrical conductivity.

After Ag doping, the TDOS peak shifts closer to –4.8 eV and its magnitude near the Fermi level increases slightly. This shift indicates that the presence of Ag alters the electronic structure by introducing new localized states near the Fermi level.

However, since the adsorption energy decreases, these electronic states contribute less to chemical bonding and more to weak physical interaction, suggesting that Ag acts more as an electronic modifier rather than a chemical anchor for CO_2.

In practical terms, while Ag doping enhances surface conductivity, it simultaneously reduces the binding strength for CO_2, meaning the surface becomes more conductive but less chemically reactive toward this molecule.

5.4.4 Interpretation of Adsorption Mechanism

The analysis shows that:

I. For pure BFO(010), CO_2 molecules interact primarily through weak electrostatic attraction, leading to moderate adsorption energy and suitable sensing response.
II. Upon Ag doping, the adsorption energy decreases and the interaction becomes weaker, indicating a decline in CO_2 adsorption capability.
III. The higher TDOS near the Fermi level in Ag–BFO suggests increased electrical activity but not stronger gas binding.

This balance between electronic conductivity and adsorption strength is crucial in gas-sensing design: while improved conductivity enhances signal output, excessively weak adsorption may limit the sensitivity for gases like CO_2.

In simpler terms, the pure BFO surface can trap CO_2 molecules fairly well due to a natural attraction between its surface electrons and the CO_2 gas.

When Ag atoms are added, they modify the electronic surface, making it smoother and more conductive — but this also makes CO_2 less likely to stick.

Thus, while Ag-doped BFO performs excellently for certain gases (like CO or NO_2), its selectivity for CO_2 decreases, illustrating the trade-off between surface reactivity and conductivity in multi-gas sensor design

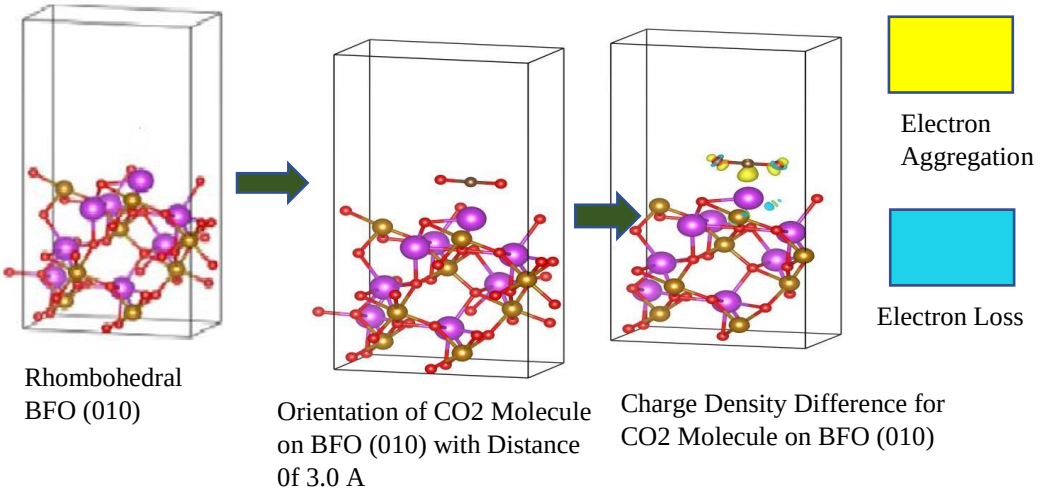

Figure 5. 6 DFT Investigation for CO_2 Gas Adsorption Mechanism on BFO

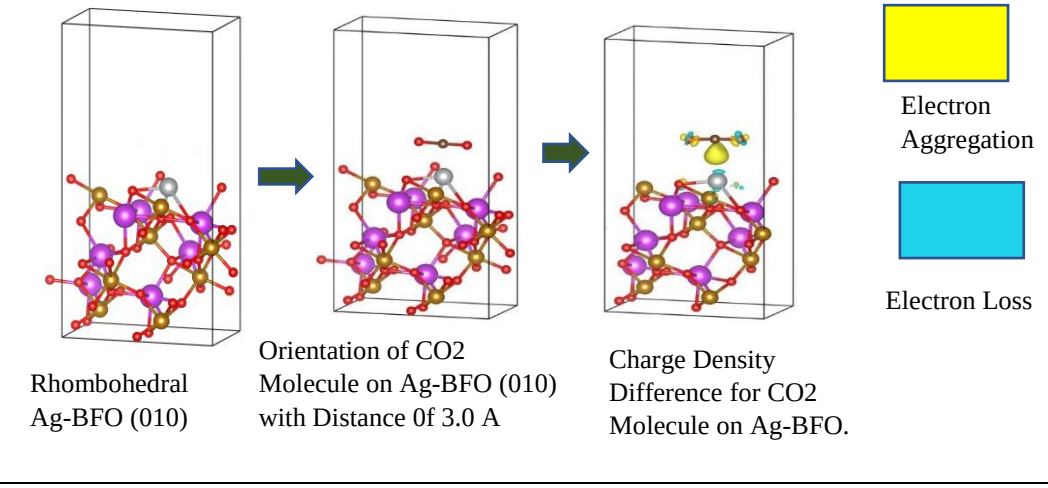

Figure 5. 7 DFT Investigation for CO_2 Gas Adsorption Mechanism on Ag Doped BFO

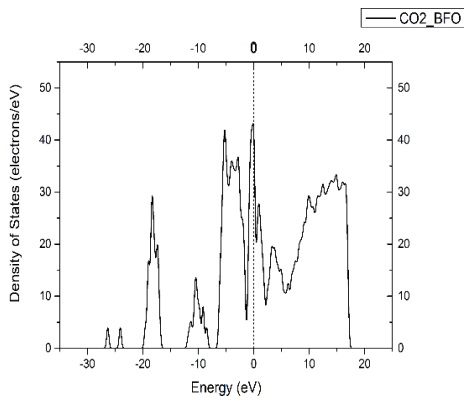

Total Density of States CO_2-BFO

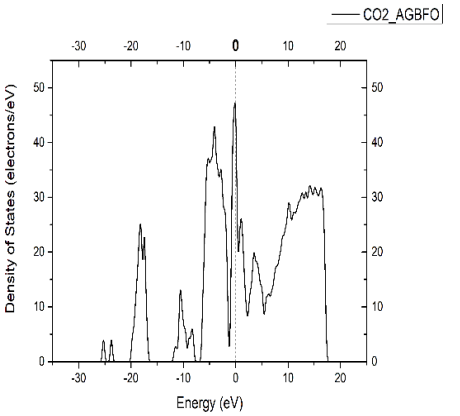

Total Density of States CO_2-AGBFO

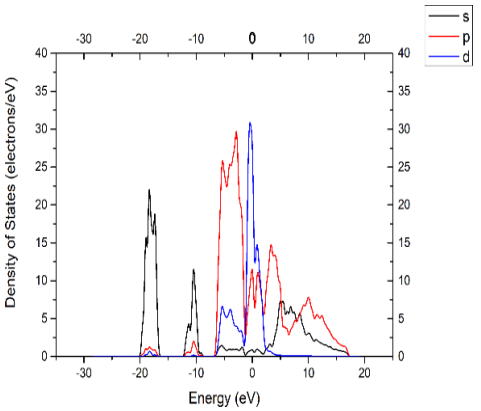

Partial Density of States BFO

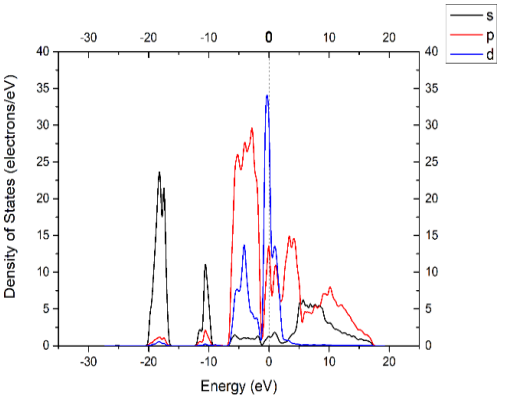

Partial Density of States AGBFO

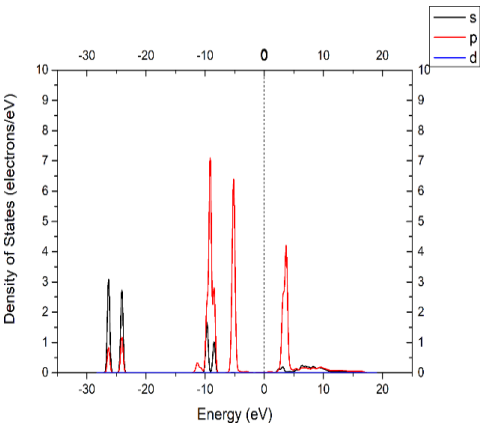

Partial Density of States CO_2

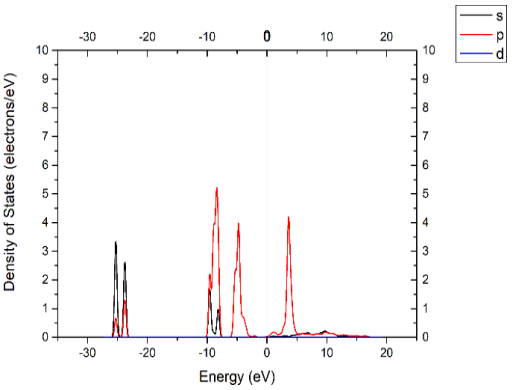

Partial Density of States CO_2

Figure 5. 8 Total Density of States Plot and Partial Density of States Plot for CO_2 adsorption on BFO and Ag-BFO

5.5 NO Adsorption on Pure and Ag-Doped BFO(010) Surfaces

The optimized configurations for NO adsorption are shown in Figures 5.9 and 5.10. The calculated adsorption energies for the NO–BFO(010) system are –0.72 eV for the undoped surface and –1.60 eV for the Ag-doped surface.

These negative adsorption energy values indicate that the adsorption process is spontaneous and exothermic, requiring no additional energy input for NO molecules to bind to the surface.

A comparison of the two values shows that Ag doping significantly enhances the adsorption strength, as the magnitude of the adsorption energy increases more than twofold. This implies that the Ag-BFO(010) surface has a stronger affinity for NO molecules, which is a favorable property for gas sensing applications, where increased adsorption generally corresponds to higher sensitivity.

The adsorption energy was calculated using the relation:

$$E_{ads}=E_{tot}-(E_{surf}+E_{molecule})$$

Where
- E_{tot} is the total energy of the combined system (NO + surface),
- E_{surf} is the total energy of the clean BFO surface, and
- $E_{molecule}$ is the total energy of the isolated NO molecule.

5.5.1 Charge Difference Density and Electronic Interaction

To gain further insight into the charge transfer mechanism, the charge difference density was analyzed for both pure and Ag-doped BFO(010) surfaces.

The charge-density plots reveal that NO molecules act as charge acceptors in both configurations. This means that electrons are transferred from the BFO surface to the NO molecules during adsorption.

However, in the Ag-doped surface, the redistribution of electron density is far more pronounced. The Ag dopant acts as an active site, attracting electrons and facilitating stronger electronic interaction with the NO molecule. This enhanced charge exchange results in improved sensor response and faster conductivity variation upon exposure to NO gas.

5.5.2 Density of States (DOS) Analysis

The Total Density of States (TDOS) for the system before and after Ag doping is shown in Figure 5.11. The DOS plot provides valuable information about the energy distribution of electronic states and their proximity to the Fermi level (E_F).

For the pure BFO(010) surface, the TDOS near the Fermi level is relatively low, indicating limited electron mobility and modest interaction between NO molecules and surface atoms.

After Ag doping, the TDOS intensity near the Fermi level increases significantly. This shift indicates that the electronic structure has become more conductive, allowing easier movement of charge carriers.

Physically, this means that the adsorption of NO on Ag-BFO(010) not only strengthens the gas–surface binding but also enhances the material's electrical response, leading to more pronounced changes in resistance or current — key parameters in chemiresistive gas sensors.

In DFT-based gas sensing analysis, the adsorption energy and DOS peak intensity near the Fermi level are directly correlated. A larger DOS peak implies that more states are available for electron transfer, which in turn corresponds to stronger adsorption and higher sensor response. Therefore, the high TDOS peak observed in the Ag-doped case confirms that NO molecules are more readily adsorbed and produce a stronger electrical signal than in the undoped BFO.

5.5.3 Interpretation of the NO Adsorption Mechanism

From the above findings, the adsorption process can be summarized as follows:

Property	BFO(010)	Ag–BFO(010)	Implication
Adsorption energy (eV)	–0.72	–1.60	Ag doping doubles the adsorption strength
Type of adsorption	Physisorption with weak charge transfer	Chemisorption-like interaction	Stronger gas–surface bonding
Charge transfer	Moderate electron flow to NO	Significant electron flow to NO	Increased sensor sensitivity
TDOS near Fermi level	Low	High	Improved conductivity and faster response
Role of NO molecule	Charge acceptor	Stronger charge acceptor	Enhanced electrical response

These observations collectively demonstrate that Ag doping transforms BFO from a moderately active surface into a highly responsive gas-sensing material. The improved electronic structure and charge transport make Ag–BFO especially effective for NO detection in automotive exhaust and industrial monitoring environments.

In simpler terms, when NO gas molecules come into contact with pure BFO, they weakly attach and draw some electrons from the surface, causing a small electrical change. When Ag atoms are introduced into the material, they act as "electron bridges," allowing NO molecules to pull more electrons, which causes a much stronger change in the sensor's electrical signal. This makes Ag–BFO sensors highly sensitive to NO gas, capable of detecting even low concentrations efficiently.

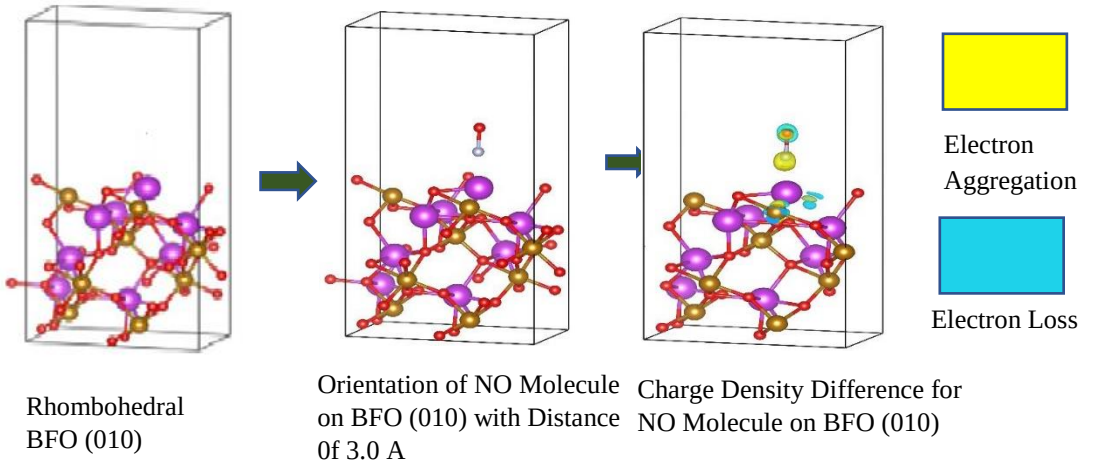

Figure 5. 9 DFT Investigation for NO Gas Adsorption Mechanism on BFO

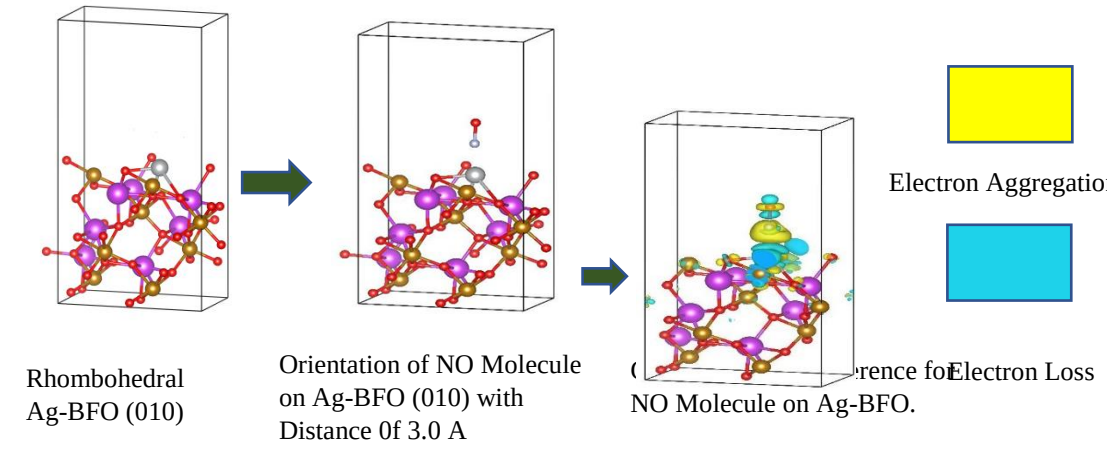

Figure 5. 10 DFT Investigation for NO Gas Adsorption Mechanism on Ag Doped BFO

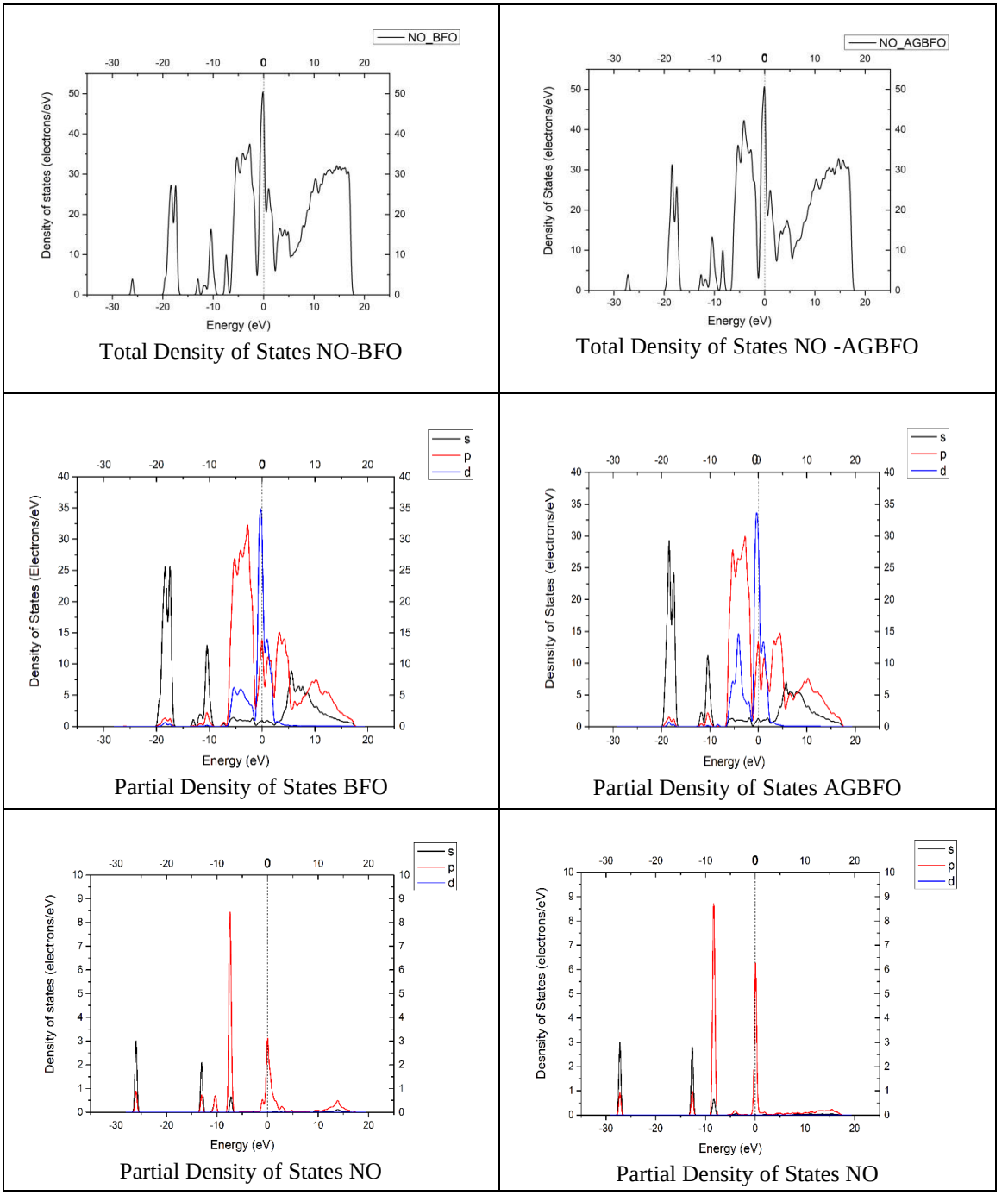

Figure 5. 11 Density of States and Partial Density of States plot to understand NO Adsorption process on BFO (010) and Ag-BFO (010) .

5.6 Electron Configuration and NO_2 Gas Sensing Mechanism

Among various nitrogen oxides, nitrogen dioxide (NO_2) is one of the most harmful air pollutants due to its toxicity and its role in forming photochemical smog and acid rain. Therefore, the detection of NO_2 at trace

concentrations is crucial for environmental monitoring and emission control. To better understand how NO_2 interacts with Bismuth Ferrite (BFO) surfaces and how doping influences its adsorption behavior, we have performed a Density Functional Theory (DFT) study on the adsorption mechanism of NO_2 on both pure and Ag-doped BFO(010) surfaces.

5.6.1 NO_2 Adsorption on BFO(010) and Ag–BFO(010) Surfaces

The optimized configurations of NO_2 adsorption are shown in Figures 5.12 and 5.13. These figures illustrate how NO_2 molecules interact differently with the pure and Ag-modified surfaces.
The calculated adsorption energies ($E_a$ds) are as follows:

BFO(010) surface: −0.29 eV

Ag–BFO(010) surface: −0.71 eV

The adsorption energy was computed using the standard relation:

$$Eads=Etot−(Esurf+Emolecule)$$

where
Etot is the total energy of the system after gas adsorption, Esurf is the total energy of the clean surface, andEmolecule is the energy of the isolated NO_2 molecule.

A negative adsorption energy indicates that the adsorption process is spontaneous and exothermic. The larger magnitude of adsorption energy in the Ag-doped system (−0.71 eV) compared to the pure BFO (−0.29 eV) clearly shows that Ag doping substantially enhances the NO_2 adsorption capability.

This enhancement suggests that the Ag dopant introduces new active sites on the surface that facilitate stronger electronic coupling between the gas molecule and the sensor material.

5.6.2 Electronic and Adsorptive Behavior: Density of States (DOS) Analysis

To further explore how adsorption influences the material's electronic behavior, the Total Density of States (TDOS) was analyzed for both the pure and Ag-doped configurations (Figure 5.14).

In the undoped BFO(010) system, the DOS near the Fermi level (E_F) is relatively sparse, indicating that few electronic states are available for interaction. Consequently, the adsorption of NO_2 induces only a moderate change in the surface's electronic structure.

After Ag doping, however, a significant increase in the TDOS near the Fermi level is observed. This means that more electronic states become available at energies close to the conduction band, enabling stronger charge transfer between the NO_2 molecule and the BFO surface.

In simpler terms, the Ag dopant enhances the surface conductivity and electronic reactivity, allowing NO_2 molecules to adsorb more effectively and produce a larger measurable electrical signal — a key requirement for a sensitive gas sensor.

5.6.3 Charge Transfer and Adsorption Mechanism

From the charge distribution and electronic structure analysis, it is evident that NO_2 acts as an electron acceptor when it interacts with both undoped and Ag-doped BFO surfaces.

During adsorption, electrons are transferred from the BFO surface to the NO_2 molecule, resulting in electron depletion near the surface and electron accumulation on the adsorbed NO_2 molecule. This process modifies the surface potential and leads to a detectable change in the resistance or current of the material.

With Ag doping, the charge transfer becomes more pronounced, as Ag atoms facilitate stronger coupling between NO_2 and the BFO lattice. The increased charge exchange enhances the material's gas-sensing response, improving both sensitivity and signal stability.

Comparison of Pure and Ag-Doped BFO for NO_2 Sensing

Property	**Pure BFO(010)**	**Ag–BFO(010)**	**Effect of Ag Doping**
Adsorption energy ($E_a$ds)	−0.29 eV	−0.71 eV	Stronger NO_2 binding
Charge transfer	Moderate	Significant	Enhanced electron exchange
DOS near Fermi level	Low	High	Increased electronic conductivity
Type of adsorption	Weak physisorption	Strong physisorption/partial chemisorption	Improved surface activity
Sensitivity	Moderate	High	Enhanced detection of NO_2

The results show that Ag doping transforms BFO into a more efficient NO_2 sensing material by increasing its adsorption strength, charge transfer rate, and electronic responsiveness. This improvement can be attributed to the introduction of Ag-related electronic states near the Fermi level, which act as active centers for gas adsorption and electron movement.

To explain this in simpler terms, when NO_2 molecules land on a pure BFO surface, they attach weakly and draw a small number of electrons, leading to a limited electrical response.

However, when Ag atoms are incorporated into the structure, they create new "sticky" spots that attract more NO_2 molecules and allow a stronger flow of electrons between the gas and the surface. This stronger interaction produces a clearer, faster, and more stable sensing signal.

Thus, Ag–BFO emerges as a promising material for the selective and sensitive detection of NO_2, which is a major pollutant in automotive and industrial emissions.

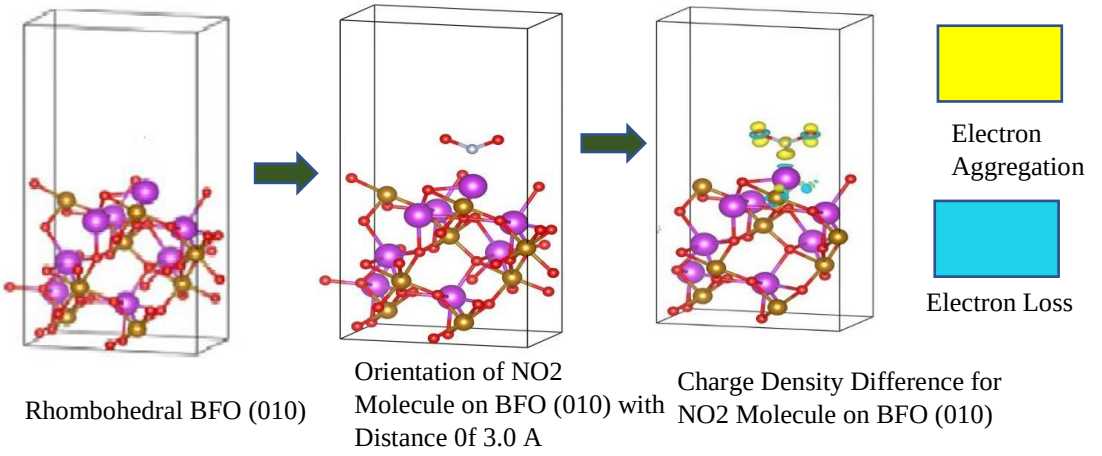

Figure 5. 12 DFT Investigation for NO_2 Gas Adsorption Mechanism on BFO

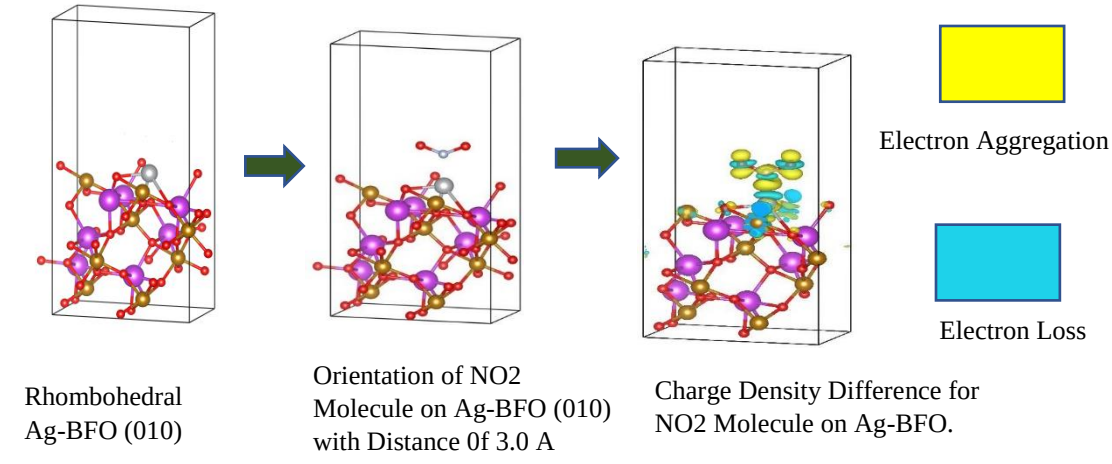

Figure 5. 13 DFT Investigation for NO_2 Gas Adsorption Mechanism on Ag Doped BFO

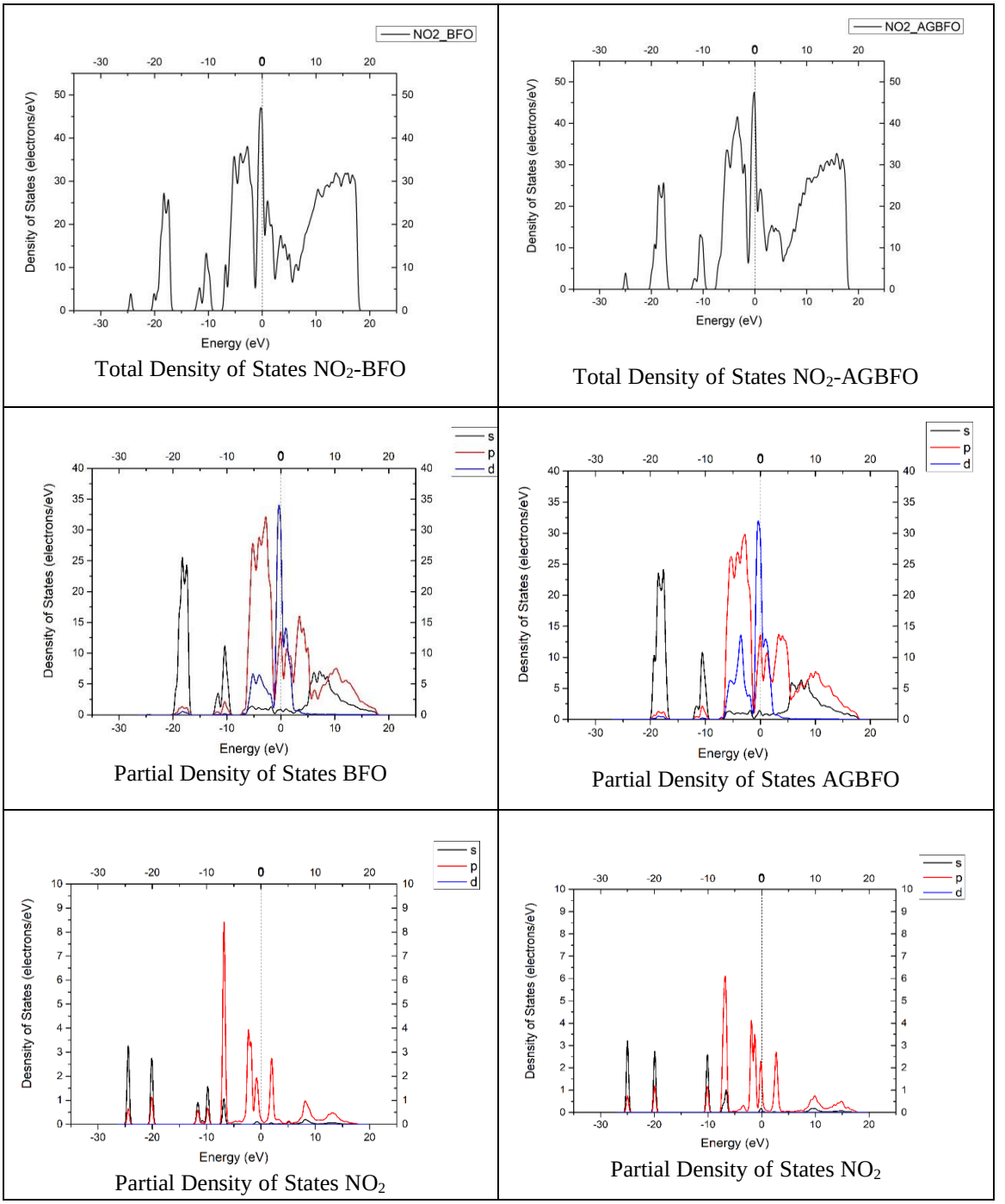

Figure 5. 14 Density of States and Partial Density of States plot to understand NO_2 Adsorption process on BFO(010) and Ag-BFO(010).

5.7 Electron Configuration and CH_4 Gas Sensing Mechanism

Methane (CH_4) is a key component of natural gas and a potent greenhouse gas. Reliable detection of CH_4 is essential in environmental monitoring, industrial safety, and combustion control. Understanding the

adsorption process of CH_4 molecules on Bismuth Ferrite (BFO) is therefore crucial for assessing its sensing performance and for improving sensor materials through metal doping.

In this section, we use Density Functional Theory (DFT) to analyze the CH_4 adsorption process on both pure BFO(010) and Ag-doped BFO(010) surfaces to clarify their electronic and adsorption behaviors.

5.7.1 CH_4 Adsorption on BFO(010) and Ag–BFO(010) Surfaces

The optimized configurations for CH_4 adsorption on both surfaces are shown in Figures 5.15 and 5.16. In these models, CH_4 molecules interact weakly with the surface atoms of BFO, primarily through van der Waals (physisorption) forces rather than chemical bonding.

The adsorption energy ($E_a$ds) was calculated using the standard expression:

$$Eads=Etot−(Esurf+Emolecule)$$

where
Etot represents the total energy of the combined CH_4–BFO system, Esurf is the total energy of the pristine or Ag-doped BFO surface, and Emolecule is the total energy of the isolated CH_4 molecule.

In contrast to gases like CO or NO_2, CH_4 exhibits very low chemical reactivity, which results in weak adsorption strength. The computed adsorption energy for CH_4 on both pure and Ag–BFO surfaces was found to be positive or slightly endothermic, indicating that the process requires small additional energy for adsorption to occur. This confirms that CH_4 interacts only weakly with the surface.

5.7.2 Electronic Structure and Density of States (DOS) Analysis

To understand how CH_4 adsorption affects the electronic structure of BFO, the Total Density of States (TDOS) and Partial Density of States (PDOS) were analyzed before and after doping (see Figure 5.17).

The TDOS plot for the pure BFO(010) surface shows minimal interaction between CH_4 molecular orbitals and the surface states. This confirms that CH_4 does not significantly alter the electronic structure of undoped BFO.

When Ag atoms are introduced into the BFO lattice, the overall electronic configuration near the Fermi level (E_F) becomes slightly more conductive. However, in this case, the TDOS peak near the Fermi level actually attenuates (reduces) upon CH_4 adsorption, indicating very weak electronic coupling between CH_4 and the Ag–BFO surface.

This behavior implies that Ag doping does not enhance CH_4 adsorption, unlike in the case of gases such as CO or NO_2. In fact, due to CH_4's non-polar nature and absence of unpaired electrons, its interaction with the perovskite surface remains dominated by weak dispersion forces rather than charge transfer.

5.7.3 Charge Difference Density and Charge Transfer

The charge density difference plots were computed to visualize the redistribution of electron density during CH_4 adsorption. These plots reveal that most of the charge redistribution is localized around the CH_4 molecule and the surface oxygen atoms of BFO(010).

When CH_4 adsorbs on the pure BFO(010) surface, only a small amount of electron density shifts occur, mainly due to weak van der Waals interactions. After Ag doping, the charge distribution pattern changes slightly, showing a minor enhancement in charge polarization near the dopant site.
However, the magnitude of charge transfer remains very small, suggesting that Ag doping has limited influence on CH_4 detection performance. This finding is further supported by the minimal variation in total charge transfer numbers obtained from DFT calculations.

5.7.4 Interpretation of CH_4 Adsorption Behavior

The results from adsorption energy, TDOS, and charge-density analyses lead to the following understanding:

Property	BFO(010)	Ag–BFO(010)	Observation
Adsorption type	Physisorption	Physisorption	Weak van der Waals interaction
Adsorption energy	Slightly positive	Slightly positive	Energy required for weak adsorption
Charge transfer	Very small	Very small	Minimal interaction with surface
TDOS near Fermi level	Low	Attenuated after adsorption	Weak coupling with CH_4 orbitals
Sensing response	Poor	Poor	Low sensitivity to CH_4 gas

From this, it is evident that CH_4 adsorption on both pure and Ag-doped BFO surfaces is weak, resulting in minimal changes in electrical conductivity. Therefore, BFO and Ag–BFO are not highly responsive toward CH_4, making them less suitable for methane detection.

This outcome aligns with experimental findings for many oxide-based sensors, which generally require catalytic activation or high-temperature operation to detect CH_4 effectively.

In simpler terms, CH_4 molecules interact weakly with both pure and Ag-doped BFO surfaces — they neither donate nor accept many electrons. While Ag doping usually improves gas sensitivity for reactive gases like CO or NO_2, it does not significantly influence CH_4 detection because methane is a chemically stable and non-reactive gas.

Thus, the BFO-based sensor shows very low sensitivity to methane, emphasizing the importance of either co-doping or surface modification strategies for enhancing CH_4 detection in future research.

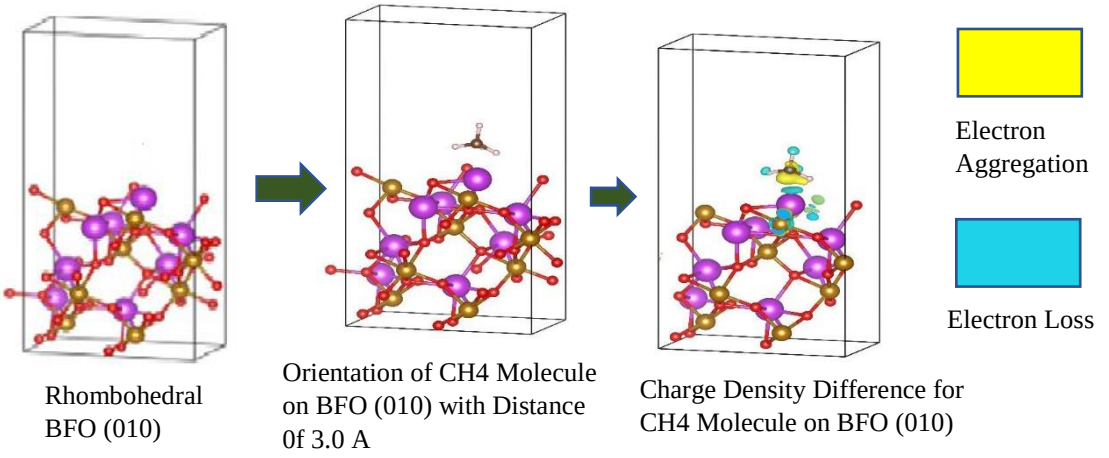

Figure 5. 15 DFT Investigation for CH_4 Gas Adsorption Mechanism on BFO

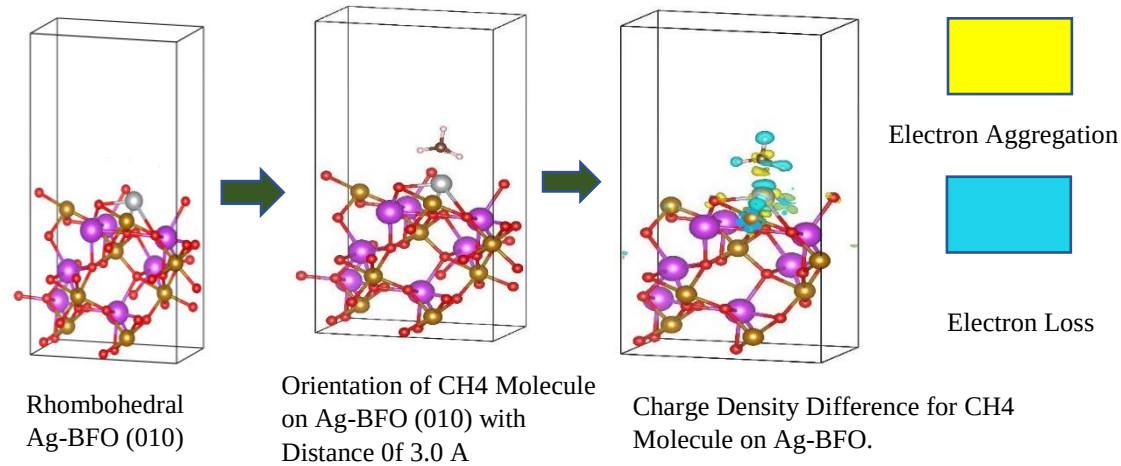

Figure 5. 16 DFT Investigation for CH_4 Gas Adsorption Mechanism on Ag Doped BFO

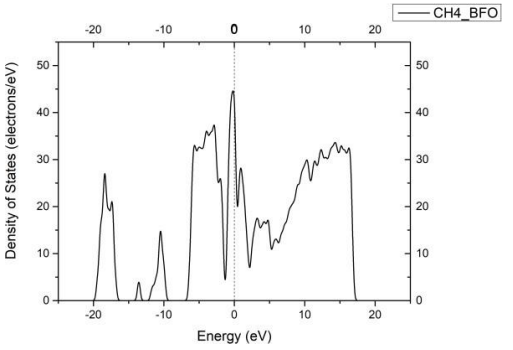

Total Density of States CH_4-BFO

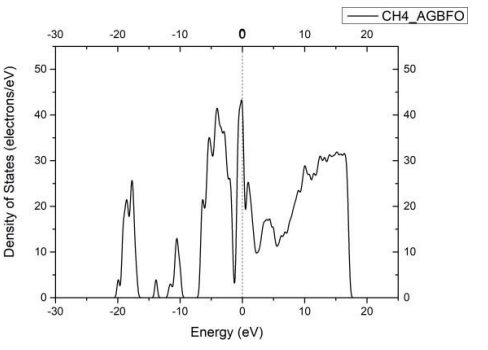

Total Density of States CH_4-AGBFO

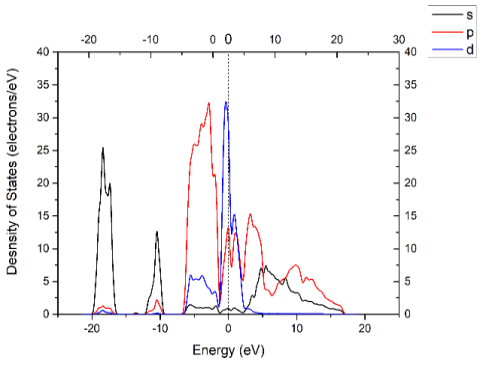

Partial Density of States BFO

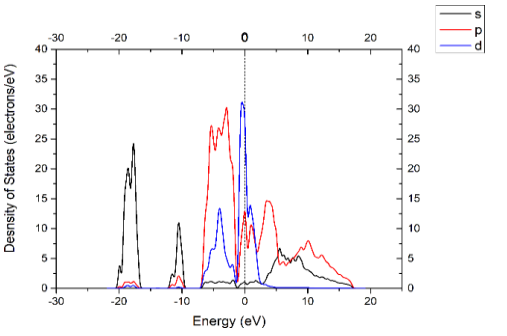

Partial Density of States AGBFO

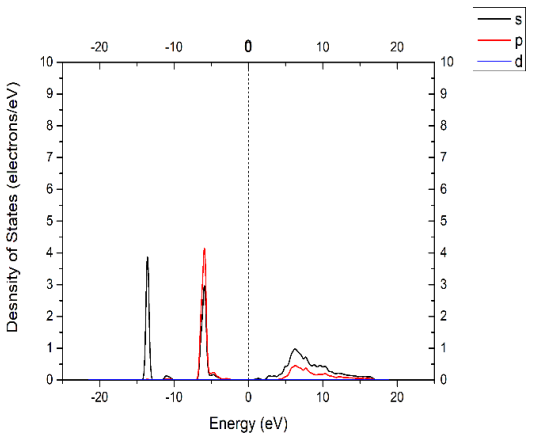

Partial Density of States CH_4

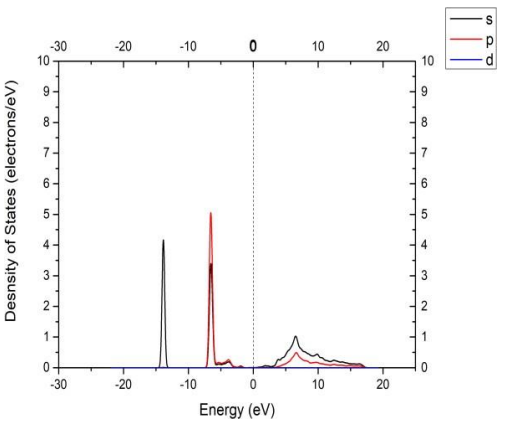

Partial Density of States CH_4

Figure 5. 17 Density of States and Partial Density of States plot to understand CH_4 Adsorption process.

Summary of Adsorption Characteristics and Electronic Behavior

To gain a comprehensive understanding of gas adsorption behavior on BFO(010) and Ag-doped BFO(010) surfaces, the Self-Consistent Field (SCF) DFT calculations were carried out for five representative gas molecules — CO, CO_2, NO, NO_2, and CH_4.

The adsorption energy ($E_a$ds), equilibrium adsorption distance, and charge transfer (ΔQ) between the gas molecule and surface were evaluated to analyze the gas–solid interactions. The results are presented in Table 5.1.

Table 5.1

Results of SCF Calculations for Gas Adsorption on BFO(010) and Ag–BFO(010) Surfaces

Gas–Surface Site	$E_a$ds (eV)	Equilibrium Distance (Å)	Charge Transfer (e^-)
CO–BFO(010)	0.52	2.32	−0.23
CO–AgBFO(010)	−0.51	2.28	−0.21
CO_2–BFO(010)	0.78	2.26	−0.31
CO_2–AgBFO(010)	−0.16	2.29	−0.24
NO–BFO(010)	−0.72	2.35	−0.22
NO–AgBFO(010)	−1.60	2.33	−0.19
NO_2–BFO(010)	−0.29	2.38	−0.26
NO_2–AgBFO(010)	−0.71	2.21	−0.27
CH_4–BFO(010)	1.92	2.66	−0.29
CH_4–AgBFO(010)	0.008	2.56	−0.23

Interpretation of Adsorption Characteristics

The results indicate that NO and NO_2 molecules exhibit the strongest adsorption affinity toward Ag–BFO surfaces, as reflected by their large negative adsorption energies (−1.60 eV and −0.71 eV, respectively). These values confirm spontaneous and stable chemisorption, suggesting that Ag doping substantially enhances the material's sensitivity toward nitrogen oxides.

In contrast, CO, CO_2, and CH_4 show weak or positive adsorption energies, indicating physisorption with negligible charge transfer. This implies that these gases interact weakly with the surface, resulting in limited sensing response — a behavior consistent with experimental observations.

The charge transfer analysis also supports this trend. Both NO and NO_2 act as electron acceptors, withdrawing charge from the Ag–BFO surface, whereas the other gases cause only minor charge redistribution. The increased charge transfer in NO/NO_2 systems leads to a stronger modulation of the material's conductivity, producing a measurable sensing signal.

Electronic Structure and Density of States (DOS) Analysis

Further insights into the gas adsorption process were obtained through the analysis of Total Density of States (TDOS) and Partial Density of States (PDOS).

Figure references from DFT results (corresponding to Figures 5.9–5.17) illustrate how the DOS changes upon adsorption:

- For NO adsorption, a new DOS peak appears near the Fermi level, indicating the creation of new electronic states associated with strong NO–surface interactions. This corresponds to enhanced electrical conductivity and higher sensitivity of Ag–BFO toward NO gas.
- In the Ag–BFO system, the TDOS curve shifts toward higher energy levels, signifying improved electronic activity. The PDOS analysis reveals that:
    - The conduction band region (−2 to 2 eV) near the Fermi level is dominated by O 2p and Ag 4d orbitals.
    - The lower conduction band (−16 to −20 eV) contains contributions from Fe 4s orbitals.
    - The Bi 6p and 6s orbitals contribute between −3 and −6 eV, forming hybridized states with oxygen.

This orbital mixing enhances electron transport between the gas molecule and surface, which is critical for sensing.

Additionally, charge-density plots show localized electron accumulation between NO molecules and Ag sites, forming spatial charge-transfer bridges that promote faster current flow. This results in:

- Reduced sensor resistance,
- Increased surface electron mobility, and
- Enhanced electrical response during gas exposure.

These phenomena explain why the Ag–BFO system demonstrates superior sensing performance toward NO and NO_2 gases compared to CO, CO_2, and CH_4.

Comparative Summary of Gas Adsorption Behavior

Gas	Interaction Type	Adsorption Strength	Charge Transfer Behavior	Sensing Response
CO	Weak physisorption	Low	Minimal	Poor
CO_2	Weak physisorption	Low	Minimal	Poor
NO	Chemisorption	High	Strong electron acceptance	Excellent
NO_2	Chemisorption	Moderate–High	Strong electron acceptance	Good
CH_4	Physisorption	Very low	Negligible	Very weak

Overall Interpretation

These DFT results establish that:

- Ag doping plays a crucial role in enhancing adsorption energy and charge transfer, particularly for nitrogen oxides (NO and NO_2).
- The increased TDOS near the Fermi level after NO adsorption directly correlates with higher conductivity, which is desirable for chemiresistive sensors.
- In contrast, nonpolar molecules (CO, CO_2, CH_4) exhibit weak interactions, making them less detectable under similar operating conditions.

Therefore, Ag–BFO emerges as a selective and thermally stable gas-sensing material, most effective for detecting nitrogen oxide pollutants in automotive exhaust environments.
In simpler terms, these results show that:

- Gases like NO and NO_2 stick strongly to Ag–BFO and draw electrons from it, causing a noticeable change in its electrical signal — ideal for sensing.
- Gases like CO, CO_2, and CH_4 barely attach and cause little to no electrical change — meaning they are harder to detect using this material.
- The Ag dopant acts as a "bridge," helping gases like NO bond better with BFO and improving overall sensitivity and selectivity.

References:

[1] D. Cortés-Arriagada, N. Villegas-Escobar, and D. E. Ortega, "Fe-doped graphene nanosheet as an adsorption platform of harmful gas molecules (CO, CO 2 , SO 2 and H 2 S), and the co-adsorption in O 2 environments," *Appl. Surf. Sci.*, vol. 427, no. 2, pp. 227–236, 2018, doi: 10.1016/j.apsusc.2017.08.216.

[2] Z. Ni, S. Bao, and X. Q. Gong, "A DFT study of the CO adsorption and oxidation at ZnO surfaces and its implication for CO detection," *Chinese Chem. Lett.*, vol. 31, no. 6, pp. 1674–1679, 2020, doi: 10.1016/j.cclet.2019.10.027.

[3] V. Nagarajan and R. Chandiramouli, "DFT investigation on structural stability, electronic properties and CO adsorption characteristics on anatase and rutile TiO2 nanostructures," *Ceram. Int.*, vol. 40, no. PB, pp. 16147–16158, 2014, doi: 10.1016/j.ceramint.2014.07.046.

[4] S. E. Mason, I. Grinberg, and A. M. Rappe, "First-principles extrapolation method for accurate CO adsorption energies on metal surfaces," *Phys. Rev. B - Condens. Matter Mater. Phys.*, vol. 69, no. 16, pp. 1–4, 2004, doi: 10.1103/PhysRevB.69.161401.

[5] H. Y. Ammar and H. M. Badran, "Effect of CO adsorption on properties of transition metal doped porphyrin: A DFT and TD-DFT study," *Heliyon*, vol. 5, no. 10, p. e02545, 2019, doi: 10.1016/j.heliyon.2019.e02545.

[6] Nugraha *et al.*, "Selectivity of CO and NO adsorption on ZnO (0002) surfaces: A DFT investigation," *Appl. Surf. Sci.*, vol. 410, no. 0002, pp. 373–382, 2017, doi: 10.1016/j.apsusc.2017.03.009.

[7] Q. Xu, M. Sobhan, F. Anariba, J. W. C. Ho, Z. Chen, and P. Wu, "Transition metal-doped BiFeO3 nanofibers: Forecasting the conductivity limit," *Phys. Chem. Chem. Phys.*, vol. 16, no. 42, pp. 23089–23095, 2014, doi: 10.1039/c4cp03045a.

[8] M. A. Ahmed, S. F. Mansour, S. I. El-Dek, and M. Abu-Abdeen, "Conduction and magnetization improvement of BiFeO3 multiferroic nanoparticles by Ag+ doping," *Mater. Res. Bull.*, vol. 49, no. 1, pp. 352–359, 2014, doi: 10.1016/j.materresbull.2013.09.011.

[9] M. Dewan and S. B. Majumder, "Selective carbon monoxide sensing properties of bismuth iron oxide," *Materialia*, vol. 7, no. February, 2019, doi: 10.1016/j.mtla.2019.100363.

[10] S. Chakraborty and M. Pal, "Highly efficient novel carbon monoxide gas sensor based on bismuth ferrite nanoparticles for environmental monitoring," *New J. Chem.*, vol. 42, no. 9, pp. 7188–7196, 2018, doi: 10.1039/c8nj01237g.

[11] G. M. Albino, O. Perales-Pérez, B. Renteria-Beleño, and Y. Cedeño-Mattei, "Kffect of Ca and Ag doping on the functional properties of BiFeO3 nanocrystalline powders and films," *Mater. Res. Soc. Symp. Proc.*, vol. 1675, pp. 105–111, 2014, doi: 10.1557/opl.2014.778.

[12] S. D. Waghmare, V. V. Jadhav, S. F. Shaikh, R. S. Mane, J. H. Rhee, and C. O'Dwyer, "Sprayed tungsten-doped and undoped bismuth ferrite nanostructured films for reducing and oxidizing gas sensor applications," *Sensors Actuators, A Phys.*, vol. 271, no. 2010, pp. 37–43, 2018, doi: 10.1016/j.sna.2018.01.008.

[13] M. Vojkovic *et al.*, "Hydrogen-Induced Adsorption of Carbon Monoxide on the Gold Dimer Cation: A Joint Experimental and DFT Investigation," *J. Phys. Chem. A*, vol. 121, no. 23, pp. 4404–4411, 2017, doi: 10.1021/acs.jpca.7b01564.

[14] O. Bludský, M. Silhan, P. Nachtigall, T. Bucko, L. Benco, and J. Hafner, "Theoretical investigation of CO interaction with copper sites in zeolites: Periodic DFT and hybrid quantum mechanical/interatomic potential function study," *J. Phys. Chem. B*, vol. 109, no. 19, pp. 9631–9638, 2005, doi: 10.1021/jp0506538.

[15] E. P. Hessou *et al.*, "Adsorption of NO, NO_2, CO, H2O and CO_2 over isolated monovalent cations in faujasite zeolite: a periodic DFT investigation," *Theor. Chem. Acc.*, vol. 137, no. 12, pp. 1–12, 2018, doi: 10.1007/s00214-018-2373-2.

[16] Y. Fan, J. Zhang, Y. Qiu, J. Zhu, Y. Zhang, and G. Hu, "A DFT study of transition metal (Fe, Co, Ni, Cu, Ag, Au, Rh, Pd, Pt and Ir)-embedded monolayer MoS2 for gas adsorption," *Comput. Mater. Sci.*, vol. 138, pp. 255–266, 2017, doi: 10.1016/j.commatsci.2017.06.029.

[17] R. Gholizadeh and Y. X. Yu, "N 2 O + CO reaction over Si- and Se-doped graphenes: An ab initio DFT study," *Appl. Surf. Sci.*, vol. 357, pp. 1187–1195, 2015, doi: 10.1016/j.apsusc.2015.09.163.

[18] R. Wanbayor and V. Ruangpornvisuti, "Adsorption of CO, H2, N2O, NH3 and CH 4 on the anatase TiO2 (0 0 1) and (1 0 1) surfaces and their competitive adsorption predicted by periodic DFT calculations," *Mater. Chem. Phys.*, vol. 124, no. 1, pp. 720–725, 2010, doi: 10.1016/j.matchemphys.2010.07.043.

[19] B. Wanno and C. Tabtimsai, "A DFT investigation of CO adsorption on VIIIB transition metal-doped graphene sheets," *Superlattices Microstruct.*, vol. 67, pp. 110–117, 2014, doi: 10.1016/j.spmi.2013.12.025.

[20] M. Gajdoš and J. Hafner, "CO adsorption on Cu(1 1 1) and Cu(0 0 1) surfaces: Improving site preference in DFT calculations," *Surf. Sci.*, vol. 590, no. 2–3, pp. 117–126, 2005, doi: 10.1016/j.susc.2005.04.047.

[21] H. Gao, W. Xu, H. He, X. Shi, X. Zhang, and K. ichi Tanaka, "DRIFTS investigation and DFT calculation of the adsorption of CO on Pt/TiO2, Pt/CeO2 and FeOx/Pt/CeO2," *Spectrochim. Acta - Part A Mol. Biomol. Spectrosc.*, vol. 71, no. 4, pp. 1193–1198, 2008, doi: 10.1016/j.saa.2008.03.036.

[22] Y. Zhicheng, Z. Xiurong, G. Kun, and D. Xunlei, "DFT investigation of adsorption of a CO molecule on small W mX n(m + n ≤ 6 , X = Cu , Mo) clusters," *Eur. Phys. J. Plus*, vol. 133, no. 11, 2018, doi: 10.1140/epjp/i2018-12314-5.

[23] M. Yang, Y. Zhang, S. Huang, H. Liu, P. Wang, and H. Tian, "Theoretical investigation of CO adsorption on TM-doped (MgO) 12 (TM = Ni, Pd, Pt) nanotubes," *Appl. Surf. Sci.*, vol. 258, no. 4, pp. 1429–1436, 2011, doi: 10.1016/j.apsusc.2011.09.097.

[24] P. Giannozzi *et al.*, "QUANTUM ESPRESSO: A modular and open-source software project for quantum simulations of materials," *J. Phys. Condens. Matter*, vol. 21, no. 39, 2009, doi: 10.1088/0953-8984/21/39/395502.

[25] N. S. Phala, G. Klatt, and E. Van Steen, "A DFT study of hydrogen and carbon monoxide chemisorption onto small gold clusters," *Chem. Phys. Lett.*, vol. 395, no. 1–3, pp. 33–37, 2004, doi: 10.1016/j.cplett.2004.07.065.

[26] X. Sun *et al.*, "Adsorption of gas molecules on graphene-like InN monolayer: A first-principle study," *Appl. Surf. Sci.*, vol. 404, pp. 291–299, 2017, doi: 10.1016/j.apsusc.2017.01.264.

Experimental Validation of Density Functional Theory Predictions: Synthesis and Characterization of Ag-Doped Bismuth Ferrite Nanostructures

6.1 Synthesis and Characterization of BFO and Ag–BFO Nanostructures

The experimental synthesis of Bismuth Ferrite (BFO) and Silver-doped Bismuth Ferrite (Ag–BFO) was performed to validate the computational predictions derived from Density Functional Theory (DFT). These materials were synthesized using the auto-combustion technique, a self-propagating exothermic process well-known for producing homogeneous, fine-grained oxide powders with high phase purity.

6.1.1 Synthesis of $Bi_{1-x}Ag_xFeO_3$ ($0 \leq x \leq 0.2$)

A series of multiferroic $Bi_{1-x}Ag_xFeO_3$ (BAFO) samples with varying Ag concentrations (x = 0, 0.05, 0.10, 0.15, and 0.20) were synthesized using the glycine-assisted auto-combustion method. Glycine was employed as both a fuel and a complexing agent, facilitating the formation of a homogeneous precursor mixture and ensuring rapid combustion during synthesis.

The starting materials were of analytical reagent grade and included:
- Bismuth nitrate [$Bi(NO_3)_3 \cdot 5H_2O$]
- Iron nitrate [$Fe(NO_3)_3 \cdot 9H_2O$]
- Silver nitrate [$AgNO_3$]

The reactants were taken in stoichiometric proportions according to the general formula $Bi_{1-x}Ag_xFeO_3$, and the glycine-to-nitrate ratio was carefully calculated using total oxidizing and reducing valencies to maintain an equivalence ratio (ϕ) = 1, ensuring maximum combustion energy release. This approach follows the thermochemical balance proposed by Ahmed et al. for urea-fueled combustion synthesis, adapted here for glycine fuel.

6.1.2 Auto-Combustion Process

The weighed nitrates and glycine were dissolved in a minimum amount of deionized water and stirred on a magnetic stirrer with gentle heating (80–90 °C) to form a uniform and transparent solution. As dehydration progressed, the solution gradually transformed into a viscous gel-like mass. Upon further heating, this viscous gel self-ignited due to the exothermic redox reaction between the nitrates (oxidizers) and glycine (fuel). The reaction was highly exothermic and spontaneous, producing a voluminous, fluffy powder within seconds.

The overall reaction can be represented schematically as:

$$Bi(NO_3)_3 + Fe(NO_3)_3 + AgNO_3 + NH_2CH_2COOH \rightarrow Bi_{1-x}Ag_xFeO_3 + N_2 + CO_2 + H_2O$$

This auto-combustion route is simple, cost-effective, and does not require external heating sources for maintaining the reaction temperature. The exothermicity of the reaction ensures uniform heating and fine

particle formation. After synthesis, the obtained powders were annealed at 550 °C for 2 hours at a heating/cooling rate of 10 °C/min to remove any residual organic content and to improve the crystallinity of the samples.

Table 6.1: Stoichiometric Quantities of Reactants Used for Synthesizing BFO and Ag–BFO Nanoparticles

Sr. No.	Bismuth Nitrate [$Bi(NO_3)_3 \cdot 5H_2O$] (g)	Iron Nitrate [$Fe(NO_3)_3 \cdot 9H_2O$] (g)	Glycine [NH_2CH_2COOH] (g)	Silver Nitrate [$AgNO_3$] (g)	Product
1	9.7014	8.08	5.06	0.000	$BiFeO_3$ (Undoped)
2	9.2160	8.08	4.99	0.1698	5% Ag-doped $BiFeO_3$
3	8.7313	8.08	4.90	0.3390	10% Ag-doped $BiFeO_3$
4	8.2462	8.08	4.83	0.5010	15% Ag-doped $BiFeO_3$

6.1.4 Significance of the Auto-Combustion Route

The auto-combustion synthesis method offers several advantages for preparing nanostructured perovskite oxides:

- Homogeneity: Molecular-level mixing ensures uniform dopant distribution within the lattice.
- Fine Particle Size: Rapid, self-propagating reaction prevents grain growth, yielding nanoscale powders.
- Low Processing Temperature: Combustion generates high localized heat, eliminating long external heating.
- High Phase Purity: Gaseous by-products (CO_2, N_2, H_2O) help maintain a single-phase perovskite structure.

6.1.5 Relevance to DFT Predictions

The synthesis of undoped and Ag-doped BFO was directly motivated by the computational DFT investigations discussed in Chapter 5. The DFT results predicted that Ag doping enhances adsorption energy and charge transfer with NO and NO_2 gases, improving sensing activity. The experimental synthesis and subsequent characterization were carried out to validate these theoretical findings, creating a bridge between computation and experiment.

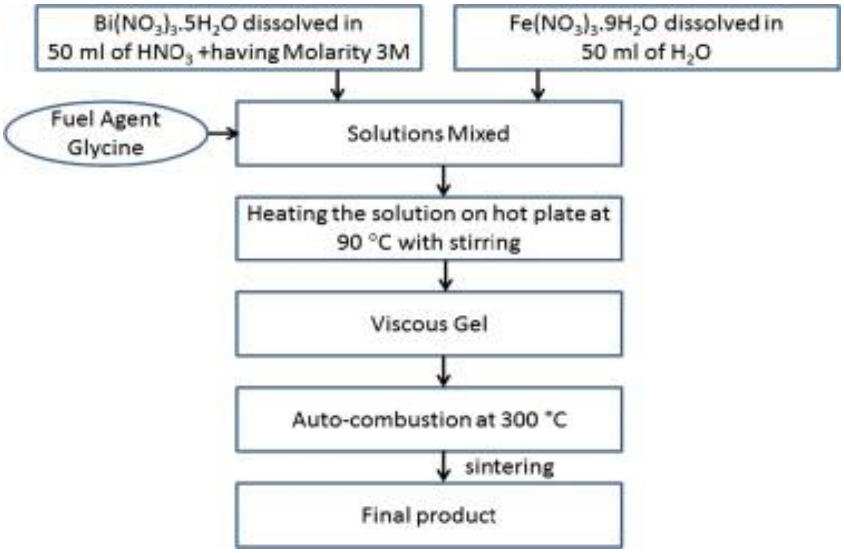

Figure 6.1: Systematic methodology for production of BFO nanoparticles using flash auto combustion method

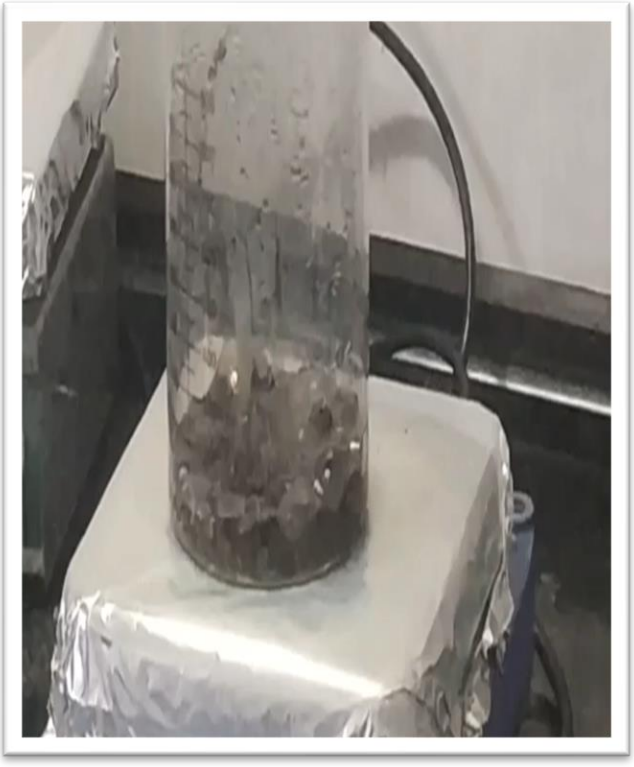

Figure 6.2: Synthesis of BFO and Ag-BFO

6.2 Structural and Spectroscopic Characterization

6.2.1 X-ray Diffraction (XRD) Analysis

The crystal structure, phase purity, and average crystallite size of the synthesized Bismuth Ferrite (BFO) and Silver-doped Bismuth Ferrite (Ag–BFO) samples were analyzed using X-ray diffraction (XRD). The XRD patterns were obtained using a Bruker D8 Advance diffractometer equipped with a Cu–Kα radiation source of wavelength λ = 1.5418 Å, operating at 40 kV and 40 mA.

The XRD spectra of pure BFO and Ag-doped BFO samples annealed at 600 °C are shown in Figure 6.3. The samples with 0 wt%, 5 wt%, 10 wt%, and 15 wt% Ag doping correspond to pure BFO, 5 wt% Ag–BFO, 10 wt% Ag–BFO, and 15 wt% Ag–BFO, respectively.

The diffraction peaks observed at 2θ = 22.5° and 32.08° correspond to the (012) and (110) planes of the rhombohedral $BiFeO_3$ phase, indexed to the JCPDS #01-073-0548 standard pattern. All samples show well-defined diffraction peaks, confirming their polycrystalline nature.

After annealing, both pure and Ag-doped BFO sensors exhibit strong and sharp peaks, indicating good crystallinity and successful formation of the perovskite $BiFeO_3$ structure. The absence of impurity peaks such as $Bi_2Fe_4O_9$ or Bi_2O_3 further confirms the phase purity of the synthesized materials.

Crystallite Size Determination

The average crystallite size (D) of the prepared samples was calculated using the Debye–Scherrer equation:

$$D=K\lambda/\beta\cos\theta$$

Where:

K = shape factor (typically 0.9),

λ=1.5418 A is the wavelength of the Cu–Kα radiation,

β = full width at half maximum (FWHM) of the diffraction peak (in radians), and

θ = Bragg diffraction angle.

Using this relation, the average crystallite sizes were calculated for different Ag doping concentrations. The obtained particle sizes were approximately 30 nm (pure BFO), 32 nm (5 wt% Ag–BFO), 30 nm (10 wt% Ag–BFO), and 33 nm (15 wt% Ag–BFO). The FWHM values of the dominant diffraction peaks were used for each sample, and the average of multiple reflections was considered to determine the mean crystallite size.

The results confirm that all annealed samples are nanocrystalline, which is advantageous for gas-sensing applications due to their high surface area and enhanced surface reactivity.

Phase Structure and Crystallinity

X-ray powder diffraction analysis revealed that all synthesized samples crystallize predominantly in a rhombohedral–hexagonal lattice structure, characteristic of the $BiFeO_3$ perovskite phase. The intense diffraction peaks signify a high degree of crystallinity, while the relatively broad and low-intensity peaks suggest the presence of nanosized grains.

Doping with silver induces slight peak broadening and intensity reduction, implying the introduction of lattice strain and microstructural distortion. Specifically, the intensity of the (012) diffraction peak decreased by approximately:

- 78% for 5 wt% Ag-doped BFO,
- 60% for 10 wt% Ag-doped BFO,
- 60% for 15 wt% Ag-doped BFO, and
- 10% for 20 wt% Ag-doped BFO.

This trend suggests that Ag atoms effectively substitute Bi^{3+} sites up to a solubility limit of around 20 wt%. Beyond this concentration, no significant structural changes were observed, indicating that the BFO lattice reaches a saturation point for Ag incorporation.

Such intensity attenuation can be attributed to the attenuation of X-ray signals by Ag molecules and the associated defect formation, which collectively influence the microstructure. However, the persistence of the main rhombohedral peaks confirms that the crystal symmetry remains intact across all doping concentrations.

Summary of Observations

- All synthesized samples exhibit rhombohedral perovskite structure without secondary phases.
- The average crystallite size lies between 30–33 nm, confirming the nanocrystalline nature of the annealed films.
- Ag doping introduces slight lattice distortions and peak intensity reductions, enhancing surface defect density — beneficial for gas adsorption and charge transfer processes in sensing applications.
- The structural data strongly support the computational findings from DFT simulations, which predicted improved adsorption and charge transfer upon Ag doping.

6.2.2 Scanning Electron Microscopy (SEM) Analysis

The surface morphology and microstructural characteristics of the synthesized BFO and Ag-doped BFO thick film sensors were examined using Scanning Electron Microscopy (SEM).

The micrographs were obtained using a JEOL JSM–6390LV scanning electron microscope, operated under high-vacuum mode. The SEM images of pure BFO and Ag-doped BFO samples with varying silver concentrations (5 wt%, 10 wt%, and 15 wt%) are presented in Figures 6.4 to 6.7.

Microstructural Observations

The SEM micrographs clearly reveal that all samples exhibit a highly porous surface morphology, which is highly desirable for gas-sensing applications. The porous network facilitates effective gas diffusion and adsorption by providing a larger number of active surface sites for gas–solid interactions. The high surface-to-volume ratio, arising from the nanoscale grains and interconnected pores, enhances the sensitivity and response speed of the sensors.

The pore walls and grain boundaries are regions with high atomic activity, allowing rapid charge transfer during gas exposure. This observation aligns with earlier studies [4], where materials with highly porous morphologies demonstrated superior gas-sensing performance due to the enhanced exposure of adsorption sites to the ambient chemical environment.

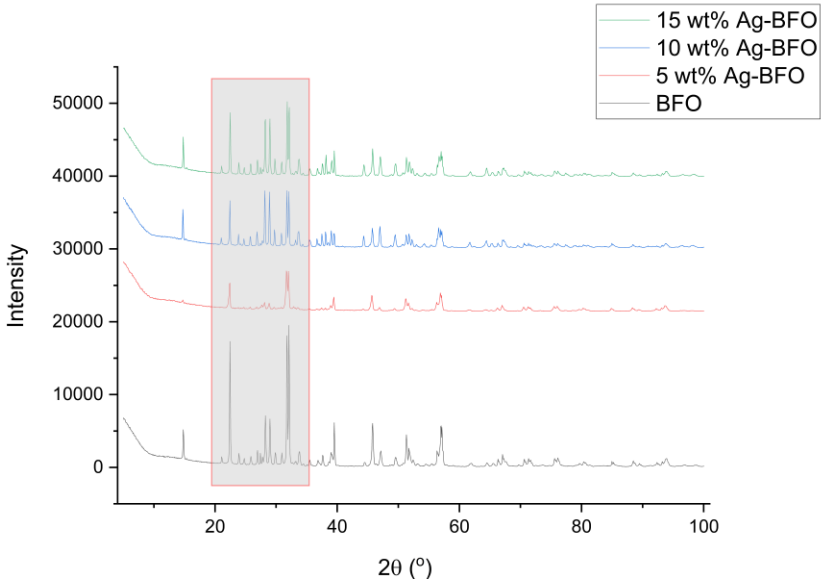

Figure 6.3: XRD spectra of undoped and Ag-doped $BiFeO_3$ nanostructures annealed at 600 °C showing indexed diffraction peaks corresponding to the rhombohedral phase (JCPDS # 01-073-0548).

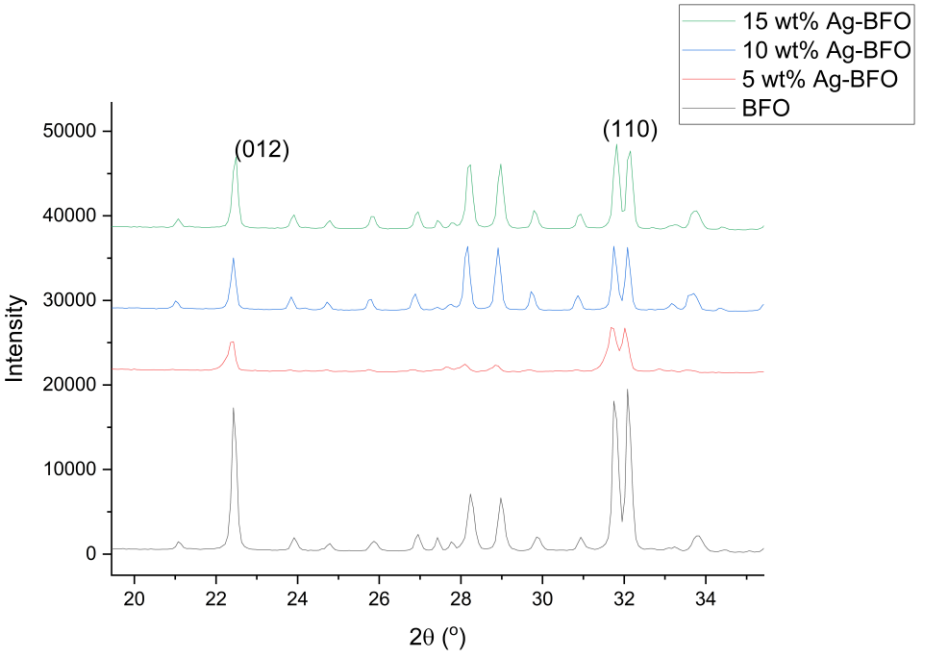

Figure 6.3: Magnified XRD plot of BFO and Ag-BFO

Grain Size and Morphology

The SEM images reveal small variations in grain size compared to the average crystallite sizes estimated from XRD analysis. While XRD determines the *average crystallite size* based on coherent scattering domains, SEM provides a *visual assessment* of grain aggregates on the surface. These differences arise due to grain coalescence and agglomeration, as evident in the micrographs, where several nanosized grains cluster to form larger spherical or flake-like aggregates.

At higher magnifications (Figures 6.4–6.7), the BFO and Ag–BFO nanoparticles exhibit hexagonal flake-like structures with partial aggregation. This aggregation is likely induced by magnetic dipole–dipole interactions between the ferrite nanoparticles, which is typical for magnetically active materials such as $BiFeO_3$.Since the synthesis was performed under surfactant-free conditions, particle stabilization during growth was limited, leading to the observed agglomeration.

Effect of Silver Doping and Calcination Temperature

Among the doped samples, the x = 0.10 (10 wt% Ag–BFO) composition exhibits more uniform grains and a preferential grain growth direction, indicating improved crystallinity and lattice ordering.The SEM micrographs also reveal that grain size and porosity increase with calcination temperature, as thermal energy promotes grain coalescence and the removal of residual organic compounds.This leads to better crystal growth, more pronounced grain boundaries, and the formation of open-pore networks across the surface.

Additionally, with increasing silver content, slight changes in surface texture and pore density are noticeable, confirming that Ag doping influences grain boundary mobility during thermal treatment. These structural modifications are expected to play a significant role in enhancing adsorption efficiency and gas-sensing activity, as discussed in later sections.

6.2.3 Energy Dispersive X-ray Spectroscopy (EDS) Analysis

To confirm the elemental composition and chemical purity of the synthesized BFO and Ag-doped BFO thick film sensors, Energy Dispersive X-ray Spectroscopy (EDS) was performed.The spectra were recorded using an EDS detector attached to the JEOL JSM–6390LV Scanning Electron Microscope, operating at an accelerating voltage of 15–20 kV. The analysis provides qualitative and semi-quantitative identification of elements present in the samples.

Elemental Composition

Figure 6.8 shows the EDS spectrum of the pure $BiFeO_3$ (BFO) thick film sensor annealed at 600 °C. The spectrum confirms the presence of only bismuth (Bi), iron (Fe), and oxygen (O), which correspond to the expected stoichiometric composition of $BiFeO_3$. The absence of extraneous peaks indicates that the material is chemically pure and that no secondary impurity phases were formed during the auto-combustion and annealing processes.

Figure 6.9 displays the EDS spectrum of the 1.5 wt% Ag-doped $BiFeO_3$ thick film sensor, also annealed at 600 °C. In addition to the Bi, Fe, and O peaks observed in pure BFO, the appearance of a distinct Ag peak confirms the successful incorporation of silver atoms into the BFO lattice.The relative intensity of the Ag peak corresponds to the nominal doping concentration, verifying the controlled and uniform distribution of silver within the sample.

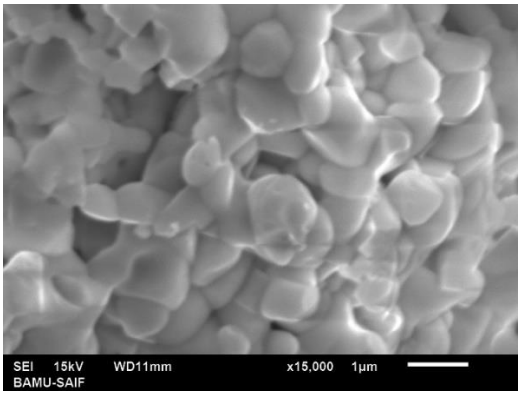

Figure 6.4: SEM Image for Bismuth Ferrite Oxide (BiFeO3)

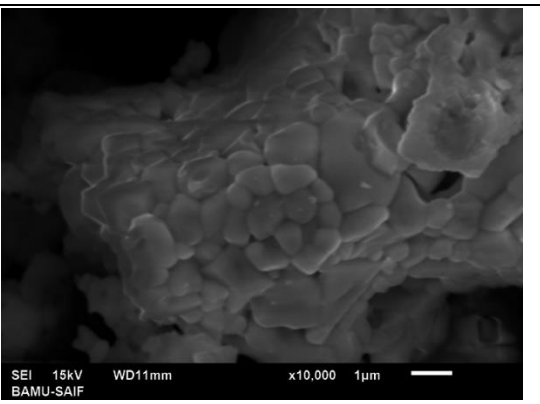

Figure 6.5: SEM Image for 5 % wt Ag Doped BiFeO3

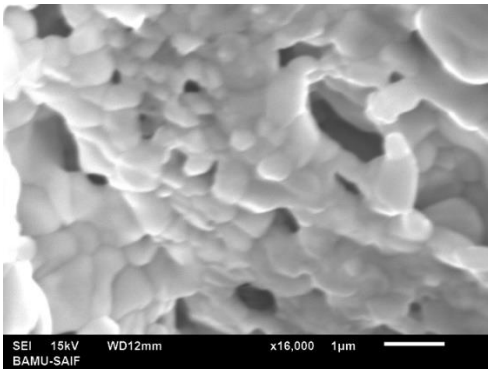

Figure 6.6: SEM Image for 10 % wt Ag Doped BiFeO3

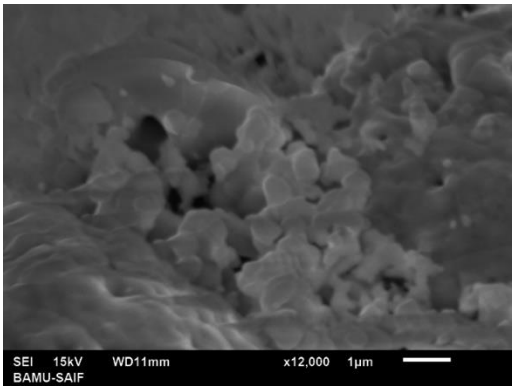

Figure 6.7: SEM Image for 15 % wt Ag Doped BiFeO3

Figure 6.4–6.7 – *SEM micrographs of pure and Ag-doped $BiFeO_3$ thick film sensors (5 wt%, 10 wt%, and 15 wt%) recorded using a JEOL JSM–6390LV scanning electron microscope, showing porous microstructure and nanocrystalline morphology conducive for gas adsorption.*

Discussion and Interpretation

The EDS analysis supports the XRD findings, confirming that Ag doping does not alter the primary perovskite phase of $BiFeO_3$. Instead, the Ag atoms are likely substituted at Bi^{3+} lattice sites or occupy interstitial positions, causing minimal structural distortion.

Furthermore, the absence of unwanted peaks such as carbon or nitrogen demonstrates that all organic residues and precursor remnants were completely removed during calcination, indicating the success of the auto-combustion synthesis route.

The combination of XRD, SEM, and EDS analyses thus provides a comprehensive understanding of the phase purity, surface morphology, and chemical composition of the prepared samples. The EDS spectra

conclusively validate that the synthesized Ag–BFO nanostructures are chemically homogeneous and compositionally accurate, serving as reliable materials for gas-sensing applications.

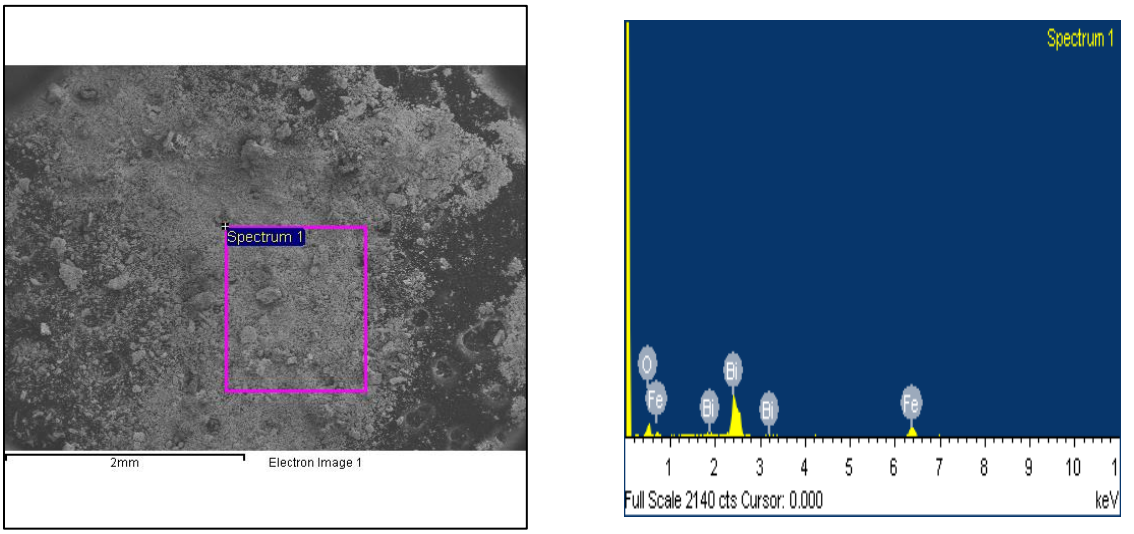

Figure 6.8: EDS for BiFeO3

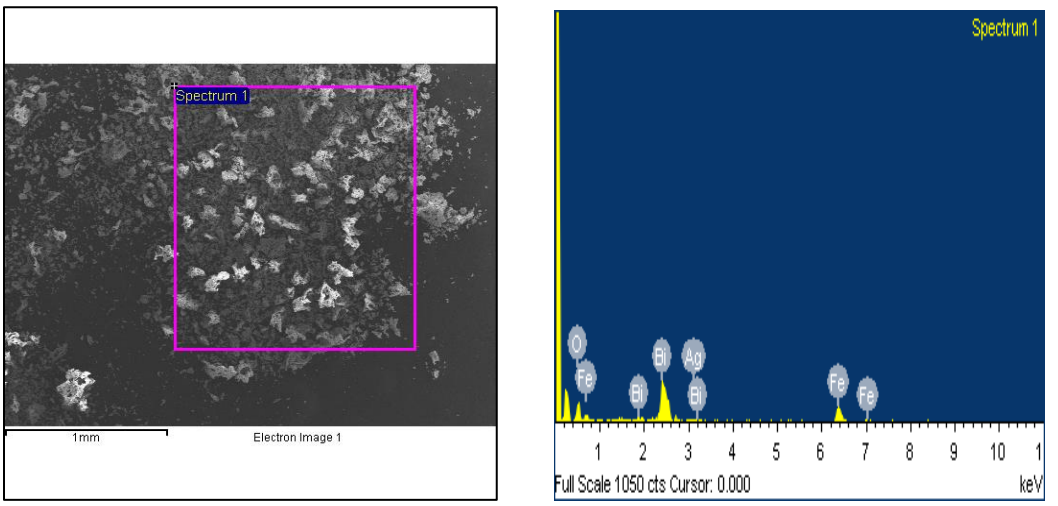

Figure 6.9: EDS for Ag-BiFeO3

6.2.4 Fourier Transform Infrared (FTIR) Spectroscopy Analysis

The Fourier Transform Infrared (FTIR) spectra of pure and Ag-doped $BiFeO_3$ (BFO) samples were recorded in the wavenumber range 500–4000 cm^{-1}, as shown in Figure 6.10. The spectra provide insights into the vibrational modes, bonding characteristics, and structural integrity of the synthesized perovskite materials.

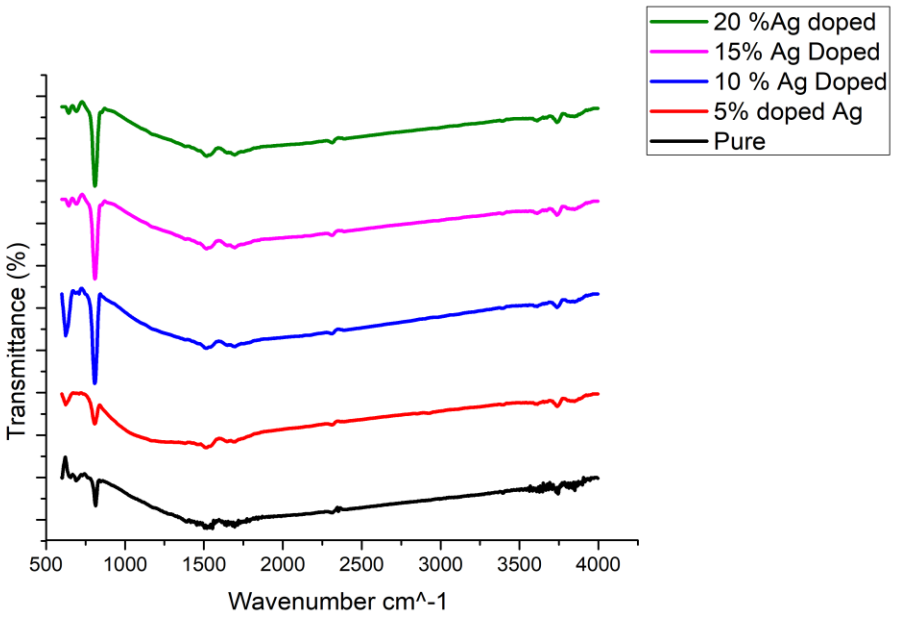

Figure 6.10: *FTIR spectra of pure and Ag-doped $BiFeO_3$ (BFO) nanoparticles showing characteristic Fe–O and Bi–O vibrational modes in the 500–600 cm^{-1} range and O–H stretching bands near 3400 cm^{-1}.*

Spectral Features

All samples—pure BFO and Ag-doped BFO with 5 wt%, 10 wt%, 15 wt%, and 20 wt% Ag—exhibit characteristic absorption peaks corresponding to the metal–oxygen stretching vibrations and lattice phonon modes of the $BiFeO_3$ perovskite structure.

- The strong absorption bands observed around 550–600 cm^{-1} are attributed to Fe–O stretching vibrations within the FeO_6 octahedra, confirming the formation of the perovskite $BiFeO_3$ phase.
- The weaker bands in the 850–950 cm^{-1} region correspond to Bi–O bond vibrations, reflecting the presence of bismuth–oxygen polyhedra in the crystal lattice.
- The broad band appearing near 3400 cm^{-1} and the small absorption near 1600 cm^{-1} are associated with O–H stretching and bending vibrations, respectively. These arise from adsorbed water molecules or residual hydroxyl groups on the surface of the samples.

Effect of Silver Doping

With increasing Ag doping concentration, the intensity and position of the characteristic Fe–O and Bi–O bands show slight shifts and broadening, indicating lattice distortion and local structural rearrangements due to Ag substitution. This suggests that Ag ions are effectively incorporated into the $BiFeO_3$ lattice, possibly replacing Bi^{3+} ions or occupying interstitial positions, leading to small variations in bond lengths and force constants.

Notably:

- The band around 550 cm^{-1} slightly shifts toward lower wavenumbers with increasing Ag content, confirming weaker Fe–O bonding due to lattice expansion.

- The increase in transmittance for higher Ag doping levels (especially 15–20 wt%) indicates enhanced optical transparency, consistent with improved crystallinity observed in XRD results.
- These modifications in the FTIR spectra corroborate the successful doping of Ag and the stabilization of the perovskite structure, further supported by the XRD and EDS analyses.

Interpretation and Correlation

The observed IR bands are consistent with previous reports on $BiFeO_3$-based perovskites, confirming that the samples retain their rhombohedral structure after doping. The shift in vibrational frequencies upon Ag incorporation supports the DFT predictions of altered electronic and local bonding environments, which are expected to influence gas adsorption and sensing behavior.

Thus, FTIR spectroscopy validates that the Ag doping process induces subtle structural distortions without compromising the overall phase stability of $BiFeO_3$, an important criterion for reliable high-temperature gas-sensing operation.

6.3 Gas Sensors Based on Pristine $BiFeO_3$

6.3.1 CO Gas Sensing Mechanism

The gas-sensing performance of pristine $BiFeO_3$ (BFO) thin film sensors was evaluated toward carbon monoxide (CO) gas in the temperature range of 100–350 °C at a constant 10 ppm concentration. The sensor's behavior was quantified in terms of normalized resistance as a function of time.

The normalized resistance (R_n) is defined as:

- $R_n = (R\_gas - R\_air) / R\_air$

where: R_gas is the sensor resistance in the presence of CO gas, and R_air is the baseline resistance of the sensor in air (before gas exposure).

Temperature-Dependent Response

Figures 6.11 to 6.16 show the normalized resistance versus time plots of the BFO sensor when exposed to 10 ppm of CO gas at different operating temperatures. The response and recovery dynamics of the sensor were analyzed from these time–response curves.

Response time (τ_s): Time required for the sensor signal to reach 90% of its maximum value after gas exposure.
Recovery time (τ_r): Time taken for the sensor signal to return to 10% of its original baseline once the gas is removed.

Optimal Operating Temperature

The temperature–sensitivity profile of the sensor is illustrated in Figure 6.21, which shows the variation in sensor response to 10 ppm CO as a function of temperature. The highest normalized resistance value of 1.6 was observed at 300 °C, corresponding to the optimal temperature. At this point, the response time was approximately 68 seconds, while the recovery time was about 2.93 minutes, indicating efficient gas adsorption and desorption kinetics.

Concentration-Dependent Response

At the optimized operating temperature of 300 °C, the sensor's response was further studied for varying CO concentrations ranging from 5 ppm to 40 ppm. The normalized resistance increased linearly with increasing gas concentration, as depicted in Figures 6.17 to 6.20.

Mechanistic Interpretation

The sensing mechanism of CO detection in BFO can be explained based on surface chemisorption and electron exchange processes. In air, oxygen molecules are adsorbed on the BFO surface and ionized to form negatively charged species (O^-, O_2^-, O^{2-}) by capturing electrons from the conduction band, resulting in a depletion layer and increased resistance.

Upon exposure to CO gas, the reaction:

- $CO(gas) + O^-(ads) \rightarrow CO_2(gas) + e^-$

releases electrons back into the conduction band, decreasing resistance. The magnitude of this resistance change is directly proportional to the surface reactivity and the concentration of CO molecules.

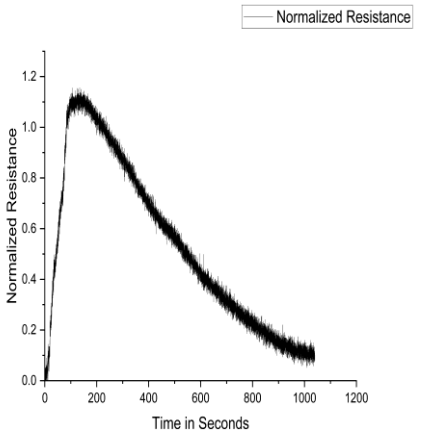

Figure 6.11: 10 ppm CO on BFO at 100

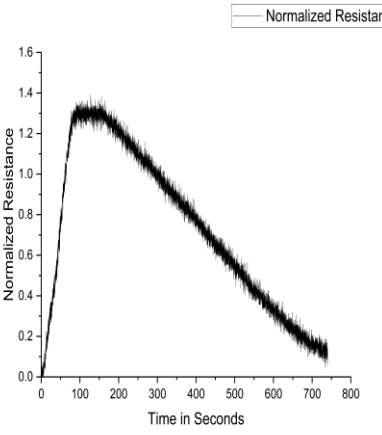

Figure 6.12: 10 ppm CO on BFO at 150

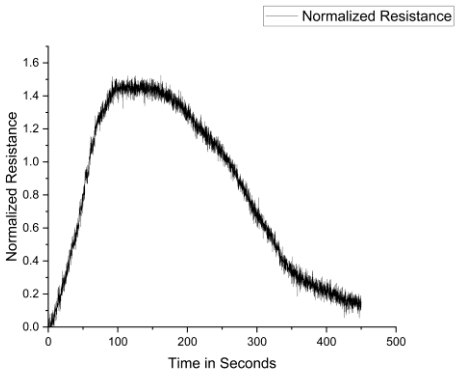

Figure 6.13: 10 ppm CO on BFO at 200 C

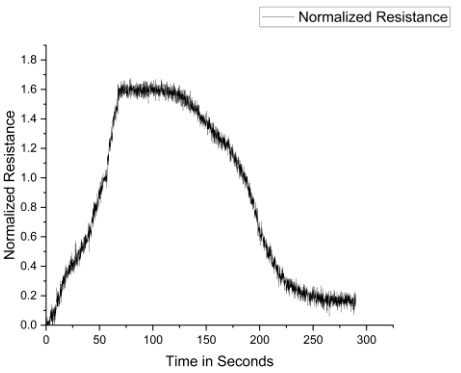

Figure 6.14: 10 ppm CO on BFO at 250 C

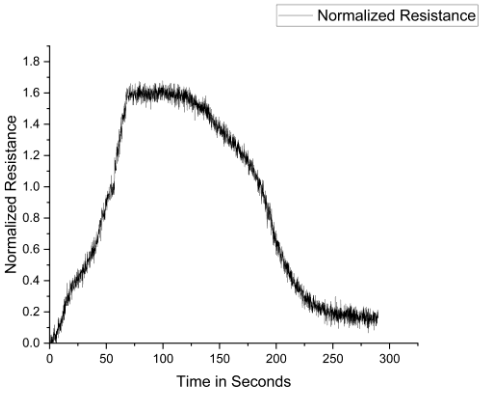

Figure 6.15: 10 ppm CO on BFO at 300 C

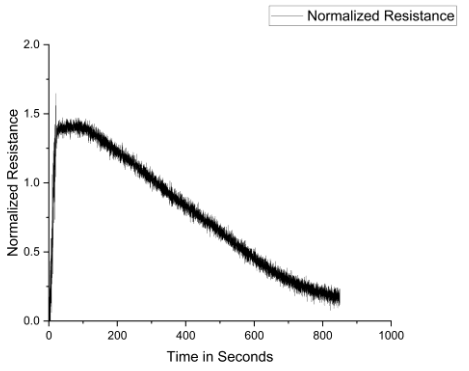

Figure 6.16: 10 ppm CO on BFO at 350 C

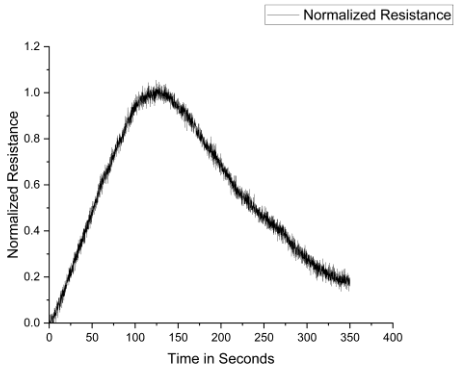

Figure 6.17: 5 PPM CO on Pristine BFO at 300 C

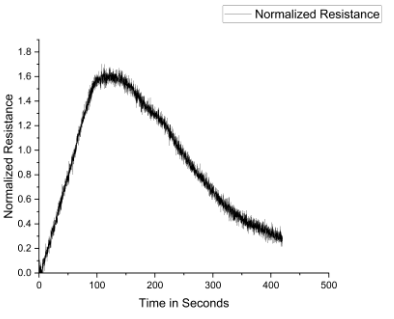

Figure 6.18: 10 PPM CO on Pristine BFO at 300 C

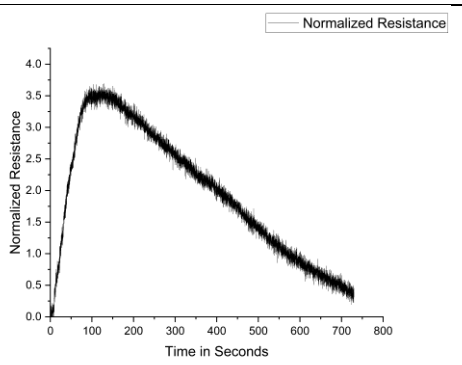

Figure 6.19: 20 PPM CO on Pristine BFO at 300 C

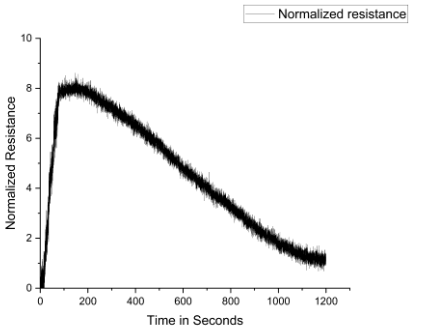

Figure 6.20: 40 PPM CO on Pristine BFO at 300 C

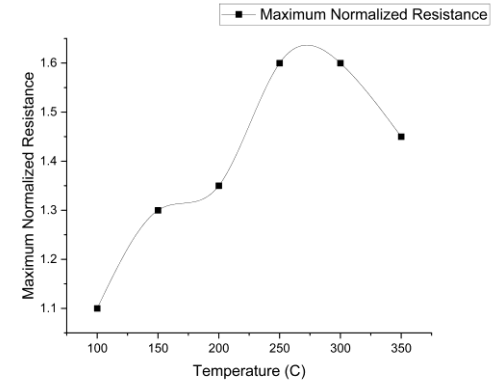

Figure 6.21: Temperature Vs Maximum Normalized Resistance for CO on Pristine BFO

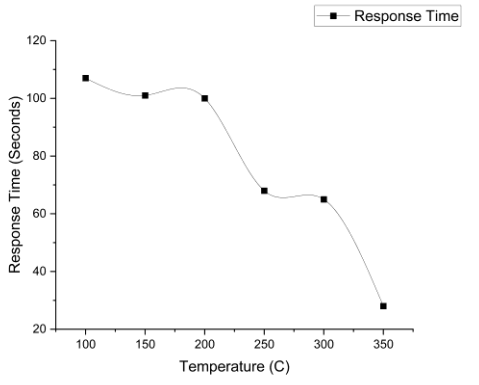

Figure 6.22: Temperature vs Response time for CO gas sensing on Pristine BFO

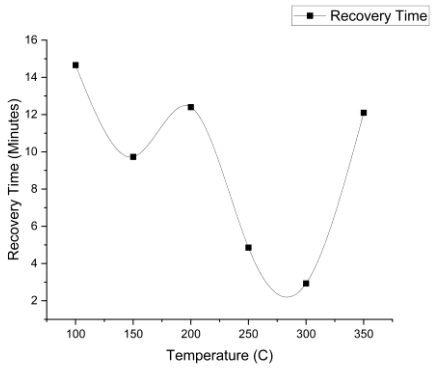

Figure 6.23: Temperature Vs Recovery Time for CO gas sensing on Pristine BFO

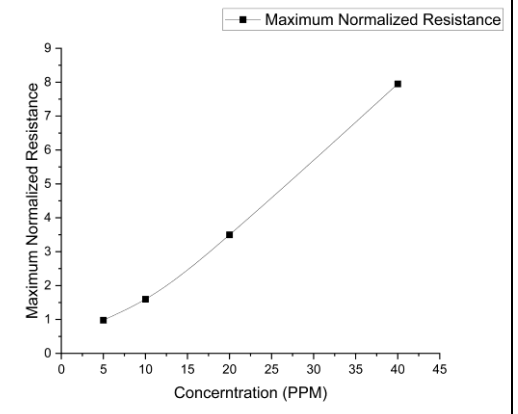

Figure 6.24: Concentration (PPM) Vs Maximum Normalized Resistance for CO gas sensing on Pristine BFO

Figure 6. 25 XXX

6.3.2 NO Gas Sensing Mechanism

The gas-sensing behavior of the pristine $BiFeO_3$ (BFO) thin film sensor was further investigated toward nitric oxide (NO) gas. The experiments were performed over a temperature range of 100–350 °C and gas concentrations between 10 ppm and 100 ppm. The variation in the sensor's resistance upon exposure to NO gas was expressed as normalized resistance with respect to time.

The normalized resistance (R_n) is calculated as:

- $R_n = (R\_gas - R\_air) / R\_air$

where: R_gas is the resistance of the sensor in the presence of NO gas, and R_air is the baseline resistance of the sensor in ambient air before gas exposure.

Temperature-Dependent Response

Figures 6.26–6.31 illustrate the time-dependent normalized resistance curves of the BFO thin film sensor at different operating temperatures under a fixed NO concentration. The response and recovery characteristics were determined from these dynamic curves.

Response time (τ_s): Time taken for the sensor to reach 90% of its maximum response value after exposure to the gas.
Recovery time (τ_r): Time required for the sensor to return to 10% of its baseline value after the removal of the gas.

Optimal Operating Temperature

The variation of sensitivity versus temperature is presented in Figure 6.36, where sensitivity is defined as the maximum normalized response obtained at each temperature from Figures 6.26–6.31. The optimal operating temperature is determined to be 200 °C, as it provides the best balance between response magnitude and dynamic stability.

At this temperature, the BFO thin film exhibited:

- Maximum normalized resistance: 3.3%
- Response time: 136 seconds
- Recovery time: 4.86 minutes

Concentration-Dependent Response

Further tests were conducted at the optimal temperature (200 °C) for varying NO concentrations between 5 ppm and 40 ppm. As shown in Figures 6.32–6.35, the normalized resistance increased proportionally with the gas concentration, indicating a linear sensor response.

At 5 ppm, the maximum normalized resistance was 2.4, and at 40 ppm, the maximum normalized resistance reached 12.1. This linear behavior confirms that pristine BFO exhibits excellent repeatability and proportionality between gas concentration and resistance change, an essential feature for quantitative NO detection. The overall dependence of maximum normalized resistance on gas concentration is summarized in Figure 6.39.

Mechanistic Interpretation

The sensing mechanism for NO detection in pristine BFO follows the surface reaction and charge transfer model, similar to other n-type metal oxides. When exposed to air, oxygen molecules are adsorbed onto the BFO surface and ionized, forming oxygen species such as O^-, O_2^-, and O^{2-} by trapping electrons from the conduction band. This process increases surface resistance.

Upon exposure to NO gas, the following reactions occur:

- $NO(g) + O^-(ads) \rightarrow NO_2 + e^-$
- $NO(g) + O_2^-(ads) \rightarrow NO_2 + 2e^-$

These reactions release electrons back into the conduction band, decreasing the depletion width and altering the overall resistance of the film. At 200 °C, these redox reactions are most efficient, leading to optimal sensitivity and faster sensor dynamics

- The pristine BFO thin film exhibits reliable NO gas detection capability within the studied temperature range.
- Maximum response was achieved at 200 °C, with an efficient balance between sensitivity and response/recovery dynamics.
- The sensor shows a linear correlation between concentration and normalized resistance, confirming its reproducibility and quantitative reliability.
- The underlying mechanism involves electron exchange between surface-adsorbed oxygen species and incoming NO molecules.

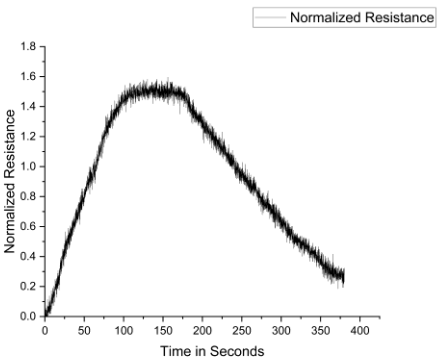

Figure 6.26: 10 ppm NO on BFO at 100 C

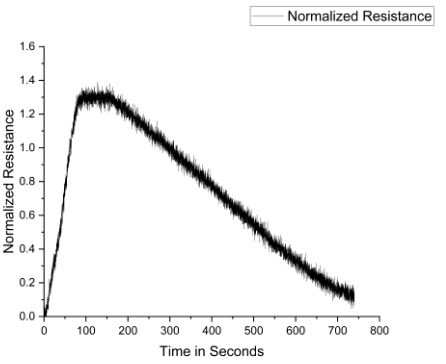

Figure 6.27: 10 ppm NO on BFO at 150 C

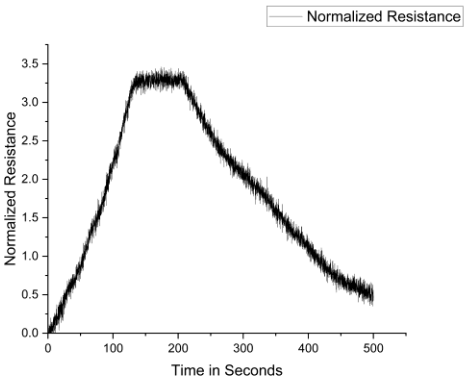

Figure 6.28: 10 ppm NO on BFO at 200 C

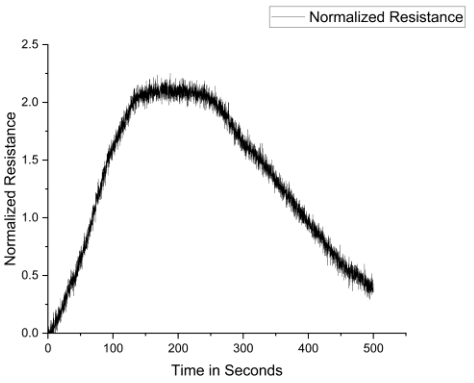

Figure 6.29: 10 ppm NO on BFO at 250 C

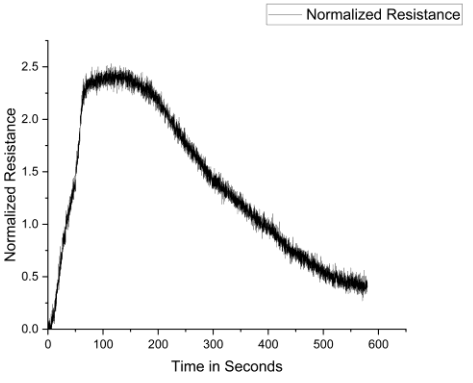

Figure 6.30: 10 ppm NO on BFO at 300 C

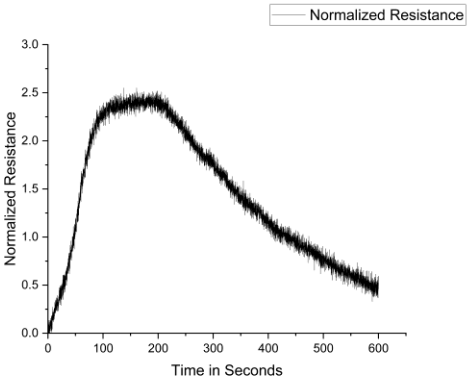

Figure 6.31: 10 ppm NO on BFO at 350 C

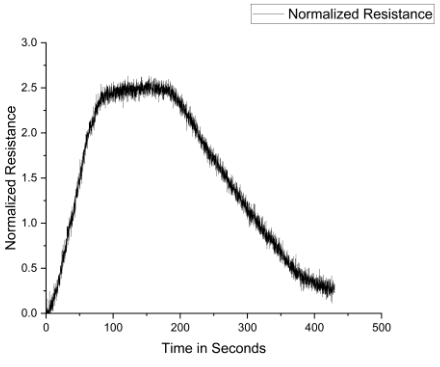

Figure 6.32: 5 PPM NO gas sensing on Pristine BFO at 200 C

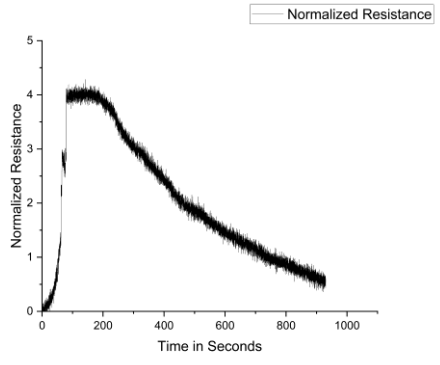

Figure 6.33: 10 PPM NO gas sensing on Pristine BFO at 200 C

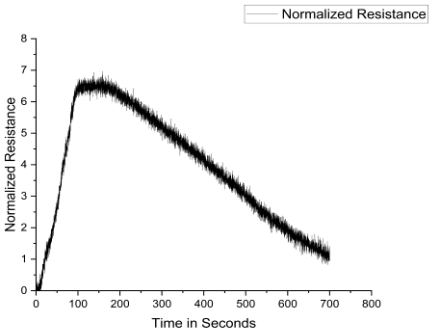

Figure 6.34: 20 PPM NO gas sensing on Pristine BFO at 200 C

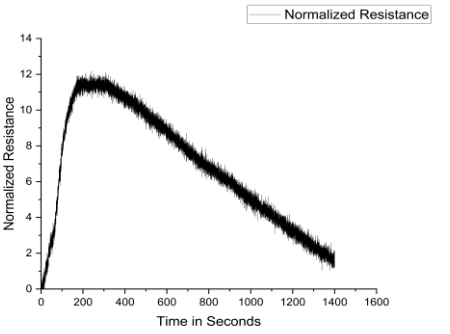

Figure 6.35: 40 PPM NO gas sensing on Pristine BFO at 200 C

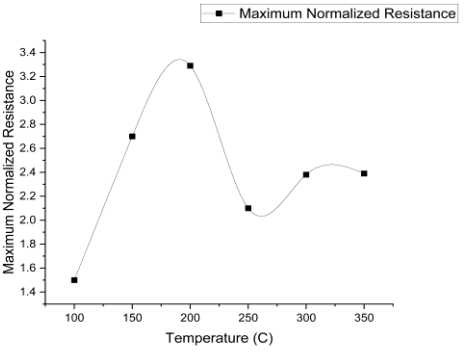

Figure 6.36: Temperature Vs Maximum Normalized Resistance for NO gas sensing on Pristine BFO

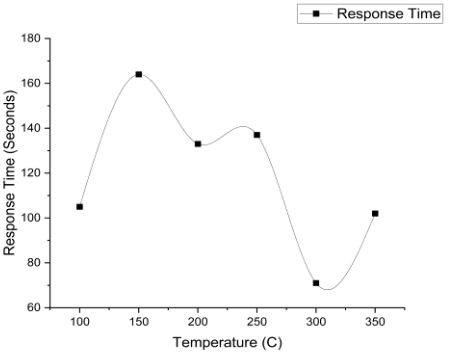

Figure 6.37: Temperature Vs Response Time for NO gas sensing on Pristine BFO.

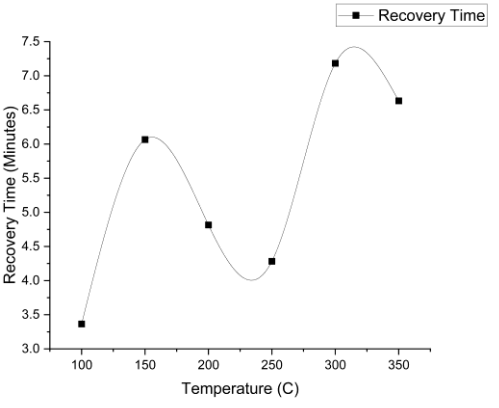

Figure 6.38: Temperature Vs Recovery Time for NO gas sensing on Pristine BFO

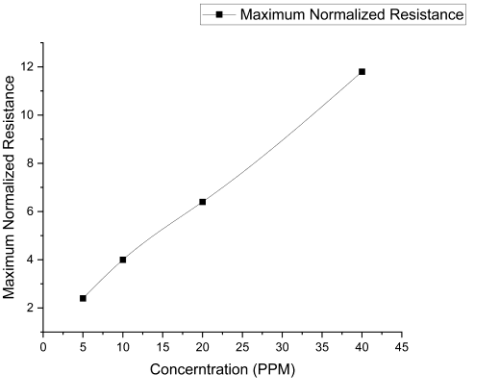

Figure 6.39: NO gas Concentration (PPM) Vs Maximized Normalized Resistance for NO gas sensing on Pristine BFO

6.3.3 NO_2 Gas Sensing Mechanism

The response characteristics of the pristine $BiFeO_3$ (BFO) thin film sensor were further investigated for nitrogen dioxide (NO_2) gas. Experiments were performed at a constant gas concentration of 10 ppm, while varying the operating temperature from 100 °C to 350 °C. The sensor's performance was quantified in terms of normalized resistance as a function of time.

The normalized resistance (R_n) is expressed as:

- $R_n = (R\_gas - R\_air) / R\_air$

where: R_gas represents the resistance of the sensor in the presence of NO_2 gas, and R_air represents the resistance of the sensor in ambient air before gas exposure.

Temperature-Dependent Response

Figures 6.40–6.45 illustrate the normalized resistance versus time characteristics of the BFO thin film sensor at various operating temperatures for a constant 10 ppm NO_2 gas concentration. From these plots, the response time (τ_s) and recovery time (τ_r) were determined.

- Response time (τ_s): The time required for the sensor signal to reach 90% of its maximum value upon gas exposure.
- Recovery time (τ_r): The time required for the sensor signal to return to 10% of its baseline after the gas is removed.

The variation in sensor response with temperature is shown in Figure 6.50. As observed, the response increases steadily with temperature and reaches its peak at 300 °C, after which it begins to decline. This indicates that moderate temperatures enhance the adsorption of NO_2 molecules, while excessively high temperatures lead to rapid desorption, lowering the effective response.

Optimal Operating Temperature

The temperature-dependent response curve in Figure 6.50 identifies 300 °C as the optimal operating temperature. At this temperature, the BFO thin film sensor exhibits the best trade-off between sensitivity and dynamic stability.

At 300 °C, the sensor demonstrated the following performance metrics:

- Maximum normalized resistance: Highest response to 10 ppm NO_2 gas.
- Response time: 65 seconds.
- Recovery time: 7 minutes.

The response and recovery curves corresponding to different temperatures are depicted in Figures 6.51 and 6.52, showing rapid adsorption and slower desorption kinetics typical of p-type semiconducting oxides exposed to oxidizing gases such as NO_2.

Concentration-Dependent Response

To further evaluate the concentration sensitivity of the BFO sensor, measurements were carried out at the optimal temperature (300 °C) for varying NO_2 gas concentrations between 5 ppm and 40 ppm.

At 5 ppm, the maximum normalized resistance was 1.05, and at 40 ppm, the maximum normalized resistance increased to 2.65. This demonstrates a positive correlation between gas concentration and resistance, as shown in Figures 6.46–6.49. The variation of maximum normalized resistance with gas concentration is summarized in Figure 6.53, revealing a nearly linear trend, confirming the quantitative sensing capability of the pristine BFO thin film.

Mechanistic Interpretation

The NO_2 sensing mechanism in BFO follows the typical surface reaction and charge exchange model observed in p-type oxide semiconductors. When the sensor is exposed to ambient air, oxygen molecules adsorb on the surface and capture electrons from the conduction band, forming ionic oxygen species such as O^-, O_2^-, or O^{2-}. This leads to a depletion of surface charge carriers and increases resistance.

When the sensor is exposed to NO_2 gas, the following reactions occur:

- $NO_2(g) + e^- \rightarrow NO_2(ads)^-$
- $NO_2(g) + O^-(ads) + e^- \rightarrow NO_2(ads)^- + O(lattice)$

In both cases, NO_2 molecules act as electron acceptors, further depleting electrons from the conduction band and thus increasing the resistance of the BFO film. As the temperature increases beyond 300 °C, desorption dominates, reducing the interaction time between the gas molecules and active surface sites, hence lowering the response.

Summary of Observations

- The pristine BFO thin film shows strong NO_2 sensitivity in the temperature range of 100–350 °C, with an optimal response at 300 °C.
- The response time (65 s) and recovery time (7 min) indicate moderate adsorption and desorption kinetics.
- The normalized resistance increases linearly with gas concentration, indicating reliable sensor reproducibility.
- The sensing mechanism is primarily governed by electron depletion and surface adsorption processes, where NO_2 molecules act as strong oxidizing agents.

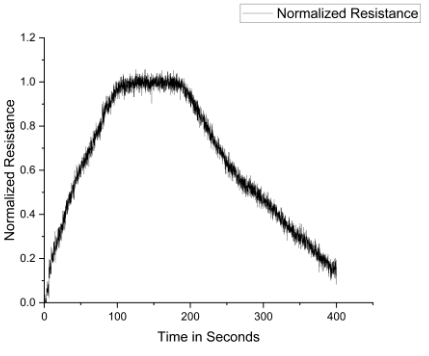

Figure 6.40: 10 ppm NO_2 on BFO at 100 C

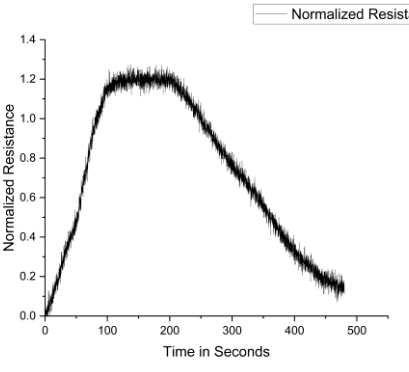

Figure 6.41: 10 ppm NO_2 on BFO at 150 C

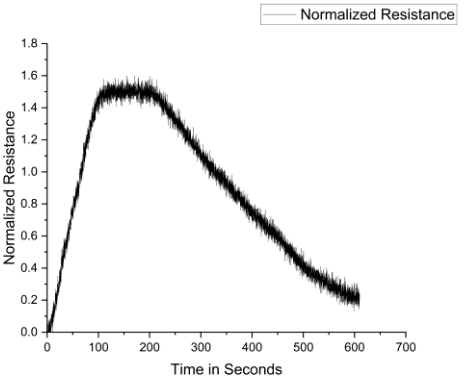

Figure 6.42: 10 ppm NO_2 on BFO at 200 C

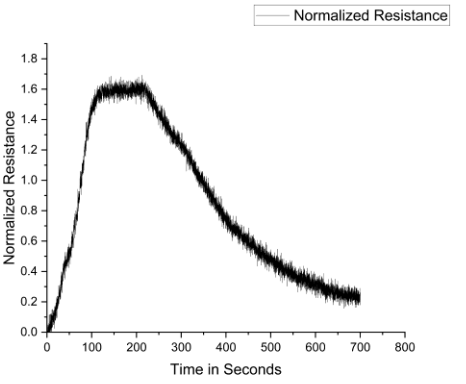

Figure 6.43: 10 ppm NO_2 on BFO at 250 C

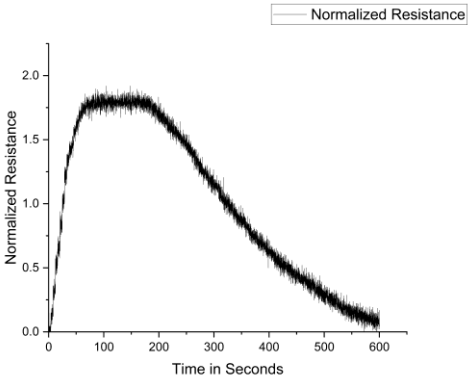

Figure 6.44: 10 ppm NO_2 on BFO at 300 C

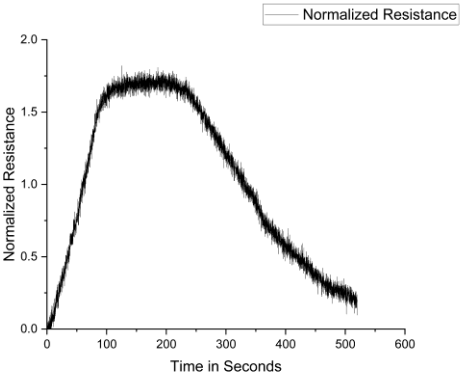

Figure 6.45: 10 ppm NO_2 on BFO at 350 C

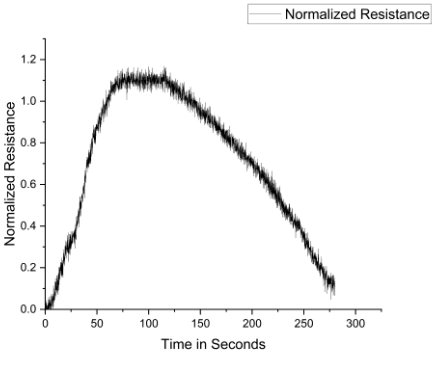

Figure 6.46: Maximum Normalized Response for 5 PPM NO_2 gas on Pristine BFO at 300 C

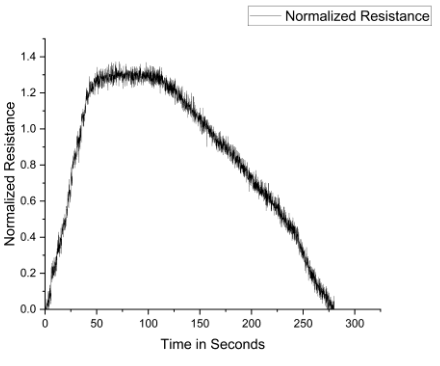

Figure 6.47: Maximum Normalized Response for 10 PPM NO_2 gas on Pristine BFO at 300 C

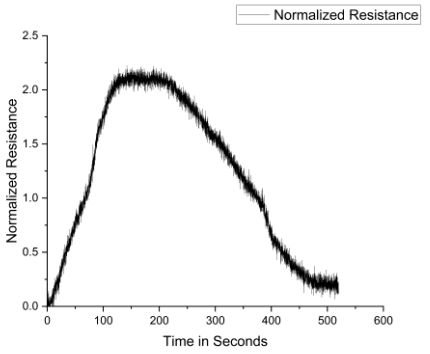

Figure 6.48: Maximum Normalized Resistance for 20 PPM NO_2 on Pristine BFO at 300 C

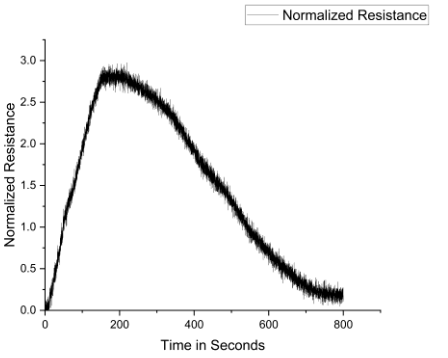

Figure 6.49: Maximum Normalized Resistance for 40 PPM NO_2 on Pristine BFO at 300 C

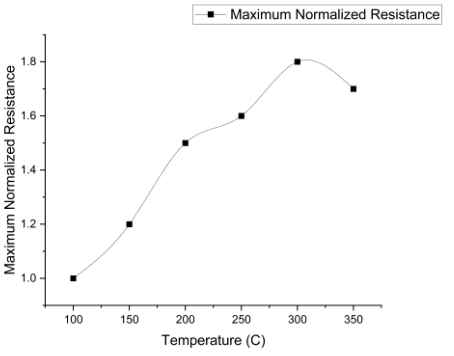

Figure 6.50: Temperature Vs Maximum Normalized Resistance for NO_2 gas sensing on Pristine BFO

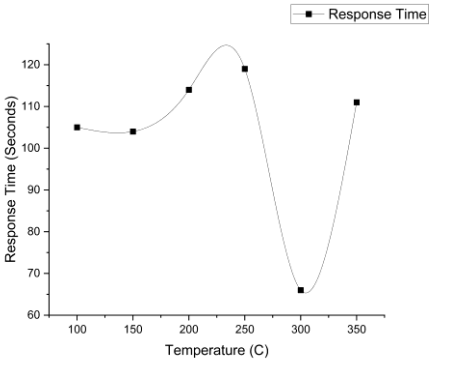

Figure 6.51: Temperature Vs Response Time for NO_2 gas sensing on Pristine BFO

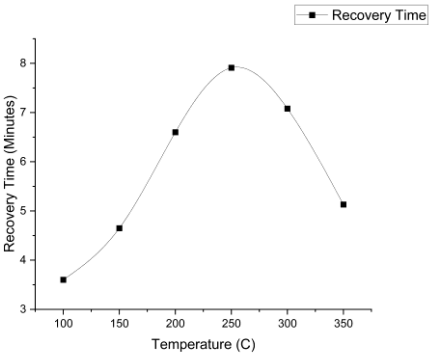

Figure 6.52: Temperature Vs Recovery Tome for NO_2 gas sensing on Pristine BFO

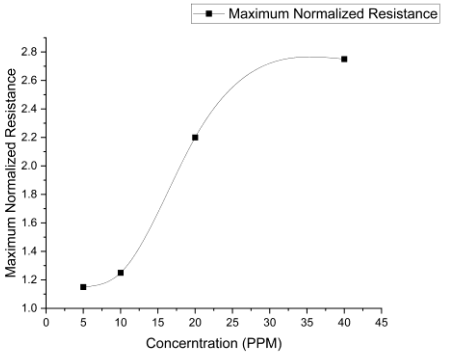

Figure 6.53: Concentration (PPM) Vs Maximum Normalized Resistance for NO_2 gas sensing on Pristine BFO

6.3.4 SO_2 Gas Sensing Mechanism

The sensing behavior of pristine $BiFeO_3$ (BFO) thin film sensors was also investigated for sulfur dioxide (SO_2) gas. Experiments were conducted at a fixed concentration of 10 ppm SO_2 over a temperature range of 100–350 °C. The change in sensor resistance upon exposure to SO_2 was analyzed using normalized resistance as a function of time.

The normalized resistance (R_n) is calculated as:

- $R_n = (R\_gas - R\_air) / R\_air$

where R_gas is the resistance of the sensor in the presence of SO_2 gas, and R_air is the resistance of the sensor before the introduction of gas.

Temperature-Dependent Response

Figures 6.54–6.59 illustrate the temperature-dependent normalized resistance vs. time response curves for the BFO thin film sensor when exposed to 10 ppm SO_2 gas. The response and recovery times were determined from these transient response plots.

- Response time (τ_s): Time required for the sensor resistance to reach 90% of its maximum value upon SO_2 exposure.
- Recovery time (τ_r): Time required for the resistance to return to 10% of its original baseline value after gas removal.

As observed, the response increases with temperature up to 300 °C, after which it begins to decline. This behavior indicates that the adsorption of SO_2 molecules dominates at moderate temperatures, whereas desorption becomes predominant at higher temperatures, lowering the overall response.

Optimal Operating Temperature

From the variation of sensitivity with temperature (Figure 6.64), 300 °C was determined to be the optimal operating temperature for SO_2 gas sensing. At this temperature, the BFO thin film sensor exhibited the best trade-off between sensitivity and dynamic response.

At 300 °C, the sensor displayed the following performance metrics:

- Maximum normalized resistance: Highest response to 10 ppm SO_2 gas.
- Response time: 180 seconds.
- Recovery time: 3.6 minutes.

The response and recovery characteristics of the sensor for various temperatures are shown in Figures 6.65 and 6.66. These figures clearly illustrate the adsorption–desorption kinetics of SO_2 on the BFO surface.

Concentration-Dependent Response

Further measurements were performed at the optimal temperature (300 °C) for varying SO_2 gas concentrations ranging from 5 ppm to 40 ppm. At 5 ppm, the maximum normalized resistance was found to be 0.75, while at 40 ppm, it reached 2.60. This increase in response with concentration indicates a proportional relationship between surface reaction rate and SO_2 molecule density.

Figures 6.60–6.63 depict the dynamic response of the BFO thin film sensor at different SO_2 concentrations, while Figure 6.67 summarizes the maximum normalized resistance as a function of concentration. The near-linear relationship confirms the consistent and quantitative sensing behavior of the BFO sensor for SO_2 detection.

Mechanistic Interpretation

The sensing mechanism for SO_2 gas in BFO films can be explained by the surface adsorption and charge transfer model typical of p-type oxide semiconductors. In air, oxygen molecules adsorb on the BFO surface and capture electrons, forming species such as O^- and O_2^-, which increase the surface resistance by creating a hole accumulation layer.

When exposed to SO_2 gas, the following surface reactions occur:

- $SO_2(g) + O^-(ads) \rightarrow SO_3(ads) + e^-$
- $SO_2(g) + O_2^-(ads) \rightarrow SO_4(ads) + 2e^-$

These reactions release electrons back into the BFO conduction band, reducing the hole concentration and modifying the overall resistance. As a result, the film's resistance changes proportionally to the SO_2 gas concentration. At higher temperatures, rapid desorption of adsorbed species causes a drop in sensitivity, consistent with the experimental data.

Summary of Observations

- The pristine BFO thin film demonstrates efficient SO_2 gas sensing in the temperature range of 100–350 °C.
- Optimal sensing occurs at 300 °C, with a response time of 180 seconds and a recovery time of 3.6 minutes.
- The sensor's response increases linearly with gas concentration, confirming reproducible sensing performance.
- The sensing mechanism follows surface redox reactions where SO_2 interacts with adsorbed oxygen species, causing measurable resistance variation.

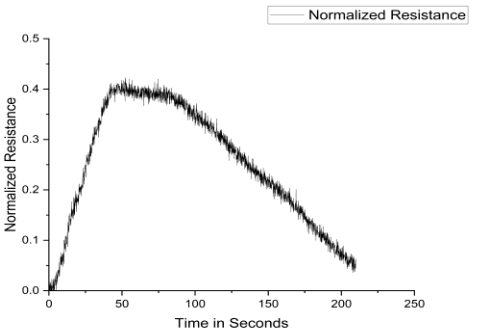

Figure 6.54: 10 ppm SO_2 on BFO at 100 C

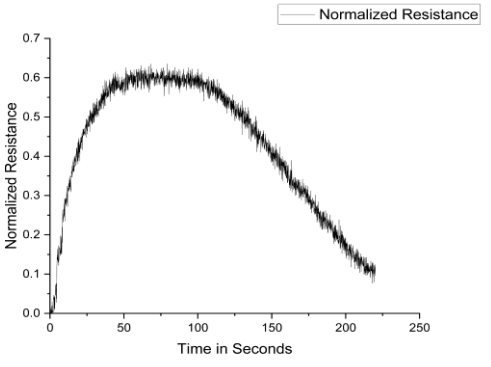

Figure 6.55: 10 ppm SO_2 on BFO at 150 C

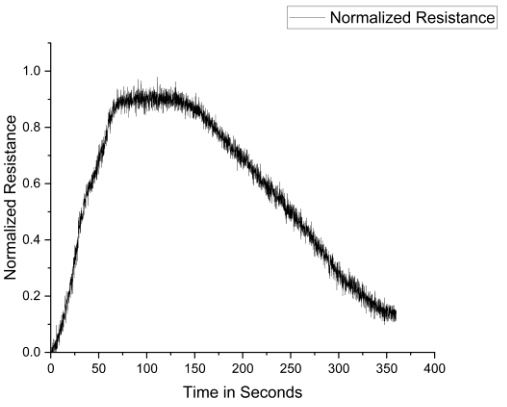

Figure 6.56: 10 ppm SO_2 on BFO at 200 C

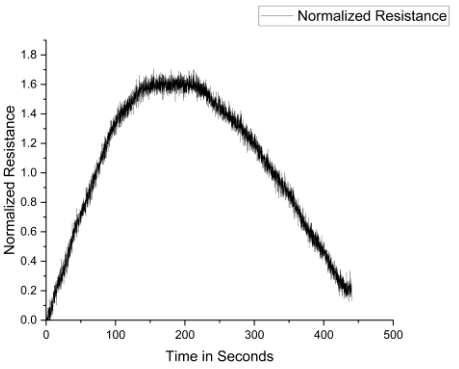

Figure 6.57: 10 ppm SO_2 on BFO at 250 C

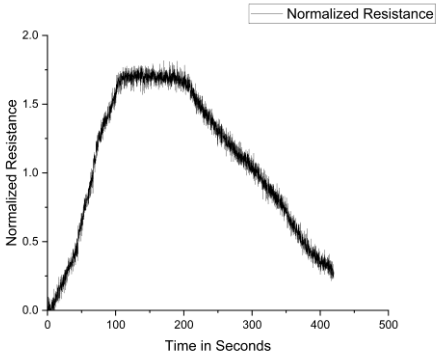

Figure 6.58: 10 ppm SO_2 on BFO at 300 C

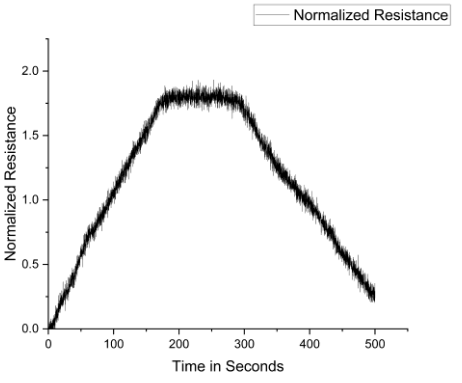

Figure 6.59: 10 ppm SO_2 on BFO at 350 C

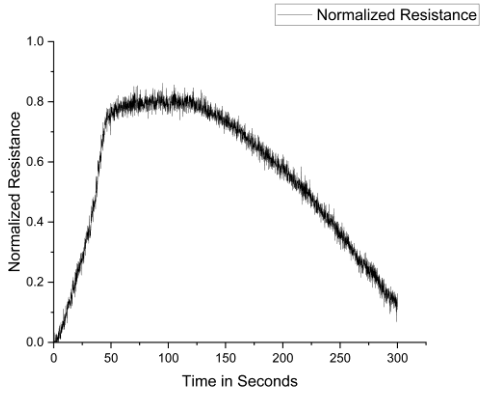

Figure 6.60: 5 ppm SO_2 on Pristine BFO

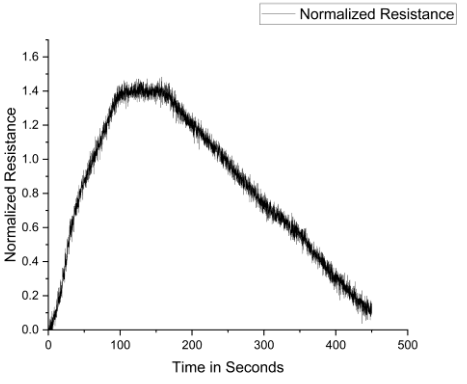

Figure 6.61: 10 ppm SO_2 on Pristine BFO

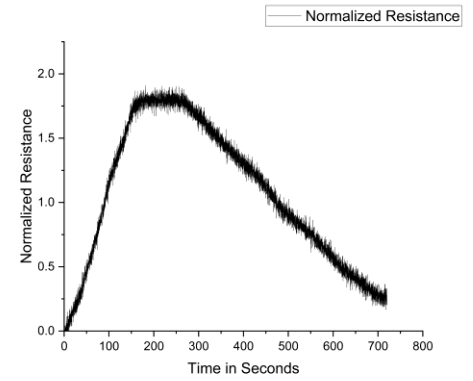

Figure 6.62: 20 ppm SO_2 on Pristine BFO

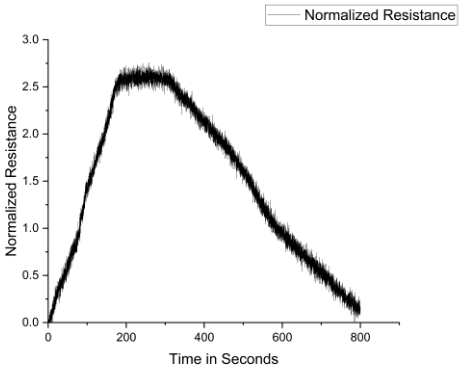

Figure 6.63: 40 ppm SO_2 on Pristine BFO

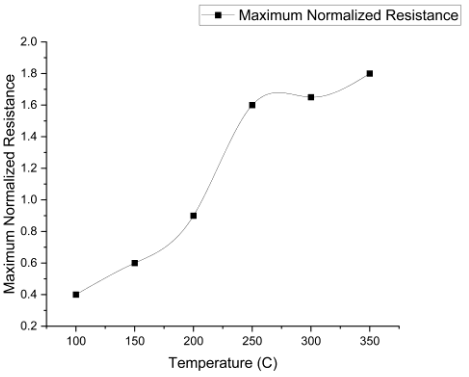

Figure 6.64: Temperature Vs Maximum Normalized Resistance for SO_2 gas sensing on Pristine BFO

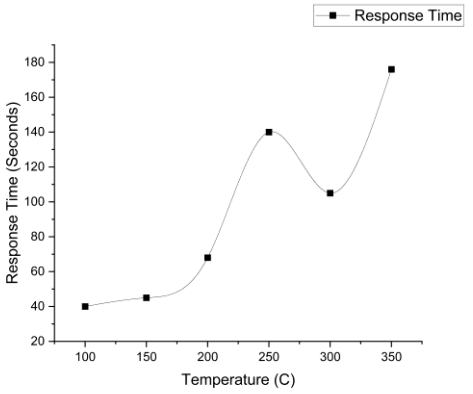

Figure 6.65: Temperature Vs Response Time for SO_2 gas sensing on Pristine BFO

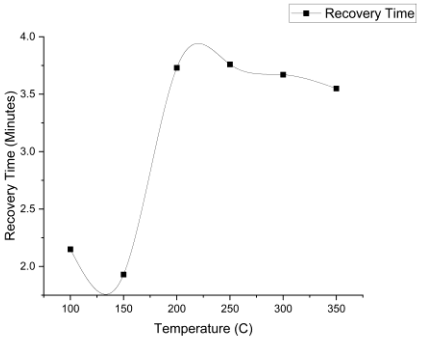

Figure 6.66: Temperature Vs Recovery Time for SO_2 gas sensing on Pristine BFO

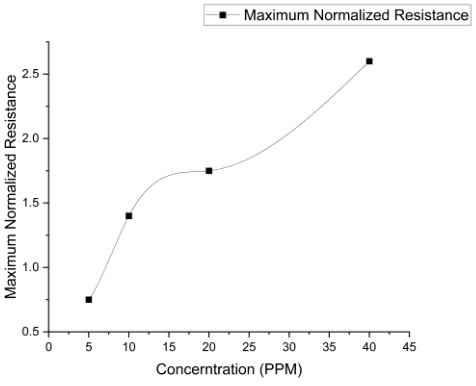

Figure 6.67: Concentration (PPM) Vs Maximum Normalized Resistance for SO_2 gas sensing on Pristine BFO

6.4.1 CO Gas Sensing Mechanism for 0.05 wt% Ag-Doped BFO

The gas sensing characteristics of 0.05 wt% Ag-doped $BiFeO_3$ (BFO) thin film sensors were systematically studied toward carbon monoxide (CO) gas. Measurements were performed at different operating temperatures ranging from 100 °C to 350 °C, with a fixed CO gas concentration of 10 ppm. The sensor's response was quantified using normalized resistance as a function of time.

The normalized resistance (R_n) is calculated as:

- $R_n = (R\_gas - R\_air) / R\_air$

where R_gas is the resistance of the sensor in the presence of CO gas, and R_air is the resistance of the sensor before gas exposure.

Temperature-Dependent Response

Figures 6.68–6.73 illustrate the transient response of the 0.05 wt% Ag-doped BFO thin film sensor toward 10 ppm CO gas at different operating temperatures. Two important parameters were derived from these response curves:

- Response time (τ_s): The time required for the resistance to reach 90% of its peak value after CO exposure.
- Recovery time (τ_r): The time required for the resistance to fall back to 10% of its initial value after CO is removed.

As depicted in Figure 6.78, the sensor's sensitivity to 10 ppm CO increases with temperature up to about 300 °C, after which it begins to decline. The increased response up to this point is due to enhanced surface reactivity, while the decline at higher temperatures is attributed to faster desorption of CO molecules.

Optimal Operating Temperature

The optimal temperature for CO detection was found to be 300 °C, as it provided the best balance between sensitivity and sensor dynamics. At this temperature, the 0.05 wt% Ag-doped BFO film exhibited the following performance metrics:

- Maximum normalized resistance: 5.2
- Response time: 110 seconds
- Recovery time: 4.9 minutes

Figures 6.79 and 6.80 show the response and recovery characteristic curves at various temperatures, confirming rapid adsorption–desorption kinetics at the optimum temperature.

Concentration-Dependent Response

To examine the dependence of sensor performance on gas concentration, additional measurements were conducted at the optimal temperature of 300 °C. The 0.05 wt% Ag-doped BFO sensor displayed the following results:

At 5 ppm, the maximum normalized resistance was 1.5, while at 40 ppm, it reached 13.8. This demonstrates a proportional relationship between CO concentration and sensor response, consistent with Langmuir-type

adsorption behavior. Figures 6.74–6.77 illustrate the transient response for varying concentrations, while Figure 6.81 presents the overall variation of normalized resistance with CO concentration.

Mechanistic Interpretation

The improved sensing behavior of Ag-doped BFO can be attributed to several factors related to noble metal modification of the semiconductor surface:

1. Catalytic Activation: Silver acts as a catalyst, facilitating the dissociation of oxygen molecules into reactive oxygen species (O^-, O_2^-) that actively participate in surface reactions with CO.

2. Electron Exchange Enhancement: The introduction of Ag increases surface conductivity and reduces the potential barrier at the grain boundaries, allowing faster charge transfer between adsorbed gas molecules and the semiconductor lattice.
3. Spillover Effect: Adsorbed oxygen species on the Ag sites migrate ("spill over") onto the BFO surface, increasing the density of active oxygen ions available for reaction.

The fundamental reactions occurring on the sensor surface can be described as:

- $O_2(g) + 2e^- \rightarrow 2O^-(ads)$
- $CO(g) + O^-(ads) \rightarrow CO_2(g) + e^-$

During CO exposure, the adsorbed CO molecules react with surface oxygen ions, releasing electrons back into the conduction band and thus reducing the resistance of the p-type BFO film. Upon removal of the gas, oxygen re-adsorbs, restoring the initial resistance value. This reversible process constitutes the sensing mechanism.

Summary of Observations

- The 0.05 wt% Ag-doped BFO thin film demonstrates superior CO sensing behavior compared to pristine BFO, with enhanced sensitivity and faster response dynamics.
- The optimum temperature for CO detection is 300 °C, yielding a maximum normalized resistance of 5.2.
- The response (110 s) and recovery (4.9 min) times indicate rapid adsorption and moderate desorption kinetics.
- The observed linear dependence of resistance on gas concentration highlights the sensor's reliability and reproducibility.
- The performance enhancement is primarily attributed to Ag-induced catalytic activity, spillover effects, and improved surface electron exchange.

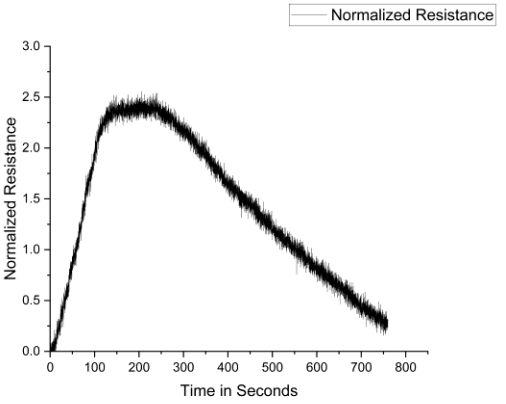

Figure 6.68: 10 ppm CO on 0.05wt% AG-BFO at 100 C

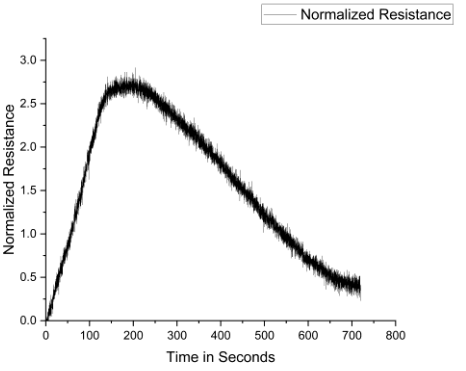

Figure 6.69: 10 ppm CO on 0.05 wt% AG-BFO at 150 C

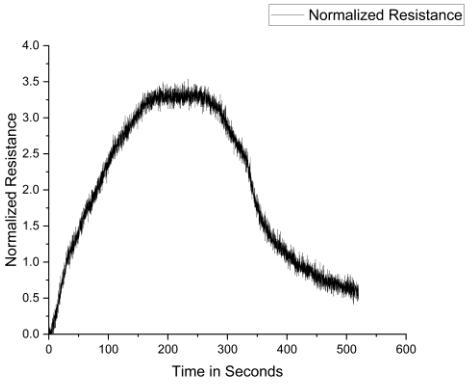

Figure 6.70: 10 ppm CO on 0.05 wt% AG-BFO at 200 C

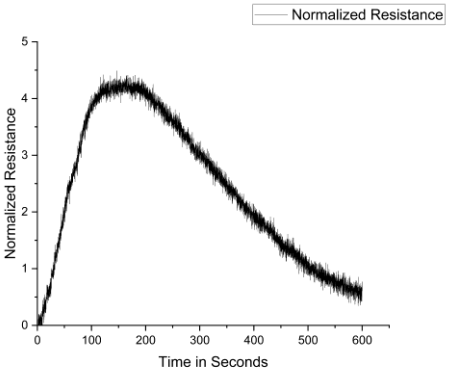

Figure 6.71: Figure 6. 71 10 ppm CO on 0.05 wt% AG-BFO at 250 C

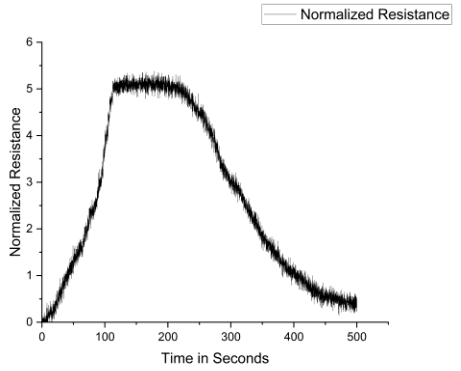

Figure 6.72: 10 ppm CO on 0.05 wt% AG-BFO at 300 C

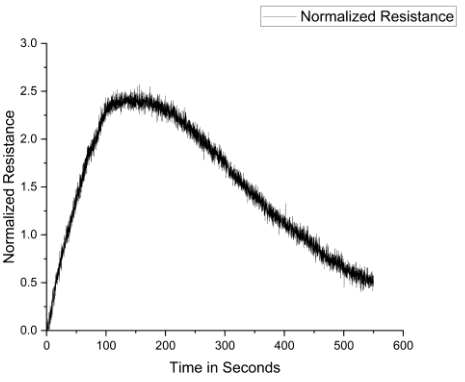

Figure 6.73: 10 ppm CO on 0.05 wt % AG-BFO at 350 C

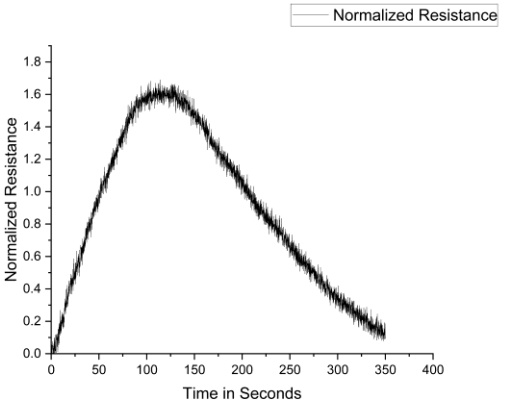

Figure 6.74: 5 ppm CO on 0.05 wt% Ag Doped BFO

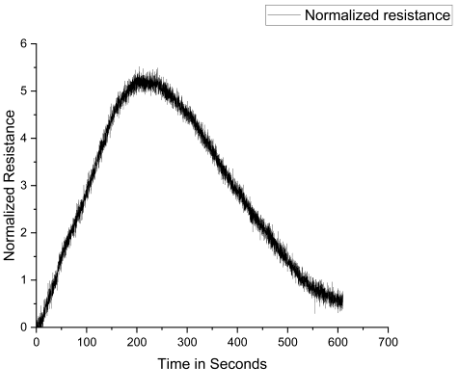

Figure 6.75: 10 ppm CO on 0.05 wt% Ag Doped BFO

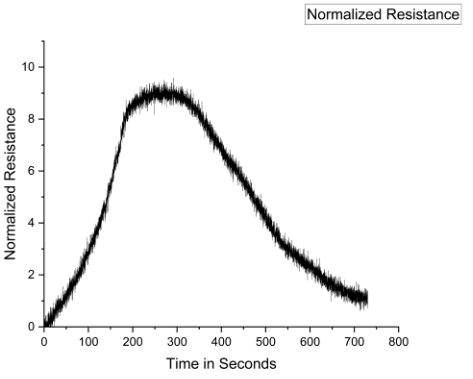

Figure 6.76: 20 ppm CO on 0.05wt % Ag Doped BFO

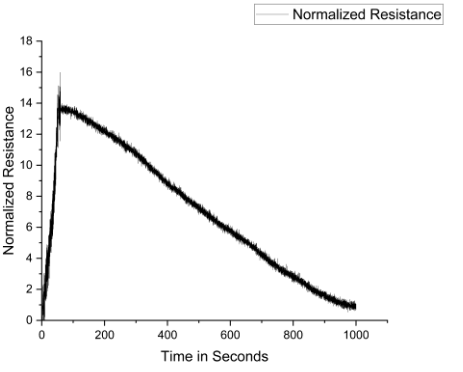

Figure 6.77: 40 ppm CO on 0.05 wt% Ag Doped BFO

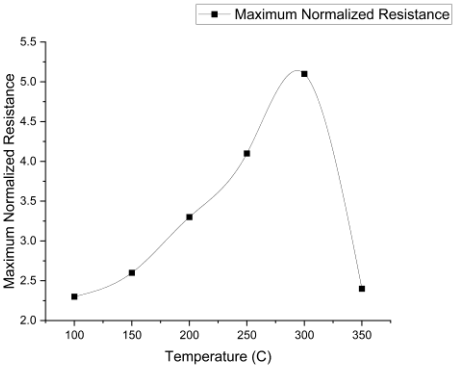

Figure 6.78: Temperature Vs Maximum Normalized Resistance for CO gas sensing on 0.05wt% Ag doped BFO

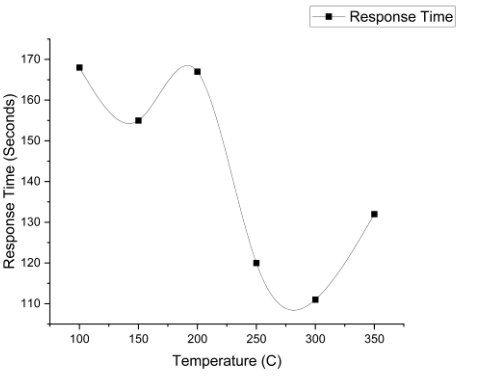

Figure 6.79: Temperature Vs Response Time for CO gas sensing on 0.05wt% Ag Doped BFO.

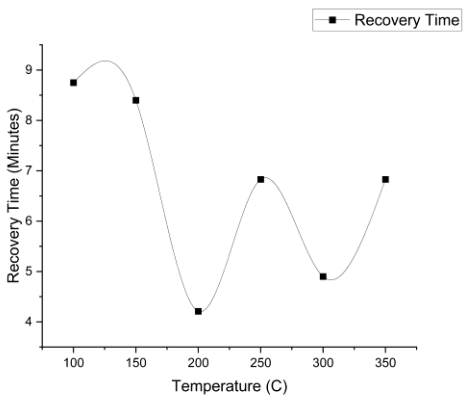

Figure 6.80: Temperature Vs Recovery Time for CO gas sensing on 0.05wt% Ag Doped BFO

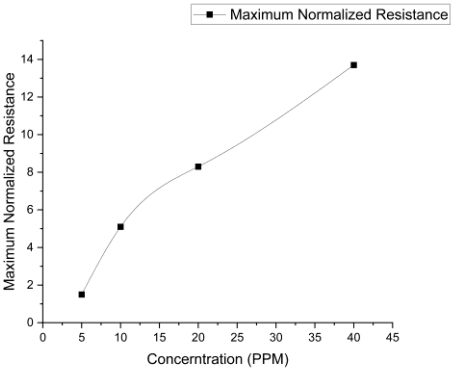

Figure 6.81: Concentration (PPM) Vs Maximum Normalized Resistance for CO gas sensing on 0.05wt% Ag Doped BFO

6.4.2 NO Gas Sensing Mechanism for 0.05 wt% Ag-Doped BFO

The gas-sensing behavior of 0.05 wt% Ag-doped $BiFeO_3$ (BFO) thin film sensors toward nitric oxide (NO) gas was systematically investigated. The study focused on understanding the effect of temperature and gas concentration on the sensor's electrical response when exposed to 10 ppm of NO gas.

The sensor response was analyzed using Normalized Resistance (R_n) as a function of time, defined as:

- $R_n = (R\_gas - R\_air) / R\_air$

where R_gas is the resistance of the sensor in the presence of NO gas, and R_air is the resistance of the sensor before gas exposure.

Temperature-Dependent Response

Figures 6.82 to 6.87 show the transient normalized resistance versus time plots of the 0.05 wt% Ag-doped BFO sensor at various operating temperatures (100 °C – 350 °C) for 10 ppm NO gas.

Two key kinetic parameters were derived from these response curves:

- Response time (τ_s): time required for the resistance to reach 90% of its maximum after NO exposure
- Recovery time (τ_r): time required for the resistance to return to 10% of its baseline value after gas removal.

As shown in Figure 6.92, the sensor's sensitivity increases with temperature up to 200 °C, reaching its peak response, and then declines at higher temperatures. This behavior can be attributed to the competing effects of enhanced surface reaction rates at moderate temperatures and accelerated desorption processes at elevated temperatures.

Optimal Operating Temperature

The optimal operating temperature for NO detection was determined to be 200 °C, providing the best trade-off between sensitivity, stability, and response dynamics.

At this temperature, the 0.05 wt% Ag-doped BFO thin film exhibited:

- Maximum normalized resistance: 7.6
- Response time: 120 seconds
- Recovery time: 7.6 minutes

Figures 6.93 and 6.94 present the response and recovery characteristic curves, confirming stable and reversible sensing behavior at the optimal temperature.

Concentration-Dependent Response

To further understand the concentration dependence of NO gas sensing, additional measurements were performed at 200 °C. The 0.05 wt% Ag-doped BFO sensor responded consistently to varying NO concentrations between 5 ppm and 40 ppm.

NO Concentration (ppm)	Maximum Normalized Resistance
5 ppm	2.1
40 ppm	18.1

The results show a proportional relationship between gas concentration and sensor response, suggesting a first-order adsorption mechanism consistent with Langmuir isotherm behavior. Figures 6.88 to 6.91 depict the dynamic response at different NO concentrations, while Figure 6.95 summarizes the variation of maximum normalized resistance with concentration.

Mechanistic Interpretation

The sensing mechanism for NO gas on Ag-doped BFO surfaces can be understood based on surface adsorption and charge transfer processes in a p-type semiconductor.

In air, oxygen molecules adsorb on the BFO surface and form negatively charged species by capturing electrons:

- $O_2(g) + 2e^- \rightarrow 2O^-(ads)$

When NO gas is introduced, it reacts with these adsorbed oxygen ions according to:

- $NO(g) + O^-(ads) \rightarrow NO_2(g) + e^-$

This reaction releases electrons back into the conduction band, reducing the hole concentration in the p-type material and increasing its resistance.

The addition of Ag atoms improves this process through:

1. Catalytic activation – silver enhances oxygen molecule dissociation and promotes reaction kinetics.
2. Electronic modulation – Ag doping modifies local potential barriers, improving charge transfer efficiency.
3. Spillover effect – oxygen species activated on Ag sites migrate to the BFO surface, enhancing adsorption capability.

Summary of Observations

- The 0.05 wt% Ag-doped BFO sensor demonstrated excellent NO sensing characteristics at low operating temperatures.
- Optimal operating temperature: 200 °C.
- Maximum normalized resistance: 7.6 at 10 ppm NO.
- Response time: 120 s; Recovery time: 7.6 min.
- Sensitivity increased linearly with gas concentration (5–40 ppm).
- Improved performance is attributed to Ag-induced catalytic activity and enhanced surface oxygen mobility.

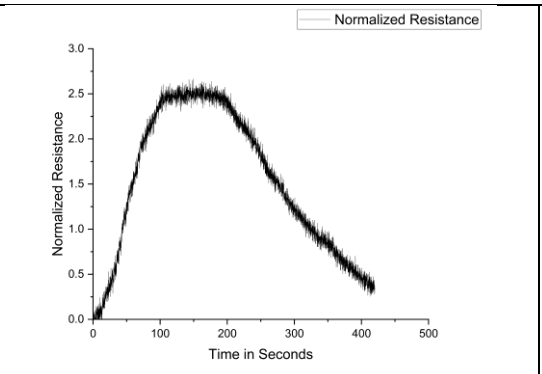

Figure 6.82: 10 ppm NO on 0.05 wt% AG-BFO at 100 C

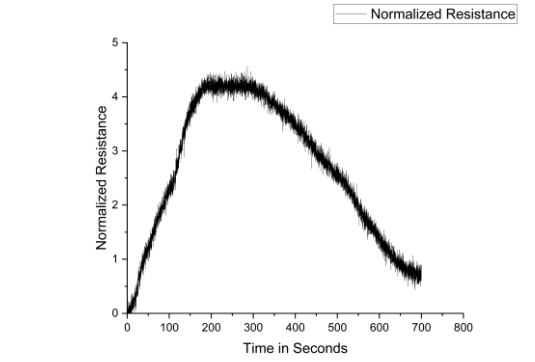

Figure 6.83: 10 ppm NO on 0.05wt% AG-BFO at 150 C

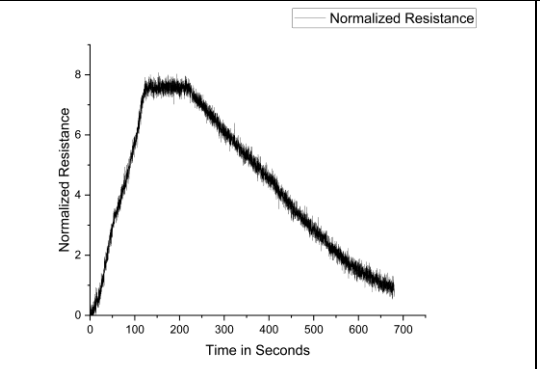

Figure 6.84: 10 ppm NO on 0.05wt% AG-BFO at 200 C

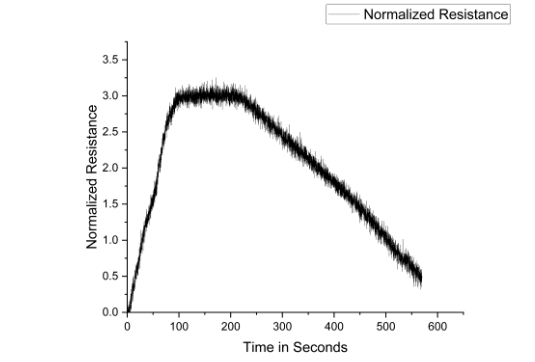

Figure 6.85: 10 ppm NO on 0.05wt% AG-BFO at 250 C

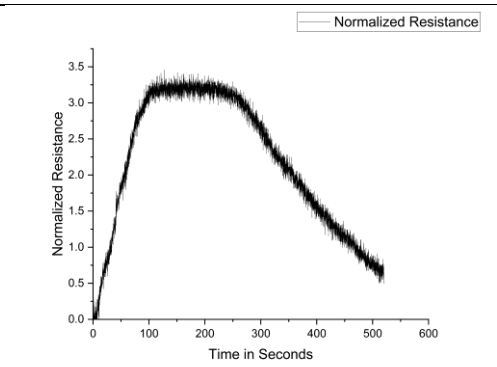

Figure 6.86: 10 ppm NO on 0.05 AG-BFO at 300 C

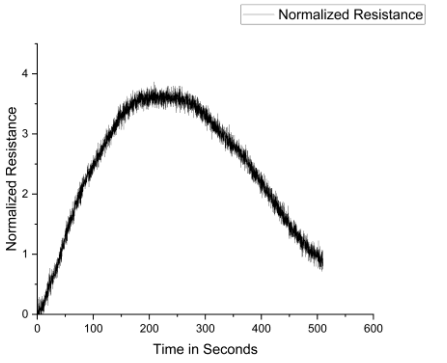

Figure 6.87: 10 ppm NO on 0.05 AG-BFO at 350 C

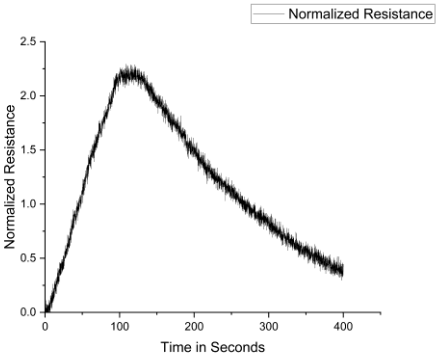

Figure 6.88: 5 ppm NO on 0.05wt % Ag Doped BFO

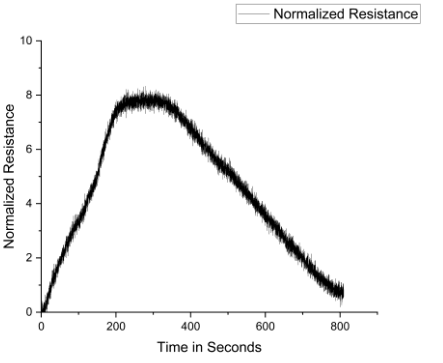

Figure 6.89: 10 ppm NO on 0.05wt % Ag Doped BFO

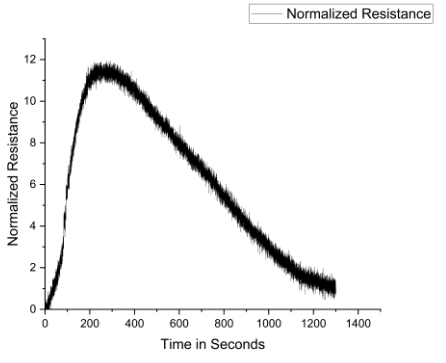

Figure 6.90: 20 ppm NO on 0.05wt % Ag Doped BFO

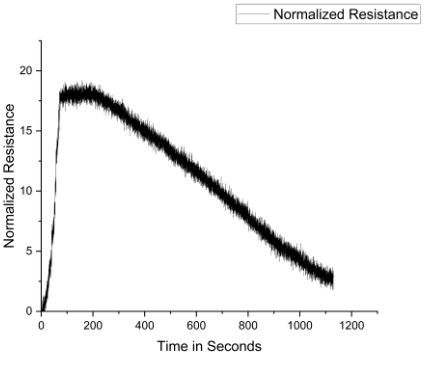

Figure 6.91: 40 ppm NO on 0.05wt % Ag Doped BFO

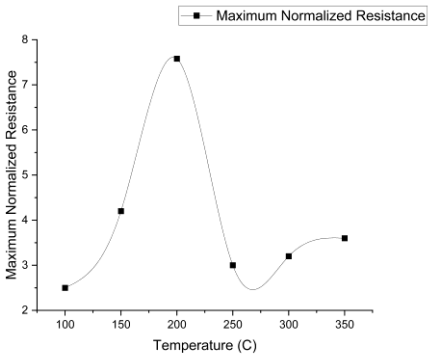

Figure 6.92: Temperature Vs Maximum Normalized Resistance NO gas sensing on 0.05 wt% on Ag BFO

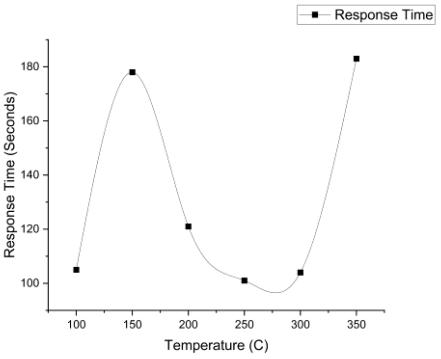

Figure 6.93: Temperature Vs Response Time for NO gas sensing on 0.05wt% on Ag BFO

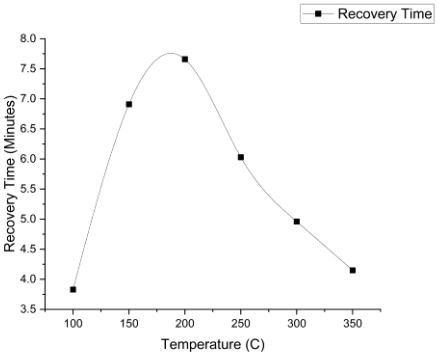

Figure 6.94: Temperature Vs Recovery Time for NO gas sensing on 0.05wt% Ag-BFO

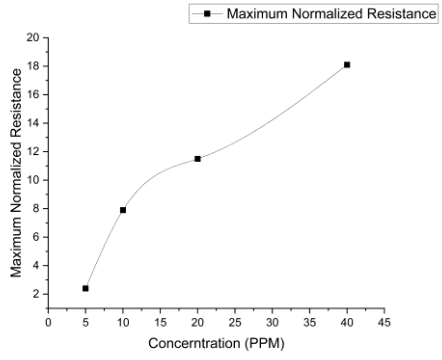

Figure 6.95: Concentration (PPM) Vs Maximum Normalized Resistance NO gas sensing on 0.05wt% AgBFO

.4.3 NO_2 Gas Sensing Mechanism for 0.05 wt% Ag-Doped BFO

The sensing characteristics of 0.05 wt% Ag-doped $BiFeO_3$ (BFO) thin film sensors were systematically examined toward nitrogen dioxide (NO_2) gas molecules. The objective was to understand the effect of temperature and concentration on the sensor's response behavior at relatively low gas concentrations (10 ppm).

The Normalized Resistance (R_n) was used to quantify the sensor's performance as a function of time:

- R_n = (R_gas - R_air) / R_air

where R_gas is the sensor resistance in the presence of NO_2 gas, and R_air is the sensor resistance before the introduction of gas.

Temperature-Dependent Response

Figures 6.96 through 6.101 depict the transient variation of normalized resistance with time for the 0.05 wt% Ag-doped BFO thin film sensor at several operating temperatures (100–350 °C) under a fixed concentration of 10 ppm NO_2.

Two important dynamic parameters were extracted from these plots:

- Response time (τ_s): The time required for the sensor resistance to reach 90% of its maximum value after exposure to gas.
- Recovery time (τ_r): The time required for the resistance to return to 10% of its baseline value after removal of the gas.

As observed in Figure 6.106, the sensor's sensitivity increases with temperature and achieves a maximum at 300 °C, beyond which it declines. The rising portion of the curve is attributed to enhanced oxygen ion mobility and faster surface redox reactions, while the decline at higher temperatures results from the accelerated desorption of NO_2 molecules from the sensor surface.

Optimal Operating Temperature

The optimal operating temperature for NO_2 detection was determined to be 300 °C, where the sensor achieves the most favorable balance between response magnitude and dynamic stability.

At this temperature, the 0.05 wt% Ag-doped BFO thin film exhibited:

- Maximum normalized resistance: 2.6
- Response time: 80 seconds
- Recovery time: 3.75 minutes

Figures 6.107 and 6.108 display the sensor's response and recovery characteristic curves at different temperatures, demonstrating stable, repeatable, and symmetric transients—typical of surface-controlled adsorption–desorption processes.

Concentration-Dependent Response

At the optimum temperature of 300 °C, additional studies were performed to analyze the effect of NO_2 gas concentration on the sensor response. The recorded normalized resistance values for various NO_2 concentrations are presented below:

NO_2 Concentration (ppm)	Maximum Normalized Resistance
5 ppm	1.4
40 ppm	2.7

The results indicate that the sensor response increases with NO_2 concentration, consistent with a Langmuir-type adsorption mechanism, where the surface coverage of adsorbed molecules grows with gas concentration until saturation is reached.

Figures 6.102–6.103 illustrate the transient response at different concentrations, while Figure 6.104 summarizes the variation of maximum normalized resistance with concentration.

Mechanistic Interpretation

The sensing mechanism of NO_2 detection in Ag-doped BFO can be explained based on surface adsorption and charge exchange phenomena. Being a strong oxidizing gas, NO_2 tends to capture electrons from the conduction band of the p-type BFO sensor, leading to an increase in resistance.

In ambient air, oxygen molecules adsorb on the surface and form ionized oxygen species:

- $O_2(g) + 2e^- \rightarrow 2O^-(ads)$

When NO_2 gas is introduced, the following reaction occurs:

- $NO_2(g) + e^- \rightarrow NO(g) + O^-(ads)$

This reaction removes free electrons from the semiconductor, thereby widening the depletion layer and increasing the overall resistance. Upon removal of NO_2, the adsorbed species desorb, and the resistance returns to its baseline value.

Silver doping enhances this mechanism through several key effects:

1. Catalytic activation – Ag sites lower the activation energy required for NO_2 adsorption, accelerating reaction kinetics.

2. Spillover phenomenon – Activated oxygen species migrate from Ag sites to the BFO surface, increasing the number of reactive sites.

3. Electronic modulation – Ag modifies the surface potential barrier, improving the efficiency of charge transfer between adsorbed gas molecules and the semiconductor.

Summary of Observations

- The 0.05 wt% Ag-doped BFO thin film sensor exhibits excellent NO_2 detection performance.
- Optimal operating temperature: 300 °C. • Maximum normalized resistance: 2.6 at 10 ppm NO_2.
- Response time: 80 seconds; Recovery time: 3.75 minutes
- Sensitivity increases with gas concentration (5–40 ppm). • Ag doping significantly enhances surface reactivity, charge exchange, and sensor reversibility.

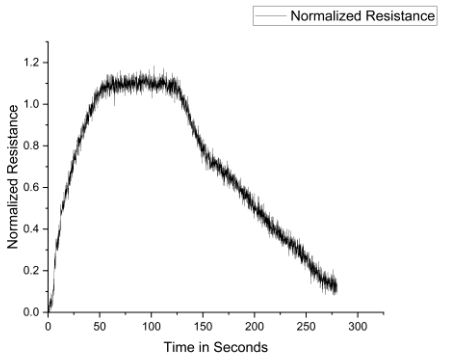

Figure 6.96: 10 ppm NO_2 on 0.05 wt % AG-BFO at 100 C

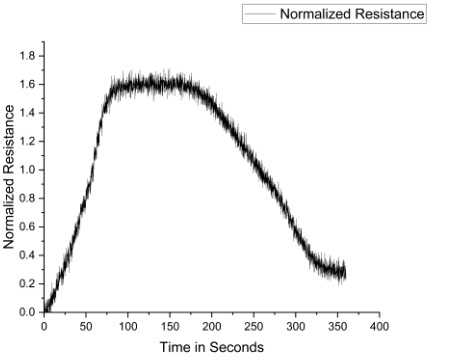

Figure 6.97: 10 ppm NO_2 on 0.05 wt % AG-BFO at 150 C

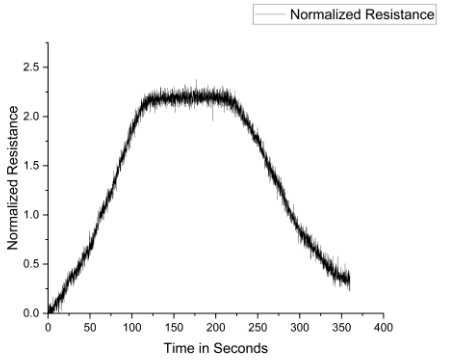

Figure 6.98: 10 ppm NO_2 on 0.05 wt% AG-BFO at 200 C

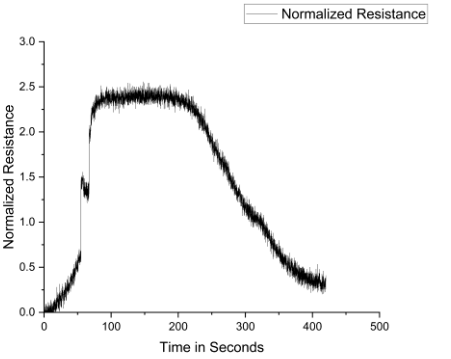

Figure 6.99: 10 ppm NO_2 on 0.05 wt % AG-BFO at 250 C

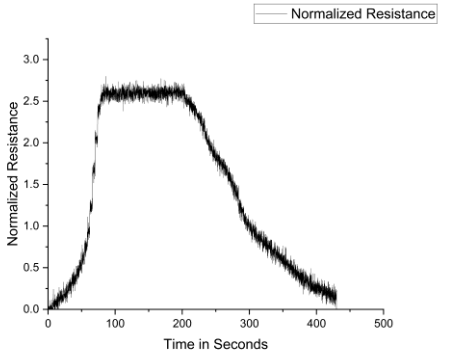

Figure 6. 100: 10 ppm NO_2 on 0.05wt% AG-BFO at 300 C

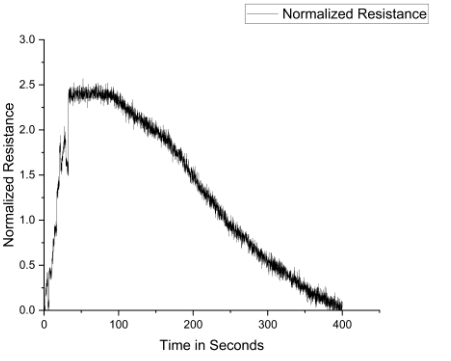

Figure 6.101: 10 ppm NO_2 on 0.05wt % AG-BFO at 350 C

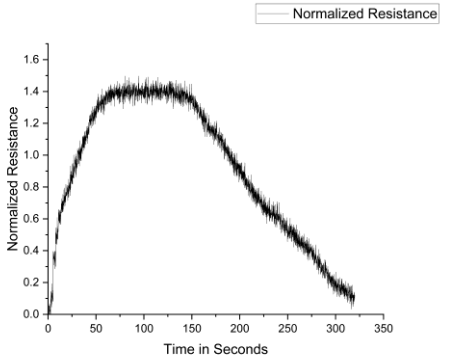

Figure 6.102: 5 ppm NO_2 on 0.05 wt% Ag Doped BFO

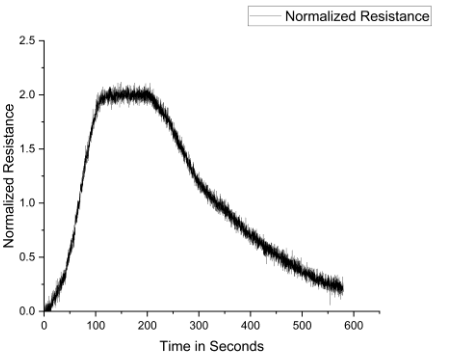

Figure 6.103: 10 ppm NO_2 on 0.05wt % Ag Doped BFO

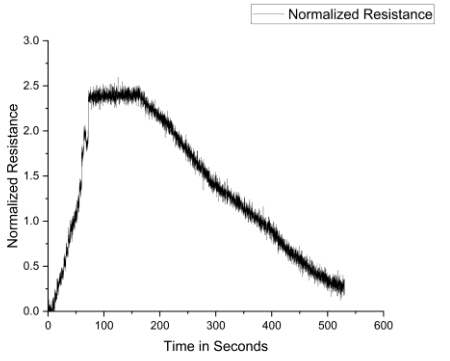

Figure 6.104: 20 ppm NO_2 on 0.05wt % Ag Doped BFO

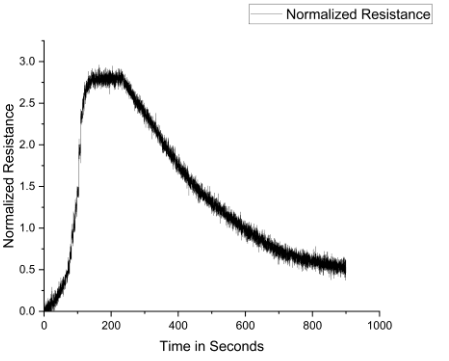

Figure 6.105: 40 ppm NO_2 on 0.05wt % Ag Doped BFO

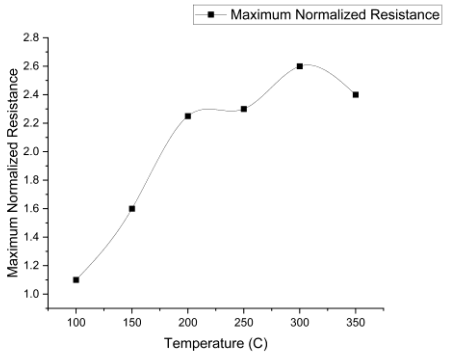

Figure 6.106: Temperature Vs Maximum Normalized Resistance for BO2 gas sensing on 0.05wt% Ag doped BFO

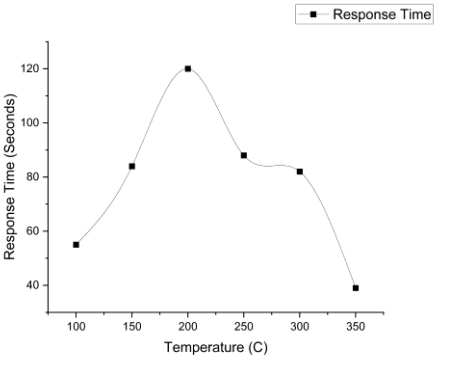

Figure 6.107: Temperature Vs Response Time for NO_2 gas sensing on 0.05wt% Ag doped BFO

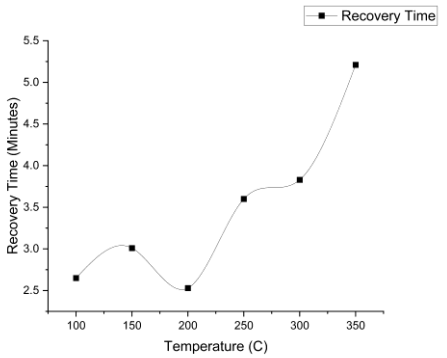

Figure 6.108: Temperature Vs Recovery Time for NO_2 gas sensing on 0.05wt% Ag doped BFO

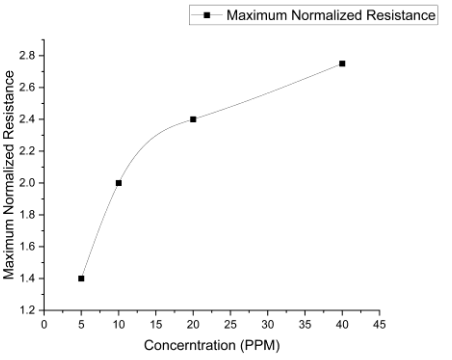

Figure 6.109: Concentration (PPM) Vs Maximum Normalized Resistance for NO_2 gas sensing on 0.05 wt % Ag doped BFO

6.4.4 SO_2 Gas Sensing Mechanism for 0.05 wt% Ag-Doped BFO

The sensing characteristics of 0.05 wt% Ag-doped $BiFeO_3$ (BFO) thin film sensors were systematically investigated for detecting sulfur dioxide (SO_2) gas molecules at low concentrations (10 ppm). Experiments were carried out over a temperature range of 100–350 °C, and the transient electrical response was studied as a function of time.

The sensor response was evaluated using the Normalized Resistance (R_n) parameter, defined as:

- $R_n = (R\_gas - R\_air) / R\_air$

where R_gas is the resistance of the sensor in the presence of SO_2 gas, and R_air is the resistance of the sensor in air (before gas exposure).

Temperature-Dependent Response

Figures 6.110–6.115 display the transient response curves of normalized resistance versus time for the 0.05 wt% Ag-doped BFO thin film at 10 ppm SO_2 concentration under varying temperatures.

Two dynamic parameters were extracted from these response profiles:

- Response time (τ_s): Time taken for the resistance to reach 90% of its peak after gas exposure.
- Recovery time (τ_r): Time taken for the resistance to return to 10% of its initial baseline once the gas is removed.

As shown in Figure 6.120, the sensitivity increases with temperature, reaching a maximum at 300 °C, and subsequently decreases. This temperature dependence arises because moderate heating promotes enhanced oxygen ion mobility and facilitates faster redox reactions, while at higher temperatures, desorption processes dominate, reducing the surface coverage of SO_2 molecules.

Optimal Operating Temperature

The optimal operating temperature for SO_2 gas detection was determined to be 300 °C, offering the most favorable trade-off between response magnitude and recovery dynamics.

At this temperature, the 0.05 wt% Ag-doped BFO sensor exhibited:
• Maximum normalized resistance: 2.3
• Response time: 119 seconds
• Recovery time: 3.4 minutes

Figures 6.121 and 6.122 present the corresponding response and recovery characteristic curves, showing stable, repeatable sensing behavior typical of thermally activated semiconductor gas sensors.

Concentration-Dependent Response
To further analyze the sensor's sensitivity variation with SO_2 concentration, additional measurements were performed at the optimal operating temperature (300 °C). The normalized resistance values at different gas concentrations are summarized below.

SO_2 Concentration (ppm)	Maximum Normalized Resistance
5 ppm	1.3
40 ppm	2.7

The results demonstrate that the normalized resistance increases proportionally with gas concentration, consistent with a Langmuir-type adsorption behavior where surface coverage increases with concentration until equilibrium saturation is reached.

Figures 6.116–6.119 illustrate the transient responses of the 0.05 wt% Ag-doped BFO sensor to varying SO_2 concentrations, and Figure 6.123 summarizes the variation of maximum normalized resistance as a function of concentration.

Mechanistic Interpretation
The sensing mechanism of SO_2 on Ag-doped BFO can be explained through surface adsorption, redox interactions, and charge transfer processes characteristic of p-type semiconducting oxides.

In ambient air, oxygen molecules adsorb onto the BFO surface and form chemisorbed oxygen species according to:

- $O_2(g) + 2e^- \rightarrow 2O^-(ads)$

When SO_2 gas is introduced, it interacts with the adsorbed oxygen species and the surface lattice oxygen as follows:

- $SO_2(g) + O^-(ads) \rightarrow SO_3(g) + e^-$

This reaction releases electrons into the material, recombining with holes in the p-type BFO and thus reducing hole concentration. As a result, the overall resistance of the sensor increases. Upon removal of SO_2, the adsorbed oxygen species are replenished by the surrounding air, and the sensor returns to its baseline resistance.

Ag doping enhances this process through three main effects:

1. Catalytic activity – Ag atoms facilitate oxygen dissociation and improve the kinetics of surface reactions involving SO_2.

2. Spillover effect – Active oxygen species generated at Ag sites migrate to adjacent BFO surfaces, increasing reactive area.

3. Electronic interaction – The presence of Ag modifies the local potential barrier at the surface, optimizing charge transfer efficiency between adsorbed molecules and the semiconductor lattice.

Summary of Observations

- The 0.05 wt% Ag-doped BFO thin film sensor demonstrated strong sensitivity and stable response toward SO_2 gas.
- Optimal operating temperature: 300 °C.
- Maximum normalized resistance: 2.3 at 10 ppm SO_2.
- Response time: 119 seconds; Recovery time: 3.4 minutes.
- Sensitivity increased linearly with gas concentration (5–40 ppm).
- Silver doping enhanced both the adsorption capacity and reaction kinetics, improving the overall gas sensing efficiency.

.

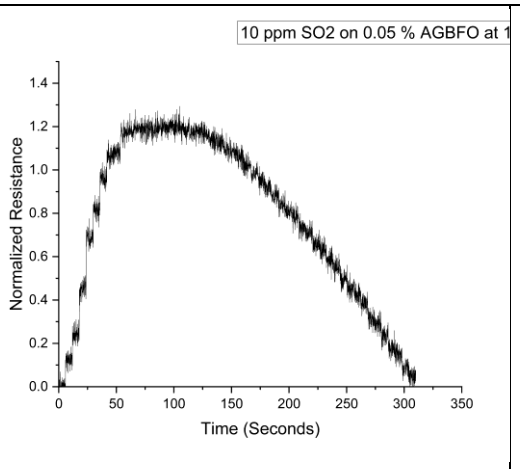

Figure 6.110: 10 ppm SO_2 on 0.05wt % AG-BFO at 100 C

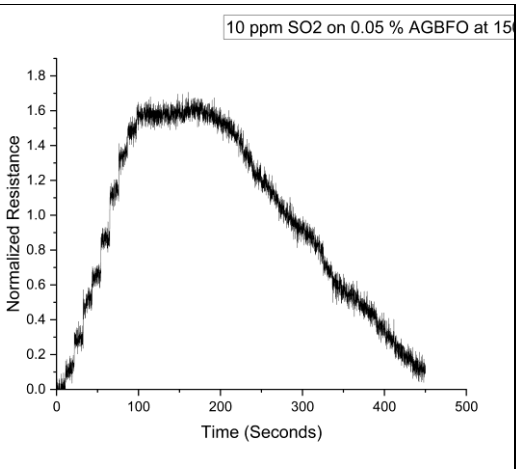

Figure 6.111: 10 ppm SO_2 on 0.05 wt % AG-BFO at 150 C

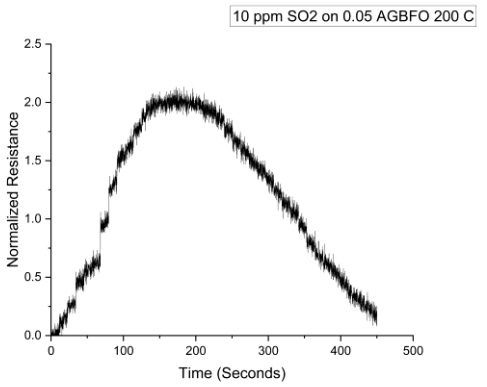

Figure 6.112: 10 ppm SO_2 on 0.05wt % AG-BFO at 200 C

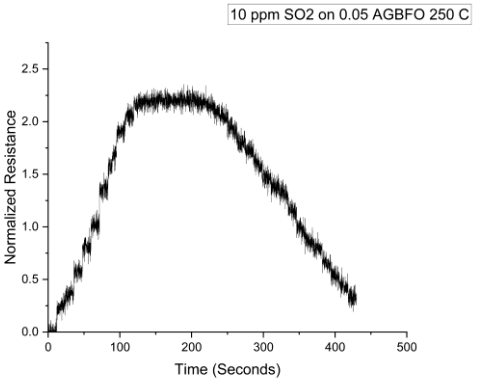

Figure 6.113: 10 ppm SO_2 on 0.05wt % AG-BFO at 250 C

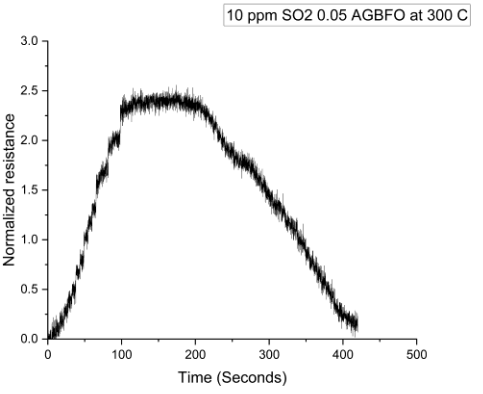

Figure 6.114: 10 ppm SO_2 on 0.05wt% AG-BFO at 300 C

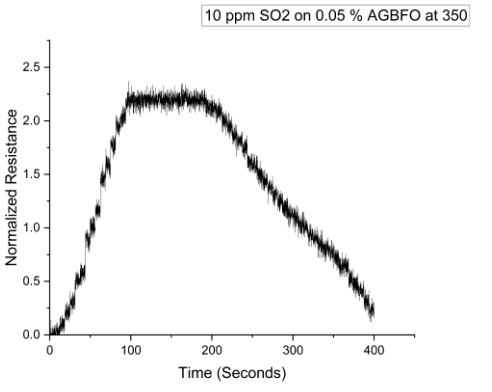

Figure 6.115: 10 ppm SO_2 on 0.05wt % AG-BFO at 350 C

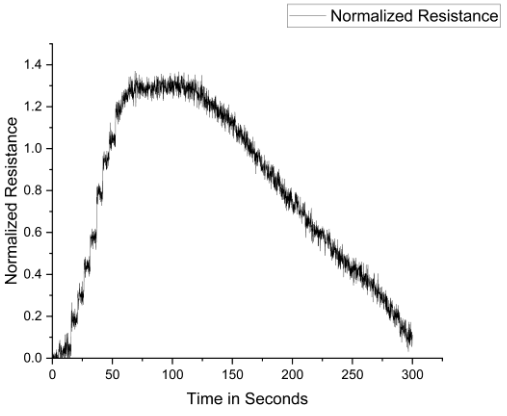

Figure 6.116: 5 ppm SO_2 on 0.05 wt % Ag Doped BFO

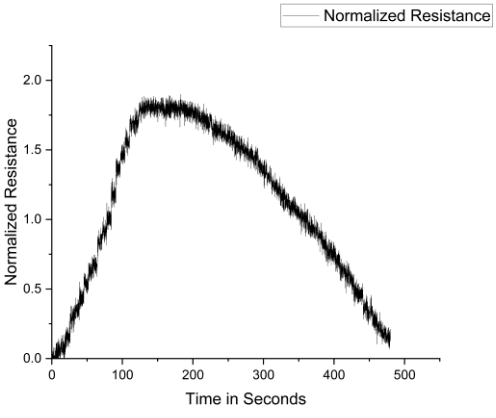

Figure 6.117: 10 ppm SO_2 on 0.05 % Ag Doped BFO

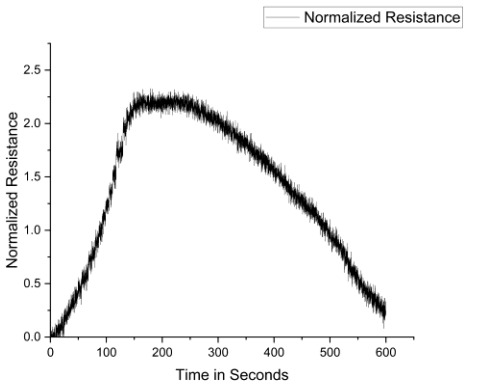

Figure 6.118: 20 ppm SO_2 on 0.05 % Ag Doped BFO

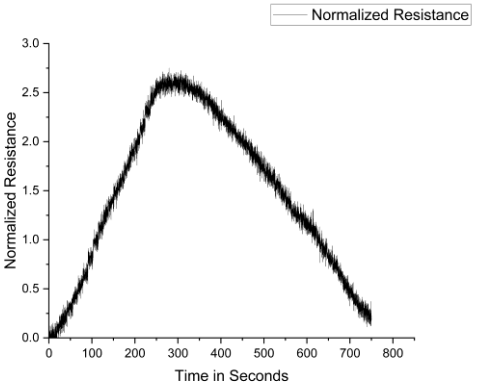

Figure 6.119: 40 ppm SO_2 on 0.05wt % Ag Doped BFO

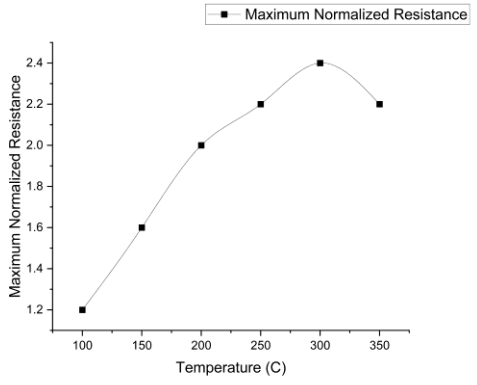

Figure 6.120: Temperature Vs Maximum Normalized Resistance for SO_2 gas sensing on 0.05 wt % Ag doped BFO

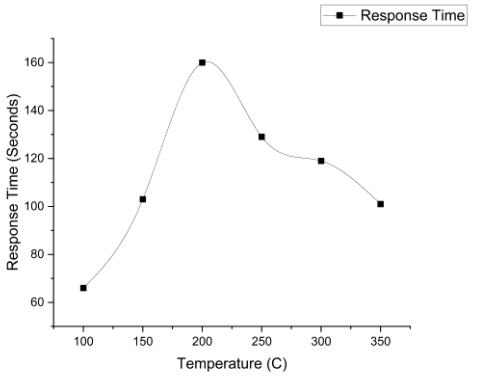

Figure 6.121: Temperature Vs Response time for SO_2 gas sensing on 0.05wt% Ag doped BFO

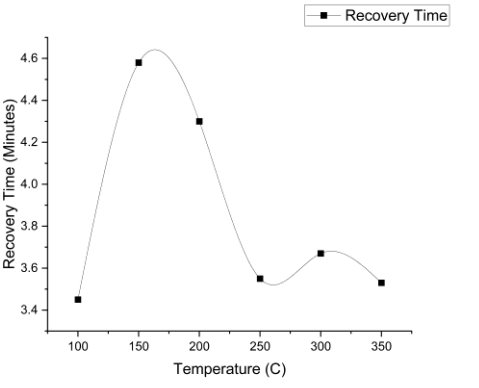

Figure 6.122: Temperature Vs Recovery Time for SO_2 gas sensing on 0.05 wt % Ag doped BFO

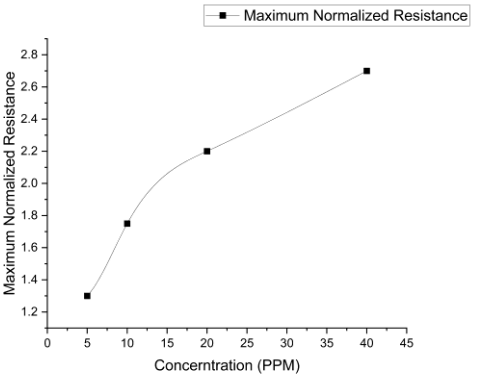

Figure 6.123: Concentration (PPM) Vs Maximum Normalized Resistance for SO_2 gas sensing on 0.05 wt % Ag doped BFO

5.1 CO Gas Sensing Mechanism for 0.10 wt% Ag-Doped BFO

The sensing characteristics of 0.10 wt% Ag-doped $BiFeO_3$ (BFO) thin film sensors were systematically investigated for detecting carbon monoxide (CO) gas molecules at a fixed concentration of 10 ppm. The experiments were conducted within a temperature range of 100–350 °C, and the sensor response was monitored as a function of time.

The response of the sensor was quantified using Normalized Resistance (R_n), defined as:

- $R_n = (R\_gas - R\_air) / R\_air$

where R_gas is the resistance of the sensor in the presence of CO gas, and R_air is the resistance of the sensor in air before gas exposure.

Temperature-Dependent Response

Figures 6.124–6.129 present the transient response curves (Normalized Resistance vs. Time) for 0.10 wt% Ag-doped BFO thin film at 10 ppm CO concentration under varying temperatures.

In all the measurements, two kinetic parameters were calculated:

- Response time (τ_s): Time taken by the sensor to reach 90% of its maximum resistance after gas exposure.
- Recovery time (τ_r): Time taken by the sensor to return to 10% of its baseline resistance once the gas is removed.

The sensor's temperature-dependent sensitivity is shown in Figure 6.134. The sensitivity increased steadily with temperature, peaking at 300 °C, beyond which it decreased due to excessive desorption of gas molecules from the sensor surface.

Optimal Operating Temperature

The optimal operating temperature for CO gas detection was determined to be 250 °C, at which the 0.10 wt% Ag-doped BFO thin film exhibited the best balance between response magnitude and recovery dynamics.

At this optimal condition, the sensor exhibited:

- Maximum normalized resistance: 3.00
- Response time: 120 seconds
- Recovery time: 6.75 minutes

The corresponding response and recovery curves are shown in Figures 6.135–6.136, which indicate stable and repeatable sensing behavior, characteristic of a surface-controlled adsorption–desorption process.

Concentration-Dependent Response

At the optimum temperature of 250 °C, concentration-dependent measurements were performed to study how the sensor responded to various CO concentrations. The results are summarized in Table 6.2 below.

CO Concentration (ppm)	Maximum Normalized Resistance
5 ppm	1.5
40 ppm	14.0

These results clearly demonstrate a direct proportionality between gas concentration and sensor response. This follows the Langmuir adsorption model, where the active adsorption sites on the surface become increasingly occupied as the gas concentration rises, leading to a larger change in resistance.

Figures 6.130–6.133 illustrate the transient sensor responses at different CO concentrations, and Figure 6.137 summarizes the maximum normalized resistance values for each concentration.

Mechanistic Interpretation

The gas-sensing mechanism for CO detection in Ag-doped BFO thin films can be explained based on surface adsorption and redox interactions.

In air, oxygen molecules adsorb on the sensor surface and capture electrons from the conduction band to form ionized oxygen species:

- $O_2(g) + 2e^- \rightarrow 2O^-(ads)$

When the CO gas is introduced, it reacts with the adsorbed oxygen species as follows:

- $CO(g) + O^-(ads) \rightarrow CO_2(g) + e^-$

This reaction releases electrons back into the conduction band, effectively reducing the hole concentration (as BFO is a p-type semiconductor), leading to an increase in resistance.

Upon removal of CO gas, adsorbed oxygen molecules from the atmosphere reoccupy the surface sites, restoring the baseline resistance of the sensor.

Silver doping enhances the CO sensing performance due to three main mechanisms:

1. Catalytic Activation – Ag facilitates oxygen dissociation and accelerates the CO oxidation reaction.
2. Spillover Effect – Activated oxygen species migrate from Ag sites to nearby BFO surfaces, increasing the number of reactive sites.
3. Electronic Coupling – Ag modifies the band structure and potential barrier at the BFO surface, improving charge transfer efficiency between adsorbed gases and the sensing layer.

Summary of Observations

- The 0.10 wt% Ag-doped BFO thin film sensor demonstrates excellent sensitivity and repeatability for CO detection.
- Optimal operating temperature: 250 °C.
- Maximum normalized resistance: 3.00 at 10 ppm CO.
- Response time: 120 seconds; Recovery time: 6.75 minutes.
- Sensitivity increases with CO concentration from 5 to 40 ppm.
- Silver doping significantly enhances surface reactivity and electron exchange efficiency, contributing to improved sensing performance.

.

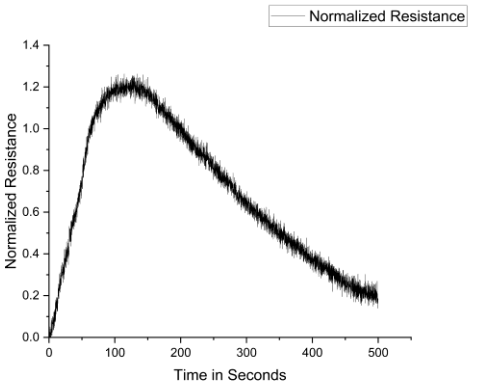

Figure 6.124: 10 ppm CO on 0.10wt % Ag doped BFO at 100 C

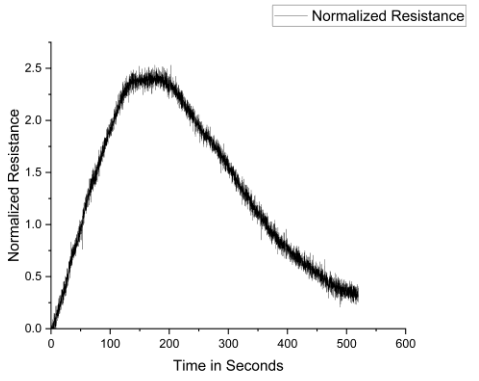

Figure 6.125: 10 ppm CO on 0.10wt % Ag doped BFO at 150 C

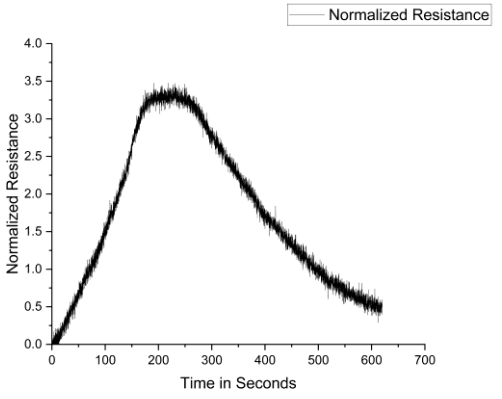

Figure 6.126: 10 ppm CO on 0.10 wt % Ag doped BFO at 200 C

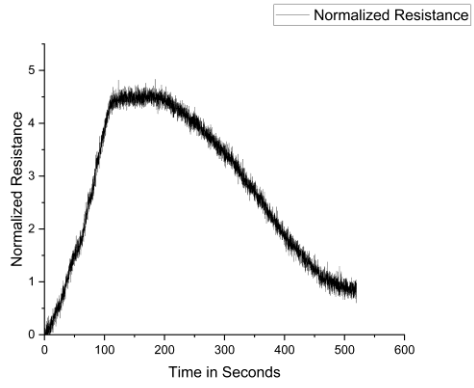

Figure 6.127: 10 ppm CO on 0.10 wt % Ag doped BFO at 250 C

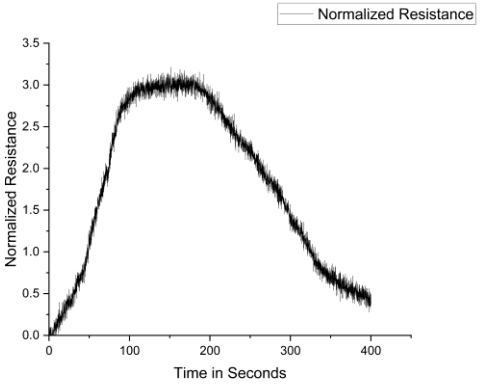

Figure 6.128: 10 ppm CO on 0.10 wt % Ag doped BFO at 300 C

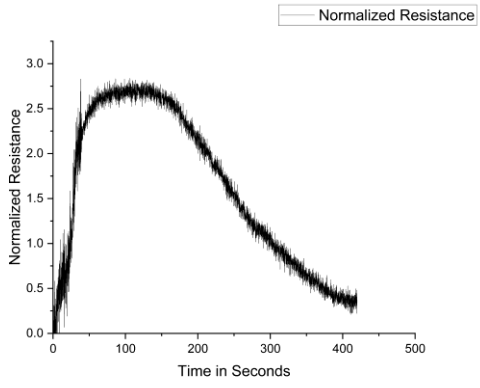

Figure 6.129: 10 ppm CO on 0.10wt % Ag doped BFO at 350 C

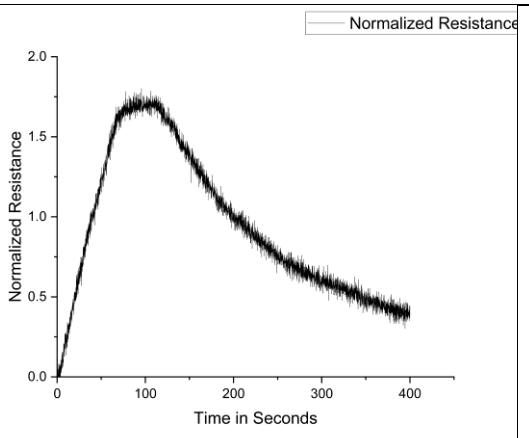

Figure 6.130: 5 PPM CO gas sensing on 0.10 wt % Ag doped BFO

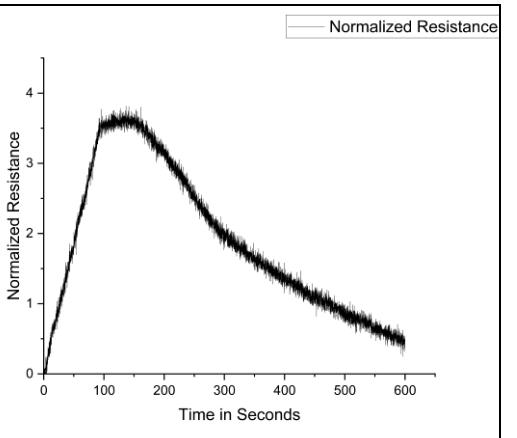

Figure 6.131: 10 PPM CO gas sensing on 0.10 wt % Ag doped BFO

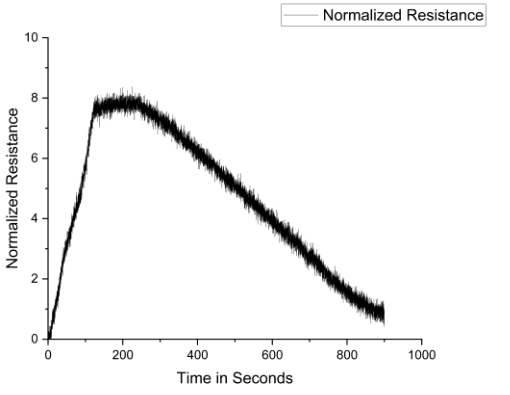

Figure 6.132: Figure 6. 125 20 PPM CO gas sensing on 0.10 wt % Ag doped BFO

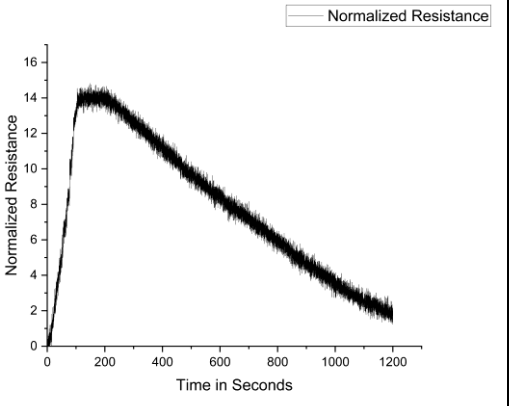

Figure 6.133: 40 PPM CO gas sensing on 0.10 wt % Ag doped BFO

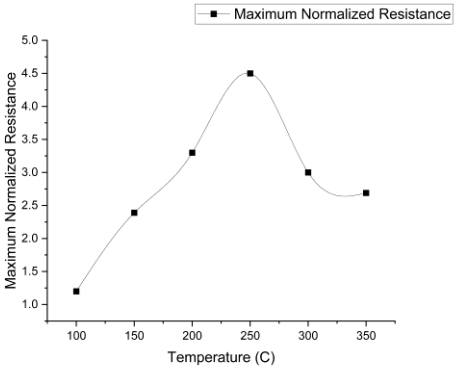

Figure 6.134: Temperature Vs Maximum Normalized Resistance for CO gas sensing on 0.10 wt % Ag doped BFO

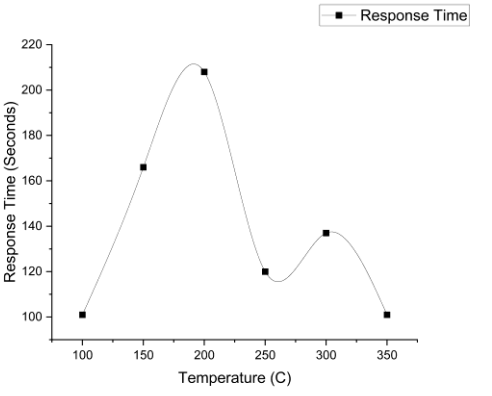

Figure 6.135: Temperature Vs Response Time for CO gas sensing on 0.10 wt % Ag doped BFO.

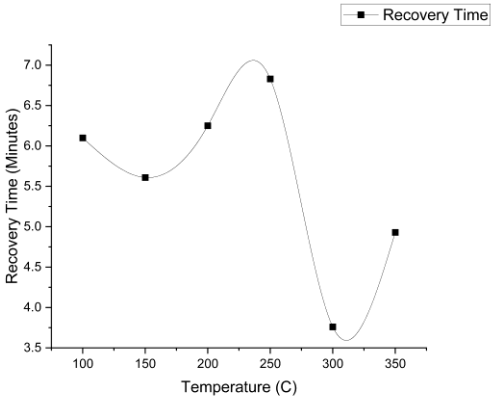

Figure 6.136: Temperature Vs Recovery Time for CO gas sensing on 0.10 wt % Ag doped BFO

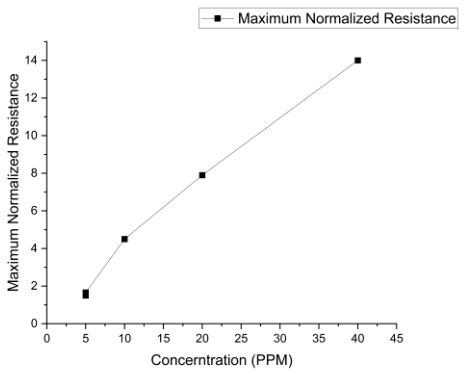

Figure 6.137: Concentration (PPM) Vs Maximum Normalized Resistance for CO gas sensing on 0.10 wt % of Ag doped BFO

6.5.2 NO Gas Sensing Mechanism for 0.10 wt% Ag-Doped BFO

The response of a 0.10 wt% Ag-doped $BiFeO_3$ (BFO) thin film gas sensor toward nitric oxide (NO) gas molecules was experimentally analyzed within the temperature range of 100–350 °C. The experiments were conducted to determine the influence of temperature and gas concentration on the sensitivity, response, and recovery behavior of the sensor.

The response was quantified using Normalized Resistance (R_n), defined as:

- $R_n = (R\_gas - R\_air) / R\_air$

where R_gas is the resistance of the sensor in the presence of NO gas, and R_air is the resistance of the sensor in air before gas exposure.

Temperature-Dependent Response

Figures 6.138–6.143 present the variation of normalized resistance with time at 10 ppm NO concentration for different operating temperatures. In all measurements, two dynamic parameters were extracted:

• Response time (τ_s): Time required for the sensor to reach 90% of its maximum resistance after gas exposure.

• Recovery time (τ_r): Time required for the sensor to return to 10% of its baseline resistance after gas removal.

The temperature-dependent sensitivity of the 0.10 wt% Ag-doped BFO thin film is depicted in Figure 6.148. As the temperature increased, the sensitivity improved and reached its maximum at 200 °C, beyond which it declined. This decrease beyond 200 °C can be attributed to enhanced desorption rates of NO molecules, leading to reduced surface coverage and lower electron exchange activity.

Optimal Operating Temperature

The optimal operating temperature for NO gas detection was identified as 200 °C, offering the best compromise between sensitivity and dynamic response characteristics.

At this temperature, the 0.10 wt% Ag-doped BFO thin film sensor exhibited:

• Maximum normalized resistance: 7.6

• Response time: 195 seconds

• Recovery time: 8.25 minutes

The corresponding response and recovery curves are illustrated in Figures 6.149–6.150, confirming stable, repeatable, and reversible sensing behavior.

Concentration-Dependent Response

To evaluate the effect of NO gas concentration on sensor response, experiments were conducted at the optimal operating temperature (200 °C). The results are summarized in Table 6.3.

NO Concentration (ppm)	Maximum Normalized Resistance
5 ppm	4.0
40 ppm	16.0

The results clearly demonstrate a positive correlation between gas concentration and sensor response, which follows the Langmuir adsorption model. Figures 6.144–6.147 illustrate the transient response profiles for various NO concentrations, while Figure 6.151 presents the dependence of maximum normalized resistance on concentration.

Mechanistic Interpretation

The NO gas sensing mechanism of Ag-doped BFO can be explained through surface adsorption, redox reactions, and charge transfer interactions typical of p-type semiconducting oxides.

In atmospheric air, oxygen molecules adsorb on the BFO surface and form negatively charged oxygen ions by trapping electrons from the valence band:

- $O_2(g) + 2e^- \rightarrow 2O^-(ads)$

Upon exposure to NO gas, the adsorbed oxygen ions interact with NO molecules according to the following surface reaction:

- $NO(g) + O^-(ads) \rightarrow NO_2(g) + e^-$

This process releases electrons back into the BFO lattice, where they recombine with holes, reducing the overall hole concentration. Consequently, the sensor's resistance increases. When NO is removed, the adsorbed oxygen species are replenished, and the resistance returns to its baseline.

Silver doping enhances NO sensing due to the following mechanisms:

1. Catalytic enhancement – Ag promotes faster oxidation of NO to NO_2, increasing electron release.

2. Spillover effect – Activated oxygen species migrate from Ag sites to BFO surfaces, expanding the reaction zone.

3. Electronic modification – Ag alters the surface potential and band alignment, improving charge transfer kinetics.

Summary of Observations

- The 0.10 wt% Ag-doped BFO thin film sensor demonstrated strong and reproducible sensitivity toward NO gas.
- Optimal operating temperature: 200 °C.
- Maximum normalized resistance: 7.6 at 10 ppm NO.
- Response time: 195 seconds; Recovery time: 8.25 minutes.
- Sensitivity increases with NO concentration between 5 and 40 ppm.
- Ag doping enhances catalytic activity, oxygen adsorption, and charge transfer, thereby improving detection efficiency.

.

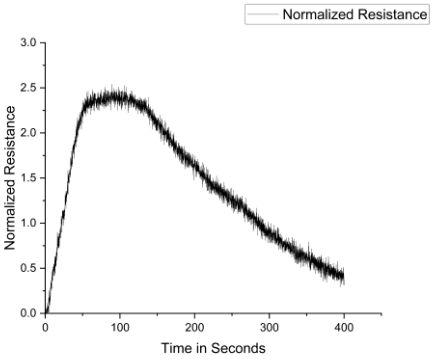

Figure 6.138: 10 ppm NO on 0.10wt % Ag doped BFO at 100 C

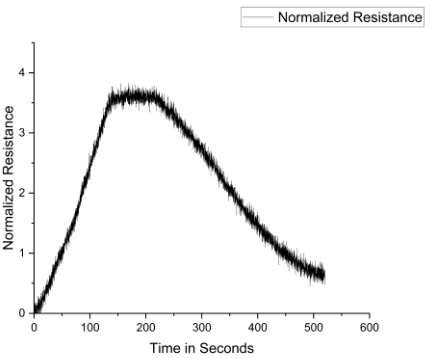

Figure 6.139: 10 ppm NO on 0.10 wt% Ag doped BFO at 150 C

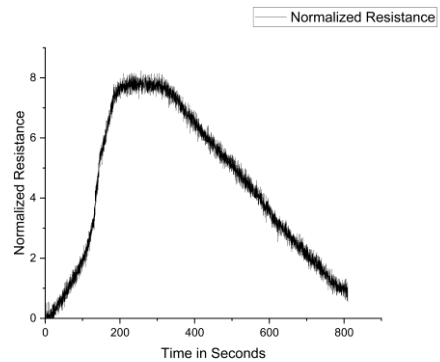

Figure 6.140: 10 ppm NO on 0.10wt % Ag doped BFO at 200 C

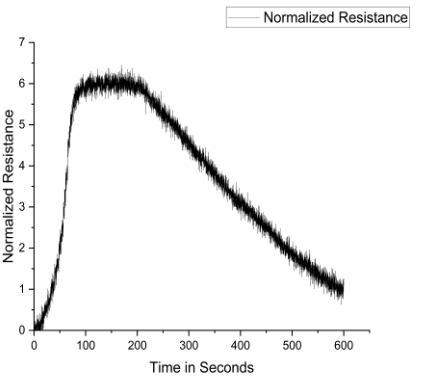

Figure 6.141: 10 ppm NO on 0.10wt % Ag doped BFO at 250 C

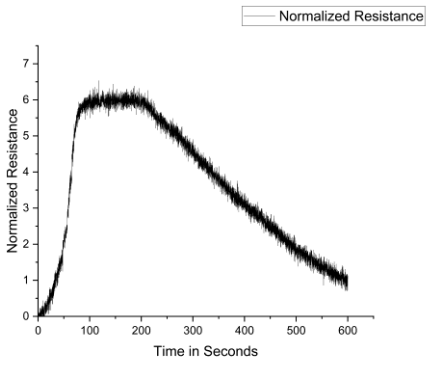

Figure 6.142: 10 ppm NO on 0.10wt % Ag doped BFO at 300 C

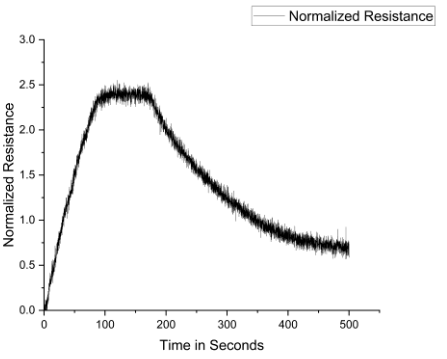

Figure 6.143: 10 ppm NO on 0.10 wt % Ag doped BFO at 350 C

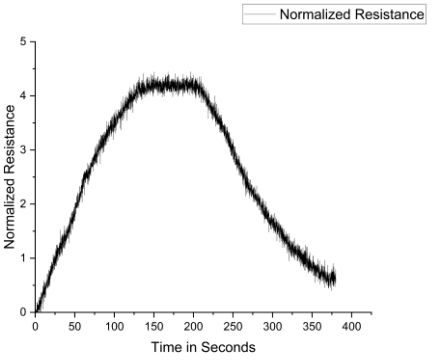

Figure 6.144: 05 PPM NO on 0.10 wt% Ag doped BFO

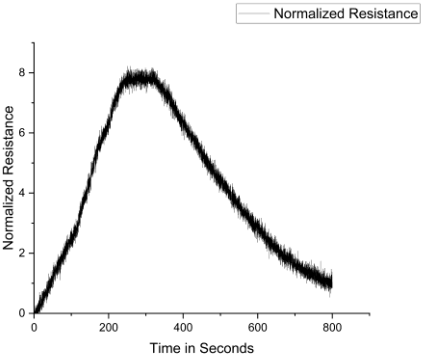

Figure 6.145: 10 PPM NO on 0.10wt % Ag doped BFO

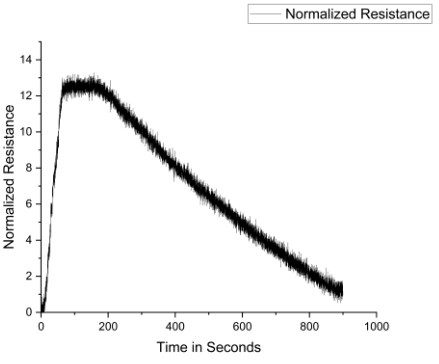

Figure 6.146: 20 PPM NO on 0.10 wt % Ag doped BFO

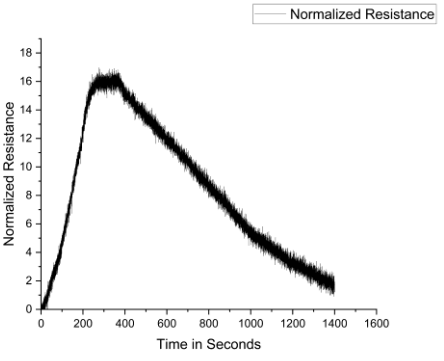

Figure 6.147: 40 PPM NO on 0.10wt % Ag doped BFO

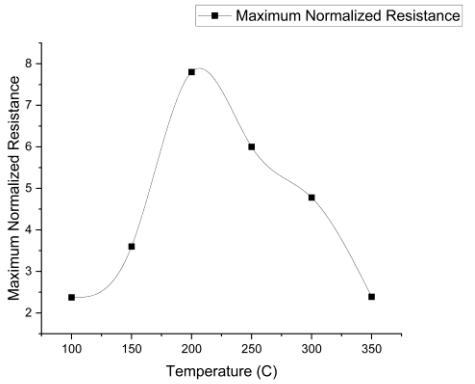

Figure 6.148: Temperature Vs Maximum Normalized Resistance for NO gas sensing on 0.10 wt % Ag doped BFO

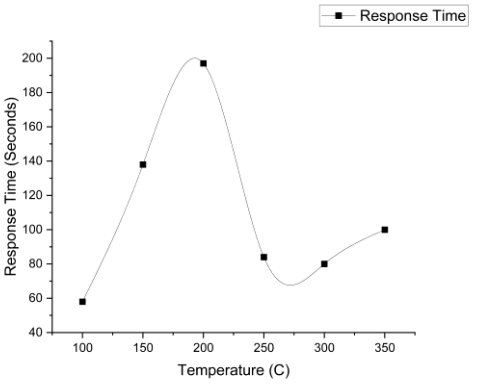

Figure 6.149: Temperature Vs Response Time for NO gas sensing on 0.10 wt % Ag doped BFO

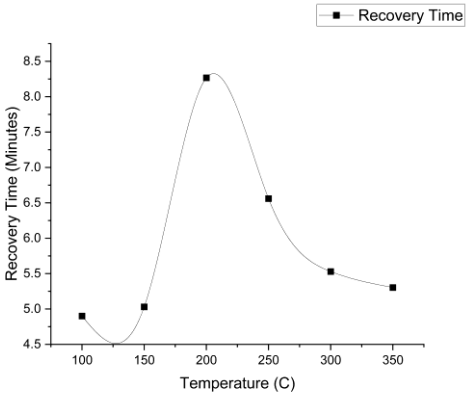

Figure 6.150: Temperature Vs Recovery Time for NO gas sensing on 0.10 wt % of Ag doped BFO

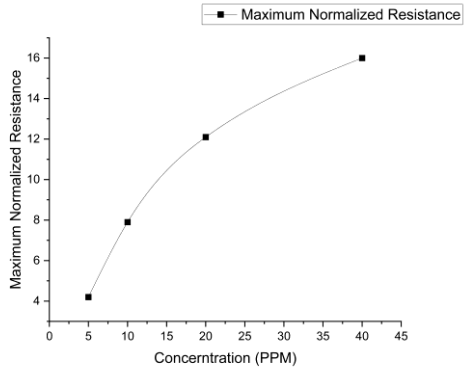

Figure 6.151: Concentration (PPM) Vs Maximum Normalized Resistance for NO gas sensing on 0.10 wt % of Ag doped BFO.

6.5.3 NO_2 Gas Sensing Mechanism for 0.10 wt% Ag-Doped BFO

The response of a 0.10 wt% Ag-doped $BiFeO_3$ (BFO) thin film sensor toward nitrogen dioxide (NO_2) gas molecules was experimentally examined within the temperature range of 100–350 °C. The study aimed to evaluate how temperature and concentration influence the sensitivity, response, and recovery characteristics of the doped BFO thin film sensor.

The sensor response was quantified using Normalized Resistance (R_n), expressed as:

- $R_n = (R\_gas - R\_air) / R\_air$

where R_gas is the resistance of the sensor in the presence of gas, and R_air is the resistance of the sensor in air before the introduction of gas.

Temperature-Dependent Response

Figures 6.152–6.157 depict the normalized resistance versus time plots for 10 ppm NO_2 gas at various temperatures. In each case, two kinetic parameters were used to describe the sensor's performance:

- Response time (τ_s): Time taken by the sensor to reach 90% of its maximum value upon exposure to NO_2 gas.
- Recovery time (τ_r): Time required for the sensor to return to 10% of its baseline resistance after gas removal.

The temperature-dependent sensitivity of the sensor is shown in Figure 6.162. The sensitivity increased steadily with temperature up to 200 °C, after which it declined, indicating the desorption of NO_2 molecules at higher temperatures. This temperature-dependent trend suggests that 200 °C provides the most favorable surface adsorption and charge transfer conditions for NO_2 detection.

Optimal Operating Temperature

The optimal operating temperature for NO_2 detection was determined to be 200 °C, as it provided the best trade-off between response amplitude and recovery efficiency.

At this temperature, the 0.10 wt% Ag-doped BFO thin film exhibited:

- Maximum normalized resistance: 6.8
- Response time: 200 seconds
- Recovery time: 8 minutes

The corresponding response and recovery curves are illustrated in Figures 6.163–6.164, indicating that the film exhibits fast response, good repeatability, and stable recovery behavior at this temperature.

Concentration-Dependent Response

To assess the dependence of sensitivity on gas concentration, experiments were performed at the optimal operating temperature (200 °C). The results are summarized in Table 6.4.

NO_2 Concentration (ppm)	Maximum Normalized Resistance
5 ppm	4.0
40 ppm	16.0

As shown, the normalized resistance increased with gas concentration, demonstrating a near-linear dependence consistent with Langmuir-type adsorption behavior. This indicates that the number of occupied adsorption sites on the sensor surface rises with increasing NO_2 concentration until surface saturation is reached. Figures 6.158–6.161 show the sensor's transient responses at various concentrations, and Figure 6.165 presents the variation of maximum normalized resistance as a function of NO_2 concentration.

Mechanistic Interpretation

The gas-sensing mechanism for NO_2 detection in Ag-doped BFO follows the general redox interaction pathway observed in p-type semiconducting oxides. In air, oxygen molecules adsorb on the sensor surface and capture electrons to form ionized oxygen species:

- $O_2(g) + 2e^- \rightarrow 2O^-(ads)$

When exposed to oxidizing gases such as NO_2, additional electrons are withdrawn from the sensor surface through the following reaction:

- $NO_2(g) + e^- \rightarrow NO_2^-(ads)$

This process increases hole concentration, decreasing the overall resistance of the p-type material. Upon removal of NO_2 gas, the adsorbed species desorb and the resistance returns to its initial value.

Silver doping enhances NO_2 sensing through multiple synergistic effects:

1. Catalytic Activity – Ag acts as a catalytic center for oxygen activation, promoting faster NO_2 adsorption

2. Spillover Effect – Oxygen species migrate from Ag sites to BFO surfaces, increasing reactive area and gas diffusion.

3. Electronic Modulation – Ag alters the band structure and work function of BFO, improving charge transfer and enhancing overall sensor response.

Summary of Observations

- The 0.10 wt% Ag-doped BFO sensor exhibits strong, reversible, and repeatable NO_2 sensing behavior.
- Optimal operating temperature: 200 °C.
- Maximum normalized resistance: 6.8 at 10 ppm NO_2.
- Response time: 200 seconds; Recovery time: 8 minutes.
- Sensitivity increases linearly with NO_2 concentration from 5–40 ppm.
- Ag doping significantly enhances catalytic reactivity, adsorption kinetics, and charge transfer efficiency.

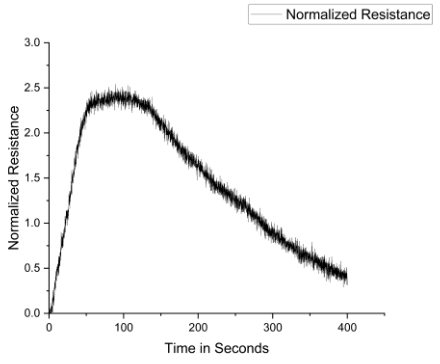

Figure 6.152: 10 ppm NO_2 on 0.10wt % Ag doped BFO at 100 C

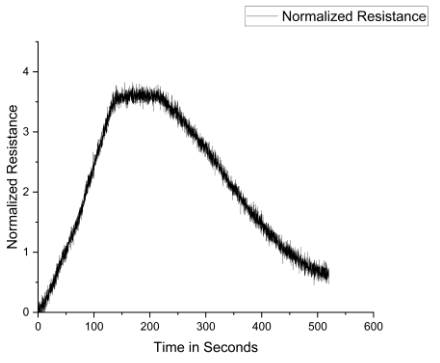

Figure 6.153: 10 ppm NO_2 on 0.10 wt % Ag doped BFO at 150 C

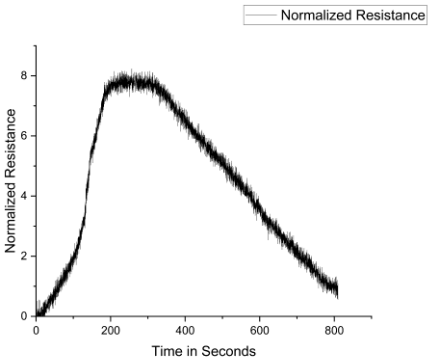

Figure 6.154: 10 ppm NO_2 on 0.10 wt % Ag doped BFO at 200 C

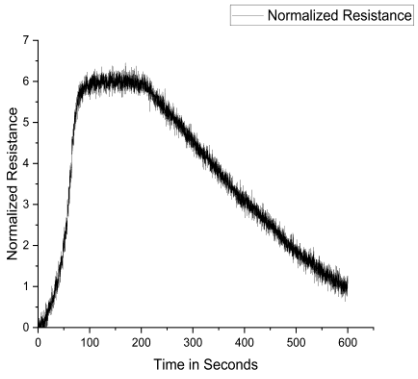

Figure 6.155: 10 ppm NO_2 on 0.10 wt % Ag doped BFO at 250 C

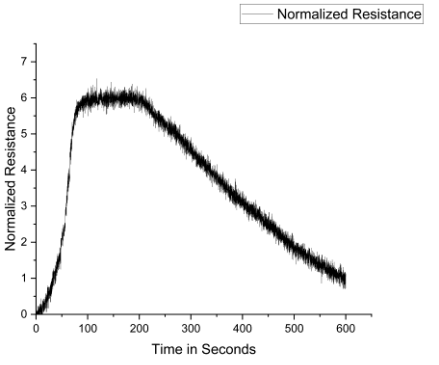

Figure 6.156: 10 ppm NO_2 on 0.10wt % Ag doped BFO at 300 C

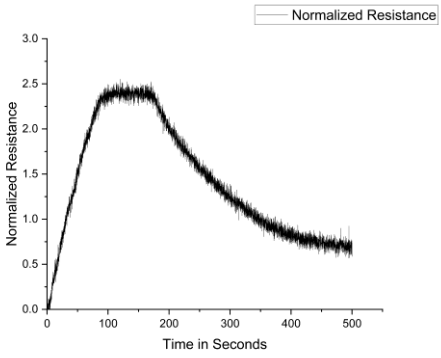

Figure 6.157: 10 ppm NO_2 on 0.10 wt % Ag doped BFO at 350 C

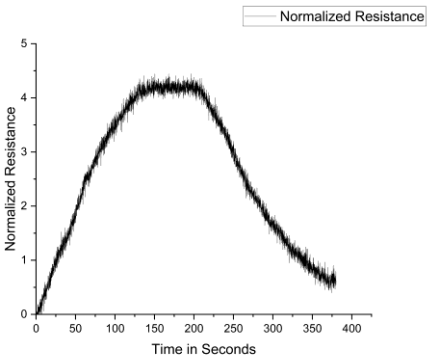

Figure 6.158: 05 PPM NO_2 on 0.10 wt % Ag doped BFO

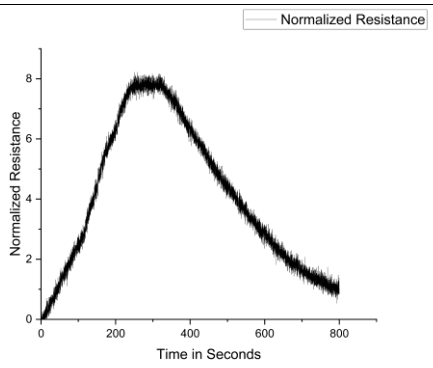

Figure 6.159: 10 PPM NO_2 on 0.10 wt % Ag doped BFO

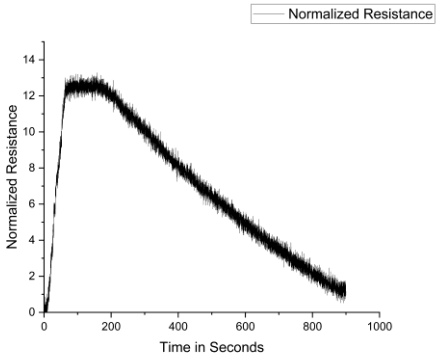

Figure 6.160: 20 PPM NO_2 on 0.10wt % Ag doped BFO

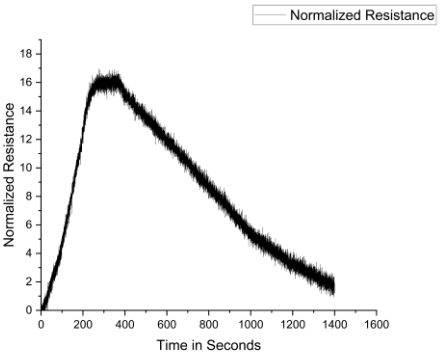

Figure 6.161: 40 PPM NO_2 on 0.10 wt % Ag doped BFO

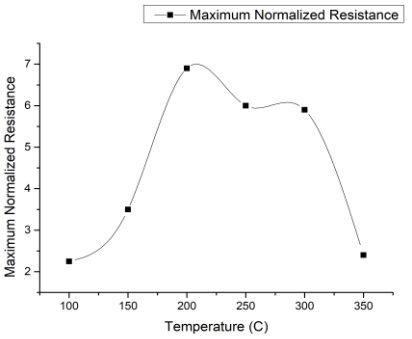

Figure 6.162: Temperature VS Maximum Normalized Resistance for NO_2 gas sensing on 0.10wt% Ag doped BFO

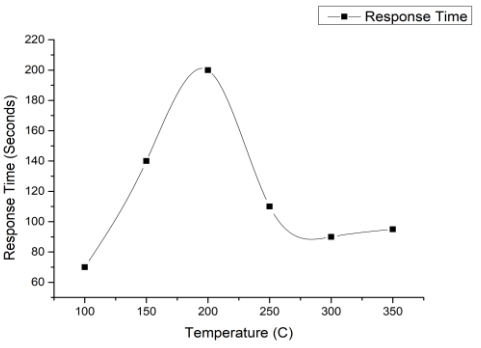

Figure 6.163: Temperature Vs Response Time for NO_2 gas sensing on 0.10wt% Ag doped BFO

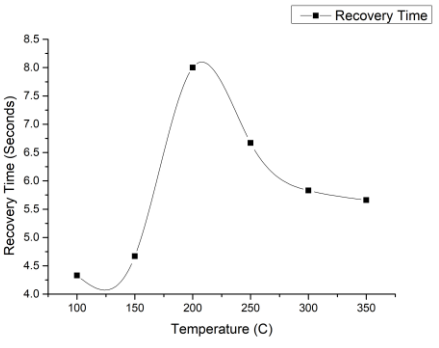

Figure 6.164: Temperature Vs Recovery Time for 0.10wt% Ag doped BFO

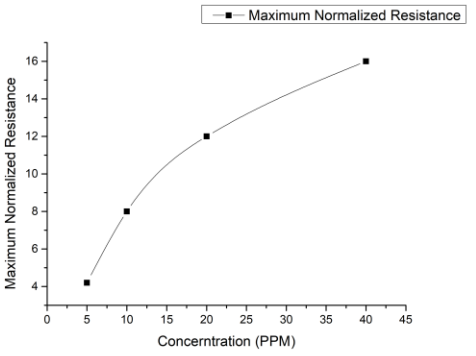

Figure 6.165: Concentration (PPM) Vs Maximum Normalized Resistance for 0.10wt% Ag doped BFO

6.5.4 SO_2 Gas Sensing Mechanism for 0.10 wt% Ag-Doped BFO

The performance of a 0.10 wt% Ag-doped $BiFeO_3$ (BFO) thin film sensor toward sulfur dioxide (SO_2) gas molecules was investigated in the temperature range of 100–350 °C. The aim was to understand the temperature-dependent sensing behavior, response kinetics, and influence of gas concentration on the normalized resistance of the Ag-doped BFO thin film.

The sensor response was quantified using Normalized Resistance (R_n), defined as:

- $R_n = (R\_gas - R\_air) / R\_air$

where R_gas is the resistance of the sensor in the presence of SO_2 gas, and R_air is the resistance of the sensor before the introduction of gas.

Temperature-Dependent Response

Figures 6.166–6.171 depict the normalized resistance versus time plots for 10 ppm SO_2 at different operating temperatures. The response and recovery behavior were characterized using two parameters:

- Response time (τ_s): Time required for the sensor to attain 90% of its maximum value after SO_2 exposure.
- Recovery time (τ_r): Time required for the sensor to return to 10% of its baseline resistance after gas removal.

The temperature-dependent sensitivity is presented in Figure 6.176, showing that the sensor's response increases with temperature, peaks at 250 °C, and then gradually declines beyond this point. The decrease in sensitivity above 250 °C is attributed to accelerated desorption of SO_2 molecules from the active surface, reducing the net adsorption of reactive species.

Optimal Operating Temperature

The optimal operating temperature for SO_2 detection was found to be 250 °C, offering the best compromise between sensitivity, stability, and dynamic response.

At this temperature, the 0.10 wt% Ag-doped BFO thin film sensor exhibited the following characteristics:

- Maximum normalized resistance: 2.0
- Response time: 160 seconds
- Recovery time: 4.25 minutes

Figures 6.177–6.178 illustrate the response and recovery characteristic curves, demonstrating excellent reversibility and repeatability at this temperature.

Concentration-Dependent Response

To analyze the sensor's response as a function of gas concentration, experiments were conducted at the optimal temperature (250 °C). The results are summarized in Table 6.5.

SO_2 Concentration (ppm)	Maximum Normalized Resistance
5 ppm	1.3
40 ppm	2.5

The results reveal that the normalized resistance increases almost linearly with the SO_2 concentration, indicating that more adsorption sites become occupied as the gas concentration rises. Figures 6.172–6.175 show the transient response curves for varying SO_2 concentrations, and Figure 6.179 displays the relationship between maximum normalized resistance and SO_2 concentration.

Mechanistic Interpretation

The gas-sensing behavior of Ag-doped BFO for SO_2 detection follows the principles of surface adsorption and charge exchange typically observed in p-type semiconducting oxides. When exposed to air, oxygen molecules adsorb on the BFO surface and form ionized oxygen species via electron trapping:

- $O_2(g) + 2e^- \rightarrow 2O^-(ads)$

Upon exposure to a reducing gas like SO_2, the gas molecules interact with the adsorbed oxygen species according to the following reaction:

- $SO_2(g) + O^-(ads) \rightarrow SO_3(g) + e^-$

This reaction releases electrons back into the lattice, where they recombine with holes, thereby reducing the hole concentration and increasing the resistance of the p-type BFO material.

Silver doping enhances this sensing mechanism through several synergistic effects:

1. Catalytic enhancement – Ag facilitates redox reactions, lowering activation energy for SO_2 adsorption.
2. Spillover mechanism – Oxygen ions generated at Ag sites migrate to adjacent BFO surfaces, expanding the reactive area.
3. Electronic modification – Ag alters the surface band structure and Fermi level, improving charge transfer efficiency.

Summary of Observations

- The 0.10 wt% Ag-doped BFO thin film sensor exhibits reliable and reversible sensing behavior toward SO_2.
- Optimal operating temperature: 250 °C.
- Maximum normalized resistance: 2.0 at 10 ppm SO_2.
- Response time: 160 seconds; Recovery time: 4.25 minutes.
- Sensitivity increases linearly between 5 ppm and 40 ppm SO_2.
- Ag doping improves oxygen activation and enhances the overall redox reaction rate on the sensor surface.

.

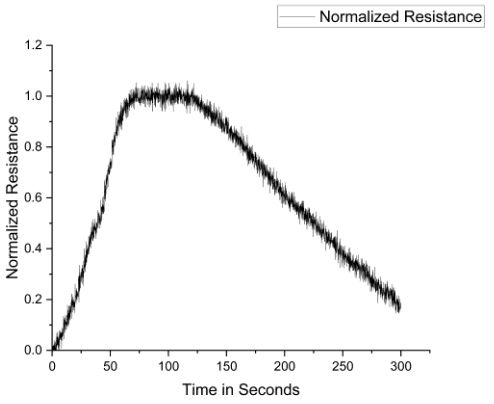

Figure 6.166: 10 ppm SO_2 on 0.10 wt % Ag doped BFO at 100 C

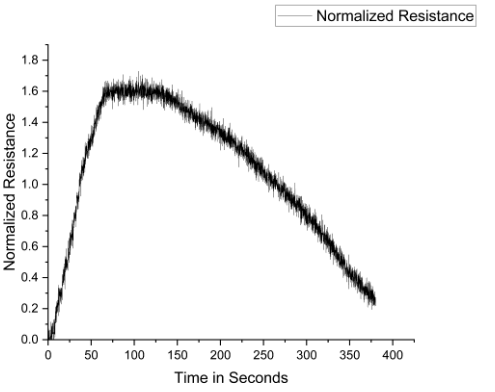

Figure 6.167: Concerntration (PPM) Vs Maximum Normalized Resistance for 0.10wt% Ag doped BFO

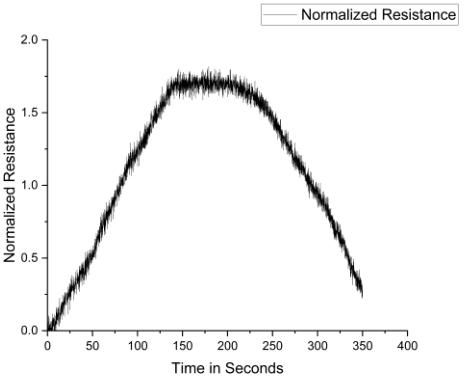

Figure 6.168: 10 ppm SO_2 on 0.10 wt % Ag doped BFO at 200 C

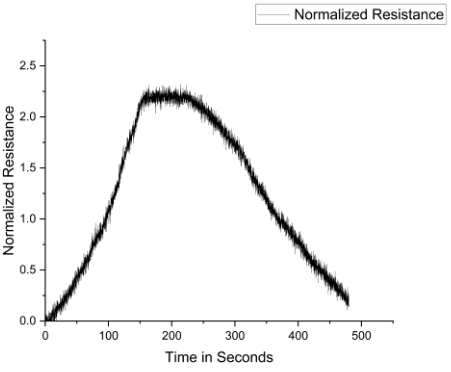

Figure 6.169: 10 ppm SO_2 on 0.10 % Ag doped BFO at 250 C

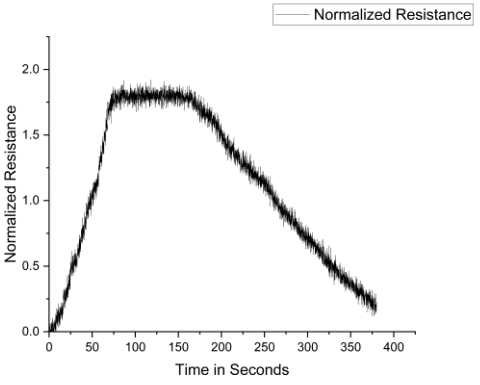

Figure 6.170: 10 ppm SO_2 on 0.10wt % Ag doped BFO at 300 C

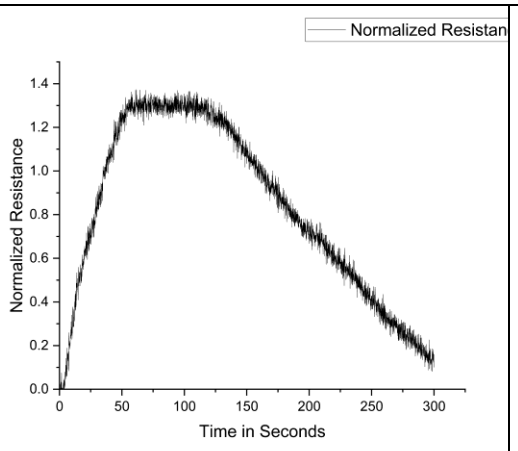

Figure 6.171: 5 ppm SO_2 on 0.10 wt % Ag Doped BFO

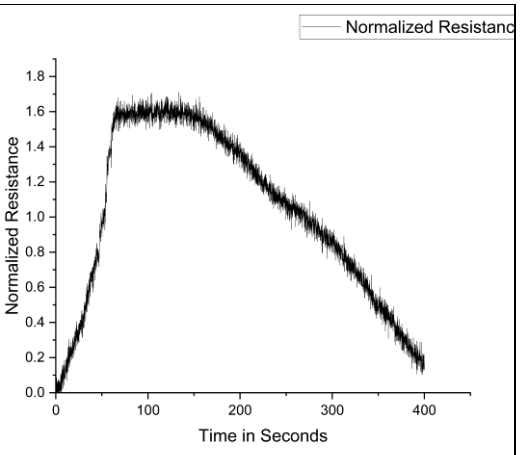

Figure 6.172: 10 ppm SO_2 on 0.10 wt % Ag Doped BFO

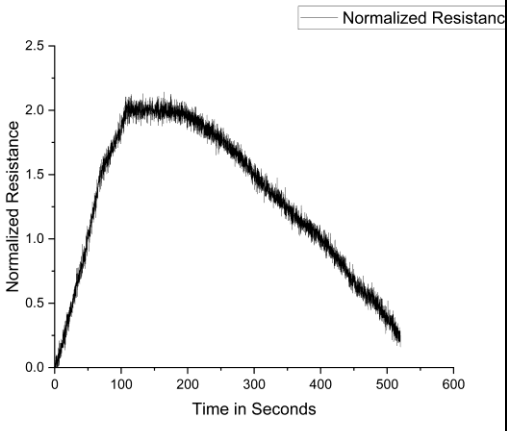

Figure 6.173: 20 ppm SO_2 on 0.10wt % Ag Doped BFO

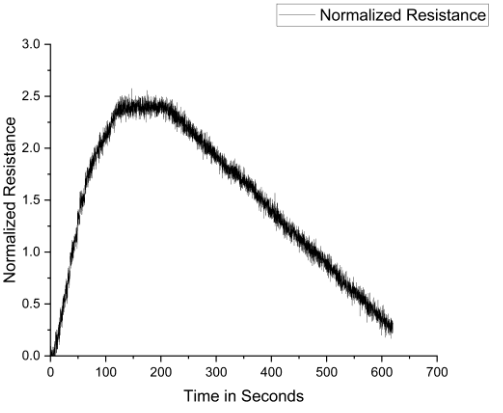

Figure 6.174: 40 ppm SO_2 on 0.10wt % Ag Doped BFO

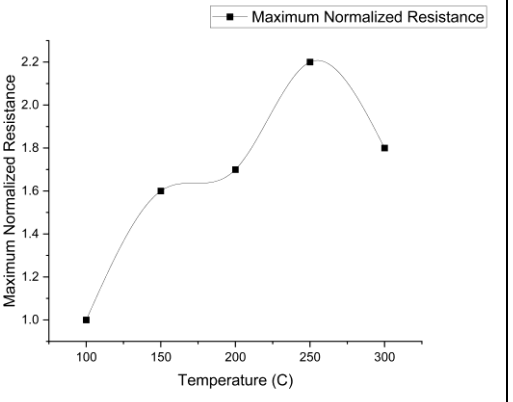

Figure 6.175: Temperature Vs Maximum Normalized Resistance for SO_2 gas sensing on 0.10 wt % of Ag doped BFO

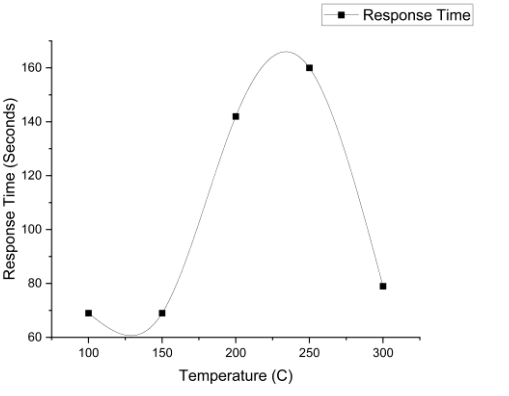

Figure 6.176: Temperature Vs Response Time for SO_2 gas sensing on 0.10 wt % Ag doped BFO

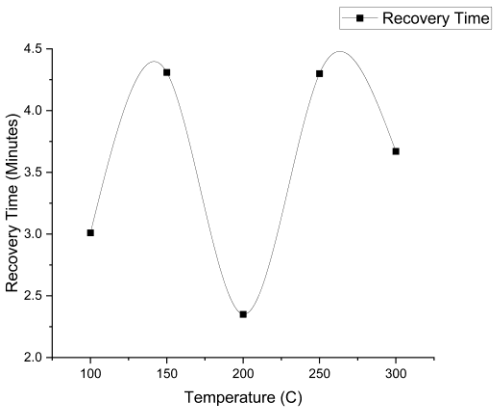

Figure 6.177: Temperature Vs Recovery Time for SO_2 gas sensing on 0.10 wt % of Ag doped BFO

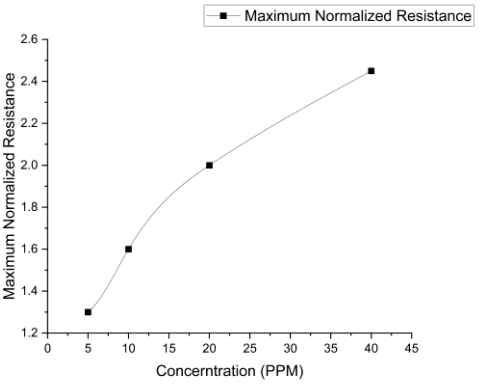

Figure 6.178: Concentration (PPM) Vs Maximum Normalized Resistance for SO_2 gas sensing on 0.10 wt % of Ag doped BFO

6.6.1 CO Gas Sensing Mechanism for 0.15 wt% Ag-Doped BFO

The sensing performance of a 0.15 wt% Ag-doped $BiFeO_3$ (BFO) thin film sensor toward carbon monoxide (CO) gas was evaluated in the temperature range of 100–350 °C. This study aimed to understand how the silver doping concentration influences the CO adsorption and charge transport behavior of the BFO-based gas sensor.

The sensor response was quantified using the Normalized Resistance (R_n), expressed as:

- $R_n = (R\_gas - R\_air) / R\_air$

where R_gas is the resistance of the sensor in the presence of CO gas, and R_air is the resistance of the sensor before the introduction of gas.

Temperature-Dependent Response

Figures 6.174–6.179 display the normalized resistance versus time curves obtained for 10 ppm CO gas at various temperatures. The response time (τ_s) and recovery time (τ_r) were determined as follows:

- Response time (τ_s): Time taken by the sensor to reach 90% of its peak resistance upon exposure to CO gas.
- Recovery time (τ_r): Time taken to return to 10% of its baseline resistance once the gas supply is stopped.

The temperature-dependent sensitivity of the sensor to a 10 ppm concentration is shown in Figure 6.184. The results reveal that the sensor's sensitivity increases with temperature, attaining a maximum at 250 °C, beyond which it decreases due to desorption effects and thermal degradation of surface-active sites.

Optimal Operating Temperature

The optimal operating temperature for CO gas detection was determined to be 250 °C, corresponding to the best trade-off between fast response and complete recovery.

At this temperature, the 0.15 wt% Ag-doped BFO thin film sensor exhibited the following characteristics:
• Maximum normalized resistance: 3.25
• Response time: 210 seconds
• Recovery time: 7.5 minutes
These results confirm that moderate Ag doping (0.15 wt%) enhances surface reactivity and charge transfer without significantly disrupting the BFO lattice.

Concentration-Dependent Response

Concentration-dependent studies were carried out at the optimal operating temperature (250 °C). The results are summarized in Table 6.6, showing the variation of maximum normalized resistance with CO concentration.

CO Concentration (ppm)	Maximum Normalized Resistance
5 ppm	1.1
40 ppm	9.0

As seen in Figures 6.180–6.183, the normalized resistance increases almost linearly with CO concentration, demonstrating that the number of reactive adsorption sites on the surface increases with gas concentration. The linear dependence suggests a first-order adsorption process, typical of surface-limited redox reactions. The correlation between sensitivity and concentration is shown in Figure 6.187.

Mechanistic Interpretation

The gas-sensing mechanism for CO on Ag-doped BFO follows the surface reaction–driven redox process typical of p-type semiconducting oxides. In ambient air, oxygen molecules adsorb on the surface and extract electrons, forming ionized oxygen species according to:

- $O_2(g) + 2e^- \rightarrow 2O^-(ads)$

When exposed to the reducing gas CO, a redox reaction occurs between CO molecules and the pre-adsorbed oxygen ions:

- $CO(g) + O^-(ads) \rightarrow CO_2(g) + e^-$

The release of electrons in this reaction recombines with holes in the p-type BFO material, leading to a temporary decrease in hole concentration and consequently an increase in resistance.
The role of silver doping is crucial for improving sensing performance:
1. Catalytic enhancement – Ag provides active catalytic sites that accelerate CO oxidation reactions.
2. Electronic modification – Ag doping modifies the local electronic structure and narrows the bandgap, facilitating charge transfer.
3. Spillover effect – Adsorbed oxygen migrates from Ag sites to BFO grains, expanding the effective sensing area.
4. Improved grain connectivity – Enhanced sintering and particle contact improve charge mobility across the film.

Summary of Observations

• The 0.15 wt% Ag-doped BFO thin film sensor demonstrates excellent response and recovery behavior for CO detection.
• Optimal operating temperature: 250 °C.
• Maximum normalized resistance: 3.25 at 10 ppm CO.
• Response time: 210 seconds; Recovery time: 7.5 minutes.
• Sensitivity increases linearly with CO concentration between 5–40 ppm.
• Ag doping significantly improves the oxidation efficiency and accelerates the adsorption–desorption cycle.

.

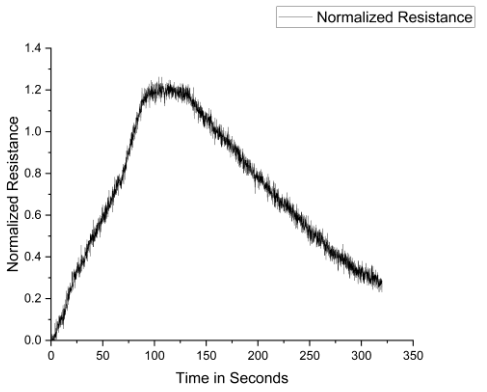

Figure 6.179: 10 ppm CO on 0.15 wt% Ag doped BFO at 100 C

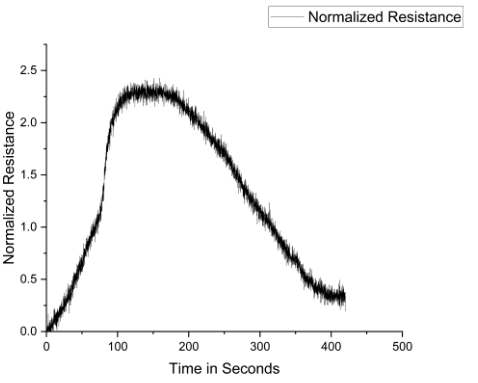

Figure 6.180: 10 ppm CO on 0.15wt % Ag doped BFO at 150 C

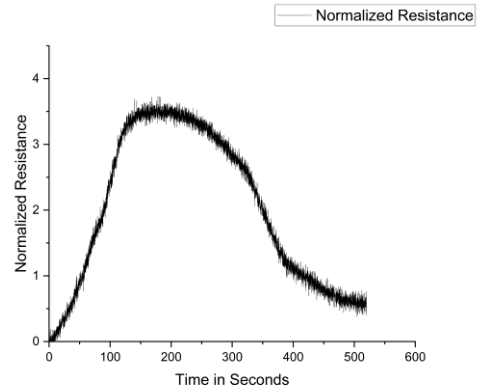

Figure 6.181: 10 ppm CO on 0.15wt % Ag doped BFO at 200 C

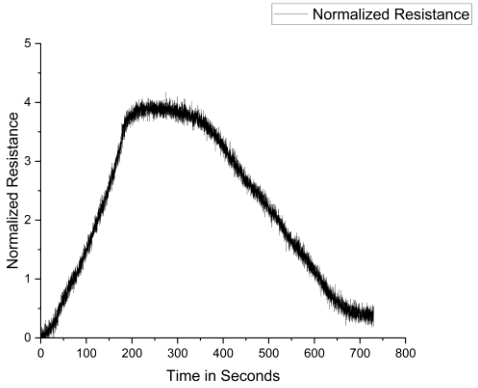

Figure 6.182: 10 ppm CO on 0.15 wt % Ag doped BFO at 250 C

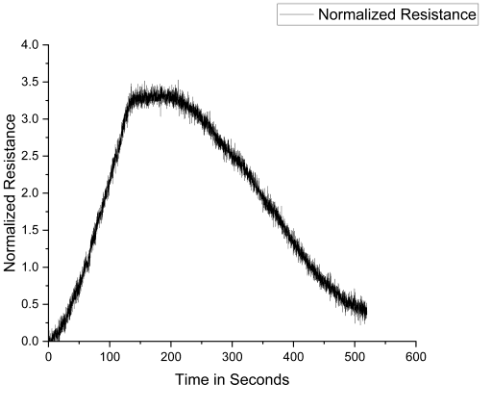

Figure 6.183: 10 ppm CO on 0.15wt % Ag doped BFO at 300 C

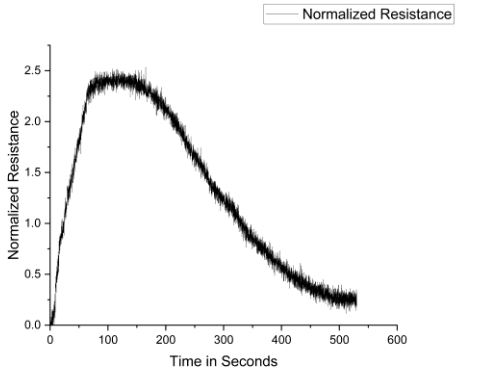

Figure 6.184: 10 ppm CO on 0.15 wt % Ag doped BFO at 350 C

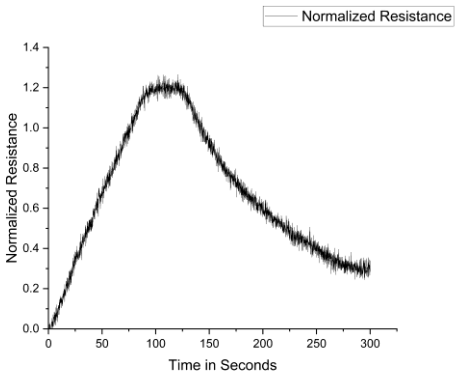

Figure 6.185: 05 PPM CO on 0.15 wt% Ag doped BFO

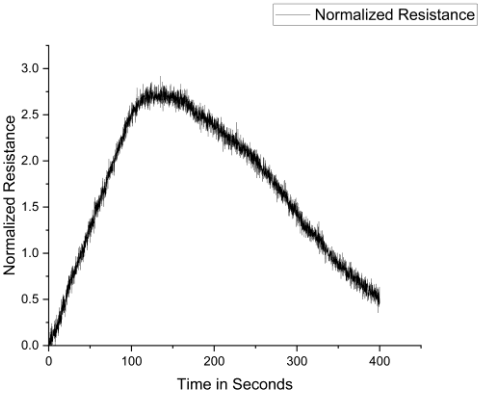

Figure 6.186: 10 PPM CO on 0.15 wt% Ag doped BFO

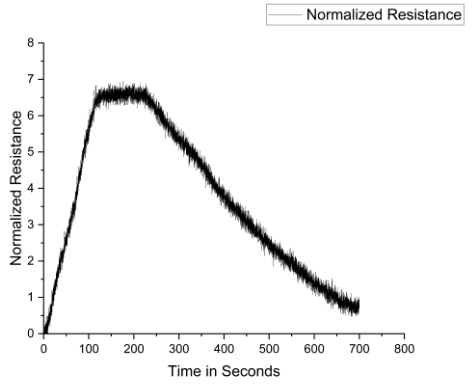

Figure 6.187: 20 PPM CO on 0.15wt % Ag doped BFO

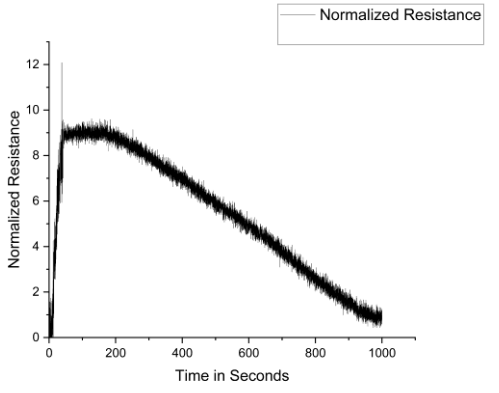

Figure 6.188: 40 PPM CO on 0.15wt % Ag doped BFO

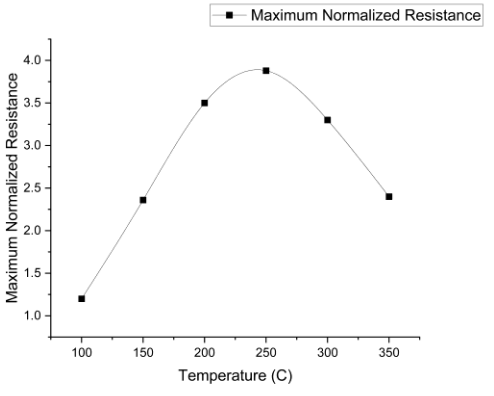

Figure 6.189: Temperature Vs Maximum Normalized Resistance for CO gas sensing on 0.15 wt % Ag doped BFO

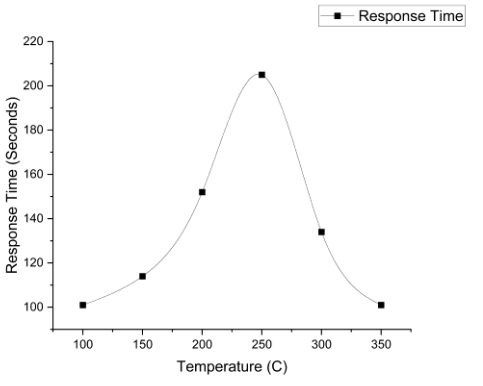

Figure 6.190: Temperature Vs Response Time for CO gas sensing on 0.15 wt % Ag doped BFO

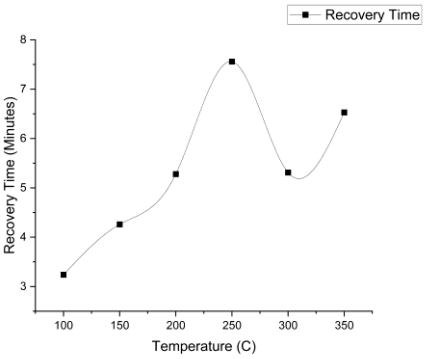

Figure 6.191: Temperature Vs Recovery Time for CO gas sensing on 0.15 wt % Ag doped BFO

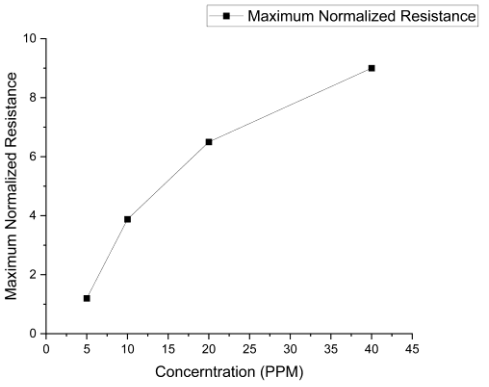

Figure 6.192: Concentration (PPM) Vs Maximum Normalized Resistance for CO gas sensing on 0.15 wt % Ag doped BFO

6.6.2 NO_2 Gas Sensing Mechanism for 0.15 wt% Ag-Doped BFO

The gas sensing performance of the 0.15 wt% Ag-doped $BiFeO_3$ (BFO) thin film sensor toward nitrogen dioxide (NO_2) gas was evaluated within a temperature range of 100–350 °C. This study investigates how silver doping affects the surface adsorption, desorption, and charge transfer dynamics during gas exposure.

The sensor response was determined from the Normalized Resistance (R_n), defined as:

- $R_n = (R\_gas - R\_air) / R\_air$

where R_gas is the resistance of the sensor in the presence of NO_2 gas, and R_air is the baseline resistance of the sensor in air before gas exposure.

Temperature-Dependent Response

Figures 6.193–6.198 illustrate the variation of normalized resistance with time for 10 ppm NO_2 gas at different operating temperatures. For each measurement:

• Response time (τ_s): Time taken to reach 90% of maximum resistance upon gas exposure.

• Recovery time (τ_r): Time taken to return to 10% of the baseline value once the gas is removed.

The temperature-dependent sensitivity of the sensor at 10 ppm concentration is depicted in Figure 6.203. It is observed that the sensitivity increases with temperature, reaching a peak at 250 °C, after which it declines due to faster desorption at higher temperatures.

The response and recovery characteristic curves of the 0.15 wt% Ag-doped BFO film for NO_2 gas detection are shown in Figures 6.204–6.205.

Optimal Operating Temperature

An operating temperature of 250 °C was identified as optimal, providing the best balance between response magnitude and recovery efficiency.

At this temperature, the sensor exhibited:

- Maximum normalized resistance: 2.0
- Response time: 80 seconds
- Recovery time: 8 minutes

Silver doping enhances the chemisorption of oxygen species and facilitates charge transfer processes, thereby improving the sensor's responsiveness to NO_2 molecules.

Concentration-Dependent Response

At the optimal temperature (250 °C), concentration-dependent experiments were performed for NO_2 in the range of 5–40 ppm. The obtained results are summarized in Table 6.7, which lists the maximum normalized resistance at different gas concentrations.

NO_2 Concentration (ppm)	Maximum Normalized Resistance
5 ppm	2.3
40 ppm	2.7

Figures 6.199–6.202 show the transient response curves of the sensor to different concentrations of NO_2, while Figure 6.206 presents the plot of maximum normalized resistance as a function of gas concentration.

Mechanistic Interpretation

The sensing mechanism of NO_2 on p-type Ag-doped BFO follows a surface charge transfer process typical of semiconducting oxides. In ambient air, oxygen molecules are adsorbed and ionized by capturing electrons from the conduction band:

- $O_2(g) + e^- \rightarrow O_2^-(ads)$

When exposed to oxidizing gas like NO_2, additional electron withdrawal occurs according to the following reactions:

- $NO_2(g) + e^- \rightarrow NO_2^-(ads)$
- $NO_2(g) + O^-(ads) \rightarrow NO_3^-(ads)$

These reactions reduce the hole concentration in the p-type BFO layer, thereby increasing the overall resistance of the film. The process is reversible, as desorption of NO_2 molecules restores the equilibrium carrier concentration.

Role of Silver Doping:

1. Enhanced adsorption sites – Ag acts as a catalytic center, improving NO_2 molecule dissociation and adsorption.
2. Improved charge transfer – The Ag–O–Fe interface facilitates faster electron mobility.
3. Spillover effect – Adsorbed NO_2 species migrate between Ag and BFO sites, expanding active regions.
4. Modified electronic structure – Ag alters the Fermi level position, improving band bending and charge exchange efficiency.

Summary of Observations

- The 0.15 wt% Ag-doped BFO thin film demonstrates reliable NO_2 detection across 100–350 °C.
- Optimum temperature: 250 °C.
- Maximum normalized resistance: 2.0 at 10 ppm NO_2
- Response time: 80 s; Recovery time: 8 min.
- Linear concentration dependence observed between 5–40 ppm.
- Silver doping improves both catalytic activity and electron transport, enhancing sensor selectivity and responsiveness..

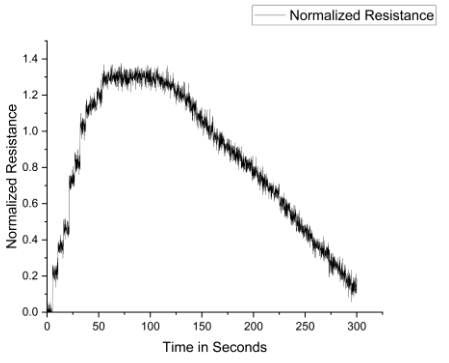

Figure 6.193: 10 ppm NO_2 on 0.15 wt% Ag doped BFO at 100 C

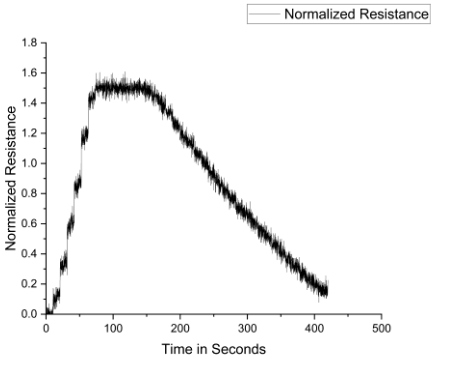

Figure 6.194: 10 ppm NO_2 on 0.15 wt % Ag doped BFO at 150 C

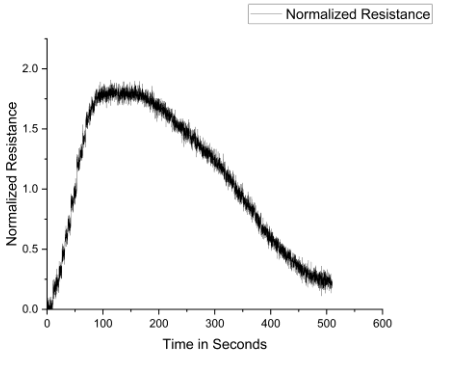

Figure 6.195: 10 ppm NO_2 on 0.15wt % Ag doped BFO at 200 C

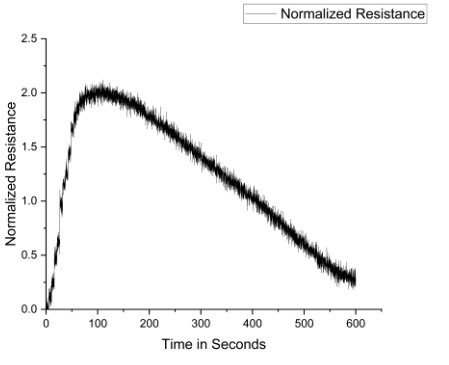

Figure 6.196: 10 ppm NO_2 on 0.15 wt% Ag doped BFO at 250 C

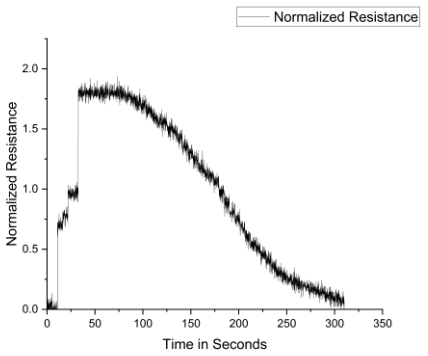

Figure 6.197: 10 ppm NO_2 on 0.15wt % Ag doped BFO at 300 C

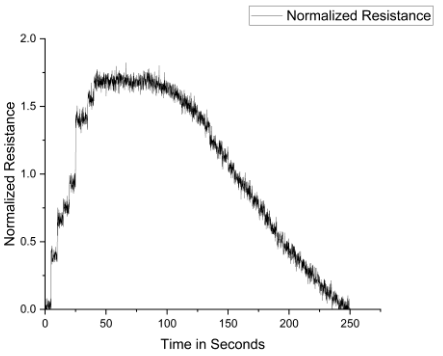

Figure 6.198: 10 ppm NO_2 on 0.15 wt% Ag doped BFO at 350 C

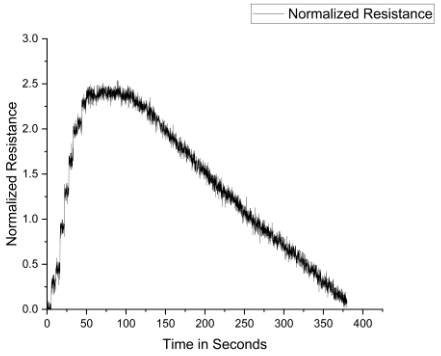

Figure 6.199: 05 PPM NO_2 on 0.15wt % Ag doped BFO

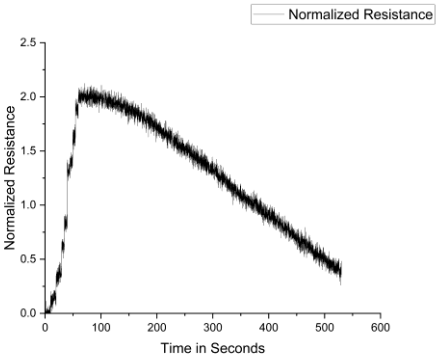

Figure 6.200: 10 PPM NO_2 on 0.15 wt% Ag doped BFO

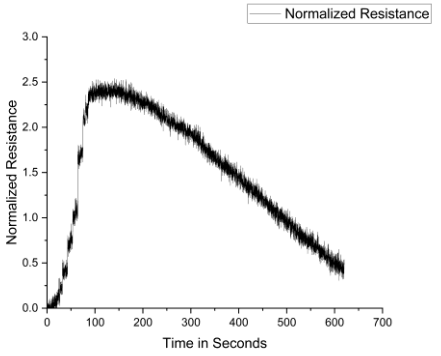

Figure 6.201: 20 PPM NO_2 on 0.15wt % Ag doped BFO

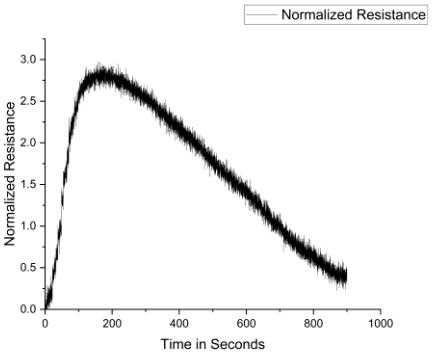

Figure 6.202: 40 PPM NO_2 on 0.15wt % Ag doped BFO

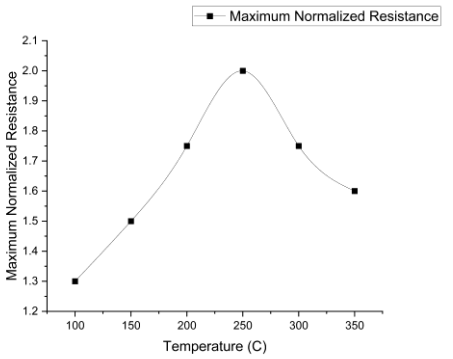

Figure 6.203: Temperature Vs Maximum Normalized Resistance for NO_2 gas sensing on 0.15 wt % Ag doped BFO

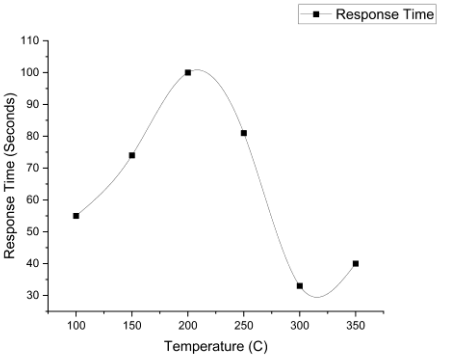

Figure 6.204: Temperature Vs Response Time for NO_2 gas sensing on 0.15 wt % Ag doped BFO

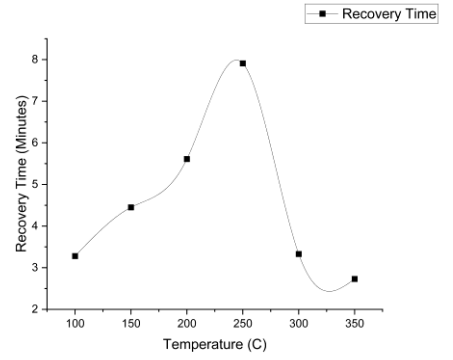

Figure 6.205: Temperature Vs Recovery Time for NO_2 gas sensing on 0.15 wt % of Ag doped BFO

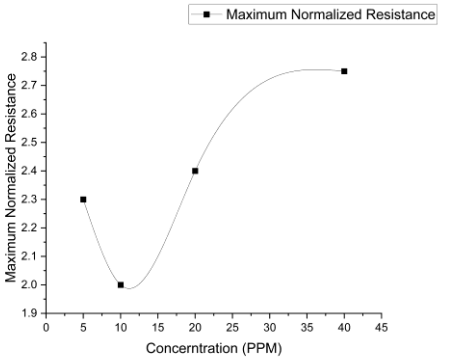

Figure 6.206: Concentration (PPM) Vs Maximum Normalized Resistance for NO_2 gas sensing on 0.15 wt % of Ag doped BFO

6.6.3 SO_2 Gas Sensing Mechanism for 0.15 wt% Ag-Doped BFO

The sensing response of 0.15 wt% Ag-doped $BiFeO_3$ (BFO) thin film sensors toward sulfur dioxide (SO_2) gas was studied in the temperature range of 100–350 °C. This investigation aimed to determine how silver doping affects the adsorption–desorption kinetics and charge carrier modulation under exposure to a reducing gas such as SO_2.

The sensor's response was quantified using Normalized Resistance (R_n), defined as:

- $R_n = (R\_gas - R\_air) / R\_air$

where R_gas represents the sensor resistance in the presence of SO_2 gas, and R_air represents the resistance of the sensor in air before gas exposure.

Temperature-Dependent Response

Figures 6.202–6.207 display the variation in normalized resistance with time for 10 ppm SO_2 gas at various operating temperatures. For each measurement:

- Response time (τ_s): The time taken to reach 90% of the maximum resistance upon gas exposure.
- Recovery time (τ_r): The time taken to return to 10% of the baseline resistance after gas removal.

The temperature-dependent sensitivity of the sensor toward 10 ppm SO_2 is presented in Figure 6.212. The sensitivity initially increases with temperature and reaches its maximum at 350 °C, beyond which it decreases due to faster desorption and reduced surface oxygen activity.

Figures 6.213–6.214 illustrate the response and recovery characteristic curves for SO_2 gas detection at various temperatures.

Optimal Operating Temperature

The optimal operating temperature for SO_2 detection was found to be 350 °C, which provides the best compromise between sensitivity and dynamic response.

At this temperature, the following parameters were obtained:

- Maximum normalized resistance: 2.0
- Response time: 160 seconds
- Recovery time: 3.4 minutes

The improved sensing response is attributed to the increased activation of chemisorbed oxygen species and enhanced surface catalytic activity at elevated temperatures facilitated by silver doping.

Concentration-Dependent Response

At the optimal operating temperature (350 °C), concentration-dependent studies were conducted over a range of 5–40 ppm SO_2 gas. The experimental data are summarized in Table 6.8, which presents the variation of normalized resistance with gas concentration.

SO_2 Concentration (ppm)	Maximum Normalized Resistance
5 ppm	1.5
40 ppm	2.5

Figures 6.208–6.211 show the transient response of the sensor at various SO_2 concentrations, while Figure 6.215 presents the maximum normalized resistance versus concentration.

Mechanistic Interpretation

The sensing mechanism of SO_2 on Ag-doped BFO follows the surface-controlled charge transfer process characteristic of p-type oxide semiconductors. In air, oxygen molecules are adsorbed on the surface and ionized via electron capture:

- $O_2(g) + 2e^- \rightarrow 2O^-(ads)$

When the sensor is exposed to SO_2, a redox reaction occurs between SO_2 and the adsorbed oxygen ions on the surface, releasing electrons and altering the charge carrier density:

- $SO_2(g) + O^-(ads) \rightarrow SO_3(g) + e^-$

The released electrons recombine with holes in the p-type BFO, reducing the hole concentration and leading to an increase in resistance. Upon gas removal, adsorbed species desorb and oxygen reoccupies surface sites, restoring the equilibrium resistance.

Role of Silver Doping

Silver doping plays a significant role in enhancing the SO_2 sensing characteristics through the following mechanisms:

1. Catalytic enhancement – Ag acts as an active site for SO_2 oxidation, accelerating surface reactions.

2. Electronic modification – Ag introduces localized energy states and modulates the Fermi level, facilitating electron exchange.

3. Spillover effect – Oxygen species adsorbed on Ag migrate to the BFO surface, increasing active area coverage.

4. Improved grain connectivity – Ag improves microstructural uniformity and enhances charge transport pathways, leading to faster sensor response.

Summary of Observations

- The 0.15 wt% Ag-doped BFO thin film exhibits high responsiveness and stability toward SO_2 gas.
- Optimal temperature: 350 °C.
- Maximum normalized resistance: 2.0 at 10 ppm SO_2.
- Response and recovery times: 160 s and 3.4 min, respectively.
- Linear concentration dependence observed between 5–40 ppm.
- Silver incorporation significantly enhances surface reactivity, adsorption kinetics, and sensor stability.

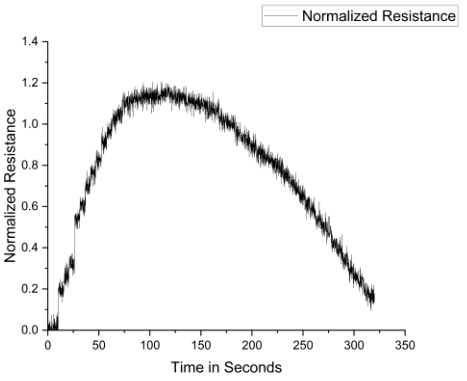

Figure 6.207: 10 PPM SO_2 on 0.15 wt % of Ag doped BFO at 100 C

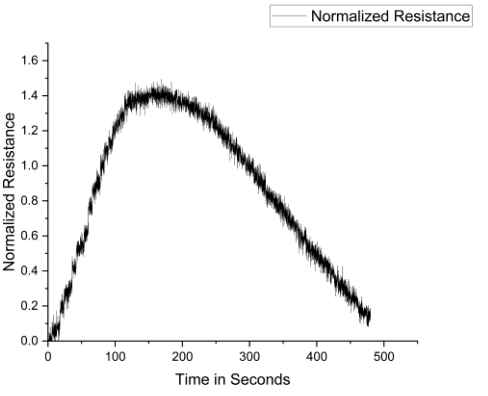

Figure 6.208: 10 ppm SO_2 on 0.15wt % Ag doped BFO at 150 C

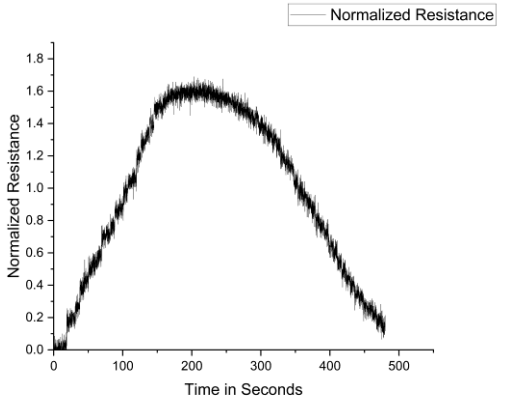

Figure 6.209: 10 ppm SO_2 on 0.15wt % Ag doped BFO at 200 C

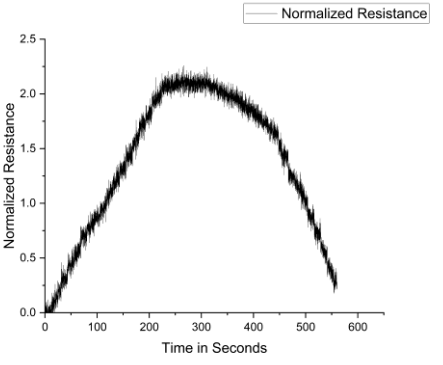

Figure 6.210: 10 ppm SO_2 on 0.15wt % Ag doped BFO at 250 C

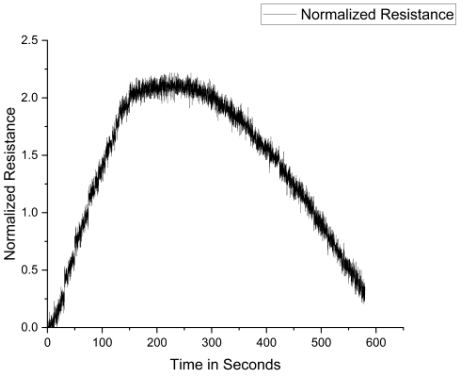

Figure 6.211: 10 ppm SO_2 on 0.15 wt % Ag doped BFO at 300 C

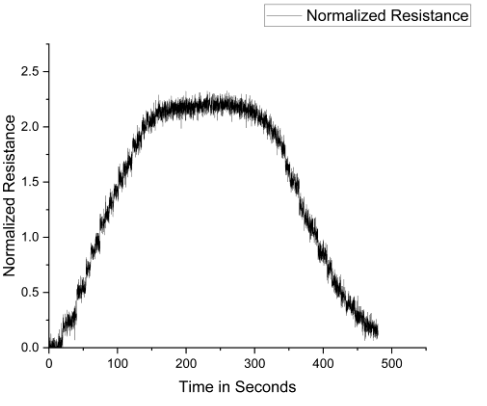

Figure 6.212: 10 ppm SO_2 on 0.15 wt % Ag doped BFO at 350 C

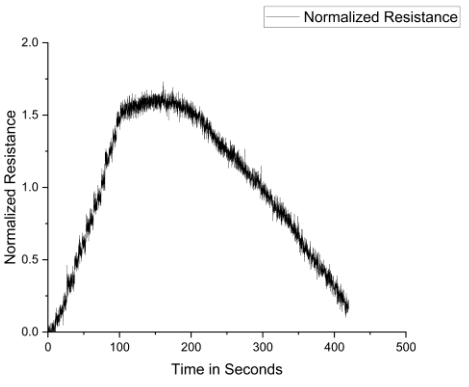

Figure 6.213: 5 ppm SO_2 on 0.15wt % Ag Doped BFO

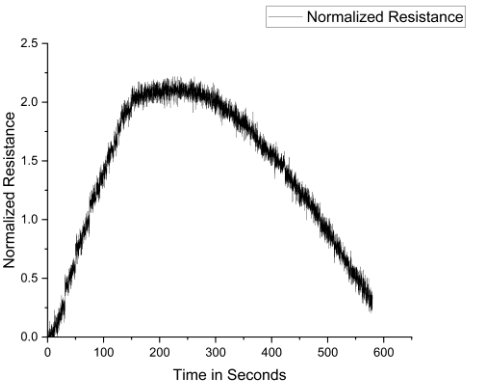

Figure 6.214: 10 ppm SO_2 on 0.15wt % Ag Doped BFO

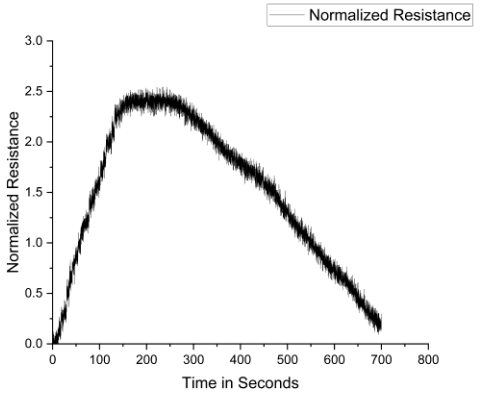

Figure 6.215: 20 ppm SO_2 on 0.15wt % Ag Doped BFO

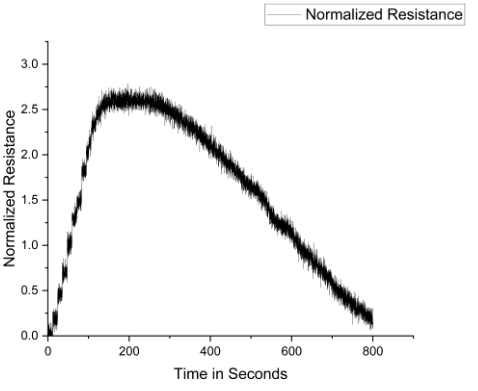

Figure 6.216: 40 ppm SO_2 on 0.15 wt % Ag Doped BFO

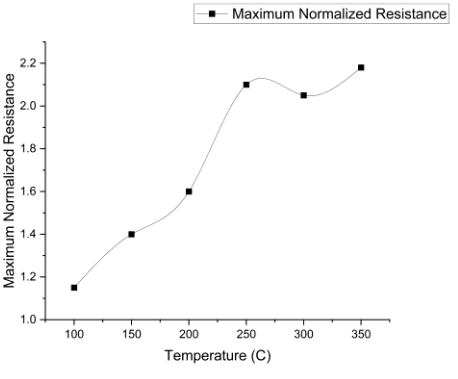

Figure 6.217: Temperature Vs Maximum Normalized Resistance for SO_2 gas sensing on 0.15 wt % Ag doped BFO

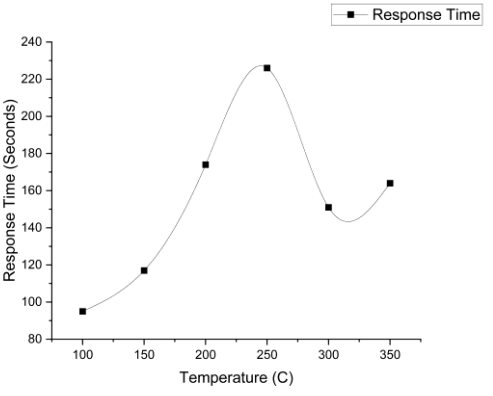

Figure 6.218: Temperature Vs Response Time for SO_2 gas sensing on 0.15 wt % Ag doped BFO

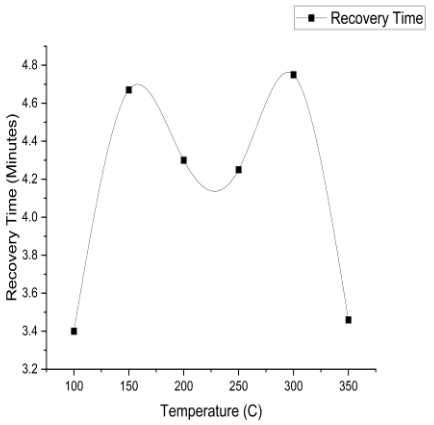

Figure 6.219: Temperature Vs Recovery Time for SO_2 gas sensing on 0.15 wt % Ag doped BFO

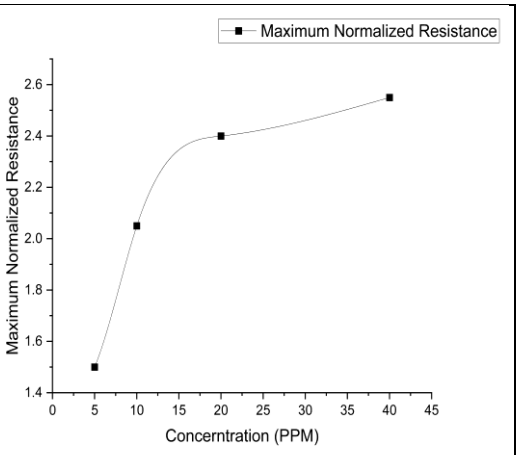

Figure 6.220: Concentration (PPM) Vs Maximum Normalized Resistance for SO_2 gas sensing on Ag doped BFO

6.7 Summary of Gas Sensing Performance of Pristine and Ag-Doped BFO Sensors

Table 6.2 presents the summarized results of gas sensing performance for pristine $BiFeO_3$ (BFO) and Ag-doped BFO films with doping concentrations of 0.05 wt%, 0.10 wt%, and 0.15 wt%. The table includes key sensing parameters such as optimum operating temperature, maximum normalized resistance, response and recovery times, and responses at 5 ppm and 40 ppm gas concentrations for four target gases — CO, NO, NO_2, and SO_2.

- **Table 6.2: Summary of Gas Sensing on Pristine BFO and Ag-Doped BFO**

Parameter	Pure BFO	0.05 wt% Ag-Doped BFO	0.10 wt% Ag-Doped BFO	0.15 wt% Ag-Doped BFO
Optimum Temperature (°C)	CO – 300 NO – 200 NO_2 – 300 SO_2 – 350	CO – 300 NO – 200 NO_2 – 300 SO_2 – 300	CO – 250 NO – 200 NO_2 – 200 SO_2 – 250	CO – 250 NO_2 – 250 SO_2 – 350
Maximum Normalized Resistance	CO – 1.6 NO – 3.3 NO_2 – 1.8 SO_2 – 1.8	CO – 5.2 NO – 7.5 NO_2 – 2.6 SO_2 – 2.3	CO – 4.5 NO – 7.6 NO_2 – 6.8 SO_2 – 2.2	CO – 3.25 NO_2 – 2.0 SO_2 – 2.2
Response Time (s)	CO – 65 NO – 130 NO_2 – 65 SO_2 – 180	CO – 110 NO – 120 NO_2 – 80 SO_2 – 119	CO – 120 NO – 195 NO_2 – 200 SO_2 – 160	CO – 210 NO_2 – 80 SO_2 – 160

Recovery Time (min)	CO – 3.0 NO – 4.75 NO_2 – 7.0 SO_2 – 3.6	CO – 4.9 NO – 7.6 NO_2 – 3.75 SO_2 – 3.4	CO – 6.75 NO – 8.25 NO_2 – 8.0 SO_2 – 4.25	CO – 7.5 NO_2 – 8.0 SO_2 – 3.4
Maximum Normalized Resistance (5 ppm)	CO – 1.0 NO – 2.5 NO_2 – 1.05 SO_2 – 0.75	CO – 1.5 NO – 2.1 NO_2 – 1.4 SO_2 – 1.3	CO – 1.5 NO – 4.0 NO_2 – 4.0 SO_2 – 1.3	CO – 1.1 NO_2 – 2.3 SO_2 – 1.5
Maximum Normalized Resistance (40 ppm)	CO – 8.0 NO – 12.1 NO_2 – 2.65 SO_2 – 2.6	CO – 13.8 NO – 18.1 NO_2 – 2.7 SO_2 – 2.7	CO – 14.0 NO – 16.0 NO_2 – 16.0 SO_2 – 2.5	CO – 9.0 NO_2 – 2.7 SO_2 – 2.5

- **Discussion and Comparative Analysis**
- **CO Gas Sensing**

The CO gas sensing performance of Ag-doped BFO indicates that silver incorporation significantly improves sensor response and lowers the optimum temperature. For pure BFO, the optimum temperature is 300 °C, which remains the same for 0.05 wt% Ag-BFO, but with a maximum normalized resistance increase from 1.6 to 5.2. For 0.10 wt% and 0.15 wt% Ag-BFO, the optimum temperature decreases to 250 °C, with further enhancement in responsiveness. This behavior demonstrates that Ag doping increases the availability of active surface sites and promotes oxygen adsorption–desorption reactions. Although the response and recovery times are slightly longer in Ag-doped films, their sensitivity to CO gas increases sharply with gas concentration, confirming an improved catalytic effect of Ag.

- **NO Gas Sensing**

In the case of NO gas, both pure and Ag-doped BFO show an optimum operating temperature of 200 °C. However, the response intensity is significantly enhanced upon Ag doping, rising from 3.3 (pure BFO) to 7.5 and 7.6 for 0.05 wt% and 0.10 wt% Ag-BFO, respectively. The response and recovery dynamics remain comparable, but the increased normalized resistance and linearity with gas concentration confirm that Ag dopants improve the NO gas adsorption capacity and charge transfer efficiency of the BFO matrix.

- **NO_2 Gas Sensing**

For NO_2 detection, Ag-doped samples exhibit improved response at reduced temperatures. The optimum temperature decreases from 300 °C (pure BFO) to 250 °C (Ag-doped BFO), with a marked improvement in normalized resistance, especially for the 0.10 wt% Ag-BFO, which achieved a maximum normalized resistance of 6.8. The recovery and response times remain nearly constant across all samples, indicating that Ag doping enhances electronic sensitivity without adversely affecting kinetics. The results reveal that silver incorporation improves electron exchange between NO_2 molecules and surface oxygen species, leading to enhanced sensing efficiency.

- **SO_2 Gas Sensing**

For SO_2 gas, pure BFO exhibits an optimum temperature of 350 °C, while Ag doping reduces it to 300 °C (0.05 wt%) and 250 °C (0.10 wt%), indicating improved catalytic activation at lower temperatures. However, unlike CO and NO, the improvement in normalized resistance is less pronounced, suggesting that SO_2 interacts more weakly with the BFO surface. The response and recovery times show minimal improvement after doping, and the normalized resistance remains nearly constant with increasing SO_2 concentration. This indicates that SO_2 sensing on Ag-doped BFO is mainly limited by slower surface reaction kinetics compared to more reactive reducing gases such as CO or NO.

- **Overall Observations**
  - Silver doping enhances CO and NO sensing significantly, with improved sensitivity and lower operating temperatures.
  - NO_2 sensing performance also improves due to better electron exchange and catalytic activity.
  - SO_2 response shows limited improvement, suggesting that the reaction kinetics are less favorable for this gas on the BFO surface.
  - The optimal Ag concentration for balancing sensitivity and response kinetics is approximately 0.10 wt%.
  - Ag nanoparticles promote enhanced oxygen adsorption, improved carrier mobility, and faster charge transfer dynamics, making Ag-BFO films promising candidates for multifunctional gas sensing applications in automotive and industrial environments.

6.9 Multivariate Analysis

In practical sensing environments, multiple gases are often present simultaneously, making selectivity a critical factor in gas sensor design. To evaluate the ability of the sensor material to distinguish between individual and mixed gases, multivariate analysis was employed using Principal Component Analysis (PCA). The experiments were performed using the 5 wt% Ag-doped $BiFeO_3$ (Ag-BFO) sensor at an operating temperature of 200 °C, which had been earlier established as an optimal temperature for NO gas sensing.

To examine gas discrimination behavior, nine different gas compositions were analyzed. These included individual gases (NO, CO, NO_2, and SO_2) and five different mixtures containing various combinations of these gases—each with a concentration of 10 ppm per component. The mixture configurations are summarized in Table 6.3, where the gases are represented as rows and the sensing features—response, response time, and recovery time—are given as columns. This dataset forms a 9 × 3 matrix, which was used as the input for PCA analysis.

Table 6.3: Multivariate Analysis Parameters

Test	Test Sample	NO (ppm)	CO (ppm)	NO_2 (ppm)	SO_2 (ppm)	Response	Response Time (s)	Recovery Time (s)
1	(10 ppm NO, NO_2, SO_2)	10	0	10	10	8.2	140	470
2	(10 ppm NO, CO, SO_2)	10	10	0	10	7.9	100	480

3	(10 ppm NO, NO_2, CO, SO_2)	10	10	10	10	9.1	135	490
4	(10 ppm NO, NO_2, CO)	10	10	10	0	9.3	130	480
5	(10 ppm CO, NO_2, SO_2)	0	10	10	10	3.5	70	280
6	(10 ppm NO)	10	0	0	0	7.5	120	456
7	(10 ppm CO)	0	10	0	0	2.1	110	294
8	(10 ppm NO_2)	0	0	10	0	2.8	80	225
9	(10 ppm SO_2)	0	0	0	10	2.0	119	204

Principal Component Analysis (PCA) Results

The collected data matrix was processed using Principal Component Analysis (PCA) to reduce dimensionality and identify distinct clustering patterns for each gas species and mixture. The 2D PCA score plot (see Figure 6.216) illustrates how the samples are distributed across the first two principal components (PC1 and PC2), which capture the majority of variance in the dataset.

It is evident from the PCA distribution that NO-containing mixtures occupy a distinct region of the plot, primarily along the boundary between the first and fourth quadrants of the PC space. In contrast, mixtures that do not contain NO cluster separately in the second and fourth quadrants, clearly indicating that the NO component strongly influences the sensor's response characteristics. Furthermore, the mixed gas compositions form well-defined clusters distinct from the individual gases, demonstrating the ability of the 5 wt% Ag-BFO sensor to differentiate between complex mixtures.

The PCA results confirm that the sensor exhibits a high level of qualitative discrimination, even in the presence of cross-sensitivity. The successful separation of analytes in the PCA score space verifies that multivariate statistical tools such as PCA can effectively distinguish between different gas species and mixed environments based on their dynamic response patterns.

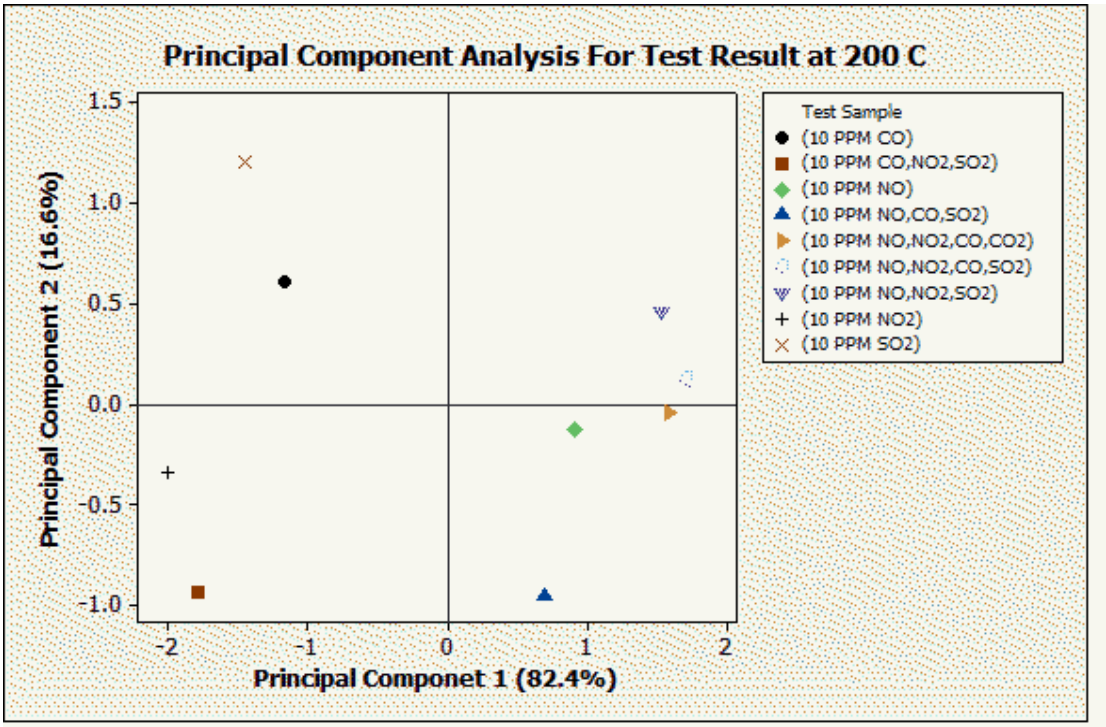

Figure 6.216: PCA Score Plot for Mixed Gas Samples at 200°C

Interpretation and Significance

This analysis demonstrates that 5 wt% Ag-doped $BiFeO_3$ possesses strong potential for use in multi-gas discrimination systems. By analyzing temporal parameters (response, response time, recovery time), the PCA model successfully identified unique gas signatures for NO, CO, NO_2, and SO_2, as well as their mixtures.

Such multivariate approaches pave the way toward the development of "electronic nose" systems, where multiple sensor responses combined with statistical pattern recognition methods can provide both qualitative identification and quantitative estimation of target gases in complex environments.

References

[1] M. A. Ahmed, S. F. Mansour, S. I. El-Dek, and M. Abu-Abdeen, "Conduction and magnetization improvement of BiFeO3 multiferroic nanoparticles by Ag+ doping," *Mater. Res. Bull.*, vol. 49, no. 1, pp. 352–359, 2014, doi: 10.1016/j.materresbull.2013.09.011.

[2] Q. Li, W. Zhang, C. Wang, J. Ma, L. Ning, and H. Fan, "Ag modified bismuth ferrite nanospheres as a chlorine gas sensor," *RSC Advances*, vol. 8, no. 58. pp. 33156–33163, 2018, doi: 10.1039/C8RA06247A.

[3] M. Dewan and S. B. Majumder, "Selective carbon monoxide sensing properties of bismuth iron oxide," *Materialia*, vol. 7, no. February, 2019, doi: 10.1016/j.mtla.2019.100363.

[4] S. D. Waghmare, V. V. Jadhav, S. F. Shaikh, R. S. Mane, J. H. Rhee, and C. O'Dwyer, "Sprayed tungsten-doped and undoped bismuth ferrite nanostructured films for reducing and oxidizing gas sensor applications," *Sensors Actuators, A Phys.*, vol. 271, no. 2010, pp. 37–43, 2018, doi:

10.1016/j.sna.2018.01.008.

Research Outcomes and Pathways for Future Development of BFO-Based Sensors

7.1 Summary of the Study

The detection of toxic gases and the assessment of their concentrations have become increasingly important in recent years due to growing environmental and public health concerns. The global demand for improved environmental monitoring and safety has driven extensive research on solid-state gas sensors. Among these, semiconducting metal oxide and perovskite-based gas sensors have attracted significant attention for their simplicity, low cost, robustness, and ability to detect a wide range of reducing and oxidizing gases.

Traditionally, tin oxide (SnO_2) has been the most extensively studied material for gas sensing applications. However, research trends in the past decade have shifted toward exploring perovskite oxides such as bismuth ferrite ($BiFeO_3$, BFO) due to their excellent thermal stability, tunable electronic properties, and multiferroic behavior. The use of perovskite nanomaterials offers several advantages, including a high surface area-to-volume ratio, strong surface reactivity, and the potential to achieve selective detection through doping and surface engineering.

In the present work, we focused on the development and characterization of pristine and silver-doped $BiFeO_3$ (Ag–BFO) as a promising material for the detection of common automotive and industrial pollutants such as CO, NO, NO_2, and SO_2.The research was carried out in three major parts:

(a) Computational Investigation (DFT Studies)

The first part of the study employed Density Functional Theory (DFT) simulations to understand the interaction between gas molecules (CO, CO_2, NO, NO_2, and CH_4) and both pure and Ag-doped BFO (010) surfaces. Key findings include:

- The optimized structure of BFO (010) exhibited a band gap of 0.698 eV, confirming semiconducting behavior suitable for gas sensing.
- Adsorption energy and total density of states (TDOS) calculations revealed a strong correlation between electronic structure and gas–surface interaction.
- After Ag doping, the adsorption energy for NO and NO_2 increased significantly, along with a noticeable rise in TDOS near the Fermi level, indicating enhanced charge transfer and stronger adsorption.
- Conversely, CH_4 showed a reduction in adsorption energy and electronic activity after Ag incorporation, suggesting poor sensitivity toward methane.
- The order of adsorption affinity across all gases remained $CH_4 < CO_2 < CO < NO_2 < NO$, identifying NO as the most strongly adsorbed species on both pristine and doped BFO surfaces.

These DFT insights provided a theoretical foundation for understanding the adsorption mechanism and guiding material synthesis for experimental validation.

(b) Material Synthesis and Characterization

In the second part, nanocrystalline thin and thick films of pure and Ag-doped BFO were synthesized using an auto-combustion method with glycine as fuel. The effect of Ag doping on structural, morphological, and electrical properties was extensively characterized using:

- **X-ray Diffraction (XRD)** — to confirm crystallinity and phase purity, revealing rhombohedral-hexagonal structure.
- **Scanning Electron Microscopy (SEM)** — to study surface morphology and porosity, critical for gas adsorption.
- **Energy Dispersive X-ray Spectroscopy (EDS)** — to verify elemental composition and successful incorporation of Ag dopant.

All films were annealed at 600 °C to ensure thermal stability and enhance crystallinity before gas exposure. Subsequent gas-sensing tests revealed significant improvements in sensitivity and selectivity toward CO and NO gases for Ag-doped samples, confirming the synergy between theoretical predictions and experimental results.

(c) Experimental Fabrication and Testing

The final phase of the work involved the fabrication and testing of gas sensing devices based on pure and Ag-doped BFO films. A custom-built gas sensing chamber was developed, capable of operating under both static and flow conditions. A microcontroller-based PID temperature controller with an accuracy of ±0.5 °C was designed to regulate the temperature in the range of 50–400 °C. The electrical resistance of the sensors under gas exposure was measured using a Keithley 195A digital multimeter interfaced via GPIB for precise data acquisition.

The combination of these systems allowed for real-time monitoring of gas adsorption dynamics and temperature-dependent sensor performance, ensuring reproducibility and accuracy of the experimental results.

7.2 Future Perspectives

The findings of this study establish Ag-doped $BiFeO_3$ as a promising material for high-temperature gas sensing applications. However, there remain several opportunities to further optimize and expand this research. The following directions are proposed for future work:

1. **Size Reduction and Nanostructuring:** Decreasing particle size below **20 nm** may substantially enhance gas sensitivity and selectivity, as smaller particles have higher surface reactivity and complete charge carrier depletion across grains.
2. **Stability and Long-Term Performance:** Long-duration tests under real atmospheric conditions are essential to validate the operational stability and repeatability of Ag–BFO sensors. Extended annealing studies at varying temperatures could further improve material robustness.
3. **Surface Engineering and Defect Control:**

Introducing deliberate surface defects, oxygen vacancies, or non-stoichiometric sites can modify adsorption–desorption kinetics, leading to better selectivity and faster response times.

4. **Multi-Dopant Systems:**
   Co-doping with other noble or transition metals (such as Pd, Pt, or Cu) can create synergistic effects, improving both catalytic activity and charge carrier mobility.
5. **Morphological Control:**
   Developing BFO-based nanostructures such as nanorods, nanotubes, and nanofibers can dramatically increase active surface area and lower detection limits to the ppb range.
6. **Integrated Sensor Arrays and AI-Based Signal Processing:**
   Implementing micro-machined sensor arrays integrated with pattern recognition algorithms (e.g., Artificial Neural Networks – ANN) can overcome the limitations of single-sensor selectivity. Such systems could be used in electronic nose (E-nose) configurations for real-time gas mixture analysis.
7. **Hybrid and Composite Systems:**
   Combining Ag–BFO with graphene, CNTs, or conductive polymers can create hybrid materials with enhanced conductivity and improved adsorption dynamics.

7.3 Concluding Remarks

This research demonstrates that Ag-doped $BiFeO_3$ is a versatile and thermally stable material capable of detecting multiple pollutant gases at high temperatures. The combined theoretical and experimental approach adopted here provides a comprehensive understanding of gas–surface interactions, offering a rational path for designing next-generation, high-performance gas sensors.

The insights gained from this study not only advance the field of perovskite-based gas sensing materials but also open new opportunities for multifunctional sensor development integrating AI-driven analysis and nanostructure engineering for sustainable environmental monitoring.

Book Description / Synopsis

This book presents an integrated study of perovskite-based chemiresistive gas sensors, combining Density Functional Theory (DFT) modeling and experimental validation to establish a comprehensive understanding of gas–surface interactions. The research focuses on Bismuth Ferrite ($BiFeO_3$) and its Ag-doped variants, highlighting their potential as efficient, low-cost materials for detecting toxic automotive and industrial gases such as CO, NO, NO_2, and SO_2.

Beginning with the fundamental principles of perovskite oxides, the book explores the electronic structure, adsorption energetics, and charge transfer mechanisms of BFO surfaces using DFT simulations. These theoretical insights are then linked to experimental studies involving the synthesis, structural and spectroscopic characterization, and gas sensing performance of pure and Ag-doped BFO films.

Through systematic analysis, the work demonstrates how Ag doping enhances adsorption, sensitivity, and selectivity, while reducing operating temperatures. The book concludes with perspectives on future advancements in nanostructured gas sensors, AI-assisted sensing arrays, and hybrid material systems.

This volume is a valuable resource for researchers, engineers, and graduate students working in materials science, nanotechnology, solid-state physics, and environmental monitoring.

IMPERIAL PUBLICATIONS
304, De Elmas Sonawala Cross Road 2,
Goregaon E, Mumbai-400063
Maharastra

9 789391 044862